



HAL
open science

Numerical modeling and simulation of steel gases combustion under flameless combustion

Huu-Tri Nguyen

► **To cite this version:**

Huu-Tri Nguyen. Numerical modeling and simulation of steel gases combustion under flameless combustion. Fluid Dynamics [physics.flu-dyn]. Normandie Université, 2022. English. NNT : 2022NORMIR38 . tel-04089000

HAL Id: tel-04089000

<https://theses.hal.science/tel-04089000>

Submitted on 4 May 2023

HAL is a multi-disciplinary open access archive for the deposit and dissemination of scientific research documents, whether they are published or not. The documents may come from teaching and research institutions in France or abroad, or from public or private research centers.

L'archive ouverte pluridisciplinaire **HAL**, est destinée au dépôt et à la diffusion de documents scientifiques de niveau recherche, publiés ou non, émanant des établissements d'enseignement et de recherche français ou étrangers, des laboratoires publics ou privés.



Normandie Université

THÈSE

Pour obtenir le diplôme de doctorat

Spécialité Energétique

Préparée à l'INSA de Rouen Normandie

NUMERICAL MODELING AND SIMULATION OF STEEL GASES COMBUSTION UNDER FLAMELESS COMBUSTION

présentée et soutenue par

HUU-TRI NGUYEN

**Thèse soutenue publiquement le 16 Décembre 2022
devant le jury composé de**

A. PARENTE	Professeur à l'Université Libre de Bruxelles	Rapporteur
J. XIA	Professeur à Brunel University Londres	Rapporteur
P-D. NGUYEN	Senior research engineer, Global R&D ArcelorMittal	Examineur
A. HADJADJ	Professeur à l'INSA de Rouen Normandie	Examineur
P. DOMINGO	Directrice de recherche CNRS	Co-directrice de thèse
L. VERVISCH	Professeur à l'INSA de Rouen Normandie	Directeur de thèse

■ Thèse dirigée par Luc VERVISCH et Pascale DOMINGO, laboratoire CORIA (UMR 6614 CNRS)



Remerciements

Je tiens tout d'abord à remercier chaleureusement mes directeurs de thèse, Pascale Domingo et Luc Vervisch, pour leur soutien et leur guidance tout au long de ce parcours de recherche. Votre expertise et votre expérience ont été précieuses pour moi, et j'ai appris beaucoup de vous.

Je tiens à exprimer ma plus sincère gratitude pour mon responsable d'ArcelorMittal, Phuc-Danh Nguyen. J'ai apprécié votre engagement, votre disponibilité ainsi que les discussions fructueuses que nous avons eues. Votre contribution a donné une dimension supplémentaire et a renforcé la pertinence de ce projet.

Je m'adresse mes remerciements les plus profonds à mes collègues du bureau, anciens et nouveaux, ainsi que mes amis, Florian Monier, Coralie Bros, Camille Barnaud, Alexandre-Henri Segond, Andréa Seltz, Emilie Yhuel, Florian Kissel, Quentin Cerutti, Louis Duhem Duvilla, Pierre Bénard pour leur amitié, leur soutien et les souvenirs inoubliables pendant cette aventure.

Je tiens à remercier toutes les personnes que j'ai rencontrées pendant ces années ainsi qu'à celles qui ont eu la gentillesse de faire cette expérience un moment très profitable.

Je tiens à remercier aussi ma famille pour leur amour inconditionnel et leur soutien sans faille tout au long de ce parcours. Leur encouragement m'a donné la force de persévérer dans les moments difficiles.

Enfin, je suis reconnaissant pour toutes les opportunités et les expériences qui ont rendu cette thèse possible. Merci encore pour votre soutien et votre aide.

Contents

1	Introduction	14
1.1	Context	14
1.1.1	The world is changing	14
1.1.2	Paris Agreement	18
1.1.3	ArcelorMittal's strategies	19
1.1.4	Flameless combustion	20
1.1.5	Combustion modelling and the role of chemistry	23
1.1.6	Cross-domain technologies - Artificial Intelligence	25
1.2	Thesis objectives	27
1.2.1	Novel strategy to include heat loss effects in chemistry reduction	27
1.2.2	Acceleration of chemistry integration using machine learning techniques and neural networks	27
1.3	Manuscript content	27
1.4	Publications	28
1.4.1	Peer-reviewed international journals	28
1.4.2	International conferences	28
2	Turbulent reacting flows	30
2.1	Turbulent reacting flows equations	30
2.1.1	Mixture composition	30
2.1.2	Thermodynamic	31
2.1.2.1	Equation of state	32
2.1.3	Equations	32
2.1.3.1	Mass conservation	33
2.1.3.2	Momentum conservation	33
2.1.3.3	Species conservation	33
2.1.3.4	Energy conservation	34
2.2	Chemical kinetics	35
2.2.1	Species source terms	35
2.2.2	Reaction rates	35
2.2.2.1	Arrhenius law	36
2.2.2.2	Reverse reaction rate constant and equilibrium	36
2.2.2.3	Gibbs free energy	37
2.3	Combustion regimes	37
2.3.1	Premixed flame	37

2.3.2	Diffusion flame	39
2.3.3	Partially premixed combustion	40
2.4	RANS-LES formalism	41
2.4.1	Turbulence introduction	41
2.4.2	Computational Fluid Dynamics (CFD) strategies	42
2.4.3	RANS modelling	43
2.4.3.1	Standard k - ϵ	45
2.4.3.2	RNG k - ϵ	45
2.4.4	LES modelling	46
2.4.4.1	Formalism	46
2.4.4.2	Turbulent sub grid scale models	48
2.5	Radiation	49
3	Chemical schemes reduction for applications under flameless combustion condition	53
3.1	Optimised and reduced chemistry (ORCh)	55
3.2	Strategy for chemical schemes reduction including heat loss	56
3.3	UMONS case configuration	57
3.4	Results and discussions	60
3.4.1	0D time evolution simulation of ORCh	60
3.4.1.1	Heat loss implementation	60
3.4.1.2	Reduction and optimisation	65
3.4.2	3D CFD RANS simulation	69
3.4.2.1	Numerical simulation setup	69
3.4.2.2	Energy balance and measurements at the furnace exit	70
3.4.2.3	Comparison of numerical results with in-furnace measurements	71
3.5	Conclusion	77
4	Machine learning for integrating combustion chemistry in numerical simulations	79
4.1	Database generation	80
4.2	Data pre-treatment	82
4.2.1	Data clustering	83
4.2.2	Local principal component analysis (LPCA)	84
4.3	Neural network	87
4.4	Results of 0D time evolution simulation of ORCh	87
4.5	ANN reduced chemistry for flameless combustion	91
4.5.1	Training database	91
4.5.2	Clustering thermochemical data and ANN structure	92
4.5.3	ANNs verification and database blurring	94
4.5.4	Flow solver and modeling	97
4.5.4.1	Turbulence-chemistry interaction modelling	98
4.5.4.2	Radiative heat transfer modelling	99
4.6	Results and comparison against measurements	99
4.7	Conclusion	104

5	General conclusions and perspectives	106
5.1	Conclusions	106
5.1.1	Chemical scheme reduction for applications under flameless combustion condition	106
5.1.2	Machine learning for integrating combustion chemistry in numerical simulation .	106
5.2	Perspectives	107
	Bibliography	110

Nomenclature

Abbreviations

Symbol	Description
AI	Artificial Intelligence
BFG	Blast Furnace Gas
BOFG	Convertor Gas
COG	Coke Oven Gas
COP	Conference of the Parties
CFD	Computational Fluid Dynamics
CPU	Central Processing Unit
DNS	Direct Numerical Simulation
DOM	Discrete Ordinates Model
DRI	Direct Reduced Iron
DRG	Directed Relation Graph
DRGEP	DRG with Error Propagation
DTRM	Discrete Transfer Radiation model
EAF	Electric Arc Furnace
GHG	GreenHouse Gas
IPCC	Intergovernmental Panel on Climate Change
INSA	National Institute of Applied Sciences
LCV	Low Calorific Fuel
LES	Large-Eddy Simulation
ORCh	Optimised and Reduced Chemistry
PDF	Probability Density Function
RTE	Radiative Transfer Equation
UN	United Nations
UNDRR	United Nations Office for Disaster Risk Reduction
UNFCCC	United Nations Framework Convention on Climate Change

Roman letters

Symbol	Description	Unit
A_j	Pre-exponential factor of reaction j	Variable
c	Normalised progress variable	—
C_k	Consumption rate of species k	$\text{kg}\cdot\text{m}^{-3}\cdot\text{s}^{-1}$
C_p	Mixture mass heat capacity at constant pressure	$\text{J}\cdot\text{kg}^{-1}\cdot\text{K}^{-1}$
$C_{p,k}$	Specific heat capacity of species k at constant pressure	$\text{J}\cdot\text{kg}^{-1}\cdot\text{K}^{-1}$
C_p^m	Mixture molar heat capacity at constant pressure	$\text{J}\cdot\text{mol}^{-1}\cdot\text{K}^{-1}$
$C_{p,k}^m$	Molar heat capacity of species k at constant pressure	$\text{J}\cdot\text{mol}^{-1}\cdot\text{K}^{-1}$
C_S	Smagorinski model constant	—
C_W	Wale model constant	—
D_k^H	Hirschfelder and Curtiss diffusion coefficient of species k	$\text{m}^2\cdot\text{s}^{-1}$
D_{kj}	Binary diffusion coefficient of species j into species k	$\text{m}^2\cdot\text{s}^{-1}$
D_{th}	Thermal diffusivity coefficient	$\text{m}^2\cdot\text{s}^{-1}$
E_j	Activation energy of reaction j	$\text{J}\cdot\text{mol}^{-1}$
F	Troe or Lindemann fall-off correction term	—
F_{ext}	External force	—
\mathcal{G}	Convolution kernel of the filter	—
H	Mixture mass enthalpy	$\text{J}\cdot\text{kg}^{-1}$
H_k	Mass enthalpy of species k	$\text{J}\cdot\text{kg}^{-1}$
H^m	Mixture molar enthalpy	$\text{J}\cdot\text{mol}^{-1}$
H_k^m	Molar enthalpy of species k	$\text{J}\cdot\text{mol}^{-1}$
h_s	Mass sensible enthalpy	$\text{J}\cdot\text{kg}^{-1}$
$h_{s,k}$	Mass sensible enthalpy of species k	$\text{J}\cdot\text{kg}^{-1}$
K_j	Arrhenius term of reaction j	Variable
K_0	Low pressure limit Arrhenius term of reaction j	Variable
K_∞	High pressure limit Arrhenius term of reaction j	Variable
$K_{eq,j}$	Equilibrium constant of reaction j	—
K_{fj}	Forward Arrhenius term of reaction j	Variable
K_{rj}	Reverse Arrhenius term of reaction j	Variable
k	Turbulent kinetic energy	$\text{m}^2\cdot\text{s}^{-2}$
L_e	Energetic length	m
l_k	Kolmogorov length	m
l_t	Integral length	m
L	Characteristic size of the flow	m

\mathcal{M}_k	Molecular formula of species k	—
m_p	Mass of particle p	kg
n	Normal to the flame front	—
N_{bits}	Number of chromosome binary digits	—
N_p	Number of stochastic particles	—
N_r	Number of reactions	—
N_{sp}	Number of species	—
P°	Reference pressure	Pa
P	Pressure	Pa
P_k	Production rate of species k	$\text{kg}\cdot\text{m}^{-3}\cdot\text{s}^{-1}$
P_r	Fall-off pressure correction term	$\text{mol}\cdot\text{m}^{-3}$
\dot{Q}	External heat sources	$\text{W}\cdot\text{m}^{-3}$
\dot{Q}_m	Total mass flow rate	$\text{kg}\cdot\text{s}^{-1}$
\dot{q}_m	Elementary mass flow rate	$\text{kg}\cdot\text{s}^{-1}$
\dot{Q}_{fj}	Forward rate of reaction j	$\text{mol}\cdot\text{m}^{-3}\cdot\text{s}^{-1}$
\dot{Q}_i	Heat flux	$\text{W}\cdot\text{m}^{-2}$
\dot{Q}_j	Rate of reaction j	$\text{mol}\cdot\text{m}^{-3}\cdot\text{s}^{-1}$
\dot{Q}_{rj}	Reverse rate of reaction j	$\text{mol}\cdot\text{m}^{-3}\cdot\text{s}^{-1}$
\mathcal{R}	Ideal gas constant	$\text{J}\cdot\text{mol}^{-1}\cdot\text{K}^{-1}$
s	Stoichiometric ratio	—
S	Mixture mass entropy	$\text{J}\cdot\text{kg}^{-1}\cdot\text{K}^{-1}$
\mathbf{S}	Strain tensor	s^{-1}
S	Flame sensor	—
S_{ij}	Strain tensor component	s^{-1}
S_k	Mass entropy of species k	$\text{J}\cdot\text{kg}^{-1}\cdot\text{K}^{-1}$
S^m	Mixture molar entropy	$\text{J}\cdot\text{mol}^{-1}\cdot\text{K}^{-1}$
S_k^m	Molar entropy of species k	$\text{J}\cdot\text{mol}^{-1}\cdot\text{K}^{-1}$
S_L^0	Laminar flame speed	$\text{m}\cdot\text{s}^{-1}$
T	Temperature	K
T_{eq}	Equilibrium temperature	K
T_0	Fresh gases temperature	K
T°	Reference temperature	K
T^∞	Temperature in the ambient atmosphere surrounding a particle	K
t	Time	s
\mathbf{u}	Velocity vector	$\text{m}\cdot\text{s}^{-1}$
u_i	Component i of the velocity vector	$\text{m}\cdot\text{s}^{-1}$

$V_{c,i}$	Correction velocity of species k in direction i	$\text{m}\cdot\text{s}^{-1}$
$V_{k,i}$	Diffusion velocity of species k in direction i	$\text{m}\cdot\text{s}^{-1}$
W	Mean molecular weight	$\text{kg}\cdot\text{mol}^{-1}$
W_k	Species k molecular weight	$\text{kg}\cdot\text{mol}^{-1}$
\mathbf{x}	Vector of position	m
x_i	Component i of the position vector	m
X_k	Species k mole fraction	—
$[X_k]$	Species k concentration	$\text{mol}\cdot\text{m}^{-3}$
Y_k	Mass fraction of species k	—
$Y_{k,\infty}$	Mass fraction of species k in the ambient atmosphere of a particle	—
$Y_{F,0}$	Fuel mass fraction in fresh gases	—
$Y_{O,0}$	Oxidiser mass fraction in fresh gases	—
$Y_{F,eq}$	Fuel mass fraction at equilibrium	—
Z	Mixture fraction	—

Greek letters

Symbol	Description	Unit
β_j	Temperature exponent for reaction j	—
β_k	Third body coefficient of species k	—
δ_{ij}	Kronecker symbol	—
δ_L	Laminar flame thickness	m
δ_L^{th}	Thermal thickness	m
Δ	Mesh size	m
$\Delta h_{f,k}^{\circ,m}$	Molar standard enthalpy of species k at reference conditions	$\text{J}\cdot\text{mol}^{-1}$
ΔG_j°	Gibbs free energy change per mole of reaction j	$\text{J}\cdot\text{mol}^{-1}$
ϵ	Viscous dissipation of the turbulent kinetic energy	$\text{m}^2\cdot\text{s}^{-3}$
θ_k	Thermal diffusion coefficient of species k	$\text{m}^2\cdot\text{s}^{-1}\cdot\text{K}^{-1}$
θ	Source term for the Lagrangian phase	Variable
λ_{th}	Mixture thermal conductivity	$\text{W}\cdot\text{m}^{-1}\cdot\text{K}^{-1}$
μ	Dynamic viscosity coefficient	$\text{kg}\cdot\text{m}^{-1}\cdot\text{s}^{-1}$
ν	Kinematic viscosity coefficient	$\text{m}^2\cdot\text{s}^{-1}$
ν_{kj}	$\nu_{kj}'' - \nu_{kj}'$	—
ν_{kj}'	Species k stoichiometric coefficient in the reactants of reaction j	—
ν_{kj}''	Species k stoichiometric coefficient in the products of reaction j	—
ρ	Density	$\text{kg}\cdot\text{m}^{-3}$

ρ_0	Fresh gases density	$\text{kg} \cdot \text{m}^{-3}$
ρ_k	Partial density of species k	$\text{kg} \cdot \text{m}^{-3}$
ρ_p	Density of particle p	$\text{kg} \cdot \text{m}^{-3}$
τ	Characteristic time	s
τ_{ij}	Viscous tensor	$\text{kg} \cdot \text{m}^{-1} \cdot \text{s}^{-2}$
χ_j	Thermal diffusion ratio of species j	K^{-1}
$\dot{\omega}_k$	Mass reaction rate of species k	$\text{kg} \cdot \text{m}^{-3} \cdot \text{s}^{-1}$
$\dot{\omega}_T$	Combustion heat release	$\text{J} \cdot \text{m}^{-3} \cdot \text{s}^{-1}$

Mathematical operators

Symbol	Description
$\langle \phi \rangle$	Statistical averaging
$\bar{\phi}$	Spatial filtering
$\hat{\phi}$	Fourier transform
$\tilde{\phi}$	RANS Favre averaging or LES Favre filtering
ϕ'	Deviation from the mean: $\phi' = \phi - \langle \phi \rangle$
ϕ''	Fluctuations: $\phi'' = \phi - \bar{\phi}$

Non dimensional numbers

Symbol	Description
Da	Damköhler number
Le_k	Lewis number associated to species k
Pr	Prandtl number
Re	Reynolds number
Sc	Schmidt number

Principal chemical species

Symbol	Description
CH	Methylidyne
CH ₂	Methylene
CH ₃	Methyl radical
CH ₄	Methane
CH ₂ O	Formaldehyde
CH ₃ O	Methoxy radical

CO	Carbon monoxide
CO ₂	Carbon dioxide
H	Hydrogen atom
H ₂	Dihydrogen
H ₂ O	Water
HCO	Formyl radical
HO ₂	Hydroperoxyl radical
H ₂ O ₂	Hydrogen peroxide
O	Oxygen atom
O ₂	Dioxygen
OH	Hydroxyl radical
N ₂	Nitrogen
NO	Nitric oxide
N ₂ O	Nitrous oxide
NO ₂	Nitrogen dioxide

Chapter 1

Introduction

Contents

1.1	Context	14
1.1.1	The world is changing	14
1.1.2	Paris Agreement	18
1.1.3	ArcelorMittal's strategies	19
1.1.4	Flameless combustion	20
1.1.5	Combustion modelling and the role of chemistry	23
1.1.6	Cross-domain technologies - Artificial Intelligence	25
1.2	Thesis objectives	27
1.2.1	Novel strategy to include heat loss effects in chemistry reduction	27
1.2.2	Acceleration of chemistry integration using machine learning techniques and neural networks	27
1.3	Manuscript content	27
1.4	Publications	28
1.4.1	Peer-reviewed international journals	28
1.4.2	International conferences	28

1.1 Context

1.1.1 The world is changing

"Code red for humanity" is the statement made by United Nations (UN) Secretary-General António Guterres for the latest report of The Intergovernmental Panel on Climate Change (IPCC [1]). According to the IPCC report, the internationally-agreed 1.5 degrees Celsius threshold of global temperature above the pre-industrial levels could be breached in near term (cf. Figure 1.1) at the current rate of human activities. The global warming level is actually in the range of 0.8°C to 1.2°C since the Industrial Revolution and keeps increasing at 0.2°C rate per decade [1].

"What happened if the global temperature exceeds the 1.5°C threshold?" is a crucial question. An inconsequential fraction of difference in global temperature could lead to a huge difference of the life on Earth. Indeed, at the 0.8°C to 1.2°C threshold nowadays, the extreme weather and climate disasters are accelerating, in both frequency and intensity, around the world (cf. Figure 1.2 and 1.3).

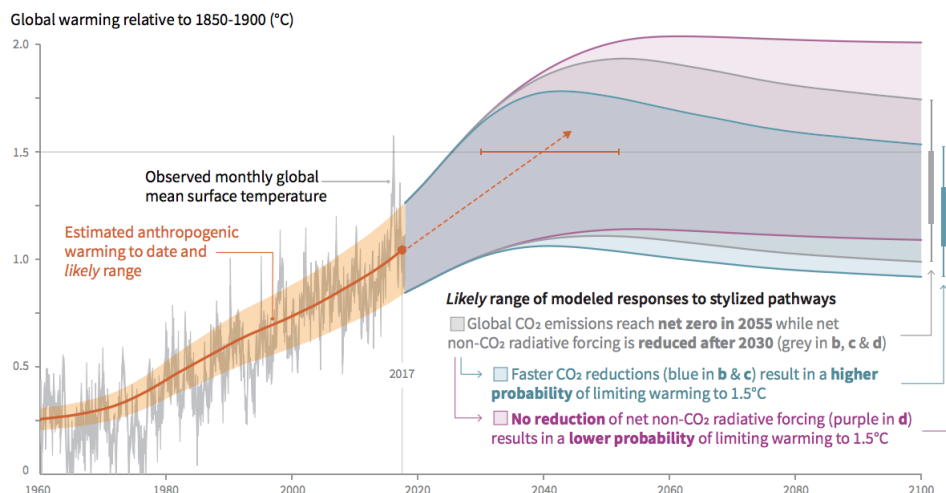


Figure 1.1: Observed and estimated global temperature change from 1960 to 2100 from IPCC report [1]. Global warming (estimated by orange line) will reach the global warming target 1.5°C between 2030 and 2052 at current rate instead of 2100.

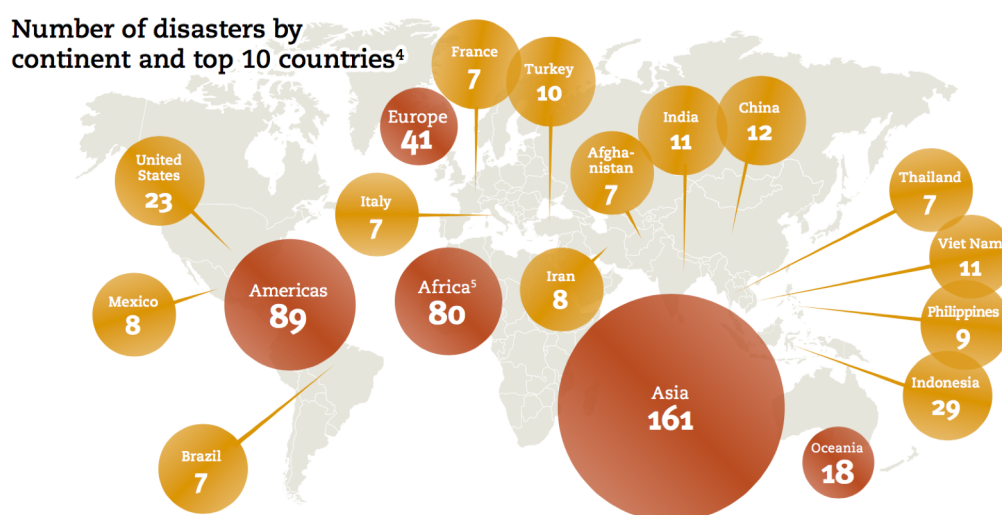


Figure 1.2: Number of disasters by continent and top 10 countries in 2020 [2].

In 2020, the United Nations Office for Disaster Risk Reduction (UNDRR) reported 389 disasters worldwide which caused 15 080 fatalities, impacted 98.4 millions people and created at least US\$171.3 billion of economic losses [2].

127 major storms and 201 severe floods occurred in 2020. These disasters surpassed 20% of the annual average between 2000 and 2019 (cf. Figure 1.3), caused 6 171 human deaths. Vietnam, one of the most weather-related hazard-prone countries, was struck by 9 destructive typhoons following ruinous floods, which led to 291 deaths, 66 missing and 7.7 million people affected in only 7 weeks of 2020 [3] (cf. figure 1.4).

In the same year, the heatwaves hit seriously Europe and became the deadliest event causing 42% of total deaths. France witnessed the hottest September since 1949, the temperature nearly reached 40°C in the South of France (cf. Figure 1.5).

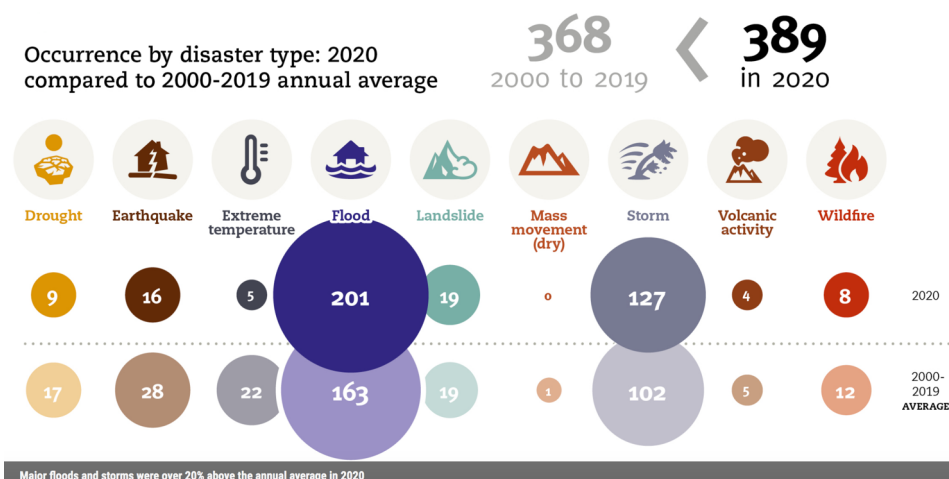


Figure 1.3: Disasters by type in 2020 compared with the annual average of period 2000-2019 [2].



Figure 1.4: Vietnam central coast during seven-week strike of typhoons and floods at October-November 2020 [4].

On the other side of the globe, at the end of 2019 and the beginning of 2020, Australia threatened by one of the hottest years in its history and suffered then a devastating 6-months wildfire which killed 33 people, burnt 19 millions hectares and destroyed over 3000 houses [6]. The data collected by Australian government shows the extreme temperature throughout the territory at December 2019 (from 40°C to 48°C) [7, 8] (cf. Figure 1.6(a) and 1.6(b)). In addition, over the years, the mean temperature anomaly is continuing to escalate (cf. Figure 1.6(c)). The worst scenario is about to come.

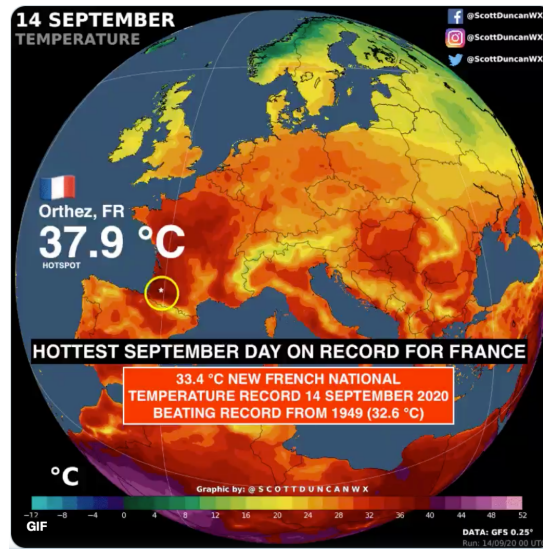


Figure 1.5: Hottest temperature record in France at 14 September 2020 during the heatwaves. Source: Scott Duncan [5].

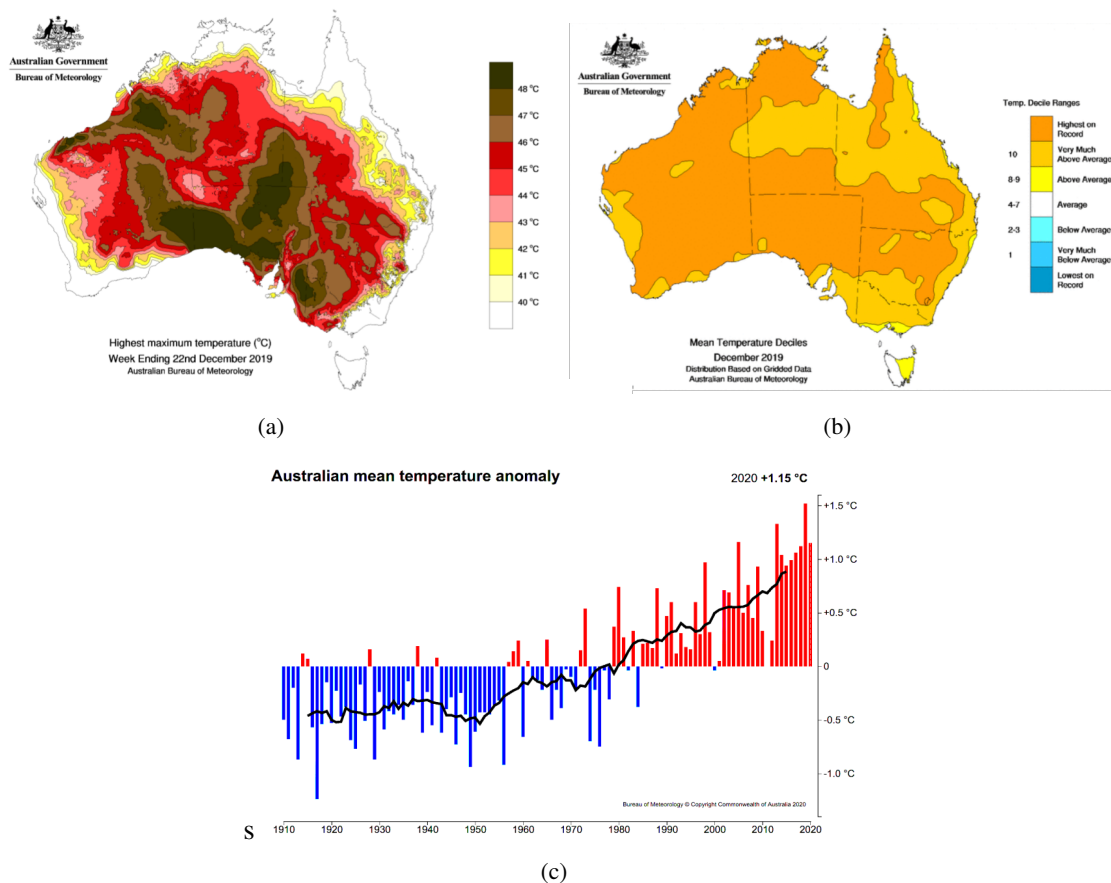


Figure 1.6: (a) Maximum temperature map in Australia at December 2019. (b) Mean temperature decile range in Australia at December 2019. (c) Australian mean temperature anomaly from 1910 to 2020. Black line represents 11-year moving average that grows constantly over the years. In 2020, the mean temperature anomaly is recorded at $1.15^{\circ}C$ [7, 8].

1.1.2 Paris Agreement

The world needs to strive decisively and pursue the most ambitious path to prevent exceeding of global warming by the end of the century. The root cause is undoubtedly the human-induced greenhouse gas (GHG) consisting essentially of carbon dioxide, methane, nitrous oxide and F-gases released by different sectors, from domestic consumption, agricultural activities to industrial demands (cf. Figure 1.7). Since the Industrial Revolution, the world observed a massive GHG emissions. Today, the level of emitted GHG reaches 50 billions tonnes per year (measured in Carbon dioxide equivalents [9]) and exponentially grows (cf. Figure 1.8 for CO₂ emissions).

Responding to such situation, the 21st Conference of the Parties (COP 21), held by the United Nations Framework Convention on Climate Change (UNFCCC) in Paris from 30 November to 12 December 2015, marked a historic turning point. 196 nations adopted an international mutual commitment to combat the climate change and forged the Paris Agreement [10]. Never before, many Heads of State and Government gathered together to a common aim: restrain global warming to well below 2°C and preferably 1.5°C by eliminating the harmful emitted GHG by 2050 [1, 10].

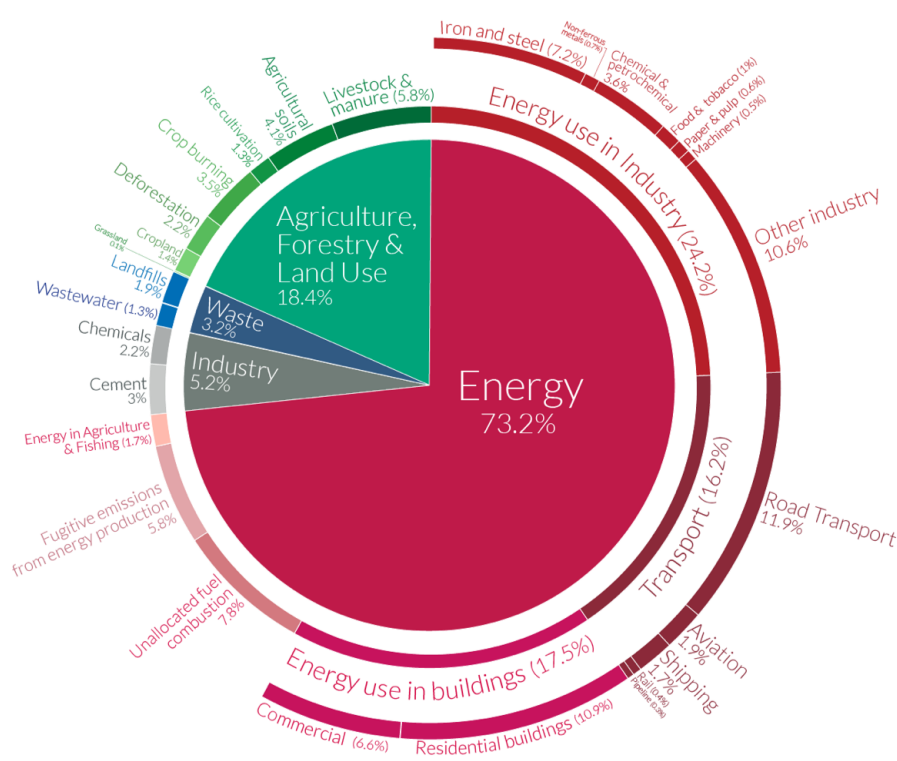


Figure 1.7: Global greenhouse gas emissions by sector (2016). Source: OurWorldInData.org - Climate Watch, the World Resources Institute [9].

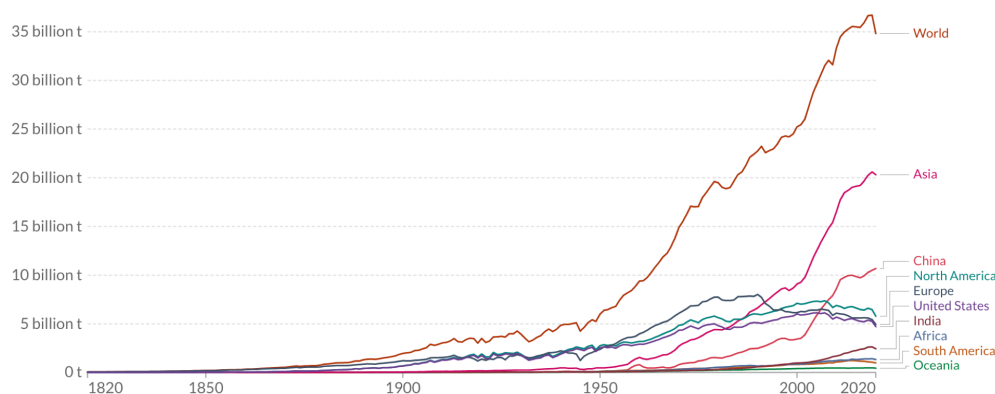


Figure 1.8: Annual CO₂ emissions from the fossil fuel burning. The global emitted CO₂ has increased more than seven times since 1950. Source: OurWorldInData.org - Global Carbon Project [9].

1.1.3 ArcelorMittal's strategies

Achieving the Paris Agreement's 1.5°C target requires the tremendous efforts and strengthened cooperations from countries and corporations in all sectors. The steel industry represents globally about 7% of the total GHG generated by humanity (cf. Figure 1.7). As a leader in the sector, ArcelorMittal commits to significantly reduce carbon footprint by 2050 in line with the commitment to the Paris Agreement. The Group targets are: 25% reduction in CO₂e emissions intensity at the global level by 2030 while the target in Europe is increased to 35% reduction in CO₂e emissions by 2030, and becoming carbon neutral by 2050. As important intermediate milestones, the Group is transforming two steel plants in Europe to become the world's first full-scale zero carbon-emissions steel plants by 2025.

The decarbonization strategy is mainly based on DRI (Direct Reduced Iron) and smart carbon routes (cf. Figure 1.9). While the electrification with green energy will play important role in some moderate temperature process, high temperature process still relies heavily on combustion released energy but with a shift to alternative reductants and fuels, optimized industrial auto-produced gases utilization such as Coke Oven Gas (COG) and Blast Furnace Gas (BFG), sustainable bio-energy, green hydrogen,... Designing new or upgrading existing combustion systems have to fulfil the requirements in terms of high energy efficiency, low pollutant emissions of soot and NO_x, and fuel flexibility, i.e. being able to run multiple fuels and/or oxidizers in a single furnace with stable combustion conditions.

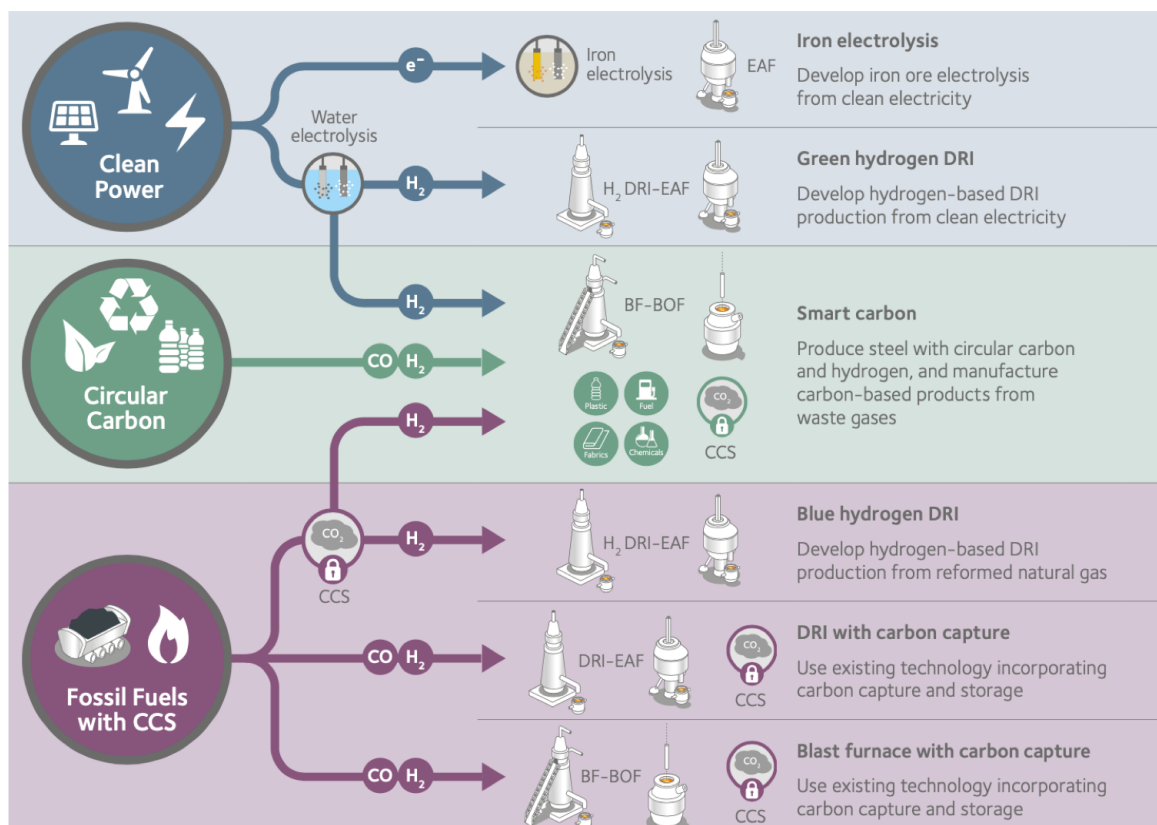


Figure 1.9: Steelmaking process from raw materials to liquid steel integrating new decarbonization routes (Climate Action Report 2019 of ArcelorMittal).

1.1.4 Flameless combustion

In the 80's, in the interest of reducing the energy losses and improving the industrial furnace thermal efficiency, the waste heat recovery system has been extensively developed in order to extract heat from the furnace flue-gases to preheat the incoming combustion air. The developed systems, such as the recuperative and regenerative burners, have capacity to recover up to 90% of the waste heat in the flue gases and allow to save an enormous amount of energy. Nevertheless, such systems lead to an inevitable negative effect of increasing the temperature peak during combustion which magnifies the production of the nitrogen oxides NO_x.

The nitrogen oxides NO_x generally indicates the nitrogen oxide NO, the nitrogen dioxide NO₂ and the nitrous oxide N₂O which lead to the deterioration of human health by causing the breathing problems, forming the harmful smog, acid rain and affecting the tropospheric ozone. The combustion predominantly emits the NO_x in the form of NO through different sources, such as thermal NO, fuel NO, prompt NO and NO formed via N₂O route:

- **Thermal NO** is formed from the nitrogen N₂ and oxygen O₂ contained in air during the combustion. The chemical path of this formation is proposed by Zel'dovich and well known as the Zel'dovich mechanism.





The thermal NO depends on the oxygen concentration and significantly on the temperature level (c.f. Figure 1.10). According to Wüning and Wüning [11], the NO is produced considerably if the oxygen is exposed to temperatures higher than 1600°C for only seconds. It will be reduced to milliseconds if the temperature is much higher than 2000°C . The thermal NO is the main source in combustion system.

- **Fuel NO** is formed by the reaction between the nitrogen in the fuel and the excess oxygen in the air. This formation is often occurred during the combustion of coal, heavy fuel or some sort of biomass which contains nitrogen.
- **Prompt NO** is revealed by Fenimore [12] by measuring the NO concentration near the low-nitrogen hydrocarbon flame front at low temperature. The NO in this case is formed in the fuel-rich zone where the radical species CH_i locate. The formation has a greater speed than the thermal NO, therefore it is called "prompt".
- **NO formation via N_2O route** is occurred under lean-fuel, low temperature and high pressure condition. Malte and Pratt [13] have proposed a 3-steps mechanism for this formation.

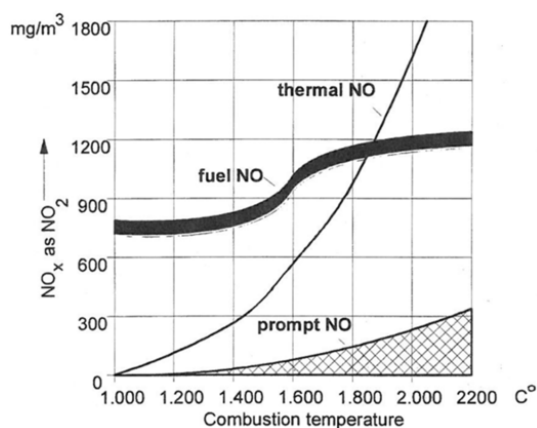
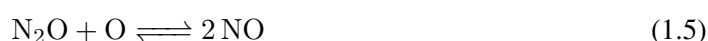
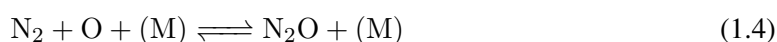


Figure 1.10: Temperature influence on NOx formation [14].

Since then, in order to preserve the benefit of the heat recovery system, many NOx reduction techniques have been investigated and classified into 2 categories. The downstream techniques treat NOx in the flue gases only after the combustion process by adding a reducing agent, such as ammonia or urea. Conversely, the upstream techniques take place during the combustion [11] and some of these techniques are listed below:

- **Staged combustion:** The combustion proceeds in several stages, normally two. In the first stage, the fuel is burnt at under-stoichiometric conditions with low concentration of oxygen. The extra air is then fed in the second stage to complete the combustion.

- **Reburning:** The combustion product containing NO is supplied by injecting fuel for an additional burning stage which transforms the NO to N₂.
- **Flame cooling:** The flame temperature is cooled down by means of forced convection, radiation, water or steam jet injections.
- **Flue gas recirculation:** The flue gas are mixed externally, or internally, with the reactants before, or during, the combustion process. The internal mixing could require the particular design of the combustion chamber and the burners in order to achieve the dynamic recirculated flow inside the chamber.

In the 90's, researchers who conducted studies with the flue gas recirculation techniques discovered the high diluted combustion regime. This combustion mode was first mentioned in the works conducted by Wüning and Wüning [11] and Hasegawa and Tanaka [15] (by measuring experimentally the temperature distribution in high temperature diluted air condition) which opened up a promising perspective for combustion technologies. This state-of-the-art combustion mode is also known as Flameless Oxidation [11], MILD Combustion (Moderate or Intense Low Oxygen Dilution) [16], High Temperature Air Combustion (HiTAC) [17, 18] or Diluted Combustion [19] acronyms which refer to slightly different concepts and operating conditions [20]. The term "flameless" indicates the absence of a visible flame front during the combustion. The flameless combustion will be retained for the rest of the present manuscript.

The principle of flameless combustion is based on high dilution by recirculating the internal exhaust gas at the temperature above the self-ignition level. The highly diluted stream reduces significantly the local concentration of oxygen in the reaction zone. As a consequence, the combustion reaction rate decreases extensively so leading to the augmentation of the reaction zone volume, then contributing to the uniformity of the temperature field and to the reduction of peak flame temperature. Milani and Saponaro [19] have proven this property by testing a 1.5MW natural gas furnace in both conventional and flameless combustion regimes (c.f. Figure 1.11). This reduction of peak flame temperature reduces substantially the thermal NOx formation which augments drastically at high temperature (c.f. Figure 1.10) while benefits from higher thermal efficiency with higher preheated air temperature thanks to heat recovery systems.

The internal recirculated burnt gas inside the combustion chamber is attained dynamically by using a special burner design in order to secure the combustion stability. According to Wüning and Wüning [11], the recirculation rate can be quantified by the ratio between the mass flow rate of recirculated burnt gases (\dot{m}_{rec}) and the mass flow rate of reactants (fuel \dot{m}_{fuel} and air \dot{m}_{air}) before the reaction (cf. equation 1.7).

$$K_v = \frac{\dot{m}_{rec}}{\dot{m}_{air} + \dot{m}_{fuel}} \quad (1.7)$$

Several combustion modes can be identified with two parameters: furnace temperature and recirculation rate K_v , as shown in figure 1.12 [11]. The stable classical flame (zone A) is observed at low recirculation rate for a wide range of furnace temperature. While increasing the recirculation rate at high furnace temperature, the flame becomes unstable, lifts off and blows out (zone B). If the recirculation rate keeps growing and the furnace temperature is maintained sufficiently high (above the self-ignition level), a steady form of flameless combustion will occur. For this reason, a preheating of furnace is required for the operation under flameless combustion mode. Flameless is often a first choice as it is an advanced combustion technology which gives positive impact on the energy saving (high combustion efficiency) and the environment (low emissions of soot and NOx), and can ensure the fuel flexibility.

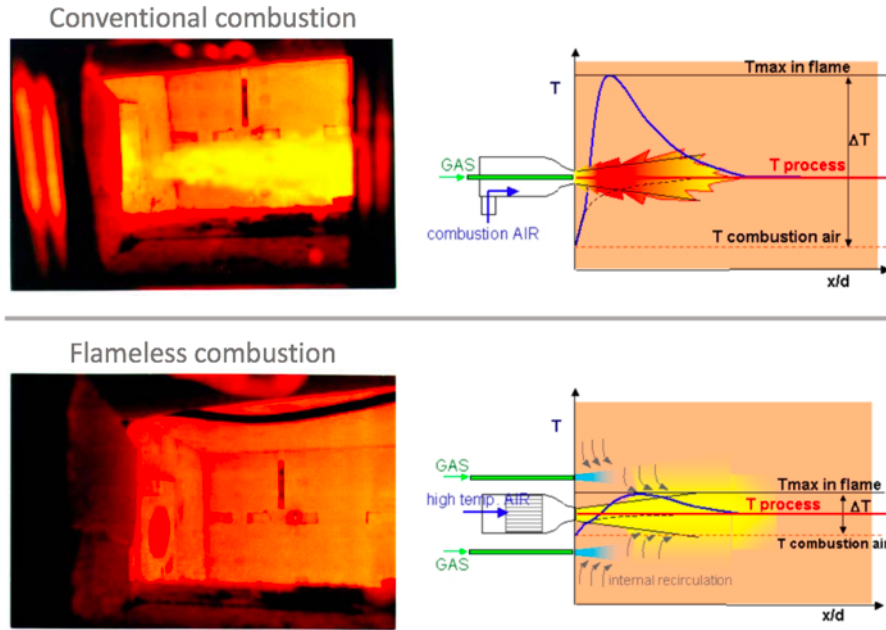


Figure 1.11: Flame images (left) and temperature distribution (right) of the conventional (top) and flameless combustion (bottom) in a 1.5MW furnace test [19]. The temperature peak is drastically decreased under flameless combustion regime, so thermal NOx.

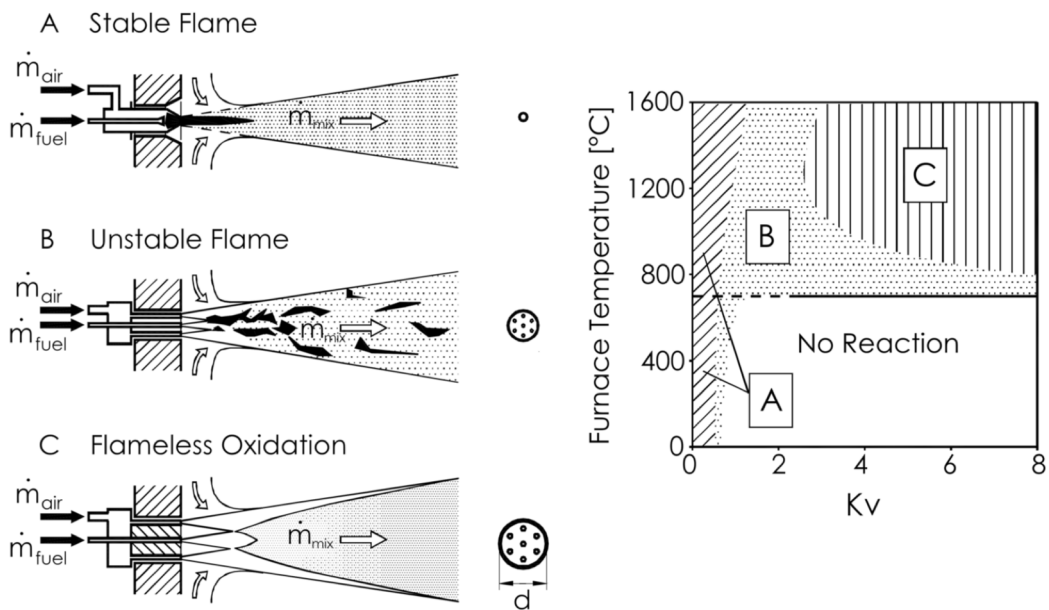


Figure 1.12: Stability limits of different combustion modes [11, 21, 22]

1.1.5 Combustion modelling and the role of chemistry

The numerical modelling of turbulent combustion has made significant progress to help in the design of systems operating with a single fuel stream, liquid or gaseous, and, a single oxidizer stream [23]. In

particular, the description of the complexity of combustion chemistry and molecular transport benefitted from the tabulation of detailed chemistry based on the hypothesis of two-inlet burners [24, 25, 26, 27, 28]. With these approaches, the control of chemistry is reduced to two variables, one describing the overall progress of the reaction and the other capturing the mixing between fuel and oxidizer streams. These methods are very efficient in terms of computing CPU cost and therefore largely used in the academic environment and also now popularised by commercial software.

As mentioned above, ArcelorMittal is operating and upgrading combustion systems featuring multiple injections of fuel and oxidizers and multiple combustion regimes (premixed, non-premixed, etc.). In these furnaces, both the enthalpy (temperature) and the chemical composition are specific to every single injection, thus covering a large range of thermochemical conditions. The objective of this project is to develop a framework/tool to address the numerical modelling of such multiple inlet combustion problems such as non-adiabatic regime (convective and radiative transfer); flameless combustion (dilution by burnt gases); multiple compositions and low calorific fuels (for energy recovery, mitigating environmental impact, and managing fuel flexibility).

Modelling the flameless combustion regime is challenging compared to the conventional combustion cases for which the approximation "mixed is burnt" [29] (for non-premixed combustion) is frequently applied. The chemistry in this approach is assumed infinitely fast and irreversible. Hence, the burnt field can be calculated through the mixture fraction by tracking the local equivalence ratio (fuel/air ratio) of the mixture (no reaction rate or chemical equilibrium information required). In furnaces, the recirculated gas dilutes strongly the reaction zone and delays the reaction speed, as a consequence, the chemistry cannot be considered infinitely fast. Several efforts from Orsino et al [30], Christo et al. [31] and Lupant et al [32] have been attempted using "mixed is burnt" approximation associated with Probability density function (PDF) in the flameless combustion cases. With this modelling approach, they reported the over-estimation of the temperature field, thus of the NO_x prediction (calculated in post-processing).

Another approach has been proposed by Magnussen and al [33, 34, 35] and are well known as "Generalized Finite Rate" (GFR). Variant models such as Eddy-Dissipation (ED), Eddy-Dissipation/Finite Rate (EDFR), Eddy-Dissipation Concept (EDC) can be mentioned. These models resolve all transport equations for each species whereas only one transport equation of mixture fraction is solved in the tabulated chemistry models. This transport equation system allows to provide the production rate of species while considering the interaction between turbulence and chemical kinetics (or reaction kinetics). The GFR models can theoretically allow to use the skeletal/detailed chemical kinetic schemes describing the reaction paths in combustion process such as GRI-3.0 [36] (53 species and 325 elementary reactions), POLOMI version 1412 [37] (107 species and 2642 reactions), AramcoMech2.0 [38] (502 species and 2716), Glarborg [39, 40, 41] (97 species and 779 elementary reactions). The number of species involved is very large and it cannot be easily introduced in the simulations of complex industrial large-scale combustion systems. There exists a large variety of highly-reduced kinetic schemes (global scheme) in the literature [42, 43, 44, 45, 46] or the semi-reduced scheme such as KEE58 [47] (18 species and 58 elementary reactions), Smooke [48] (17 species and 35 elementary reactions). However, the existing detailed mechanisms were developed and validated in conventional combustion regime with conventional fuel, while their performance for MILD combustion fed by various future fuel (bio-gas, mixture of by-product gases, etc.) is still in question. Therefore, reduced schemes that are able to imitate the detailed scheme in such conditions is highly demanded for these latter simulations.

Recently, Lu and Law developed chemistry reduction method for oxy-fuel combustion, which is based on the combination of Directed Relation Graph (DRG) [49, 50], DRG-aided sensitivity analysis

(DRGASA) [51, 52], Unimportant Reaction Elimination [53] and Quasi-Steady State Approximation (QSSA) [54]. A. Stagni et al. (2016) [55] developed an extension of the species-targeted sensitivity-analysis of DRGASA and DRGEPSA [56] reduction by shifting its focus from the ignition delay time (a single point) to the whole dynamics of formation of the considered species (a curve). However, the effect of heat loss (by radiation especially in the industrial furnaces) on the reduced scheme was not included in these works. This information is vital in systems encountered by ArcelorMittal. A strategy, called ORCh, has been recently developed at CORIA to answer these questions by automatically reducing detailed chemical schemes and optimizing their rates (reaction constant parameters) under given operating conditions [57, 58, 59]. ORCh is presented in the section 3.1.

The choice of the detailed mechanism referenced flameless combustion as the input of ORCh is quite critical. One of the important criteria to accurately predict the behaviour of flameless regimes is the ignition delay time [60]. N.A.K. Doan (2019) [61] reported the accurate estimation of the ignition delay time of GRI3.0 against the experimental data of Hu et al. [62] for CH₄-air mixture at atmospheric pressure. Nevertheless, M. Fürst et al. (2018) [60] shown that the detailed mechanism scheme POLIMI (version 1412) has the smallest average error with reference to the experimental target in their case against GRI3.0, GRI2.11, AramcoMech1.3, AramcoMech2.0 and some others detailed schemes. M. Ferraroti, M. Fürst et al. (2018) [63] also claimed via an URANS simulation for a near-industrial case that GRI2.11 over-predict the temperature and is only suited for the high temperature case (above 1300K). Two schemes POLIMI-25 (25 species & 154 reactions) and POLIMI-31 (31 species & 205 reactions) reduced from the detailed scheme POLIMI (version1412) using the procedure of Stagni et al. [55] are also tested and provide a good agreement with the experimental data. The literature review indicates that POLIMI (version 1412) is suitable for this work, nonetheless the GRI3.0 is also a strong candidate.

1.1.6 Cross-domain technologies - Artificial Intelligence

In the recent decade, the world is seeing the massive evolution of artificial intelligence based on the training of neural networks from the academic to the industry. Though, the history started in 1943 when Walter Pitts and Warren McCulloch [64] published a mathematical model for the biological neuron using electrical circuits (cf. Figure 1.13). Yet, this first ever concept of neural network had limited capability and was not able to "learn".

Until 1957, Frank Rosenblatt [65] built a modified model based on the concept of Walter Pitts and Warren McCulloch in order to discover how the human brain works. The neural net is implemented on an IBM machine at the Cornell Aeronautical Laboratory and named it Perceptron (cf. Figure 1.14) which has a learning mechanism and is able to do a binary classification (the output is 0 or 1).

Then, in 1965, Alexey Grigoryevich Ivakhnenko and Valentin Grigor'evich Lapa constructed the first ever multi-layer neural network by combining multiple perceptrons into a single network which can be called "Artificial Neural Network" (ANN). This is often considered as the begin of deep learning.

Through years of development, the neural networks have achieved remarkable milestones. Since 2015, the trained convolutional neural networks bypass the human performance on the popular ImageNet dataset [67]. Another significant breakthrough is AlphaFold, developed by Google's DeepMind AI, which could determine the 3D shape of proteins and provide a solution for a 50-year-old challenge in biology history.

Recent progress in the domain of artificial intelligence represent great opportunities for combustion modelling and simulation. Indeed, the neural networks were used to develop data driven turbulent combustion modeling [68, 69, 70, 71, 72, 73, 74], or to analyse experimental measurements [75] and to

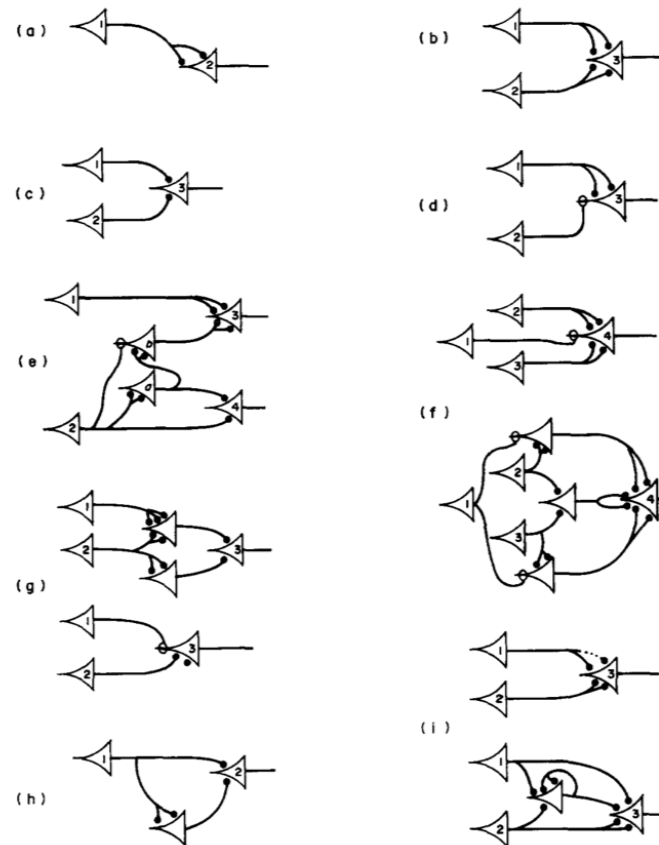


Figure 1.13: Different types of neuron modelled using electrical circuit by Walter Pitts and Warren McCulloch [64]

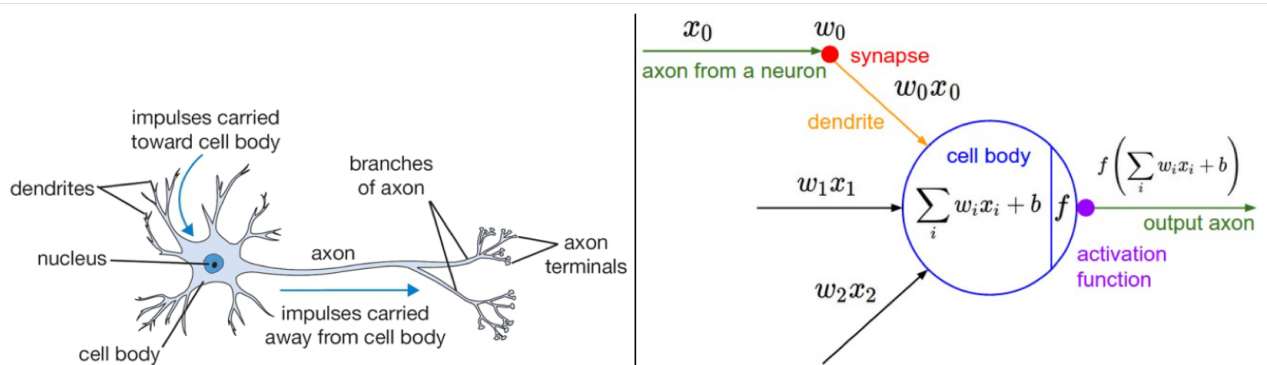


Figure 1.14: Perceptron model comparing to the biological neuron [66]

develop digital twins for process control [76]. Chemistry reduction and its time integration acceleration [77, 78, 79, 80, 81] which can be developed using machine learning techniques have special interest for CFD simulations as it allows for significant CPU times reduction and performing the multiple simulations needed for the search of optimal design for a combustion system, furthermore, create a solid database for furnace digital twins. This is one of the focus of the present thesis work.

1.2 Thesis objectives

1.2.1 Novel strategy to include heat loss effects in chemistry reduction

The first objective of this PhD work is to develop and provide ArcelorMittal access to a chemistry reduction tool, ready to generate reduced chemical schemes specifically devoted to the modelling of steel gases turbulent combustion encountered in multi-inlet conditions for future fuels (bio-gas, mixture of by-product gases, etc.) affected by heat loss and also avoiding the use of two-inlet detailed chemistry tabulation. In the first stage, an effort to implement the heat loss effect into the reduction tool ORCh, is executed. The reduction and optimisation procedure of the detailed chemical mechanism on the specific conditions of a flameless combustion system (named UMONS cases) including the proposed heat loss concept has been carried out. Four reduced chemical schemes generated, with and without heat loss, from the reference detailed scheme GRI3.0 and POLIMI1412, were implemented into Fluent to perform RANS simulations of the flameless UMONS furnace.

1.2.2 Acceleration of chemistry integration using machine learning techniques and neural networks

A novel method for chemistry integration acceleration based on machine learning techniques and neural networks is also proposed. The turbulent non-premixed database for machine learning training is constructed from the thermochemical responses of the stochastic turbulent micro-mixing. The K-means unsupervised learning algorithm is used to partition the data of similar characteristics into different clusters. The Principal Component Analysis (PCA) algorithm is then applied locally on each cluster in order to transform the correlated data in the composition space into the PCA space in which the data becomes uncorrelated to secure the performance of the artificial neural network (ANN) training. The method was tested a posteriori on the ORCh simulations of a canonical configuration with promising results and drastic reduction of CPU times. The method is also applied for the coupling with CFD simulations.

1.3 Manuscript content

Chapter 2: Turbulent reacting flows

The manuscript introduces in the first place the fundamentals of the turbulent reacting flows. The RANS-LES formalism is then presented. The radiation model used in this thesis is also mentioned.

Chapter 3: Chemical schemes reduction for industrial applications under flameless combustion condition

In this chapter, the automatic Optimised and Reduced Chemistry tool (ORCh) is first presented. In order to generate a reduced and optimised scheme for numerical simulation of furnaces operating at specific condition, an improvement by adding the capability of considering the heat loss, under flameless combustion regime, is provided. This strategy is then validated on the UMONS pilot furnace 3D RANS simulations.

Chapter 4: Machine learning for integrating combustion chemistry in numerical simulations

The chapter 5 provides a novel strategy focusing on the introduction in flow simulations of complex chemistry through the training of neural networks. This strategy is then coupled with the 3D LES simu-

lations.

Chapter 5: General conclusions and perspectives

The last chapter resumes the general conclusions and the perspectives of this thesis.

1.4 Publications

1.4.1 Peer-reviewed international journals

- Huu-Tri Nguyen, Pascale Domingo, Luc Vervisch, Phuc-Danh Nguyen, *Machine learning for integrating combustion chemistry in numerical simulations*, Energy and AI 5 (2021): 100082.
- Phuc-Danh Nguyen, Huu-Tri Nguyen, Pascale Domingo, Luc Vervisch, *Flameless combustion of low calorific value gases, experiments and simulations with advanced radiative heat transfer modeling*, Physics of Fluids 34 (2022): 045123, special topic: Development and validation of models for turbulent reacting flows.
- Huu-Tri Nguyen, Camille Barnaud, Pascale Domingo, Luc Vervisch, Phuc-Danh Nguyen, *Large-Eddy Simulation of flameless combustion with neural-network driven chemistry*, Preprint submitted to Applications in Energy and Combustion Science (2022).

1.4.2 International conferences

- Huu-Tri Nguyen, Pascale Domingo, Luc Vervisch, Phuc-Danh Nguyen, *Chemistry reduction and optimisation for multi-physics flow simulations: Combining data clustering and principal component analysis with deep learning*, in 10th ECM, Naples, Italy, 2021.

Chapter 2

Turbulent reacting flows

Contents

2.1	Turbulent reacting flows equations	30
2.1.1	Mixture composition	30
2.1.2	Thermodynamic	31
2.1.3	Equations	32
2.2	Chemical kinetics	35
2.2.1	Species source terms	35
2.2.2	Reaction rates	35
2.3	Combustion regimes	37
2.3.1	Premixed flame	37
2.3.2	Diffusion flame	39
2.3.3	Partially premixed combustion	40
2.4	RANS-LES formalism	41
2.4.1	Turbulence introduction	41
2.4.2	Computational Fluid Dynamics (CFD) strategies	42
2.4.3	RANS modelling	43
2.4.4	LES modelling	46
2.5	Radiation	49

2.1 Turbulent reacting flows equations

The turbulent reacting flows are described by a set of first principle conservation equations which are linked with the composition and thermodynamic properties of the mixture.

2.1.1 Mixture composition

A mixture consists of N_{sp} number of chemical species, with k denoted *species*. The density of the k -species mixture is determined from ρ^k the partial density of each species k .

$$\rho = \sum_{k=1}^{N_{\text{sp}}} \rho_k . \quad (2.1)$$

The mass contribution of each species in the mixture is represented by the mass fraction Y_k , defined by the ratio between the species and the overall mixture density. The mass fraction Y_k is thus bounded between zero and unity, and its sum equals unity.

$$Y_k = \frac{\rho_k}{\rho} , \quad (2.2)$$

$$\sum_{k=1}^{N_{\text{sp}}} Y_k = 1 . \quad (2.3)$$

The species mole fraction X_k is also used. The relation between mole fraction X_k and mass fraction Y_k is described in equation 2.4. Its sum on all species also equals unity.

$$X_k = \frac{W}{W_k} Y_k , \quad (2.4)$$

$$\sum_{k=1}^{N_{\text{sp}}} X_k = 1 . \quad (2.5)$$

The mixture molecular weight W is computed based on the species molecular weight W_k and the mass fraction Y_k (eq. 2.6) or mole fraction X_k (eq. 2.7).

$$\frac{1}{W} = \sum_{k=1}^{N_{\text{sp}}} \frac{Y_k}{W_k} . \quad (2.6)$$

$$W = \sum_{k=1}^{N_{\text{sp}}} X_k W_k . \quad (2.7)$$

2.1.2 Thermodynamic

At constant pressure, the species molar heat capacity $C_{p,k}^m(T, P^\circ)$ depends on the temperature T . The empirical relation between the species molar heat capacity $C_{p,k}^m(T, P^\circ)$ and the temperature T is given by the NASA polynomials.

$$\frac{C_{p,k}^m(T, P^\circ)}{\mathcal{R}} = a_{1,k} + a_{2,k}T + a_{3,k}T^2 + a_{4,k}T^3 + a_{5,k}T^4 , \quad (2.8)$$

where $\mathcal{R} = 8.314 \text{ J} \cdot \text{mol}^{-1} \cdot \text{K}^{-1}$ is the ideal gas constant and $a_{i,k}$ are known coefficients.

The species molar enthalpy and entropy is represented as a function of the species molar heat capacity $C_{p,k}^m(T, P^\circ)$ (equation 2.9 and 2.10).

$$H_k^m(T, P^\circ) = \int_{\theta=T^\circ}^T C_{p,k}^m(\theta, P^\circ) d\theta + \Delta H_{f,k}^{\circ,m} , \quad (2.9)$$

$$S_k^m(T, P^\circ) = \int_{\theta=T^\circ}^T \frac{C_{p,k}^m(\theta, P^\circ)}{\theta} d\theta , \quad (2.10)$$

where $\Delta h_{f,k}^{\circ,m}$ denotes the molar standard enthalpy of formation of species k at reference pressure P° and reference temperature T° (commonly set at 298.15 K).

Therefore, the molar enthalpy and entropy of species k could also be expressed from the NASA polynomials approximation.

$$\frac{H_k^m(T, P^\circ)}{\mathcal{R}T} = a_{1,k} + a_{2,k}T + a_{3,k}T^2 + a_{4,k}T^3 + a_{5,k}T^4 + \frac{a_{6,k}}{T}, \quad (2.11)$$

$$\frac{S_k^m(T, P^\circ)}{\mathcal{R}} = a_{1,k} \log(T) + a_{2,k}T + \frac{a_{3,k}}{2}T^2 + \frac{a_{4,k}}{3}T^3 + \frac{a_{5,k}}{4}T^4 + a_{7,k}. \quad (2.12)$$

The coefficients a is commonly documented in the thermodynamic file accompanied with the chemical kinetic schemes. There are 2 sets of coefficients for each species, at low and high temperature.

The molar heat capacity, molar enthalpy and entropy of **mixture** are calculated as follows.

$$C_p^m(T, P^\circ) = \sum_{k=1}^{N_{sp}} X_k C_{p,k}^m(T, P^\circ), \quad (2.13)$$

$$H^m(T, P^\circ) = \sum_{k=1}^{N_{sp}} X_k H_k^m(T, P^\circ), \quad (2.14)$$

$$S^m(T, P^\circ) = \sum_{k=1}^{N_{sp}} X_k \left(S_k^m(T, P^\circ) - \mathcal{R} \log\left(\frac{P}{P^\circ}\right) - \mathcal{R} \log(X_k) \right). \quad (2.15)$$

The mass specific heat capacity, enthalpy and entropy of mixture (per unity of mass) could be characterised by divided the mixture molecular weight W (cf. equation 2.6 and 2.7).

$$C_p = \frac{C_p^m}{W}, \quad (2.16)$$

$$H = \frac{H^m}{W}, \quad (2.17)$$

$$S = \frac{S^m}{W}. \quad (2.18)$$

2.1.2.1 Equation of state

The ideal gas law (so called the equation of state) is frequently used in combustion to approximate the behaviour of many gases under a wide range of conditions. The law could be presented in multiple forms. In the numerical simulation for combustion, the ideal gas law is often stated as a function of pressure P , density ρ , mixture molecular weight W and ideal gas constant $\mathcal{R} = 8.314 \text{ J} \cdot \text{mol}^{-1} \cdot \text{K}^{-1}$.

$$P = \rho \frac{\mathcal{R}}{W} T = \rho \left(\sum_{k=1}^{N_{sp}} \frac{Y_k}{W_k} \right) \mathcal{R} T. \quad (2.19)$$

2.1.3 Equations

Combustion is occurred in the fluid flows in which species are transported by velocity and diffusion effect coupled with the mixture characterised by chemical kinetic and thermodynamic. These effects are described by the balanced equations expressing mass, momentum and energy conservations. The equation derivation could be found in [82, 83].

2.1.3.1 Mass conservation

The mass conservation is described by the continuity equation.

$$\frac{\partial \rho}{\partial t} + \frac{\partial \rho u_i}{\partial x_i} = 0. \quad (2.20)$$

with the velocity u_i along the i^{th} direction.

2.1.3.2 Momentum conservation

The momentum conservation without the volume force is represented as follows.

$$\frac{\partial \rho u_j}{\partial t} + \frac{\partial \rho u_i u_j}{\partial x_i} = -\frac{\partial P}{\partial x_j} + \frac{\partial \tau_{ij}}{\partial x_i}, \quad (2.21)$$

where τ_{ij} stands for the viscous tensor and is determined for Newtonian fluid as below.

$$\tau_{ij} = -\frac{2}{3}\mu \frac{\partial u_k}{\partial x_k} \delta_{ij} + \mu \left(\frac{\partial u_i}{\partial x_j} + \frac{\partial u_j}{\partial x_i} \right). \quad (2.22)$$

where μ refers to the mixture dynamic viscosity and δ_{ij} is the Kronecker symbol.

2.1.3.3 Species conservation

The chemical species conservation is characterised by the transport equation parameterised by the diffusion velocity $V_{k,i}$ of species k along the direction i and the species k chemical source term $\dot{\omega}_k$.

$$\frac{\partial \rho Y_k}{\partial t} + \frac{\partial}{\partial x_i} (\rho (u_i + V_{k,i}) Y_k) = \dot{\omega}_k, \quad (2.23)$$

The V_k diffusion velocities is calculated by solving a linear system with N_{sp} equations.

$$\begin{aligned} \sum_{j=1}^{N_{sp}} \frac{X_k X_j}{D_{kj}} (V_j - V_k) &= \nabla X_k + (X_k - Y_k) \frac{\nabla P}{P} \\ + \frac{\rho}{P} \sum_{j=1}^{N_{sp}} Y_k Y_j (F_{ext,j} - F_{ext,k}) \\ + \sum_{j=1}^{N_{sp}} \frac{X_k X_j}{\rho D_{kj}} \left(\frac{D_{th,k}}{Y_k} - \frac{D_{th,j}}{Y_j} \right) \frac{\nabla T}{T}, \end{aligned}$$

Solving N_{sp} equations requires a considerable cost. Hirschfelder and Curtiss thus proposed a "mixture averaged" simplified estimation [84].

$$D_k = \frac{1 - Y_k}{\sum_{j \neq k} X_j / D_{kj}}, \quad (2.24)$$

in which D_{kj} stands for the binary diffusion coefficient between species k and j .

The diffusion velocity $V_{k,i}$ could then be expressed as equation 2.25 with the introduction of the correction velocity $V_{c,i}$ in order to ensure mass conservation.

$$V_{k,i} = -\frac{D_k}{X_k} \frac{\partial X_k}{\partial x_i} + V_{c,i}, \quad (2.25)$$

$$V_{c,i} = \sum_{k=1}^{N_{sp}} D_k \frac{W_k}{W} \frac{\partial X_k}{\partial x_i}. \quad (2.26)$$

In the turbulent reactive flow simulation, the transport parameters, such as the mixture dynamic viscosity μ and mixture thermal conductivity λ , are possibly approximated by empirical temperature-dependent law in order to reduce the computational time. The most popular is the Sutherland's law (cf. equation 2.27, 2.28).

$$\frac{\mu}{\mu_0} = \left(\frac{T}{T_0} \right)^{3/2} \frac{T_0 + S_\mu}{T + S_\mu}, \quad (2.27)$$

$$\frac{\lambda}{\lambda_0} = \left(\frac{T}{T_0} \right)^{3/2} \frac{T_0 + S_\lambda}{T + S_\lambda}. \quad (2.28)$$

where S_μ , S_λ are the Sutherland constants. T_0 , μ_0 and λ_0 are respectively the reference of temperature, dynamic viscosity and thermal conductivity for the considered mixture. The references and constants of air are commonly used: $\mu_0 = 1.716 \times 10^{-5} \text{kg} \cdot \text{m}^{-1} \cdot \text{s}^{-1}$, $S_\mu = 111$, $\lambda_0 = 0.0241 \text{W} \cdot \text{m}^{-1} \cdot \text{K}^{-1}$, $S_\lambda = 194$ and $T_0 = 273 \text{K}$.

For the flameless combustion, Göktoğa and al. [85] proposed a simplified relation as a function of the heat capacity C_p and the temperature T with the Prandtl number Pr (characterised the ratio between momentum diffusivity and thermal diffusivity).

$$\lambda = C_p \times 2.55 \times 10^{-5} \left(\frac{T}{298} \right)^{0.71}, \quad (2.29)$$

$$\mu = Pr \frac{\lambda}{C_p}, \quad (2.30)$$

$$Pr = 0.434 + 1.72 \times 10^{-4} T. \quad (2.31)$$

Besides, the species molecular diffusivity D_k could be also approximated by the mixture dynamic viscosity μ , the density ρ and the species Schmidt number Sc_k . This approximation results in the relation between the species molecular diffusivity D_k and the thermal diffusivity λ through the species Lewis number Le_k which is commonly considered equal to unity.

$$D_k = \frac{\mu}{\rho Sc_k}, \quad (2.32)$$

$$Le_k = \frac{D_k}{\lambda} = \frac{Sc_l}{Pr}. \quad (2.33)$$

2.1.3.4 Energy conservation

The conservation equation for the energy could be described as a function of the sensible enthalpy $h_s(T)$.

$$h_s(T) = \int_{\theta=T_0}^T C_p(\theta) d\theta, \quad (2.34)$$

$$\frac{\partial \rho h_s}{\partial t} + \frac{\partial}{\partial x_i} (\rho u_i h_s) = \frac{DP}{Dt} + \frac{\partial Q_i}{\partial x_i} + \tau_{ij} \frac{\partial u_i}{\partial x_j} + \dot{Q} + \dot{\omega}_T. \quad (2.35)$$

where Q_i stands for the heat flux (equation 2.36), λ_{th} is the mixture thermal conductivity, $\dot{\omega}_T$ represents the chemical heat source term (equation 2.37) as a function of the species formation enthalpy $\Delta h_{f,k}^0$ and species chemical source term $\dot{\omega}_k$.

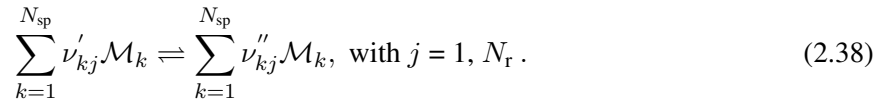
$$Q_i = \lambda_{th} \frac{\partial T}{\partial x_i} - \sum_{k=1}^{N_{sp}} \rho h_{s,k} Y_k V_{k,i}, \quad (2.36)$$

$$\dot{\omega}_T = - \sum_{k=1}^{N_{sp}} \Delta h_{f,k}^0 \dot{\omega}_k. \quad (2.37)$$

2.2 Chemical kinetics

2.2.1 Species source terms

The species source term $\dot{\omega}_k$ from equation 2.37 is modelled from chemistry through the detailed mechanisms which aggregate the N_{sp} species and its chemical paths with N_r reactions in large range of condition. The j^{th} reaction is described as below where ν'_{kj} and ν''_{kj} are respectively the reactants and products stoichiometric coefficients of species k with molecular formula \mathcal{M}_k .



The species mass variation per unit of time in this reaction is quantified by the reaction rate \dot{Q}_j (cf. section 2.2.2) with $\nu_{kj} = \nu''_{kj} - \nu'_{kj}$.

$$\dot{Q}_j = \frac{\dot{\omega}_{kj}}{W_k \nu_{kj}}, \quad (2.39)$$

Using the equation 2.39, the species variation rates of each reaction $\dot{\omega}_{kj}$ is then determined. The total reaction rate of species k is calculated by sum $\dot{\omega}_{kj}$ overall the N_r reaction.

$$\dot{\omega}_k = \sum_{j=1}^{N_r} \dot{\omega}_{kj} = W_k \sum_{j=1}^{N_r} \nu_{kj} \dot{Q}_j. \quad (2.40)$$

2.2.2 Reaction rates

The reaction rate \dot{Q}_j of j^{th} reaction consists of the forward and reverse rates (respectively \dot{Q}_{fj} and \dot{Q}_{rj}) through the relation 4.7.

$$\dot{Q}_j = \dot{Q}_{fj} - \dot{Q}_{rj}. \quad (2.41)$$

The forward rate \dot{Q}_{fj} (respectively reverse rate \dot{Q}_{rj}) is quantified by the molar concentration $[X_k]$ of species k , the forward constant K_{fj} and the reactant stoichiometric coefficients ν'_{kj} (respectively the reverse constant K_{rj} and the product stoichiometric coefficients ν''_{kj}).

$$\dot{Q}_{fj} = K_{fj} \prod_{k=1}^{N_{sp}} [X_k]^{\nu'_{kj}}, \quad (2.42)$$

$$\dot{Q}_{rj} = K_{rj} \prod_{k=1}^{N_{sp}} [X_k]^{\nu''_{kj}}. \quad (2.43)$$

in which $[X_k] = \rho Y_k / W_k$.

2.2.2.1 Arrhenius law

In combustion, the forward reaction rate K_{fj} is commonly described by the empirical Arrhenius laws as a function of the temperature T , the activation energy E_j , the exponent β_j , the pre-exponential collision frequency factor \mathcal{A}_j and the ideal gas constant \mathcal{R} . The activation energy E_j corresponds to the energy quantity that sufficiently dissociates the reactants to intermediate and radical species which then establish the final products while releasing energy through heat (cf. Figure 2.1).

$$K_{fj} = \mathcal{A}_j T^{\beta_j} \exp\left(-\frac{E_j}{\mathcal{R}T}\right). \quad (2.44)$$

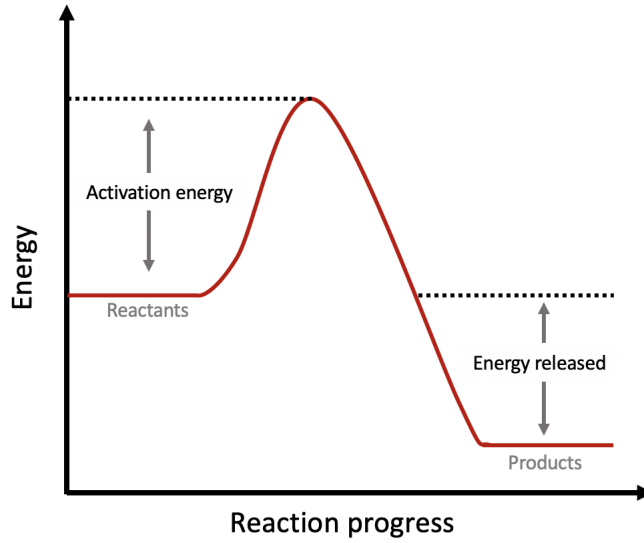


Figure 2.1: Activation energy and energy released diagram

2.2.2.2 Reverse reaction rate constant and equilibrium

The reverse rate K_{rj} is calculated indirectly through the forward rate K_{fj} and the equilibrium constant $K_{eq,j}$. The equilibrium state is occurred while the forward rate \dot{Q}_{fj} and reverse rate \dot{Q}_{rj} are equal, it leads to the relation 2.45 (cf. equation 2.43 and 2.43).

$$K_{fj} \prod_{k=1}^{N_{sp}} [X_k]^{\nu'_{kj}} = K_{rj} \prod_{k=1}^{N_{sp}} [X_k]^{\nu''_{kj}}, \quad (2.45)$$

The equilibrium constant $K_{eq,j}$ is written as the ratio between the reactants concentrations and the products concentrations, hence deduced as follows.

$$K_{eq,j} = \prod_{k=1}^{N_{sp}} [X_k]^{\nu_{kj}} = \frac{K_{fj}}{K_{rj}}. \quad (2.46)$$

The reverse reaction rate is thus calculated once the equilibrium constant $K_{eq,j}$ has been determined from the thermodynamic properties (cf. section 2.2.2.3).

2.2.2.3 Gibbs free energy

In order to quantify the chemical equilibrium constant $K_{eq,j}$, the variation of the standard Gibbs free energy is defined as the difference in potential between the reactants and its products in the j^{th} reaction. This variation is expressed as a function of the temperature T , the ideal gas constant \mathcal{R} and the partial pressure equilibrium constant $K_{p,j}$.

$$\Delta G_j^\circ = -\mathcal{R}T \ln K_{p,j}, \quad (2.47)$$

The relation between the chemical equilibrium constant $K_{eq,j}$ and the partial pressure equilibrium constant $K_{p,j}$ is given in equation 2.48 associated with the reference pressure P° .

$$K_{p,j} = K_{eq,j} \left(\frac{\mathcal{R}T}{P^\circ} \right)^{\sum_{k=1}^{N_{sp}} \nu_{kj}}, \quad (2.48)$$

By joining the equation 2.47 and 2.48, the chemical equilibrium constant $K_{eq,j}$ can be expressed as a function of the variation of entropy ΔS_j° and enthalpy ΔH_j° which could be approximated by NASA polynomials (cf. equation 2.11 and 2.12).

$$K_{eq,j} = \exp \left(\frac{\Delta S_j^\circ}{\mathcal{R}} - \frac{\Delta H_j^\circ}{\mathcal{R}T} \right) \left(\frac{P^\circ}{\mathcal{R}T} \right)^{\sum_{k=1}^{N_{sp}} \nu_{kj}}. \quad (2.49)$$

2.3 Combustion regimes

There exist two main combustion configurations: premixed and diffusion regimes. The premixed regime is represented by a preliminary mixing of the fuel and the oxidiser before the combustion occurs in the combustion chamber. The premixed configuration facilitates the flame control through the mixture equivalence ratio (or mixing proportion) resulted in the burning temperature level which is the key of pollutant emissions. Therefore, this configuration has a high thermal efficiency and eases the pollutants control. However, in the industrial applications, this flame configuration increases the accidental risk due to the premixing process which can promote flash-back.

Conversely, in the diffusion regime, the fuel and oxidiser are injected separately into the combustion chamber, it leads to the combustion at the meeting interface between the fuel and oxidiser. The separated injections help in securing the safety problem of fuel storage. Nevertheless, in view of the fact that the mixing in this configuration is not as effective as the premixing process, the combustion efficiency is decreased and it is more challenging to control the flame temperature level.

2.3.1 Premixed flame

The premixed flame structure is illustrated by the flame front separating the fresh reactants and burnt gases where the reactions take place (cf. Figure 2.2). The flame front propagates in the direction of consuming the fresh reactants with the flame velocity S_L^0 . The flame structure is possibly defined into 3 different zones: preheat zone, reaction zone and the post-flame zone.

- The **preheat zone** in the fresh reactants are heated by the thermal diffusion fluxes near the flame front,
- The **reaction zone** is characterised by the reaction rate and defined the region where the reactants are transformed to the intermediate and radical species,

- The **post-flame zone** is located behind the flame front, where the major products are formed at high temperature.

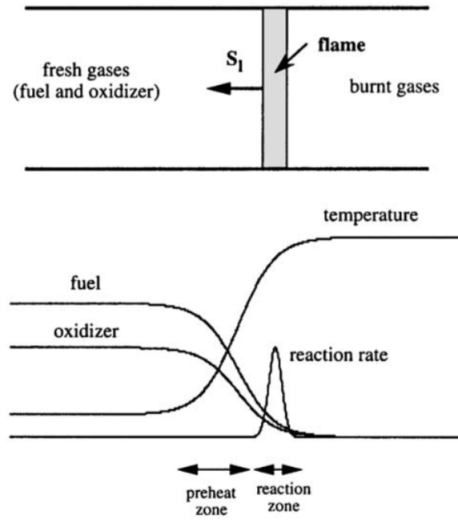


Figure 2.2: Laminar premixed flame structure [86].

Assuming a 1D steady premixed flames propagating along x direction, the mass conservation at each position x leads to the relation between the gases density ρ , the fluid velocity u , the fresh gases density ρ_0 and the laminar flame speed S_L^0 (cf. relation 2.50). Thus, the momentum equation is presumably unnecessary.

$$\frac{\partial \rho u}{\partial x} = 0 \longrightarrow \rho u = \rho_0 S_L^0, \quad (2.50)$$

The steady-form of species conservation along the x direction could be written as follows.

$$\frac{\partial}{\partial x} (\rho(u + V_k)Y_k) = \dot{\omega}_k, \quad (2.51)$$

Likewise the enthalpy conservation at steady state is simplified:

$$\frac{\partial}{\partial x} (\rho u h_s) = \frac{\partial}{\partial x} \left(\lambda_{th} \frac{\partial T}{\partial x} \right) - \frac{\partial}{\partial x} \left(\rho \sum_{k=1}^{N_{sp}} h_{s,k} Y_k V_k \right) + \dot{\omega}_T, \quad (2.52)$$

For the purpose of describing the chemical process in the premixed configuration, a progress variable, named c , is proposed. This variable c is defined in various forms and bounded between 0 (in the fresh gases) and 1 (in the burnt gases). Based on the temperature variation, the definition is:

$$c = \frac{T - T_0}{T_{eq} - T_0}, \quad (2.53)$$

where T_{eq} is the equilibrium temperature of the burning process and T_0 refers to the fresh gases temperature.

An assumption of unity Schmidt and Lewis numbers could be made to state the progress variable c as a function of mass fraction.

$$c = \frac{Y_c - Y_{c,0}}{Y_{c,eq} - Y_{c,0}}, \quad (2.54)$$

in which Y_c is commonly defined as $Y_c = Y_{CO} + Y_{CO_2} + Y_{H_2O}$ and $Y_{c_{eq}}$ is Y_c at equilibrium state.

The definitions of progress variable c allow to determine the reaction zone and analyse the flame structure. Hence, the normal of flame front n is expressed:

$$n = \frac{-\nabla c}{|\nabla c|}, \quad (2.55)$$

The equivalent ratio ϕ is another governing variable indicating the amount of fuel mixed with air. This variable is described by the stoichiometric ratios, the mass fraction of fuel and oxidiser in the fresh gases ($Y_{F,0}$ and $Y_{O,0}$ respectively).

$$\phi = s \frac{Y_{F,0}}{Y_{O,0}}, \quad (2.56)$$

The stoichiometric ratio s is expressed as a function of the molecular weights and the stoichiometric coefficients of fuel and oxidiser (W_F , W_O , ν_F and ν_O) in global reaction in which F, O, P denote the species formula of fuel, oxidiser and product.

$$s = \frac{\nu_O W_O}{\nu_F W_F}, \quad (2.57)$$

$$\nu_F F + \nu_O O \rightarrow \nu_P P, \quad (2.58)$$

The value of equivalent ratio ϕ allows to classify the mixture at stoichiometric ($\phi = 1$), lean fuel ($\phi < 1$) or rich fuel condition ($\phi > 1$).

The laminar flame speed S_L^0 defined by the integral of fuel burning rate $\dot{\omega}_F$ as follows refers to the fuel consumption speed along x direction.

$$S_L^0 = -\frac{1}{\rho_0(Y_{F,0} - Y_{F,\infty})} \int_{-\infty}^{+\infty} \dot{\omega}_F dx, \quad (2.59)$$

where ρ_0 stands for the fresh gases density, $Y_{F,0}$ and $Y_{F,\infty}$ correspond respectively to the fuel mass fraction of fresh and burnt gases.

The premixed flame is also characterised by the thermal thickness δ_L^{th} [87] described by the gradient of temperature between fresh (T_0) and burnt gases (T_{eq}) or by the gradient of the progress variable c .

$$\delta_L^{th} = \frac{T_{eq} - T_0}{\left| \frac{\partial T}{\partial x} \right|_{max}}, \quad (2.60)$$

$$\delta_L^c = \frac{1}{\left| \frac{\partial c}{\partial x} \right|_{max}}. \quad (2.61)$$

2.3.2 Diffusion flame

Contrary to the premixed configuration, the diffusion flame is essentially governed by the mixing the separated fuel and oxidiser injection. The combustion takes place at the stoichiometric line, then the heat diffuses toward both fuel and oxidiser side (cf. Figure 2.3).

In the diffusion configuration, the mixing process is characterised by the mixture fraction Z based on the mass fraction of atom C, H and O. There exist several definitions of the mixture fraction. In the present work, the Bilger's definition [88] is retained.

$$Z = \frac{2(Y_C - Y_{C_{Oxidiser}})/W_C + (Y_H - Y_{H_{Oxidiser}})/2W_H + (Y_O - Y_{O_{Oxidiser}})/W_O}{2(Y_{C_{Fuel}} - Y_{C_{Oxidiser}})/W_C + (Y_{H_{Fuel}} - Y_{H_{Oxidiser}})/2W_H + (Y_{O_{Fuel}} - Y_{O_{Oxidiser}})/W_O}, \quad (2.62)$$

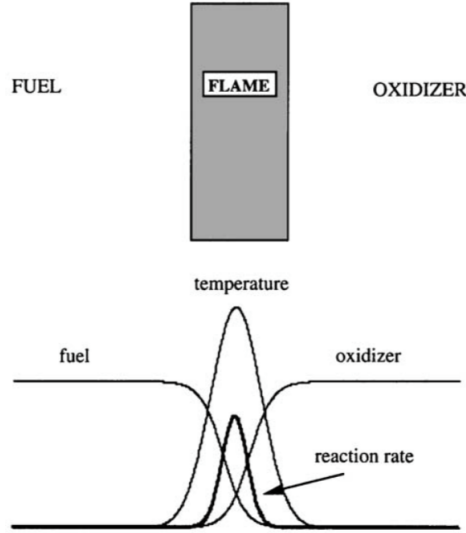


Figure 2.3: Structure of a laminar diffusion flame [86].

where Y_C , Y_H and Y_O refer to the atom mass fraction of the considered mixture; $Y_{C_{Oxidiser}}$, $Y_{H_{Oxidiser}}$ and $Y_{O_{Oxidiser}}$ (respectively $Y_{C_{Fuel}}$, $Y_{H_{Fuel}}$ and $Y_{O_{Fuel}}$) stand for the atom mass fraction of oxidiser (respectively fuel) injection.

The mass fraction of atom j^{th} (C, H or O), denoted Y_j , is determined from all species k and characterised by the number of j^{th} atom in species k (α_{jk}), the atom molecular weight (W_j) and the species molecular weight (W_k) through the following relation.

$$Y_j = \sum_{k=1}^{N_{sp}} \frac{\alpha_{jk} W_j}{W_k} Y_k. \quad (2.63)$$

It should be noted that the mixture fraction Z is a passive scalar and bounded between 0 (at oxidiser injection) and 1 (at fuel injection).

2.3.3 Partially premixed combustion

In the real world, the complex industrial systems could also operate in the partially-premixed combustion [89] which possesses properties of both premixed and diffusion configurations. This regime is often observed with separated injection of fuel and oxidiser enhanced mixing process leading to partial premixing of the reactants before combustion. From the turbulent combustion modelling point of view, the partially premixed could be modelled using the tool from the two above configurations. In order to distinguish the nature of combustion regime, H. Yamashita et al. [90] proposed the Takeno index T_I based on the gradient of fuel and oxidiser mass fraction. The index is bounded between 0 (premixed flame) and 1 (diffusion flame).

$$T_I = \frac{\nabla Y_{Fuel} \cdot \nabla Y_{Oxidiser}}{|\nabla Y_{Fuel} \cdot \nabla Y_{Oxidiser}|}. \quad (2.64)$$

2.4 RANS-LES formalism

2.4.1 Turbulence introduction

In the nature, the flow exists in different states: laminar or turbulent [91]. At small velocities, the perturbations is immediately absorbed by the molecular viscosity, hence, the fluid flows in parallel layers with only slow mixing in the transverse direction. This phenomena is so called the laminar regime. On the contrary, while increasing the fluid velocity, the perturbations grow due to the non-linear convective effects and are unable to be dissipated by the molecular viscosity. The perturbations are furthermore amplified by different instability mechanisms (such as Kelvin-Helmholtz, Rayleigh-Taylor, etc.), thus, the fluid becomes turbulent.

For the purpose of quantifying the turbulent characteristic, O. Reynolds [91] proposed a non-dimensional number Re expressing the ratio between the fluid movement (velocity u and characteristic dimension L) and its kinematic viscosity ν . It is noteworthy that the kinetic viscosity ν is possibly represented as the function of the dynamic viscosity μ and density ρ . The laminar flow is represented by a small value of the Reynolds number Re while the large Re refers to the turbulent state.

$$Re = \frac{uL}{\nu} . \quad (2.65)$$

$$\nu = \frac{\mu}{\rho} . \quad (2.66)$$

The turbulence is characterised in different scales, based on its energy state [92].

- The most energetic and the largest scale is named the **macroscopic scale**. The kinetic energy k_t of turbulent structure in macroscopic scale is defined by the velocity fluctuations from different direction i depending on the studied geometry.

$$k_t = \sum_{i=1}^3 \frac{1}{2} u_i'^2 . \quad (2.67)$$

Thus, under the local isotropy hypothesis, the velocity fluctuation can be deduced as follows.

$$u' = \sqrt{\frac{2}{3} k_t} . \quad (2.68)$$

In the macroscopic point of view, the turbulence structure is also described by the energetic length L_e and the integral length l_t which are represented as a function of the turbulent kinetic energy k_t , the turbulent dissipation ϵ and the velocity fluctuation u' .

$$L_e = \frac{k_t^{3/2}}{\epsilon} , \quad (2.69)$$

$$l_t = \frac{u'^3}{\epsilon} . \quad (2.70)$$

These definitions lead to the relation between the energetic length L_e and the integral length l_t .

$$\frac{l_t}{L_e} = \left(\frac{2}{3} \right)^{3/2} . \quad (2.71)$$

From the definition of O. Reynolds (cf. equation 2.65), in the macroscopic scale, the turbulent Reynolds number Re_t is expressed by the integral length l_t , the velocity fluctuation u' and the fluid kinematic viscosity ν .

$$Re_t = \frac{u' l_t}{\nu}. \quad (2.72)$$

- The **intermediate scale** refers to the Taylor scale, denoted λ . In this scale, the large turbulent structure is dissipated into the smaller ones. The energy is also transferred and followed the $k_t^{-\frac{5}{3}}$ rule.
- The **viscous dissipation scale**, or the **Kolmogorov scale** [93] - denoted l_K , corresponds to the smallest scale where the turbulence structure is completely dissipated into heat. The Kolmogorov length l_K and velocity u_K are able to be expressed as a function of the turbulent dissipation ϵ and the fluid kinematic viscosity ν .

$$l_K = \left(\frac{\nu}{\epsilon}\right)^{1/4}. \quad (2.73)$$

$$u_K = (\nu\epsilon)^{1/4}. \quad (2.74)$$

By these definitions, the Reynolds number in this scale is assumed equal to unity.

$$Re_K = \frac{u'_K l_K}{\nu} \approx 1. \quad (2.75)$$

2.4.2 Computational Fluid Dynamics (CFD) strategies

In CFD, the brute force approach is *Direct Numerical Simulation*, denoted **DNS**, where the Navier-Stokes equations are fully resolved. In order to capture all scales of turbulence mentioned above, the simulations requires a sufficient fined mesh. Assuming the mesh resolution Δ , the smallest mesh size can be estimated by the Kolmogorov length scale l_K [94]. Using definition in section 2.4.1, this estimation can be approximated as a function of the macroscopic length scale l_t and the turbulent Reynolds number Re_t .

$$\Delta = 2l_K \approx \frac{l_t}{Re_t^{3/4}}. \quad (2.76)$$

This relation shows that the mesh resolution Δ is negatively proportional to the turbulent Reynolds number Re_t with the power of $\frac{3}{4}$. In the industrial applications, the turbulent Reynolds number Re_t is frequently high, thus, the necessary mesh resolution becomes extremely small. Furthermore, the industrial geometries (such as furnaces) are commonly large, that means that the enormous number of mesh cells is required and also a considerable computational cost.

To cope with the mesh size requirement associated to Reynolds number, two other approaches are introduced with different levels of modelling (cf. Figure 2.4)

- *Reynolds Averaged Numerical Simulation*, denoted **RANS**, modelled the Navier-Stokes equations by Reynolds time-averaging. The flow velocity $u(x, t)$ is decomposed into the mean component $\bar{u}(x)$ and the fluctuation component $u'(x, t)$ whose temporal mean is equal to zeros ($\bar{u}' = 0$).

$$u(x, t) = \bar{u}(x) + u'(x, t). \quad (2.77)$$

In RANS, only the averaged variables are calculated, so the unsteady dynamics of the fluid flow cannot be represented. Nevertheless, the mesh resolution is conceivably larger leading to a significant reduction of computational effort. For this reason, this approach is suitable for industrial applications.

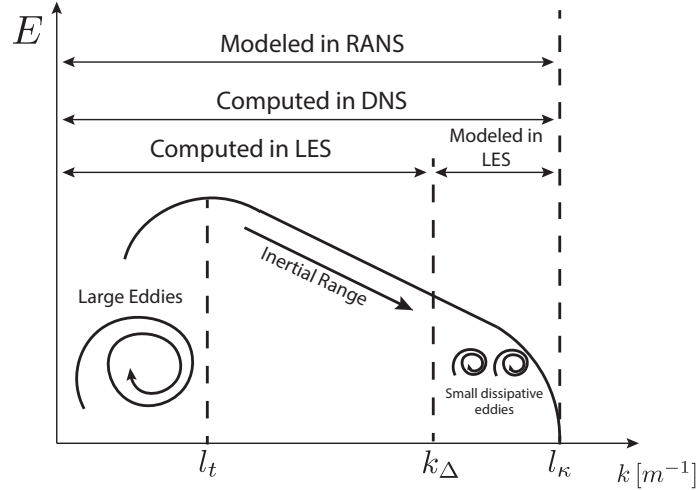


Figure 2.4: Different levels of resolution and modelling - Comparison between DNS, LES and RANS [95].

- In 1963, Smagorinsky [96] proposed *Large Eddy Simulation* (denoted **LES**), an intermediate approach in between DNS and RANS. In LES, the smallest turbulent structures are modelled while only the largest eddies are resolved. The separation between resolved and modelled scales is realised using the spatial filters depending on the mesh size Δ . By modelling the smallest structure, the required mesh resolution could be increased compared to DNS.

2.4.3 RANS modelling

As mentioned above, in RANS approach, time-averaging is applied to the Navier-Stokes equations. The conventional time-averaging is called Reynolds averaging which is defined as follows (average $\bar{f}(x, t)$ of a physical variable $f(x, t)$).

$$\bar{f}(x, t_0) = \lim_{\Delta t \rightarrow \infty} \frac{1}{\Delta t} \int_{t_0}^{t_0 + \Delta t} f(x, t) dt. \quad (2.78)$$

The physical variable $f(x, t)$ could be represented by its average $\bar{f}(x, t)$ and its fluctuation $f'(x, t)$.

$$f(x, t) = \bar{f}(x, t) + f'(x, t). \quad (2.79)$$

It is worth noting several properties of Reynolds averaging.

$$\overline{f'} = 0, \quad (2.80)$$

$$\overline{f + g} = \bar{f} + \bar{g}, \quad (2.81)$$

$$\overline{\alpha f} = \alpha \bar{f} \text{ with } \alpha = \text{constant}, \quad (2.82)$$

$$\overline{\frac{\partial f}{\partial x}} = \frac{\partial \bar{f}}{\partial x}, \quad (2.83)$$

$$\overline{fg} = \bar{f}\bar{g} + \overline{f'g'}. \quad (2.84)$$

For the variable density flows (such as compressible state or combustion), the RANS averaging shows its inconvenient by introducing many unclosed correlations [97]. Therefore, the mass-weighted Favre averaging are proposed.

$$\tilde{f} = \frac{\overline{\rho f}}{\bar{\rho}}. \quad (2.85)$$

$$f = \tilde{f} + f'' . \quad (2.86)$$

Several important properties are shown as follows.

$$\tilde{f}'' = 0 , \quad (2.87)$$

$$\widetilde{f + g} = \tilde{f} + \tilde{g} , \quad (2.88)$$

$$\widetilde{\alpha f} = \alpha \tilde{f} \text{ with } \alpha = \text{constant} , \quad (2.89)$$

$$\frac{\partial \tilde{f}}{\partial x} = \frac{\partial \tilde{f}}{\partial x} , \quad (2.90)$$

$$\widetilde{fg} = \tilde{f}\tilde{g} + \widetilde{f''g''} . \quad (2.91)$$

The Favre mass conservation and momentum conservation equations (cf . equations 2.20 and 2.21) of the fluid flow could be rewritten as follows.

$$\frac{\partial \bar{\rho}}{\partial t} + \frac{\partial \bar{\rho} \tilde{u}_i}{\partial x_i} = 0 . \quad (2.92)$$

$$\frac{\partial \bar{\rho} \tilde{u}_i}{\partial t} + \frac{\partial \bar{\rho} \tilde{u}_i \tilde{u}_j}{\partial x_j} = -\frac{\partial \bar{P}}{\partial x_i} + \frac{\partial}{\partial x_j} (\bar{\tau}_{ji} - \overline{\rho u''_j u''_i}) . \quad (2.93)$$

where $\bar{\tau}_{ji}$ stands for the viscosity tensor calculated from the averaged velocities.

$$\bar{\tau}_{ji} = -\frac{2}{3}\mu \frac{\partial \tilde{u}_k}{\partial x_k} \delta_{ji} + \mu \left(\frac{\partial \tilde{u}_i}{\partial x_j} + \frac{\partial \tilde{u}_j}{\partial x_i} \right) . \quad (2.94)$$

The rewritten equations with Reynolds average have the general form of the instantaneous Navier-Stokes equations with an additional term $-\overline{\rho u''_j u''_i}$ signified the Reynolds stresses. This term is not resolved and needed to be modelled to close the above equations. Following the Boussinesq hypothesis, the Reynolds stresses are stated as the function of the averaged velocity gradients, the turbulent viscosity μ_t and the turbulent kinetic energy $k = \frac{1}{2} \sum_{k=1}^3 \overline{u''_k u''_k}$. In this hypothesis, the turbulent viscosity μ_t is assumed isotropic.

$$-\overline{\rho u''_j u''_i} = -\frac{2}{3} \left(\bar{\rho} k + \mu_t \frac{\partial \tilde{u}_k}{\partial x_k} \right) \delta_{ji} + \mu_t \left(\frac{\partial \tilde{u}_i}{\partial x_j} + \frac{\partial \tilde{u}_j}{\partial x_i} \right) . \quad (2.95)$$

It is necessary to calculate the turbulent viscosity μ_t using models. In literature, several models have been proposed: one-equation Spalart-Allmaras model [98], two-equations k - ϵ model [99], two-equations k - ω model [100], etc. A discussion on the model selection for the studied configuration under flameless combustion regime in this present thesis may be found in the thesis of D. Lupant [32]. This work concluded that the two-equations RNG k - ϵ model, is the most suitable.

2.4.3.1 Standard k - ϵ

It is useful at first to represent the standard k - ϵ . Proposed by Launder and Spalding in 1972 [99], k - ϵ becomes one of the most popular models for the industrial applications. The turbulent viscosity μ_t is modelled as a function of the density $\bar{\rho}$, the turbulence kinetic energy k , the dissipation rate ϵ and a model constant C_μ .

$$\mu_t = \bar{\rho} C_\mu \frac{k^2}{\epsilon}. \quad (2.96)$$

The turbulence kinetic energy k and the dissipation rate ϵ are acquired by solving its transport equations.

$$\frac{\partial}{\partial t}(\bar{\rho}k) + \frac{\partial}{\partial x_i}(\bar{\rho}\tilde{u}_i k) = \frac{\partial}{\partial x_i} \left[\left(\mu + \frac{\mu_t}{\sigma_k} \right) \frac{\partial k}{\partial x_i} \right] - \widetilde{\bar{\rho}u''_i u''_j} \frac{\partial \tilde{u}_i}{\partial x_j} - \bar{\rho}\epsilon, \quad (2.97)$$

$$\frac{\partial}{\partial t}(\bar{\rho}\epsilon) + \frac{\partial}{\partial x_i}(\bar{\rho}\tilde{u}_i \epsilon) = \frac{\partial}{\partial x_i} \left[\left(\mu + \frac{\mu_t}{\sigma_\epsilon} \right) \frac{\partial \epsilon}{\partial x_i} \right] - C_{1\epsilon} \frac{\epsilon}{k} \widetilde{\bar{\rho}u''_i u''_j} \frac{\partial \tilde{u}_i}{\partial x_j} - C_{2\epsilon} \bar{\rho} \frac{\epsilon^2}{k}. \quad (2.98)$$

The model constants could be cited as default values (from Launder et Spalding's article [99]).

$$C_{1\epsilon} = 1.44, C_{2\epsilon} = 1.92, C_\mu = 0.09, \sigma_k = 1.0, \sigma_\epsilon = 1.3. \quad (2.99)$$

2.4.3.2 RNG k - ϵ

In the standard k - ϵ model, the transport equation of k is derived from the exact equation while the transport equation of ϵ is written based on the physical reasoning. By this reason, Yakhot et al. [101] proposed the RNG k - ϵ model, using the renormalisation group theory (RNG), in order to improve the accuracy of the standard k - ϵ model. In RNG k - ϵ model, the coefficient $C_{2\epsilon}$ is modified, denoted $C_{2\epsilon}^*$.

$$\frac{\partial}{\partial t}(\bar{\rho}\epsilon) + \frac{\partial}{\partial x_i}(\bar{\rho}\tilde{u}_i \epsilon) = \frac{\partial}{\partial x_i} \left[\left(\mu + \frac{\mu_t}{\sigma_\epsilon} \right) \frac{\partial \epsilon}{\partial x_i} \right] - C_{1\epsilon} \frac{\epsilon}{k} \widetilde{\bar{\rho}u''_i u''_j} \frac{\partial \tilde{u}_i}{\partial x_j} - C_{2\epsilon}^* \bar{\rho} \frac{\epsilon^2}{k}. \quad (2.100)$$

The $C_{2\epsilon}^*$ coefficient could be calculated from the constant $C_{2\epsilon}$, the constant C_μ , the density ρ , the turbulent kinetic energy k and the dissipation rate ϵ with additional constants $\eta_0 = 4.38$ and $\beta = 0.012$.

$$C_{2\epsilon}^* = C_{2\epsilon} + \frac{C_\mu \eta^3 (1 - \eta/\eta_0)}{1 + \beta \eta^3}. \quad (2.101)$$

in which η is described as the function of turbulent kinetic energy k , dissipation rate ϵ and modulus S of mean rate-of-strain tensor S_{ij} .

$$\eta = \frac{Sk}{\epsilon}, \quad (2.102)$$

$$S = (2S_{ij}S_{ij})^{\frac{1}{2}}, \quad (2.103)$$

$$S_{ij} = \frac{1}{2} \left(\frac{\partial \tilde{u}_j}{\partial x_i} + \frac{\partial \tilde{u}_i}{\partial x_j} \right). \quad (2.104)$$

Besides, the model constants are explicitly acquired in the RNG procedure [102, 103].

$$C_{1\epsilon} = 1.42, C_{2\epsilon} = 1.68, C_\mu = 0.0045, \sigma_k = 0.7194, \sigma_\epsilon = 0.7194. \quad (2.105)$$

2.4.4 LES modelling

2.4.4.1 Formalism

As previously mentioned, in LES, the small scales are modelled while the large scales are solved. The scale partitioning is accomplished through a spatial filter \mathcal{G}_Δ which depends on the resolution Δ . A filtered scalar $\bar{\phi}(\mathbf{x}, t)$ could be stated as follows.

$$\bar{\phi}(\mathbf{x}, t) = \int_{\mathbb{R}^3} \phi(\mathbf{y}, t) \mathcal{G}_\Delta(\mathbf{y} - \mathbf{x}) d\mathbf{y}. \quad (2.106)$$

$$\int_{\mathbb{R}^3} \mathcal{G}_\Delta(\mathbf{x}) d\mathbf{x} = 1. \quad (2.107)$$

It is worth mentioning that the filtering verifies the commutativity in spatial and temporal derivation operators.

$$\frac{\partial \bar{\phi}}{\partial t} = \overline{\frac{\partial \phi}{\partial t}}. \quad (2.108)$$

$$\frac{\partial \bar{\phi}}{\partial x_i} = \overline{\frac{\partial \phi}{\partial x_i}}. \quad (2.109)$$

The scalar $\phi(\mathbf{x}, t)$ is decomposed as the function of the filtered part $\bar{\phi}(\mathbf{x}, t)$ and the fluctuation part $\phi'(\mathbf{x}, t)$.

$$\phi(\mathbf{x}, t) = \bar{\phi}(\mathbf{x}, t) + \phi'(\mathbf{x}, t). \quad (2.110)$$

In the variable density cases (such as combustion), the filtered scalar $\bar{\phi}$ could also be weighted by density ρ by introducing Favre averaging (denoted $\tilde{\phi}$).

$$\tilde{\phi} = \frac{\overline{\rho \phi}}{\bar{\rho}}. \quad (2.111)$$

With the Favre averaging, the scalar $\phi(\mathbf{x}, t)$ could also be partitioned into the Favre filtered part $\tilde{\phi}(\mathbf{x}, t)$ and the Favre fluctuating part $\phi''(\mathbf{x}, t)$

$$\phi(\mathbf{x}, t) = \tilde{\phi}(\mathbf{x}, t) + \phi''(\mathbf{x}, t). \quad (2.112)$$

Opposed to RANS, it is important to note that the $\bar{\phi}'$ filtered and $\tilde{\phi}''$ Favre-averaged fluctuation are not equal to zeros.

$$\bar{\phi}' \neq 0, \quad (2.113)$$

$$\tilde{\phi}'' \neq 0. \quad (2.114)$$

The Favre averaged form of conservation equations are deduced from the instantaneous equations described in section 2.1.3.

- **Filtered mass conservation**

$$\frac{\partial \bar{\rho}}{\partial t} + \frac{\partial \bar{\rho} \tilde{u}_i}{\partial x_i} = 0. \quad (2.115)$$

- **Filtered momentum conservation**

$$\frac{\partial \bar{\rho} \tilde{u}_j}{\partial t} + \frac{\partial \bar{\rho} \tilde{u}_i \tilde{u}_j}{\partial x_i} = - \frac{\partial}{\partial x_i} \underbrace{[\bar{\rho} (\tilde{u}_i \tilde{u}_j - \tilde{u}_i \tilde{u}_j)]}_{(1)} - \frac{\partial \bar{P}}{\partial x_j} + \frac{\partial \bar{\tau}_{ij}}{\partial x_i}. \quad (2.116)$$

- **Filtered species conservation**

$$\frac{\partial \bar{\rho} \widetilde{Y}_k}{\partial t} + \frac{\partial \bar{\rho} \widetilde{u}_i \widetilde{Y}_k}{\partial x_i} = - \underbrace{\frac{\partial}{\partial x_i} [\bar{\rho} (\widetilde{u}_i \widetilde{Y}_k - \widetilde{u}_i \widetilde{Y}_k)]}_{(2)} - \underbrace{\frac{\partial}{\partial x_i} (-\rho V_{k,i} Y_k)}_{(3)} + \underbrace{\bar{\omega}_k}_{(4)}. \quad (2.117)$$

- **Filtered energy conservation**

$$\frac{\partial \bar{\rho} \widetilde{h}_s}{\partial t} + \frac{\partial \bar{\rho} \widetilde{u}_i \widetilde{h}_s}{\partial x_i} = - \underbrace{\frac{\partial}{\partial x_i} [\bar{\rho} (\widetilde{u}_i \widetilde{h}_s - \widetilde{u}_i \widetilde{h}_s)]}_{(5)} + \frac{D\bar{P}}{Dt} + \underbrace{\frac{\partial}{\partial x_i} \left(\lambda_{th} \frac{\partial T}{\partial x_i} \right)}_{(6)} \quad (2.118)$$

$$- \underbrace{\frac{\partial}{\partial x_i} \left(\rho \sum_{k=1}^{N_{sp}} h_{s,k} Y_k V_{k,i} \right)}_{(7)} + \underbrace{\bar{\omega}_T}_{(8)}. \quad (2.119)$$

The terms noted from (1) to (8) are the unresolved terms appeared after Favre averaging procedure and should be modelled. The models are introduced as below.

- The first term (1) $\bar{\rho} (\widetilde{u}_i \widetilde{u}_j - \widetilde{u}_i \widetilde{u}_j)$ stands for **the sub grid Reynolds stress tensor**, denoted τ'_{ij} , which corresponds to the transport of momentum by unresolved velocity fluctuation and the energy transfer between the solved and modelled scales. Using the Boussinesq hypothesis [104], the sub grid Reynolds stress tensor τ'_{ij} is rewritten.

$$\tau'_{ij} = \mu_t \left(\frac{\partial \widetilde{u}_i}{\partial x_j} + \frac{\partial \widetilde{u}_j}{\partial x_i} \right) - \frac{2}{3} \mu_t \frac{\partial \widetilde{u}_k}{\partial x_k} \delta_{ij}, \quad (2.120)$$

in which the turbulent dynamic viscosity $\mu_t = \bar{\rho} \nu_t$ is later modelled by several turbulent sub grid scale models, such as the Smagorinsky model, the dynamic Smagorinsky model or the WALE model which are aggregated in section 2.4.4.2 below.

- The second (2) and fifth (5) terms are respectively **the sub grid species** $\mathcal{F}'_{k,i}$ and **the enthalpies flux** \mathcal{Q}'_i . These terms are modelled by introducing the turbulent Schmidt number Sc_t and the turbulent Prandtl number Pr_t . The two numbers could be constant or adjustable through other variables (for example, equation 2.31).

$$\mathcal{F}'_{k,i} = \bar{\rho} (\widetilde{u}_i \widetilde{Y}_k - \widetilde{u}_i \widetilde{Y}_k) = - \frac{\mu_t}{Sc_t} \frac{\partial \widetilde{Y}_k}{\partial x_i}. \quad (2.121)$$

$$\mathcal{Q}'_i = \bar{\rho} (\widetilde{u}_i \widetilde{h}_s - \widetilde{u}_i \widetilde{h}_s) = - \frac{\mu_t}{Pr_t} \frac{\partial \widetilde{h}_s}{\partial x_i}. \quad (2.122)$$

- The third (3) term is **the filtered laminar diffusive fluxes of species**. And the sixth (6) and seventh (7) terms are **the filtered laminar diffusive fluxes of enthalpy**. These terms are commonly described by the resolved variables while neglecting the sub grid scale part.

$$\overline{\rho V_{k,i} Y_k} = - \bar{\rho} D_k \frac{W_k}{\bar{W}} \frac{\partial \widetilde{X}_k}{\partial x_i}, \quad (2.123)$$

$$\overline{\lambda \frac{\partial T}{\partial x_i}} = \bar{\lambda} \frac{\partial \widetilde{T}}{\partial x_i}, \quad (2.124)$$

$$\overline{\rho \sum_{k=1}^{N_{sp}} h_{s,k} Y_k V_{k,i}} = - \bar{\rho} \sum_{k=1}^{N_{sp}} D_k \frac{W_k}{\bar{W}} \frac{\partial \widetilde{X}_k}{\partial x_i} \widetilde{h}_{s,k}. \quad (2.125)$$

- The fourth (4) and the eighth (8) terms are respectively **the filtered species chemical rate** and **the filtered enthalpy source term**. These terms could be modelled by the tabulation methods (PDF) or the transported methods coupling with the detailed or skeletal chemical mechanism. In this present thesis, another approach applying the machine learning and neural networks is proposed. Further details are shown in chapter 4.

2.4.4.2 Turbulent sub grid scale models

The effect of the unresolved small turbulent structure is deciphered into the variation of the turbulent dynamic viscosity μ_t in the first (1) term mentioned above.

- The first model is proposed by Smagorinsky [96], named **the Smagorinsky model** which relies on the equilibrium of the energy production and dissipation of the small scale structure. In this model, the turbulent dynamic viscosity μ_t is described by the density ρ , the characterised mixing length $L_s = C_s \Delta$ and the modulus \tilde{S} of the filtered mean rate-of-strain tensor \tilde{S}_{ij}

$$\mu_t = \bar{\rho} L_s^2 |\tilde{\mathbf{S}}| = \bar{\rho} (C_s \Delta)^2 |\tilde{\mathbf{S}}| = \bar{\rho} (C_s \Delta)^2 \sqrt{2 \tilde{S}_{ij} \tilde{S}_{ij}}, \quad (2.126)$$

$$\tilde{S}_{ij} = \frac{1}{2} \left(\frac{\partial \tilde{u}_i}{\partial x_j} + \frac{\partial \tilde{u}_j}{\partial x_i} \right), \quad (2.127)$$

in which C_s is the Smagorinsky constant (commonly $C_s = 0.77$) and Δ is the characteristic filter width. In practice, the characteristic filter width Δ is taken as the local grid scale which can be determined by the mesh cell volume V .

$$\Delta = V^{\frac{1}{3}} \quad (2.128)$$

- The constant C_s is not universal and is the shortcoming on the Smagorinsky model. Germano [105] and Lilly [106] developed a procedure that allows to calculate dynamically and locally C_s based on the informations of resolved scales. By this reasoning, the model named **the dynamic Smagorinsky model**. The model employs a second filter, denoted $\widehat{(\cdot)}$, with the second filter width $\hat{\Delta}$ which is commonly equal to twice the first grid filter Δ ($\hat{\Delta} = 2\Delta$). Both filters provide the filtered sub grid tensor τ_{ij} and T_{ij} .

$$\tau_{ij} = 2\bar{\rho} (C_s \Delta)^2 |\tilde{\mathbf{S}}| \left(\tilde{S}_{ij} - \frac{1}{3} \tilde{S}_{kk} \delta_{ij} \right), \quad (2.129)$$

$$T_{ij} = 2\hat{\rho} (C_s \hat{\Delta})^2 |\hat{\mathbf{S}}| \left(\hat{S}_{ij} - \frac{1}{3} \hat{S}_{kk} \delta_{ij} \right). \quad (2.130)$$

The Germano identity is retained to attach two filtered tensors.

$$L_{ij} = T_{ij} - \hat{\tau}_{ij} = \bar{\rho} \left(\widehat{\tilde{u}_i \tilde{u}_j} - \widehat{\tilde{u}_i} \widehat{\tilde{u}_j} \right). \quad (2.131)$$

The locally-varied coefficient C_s is then expressed as follows.

$$C_s = \frac{(L_{ij} - L_{kk} \delta_{ij} / 3)}{M_{ij} M_{ij}}. \quad (2.132)$$

in which

$$M_{ij} = -2(\hat{\Delta}^2 \hat{\rho} |\hat{\mathbf{S}}| \hat{S}_{ij} - \Delta^2 \bar{\rho} |\tilde{\mathbf{S}}| \tilde{S}_{ij}). \quad (2.133)$$

- As indicated previously, the turbulent viscosities (μ_t or ν_t) represent the energy transfer from the resolved scale to the modelled sub grid scale through the sub grid dissipation. The Smagorinsky models considered the sub grid dissipation as the local strain rate of the smallest resolved scales. In 1989, Wray and Hunt [107] demonstrated through DNS simulations that the turbulence concentrated not only around the zones with the strain rate but also with the vorticity (ie. rotational rate). This study showed the shortcoming of the Smagorinsky models. In addition, the Smagorinsky model gives the non-zeros values of the turbulent viscosities near wall while they should be (the turbulence are damped at walls). The dynamic procedure solved the problem but created conceivably the large negative coefficients C_s resulting in the numerical instability.

Therefore, Nicoud et al [108] conceived **Wall-Adapting Eddy-Viscosity model** or **WALE** adapting both the strain rate and vorticity, leading to a better prediction around the near-wall zones. In this model, the turbulent dynamic viscosity μ_t is expressed as a function of the model constant C_ω (0.5 by default [108], 0.325 in Fluent and Code-Saturne), the tensor s_{ij}^d and \tilde{S}_{ij} .

$$\mu_t = \rho C_\omega^2 \Delta^2 \frac{(s_{ij}^d s_{ij}^d)^{3/2}}{(\tilde{S}_{ij} \tilde{S}_{ij})^{5/2} + (s_{ij}^d s_{ij}^d)^{5/4}}, \quad (2.134)$$

The tensor s_{ij}^d is determined as follows.

$$s_{ij}^d = \frac{1}{2} (\tilde{h}_{ij} + \tilde{h}_{ji}) - \frac{1}{3} \tilde{h}_{kk} \delta_{ij}, \quad (2.135)$$

$$\tilde{h}_{ij} = \tilde{g}_{ik} \tilde{g}_{kj}, \quad (2.136)$$

$$\tilde{g}_{ij} = \frac{\partial \tilde{u}_i}{\partial x_j}. \quad (2.137)$$

2.5 Radiation

The effect of heat transfer is considerable in the industrial furnaces. The heat transfer in the configuration under flameless combustion regime studied in the present work is dominated by the radiation (80% on overall the heat released by combustion). Hence, the effect of radiative transfer is essential for the numerical simulations. Nevertheless, this thesis focuses on the combustion modelling, thus, the classical radiative models are chosen and briefly described in this section. The radiative impacts are in the scope of the subsequent project.

The radiation is represented by the spectral radiation intensity I_ν determined by solving the radiative transfer equations (RTE) [109]. There are several methods to solve the RTE equations, such as P-1 model, Discrete Transfer Radiation model (DTRM), Discrete Ordinates model (DOM), etc. The DOM method gives a fair accuracy with the reasonable computational cost, hence, it is widely used in the industrial applications. The RTE of this model is written as below [109].

$$\frac{dI_\nu}{ds}(r, s) + (a + \sigma_s) I_\nu(r, s) = an^2 \frac{\sigma T^4}{\pi} + \frac{\sigma_s}{4\pi} \int_{4\pi} I_\nu(r, s') \phi_\nu(s, s') d\Omega'. \quad (2.138)$$

in which r is the considered position, s and s' refers respectively to the propagation and scattering direction, a represents the absorption coefficient, σ_s stands for the scattering coefficient, n characterises the refractive index, the Stefan-Boltzmann constant σ equals to $5.669 \cdot 10^{-8} \frac{W}{m^2 \cdot K^4}$, T describes the local temperature, ϕ_ν is defined as the phase function and Ω' depicts the solid angle.

At each position r , the DOM solves a system of M transport equations of the radiation intensity I_ν in M corresponding directions s (that also means the M corresponding solid angles in 4π steradians around the mesh node r). The number of directions M is selected by the DOM numerical quadratures S_N (or numerical integration) where N is the quadrature order. The relation between the direction number M and the quadrature order N is $M = N(N + 2)$. Therefore, the quadrature S_4 ($N = 4$) has $M = 24$ directions. The DOM- S_4 is retained in this work.

The combustion occurred in the furnace modifies the radiative properties of the fluid flow through the absorption coefficient characterised by the radiant gaseous species, typically in the flue gases, such as H_2O , CO_2 and CO . The modelling of this radiative properties is complex since the absorption coefficient is frequently described by millions of spectral lines. Modest et al [109] showed that the water vapor has 9.5 millions of spectral lines in only $6.3\mu\text{m}$ band at $P = 1\text{bar}$ and $T = 1000\text{K}$ (cf. figure 2.5).

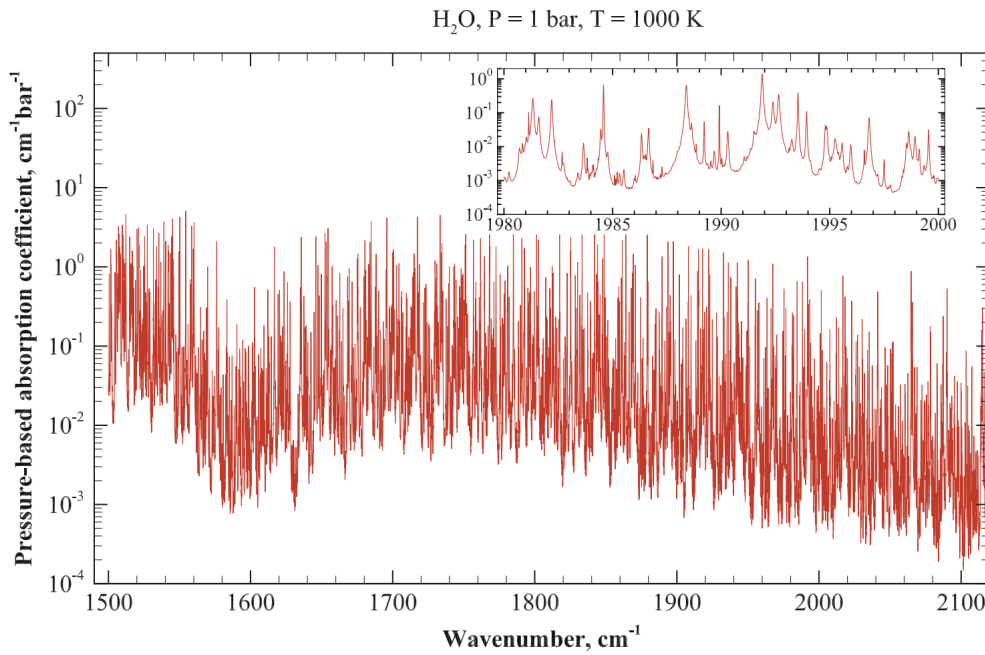


Figure 2.5: Absorption coefficient spectral lines of water vapor in $6.3\mu\text{m}$ band at $P = 1\text{ bar}$ and $T = 1000\text{K}$ [109].

The absorption coefficient calculation through all spectral lines is possible by using the line-by-line method [110], however, the computational cost is undoubtedly tremendous. In order to cope with this bottleneck, the Weighted-Sum-of-Gray-Gases (WSGG) is proposed and becomes popular for industrial applications. This model assumed that the spectral lines are characterised by I gray gases which contribute to the fluid radiative properties calculation (the fluid absorption coefficient a and the fluid emissivity ϵ). The formulas are represented as follows.

$$a = -\frac{\ln(1 - \epsilon)}{s} \quad (2.139)$$

$$\epsilon = \sum_{i=0}^I a_{\epsilon,i}(T) (1 - e^{-\kappa_i P s}) \quad (2.140)$$

$$a_{\epsilon,i} = \sum_{j=1}^J b_{\epsilon,i,j} T^{j-1} \quad (2.141)$$

in which the κ_i and $b_{\epsilon,i,j}$ refers respectively to the absorption coefficient and the temperature-dependent emissivity polynomial coefficient of i^{th} gray gases which could be found in [111], p stands for the sum partial pressure of the radiant gases (such as H₂O, CO₂ and CO) and s corresponds to the path length.

In practice, the sum partial pressure p and the path length s could be determined as follows.

$$p = P(X_{\text{H}_2\text{O}} + X_{\text{CO}_2} + X_{\text{CO}}) \quad (2.142)$$

$$s = \frac{3.6V}{A} \quad (2.143)$$

where P is the total pressure; $X_{\text{H}_2\text{O}}$, X_{CO_2} and X_{CO} correspond respectively the mole fraction of H₂O, CO₂ and CO; V and A stand respectively for the volume and area of the considered configuration.

Chapter 3

Chemical schemes reduction for applications under flameless combustion condition

Contents

3.1 Optimised and reduced chemistry (ORCh)	55
3.2 Strategy for chemical schemes reduction including heat loss	56
3.3 UMONS case configuration	57
3.4 Results and discussions	60
3.4.1 0D time evolution simulation of ORCh	60
3.4.2 3D CFD RANS simulation	69
3.5 Conclusion	77

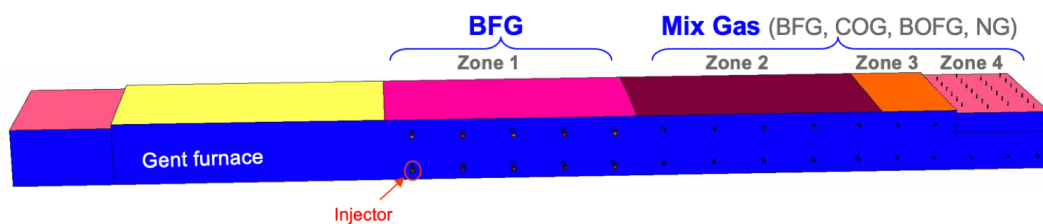
ArcelorMittal is operating, designing and upgrading large scale and high-power combustion systems for applications ranging from upstream primary to finishing steelmaking processes, including coke battery, blast, reheating, treatment and annealing furnaces. The energy released by combustion serves to transform the materials and to reheat the products for rolling or treatment.

In the context of decarbonization, CO₂ emissions mitigation, increasing energy costs and more stringent regulation on environment (NO_x emissions), it is mandatory to revisit these industrial combustion systems. Actions must be taken at every single opportunity we have regarding the valorization of any type of Low Carbon Fuel (LCF) gases produced by our plants or by external parties for our steelmaking processes or for other industries. Multi-fuel injection is an efficient way to valorize LCF gases. LCF includes auto-produced by-product steel gases (Coke Oven Gas (COG), Blast Furnace Gas (BFG), Basic Oxygen Furnace Gas (BOFG)), biogases, green hydrogen, ... Figure 3.1 shows a very large-scale steel slab reheating furnace (60m x 12m x 5m) featuring multi-fuel LCF injection systems. The use of auto-produced steel gases can significantly reduce the environmental impact and contribute to energy saving [112, 113, 114]. The use of biogases and green hydrogen issued from renewable energy sources leads to the decarbonization. In practice, these situations often lead to systems featuring multiple injections of fuel and oxidizers, and flameless oxidation technology appears to be the best choice to stabilize such combustion.

Computational Fluid Dynamics (CFD) is a well-adapted tool to help in the design phase. It is important to note that 3D simulation with detailed chemical schemes such as GRI3.0 [36] (53 species and 325 elementary reactions) or POLIMI version 1412 [37] (107 species and 2642 reactions) is not practicable for industrial applications. This is due to the very high number of species involved and their stiff complicated chemical paths. Along this line, the numerical tool ORCh (<http://orch.coria-cfd.fr>) for chemistry reduction was extended to account for specific application conditions. To this end, heat loss effect due to radiative heat transfer and dilution by burnt gases will be introduced into ORCh, to which accurate control of the reduced scheme stiffness will be added. Then, reduced chemistries will be produced for conditions of interest and applied to the numerical simulation of lab-scale furnace for validation against experimental measurements.



(a)



(b)

Figure 3.1: ArcelorMittal Gent's steel slab reheating furnace (a) and its schematic showing multi-fuel injection (b)

3.1 Optimised and reduced chemistry (ORCh)

ORCh (Optimised and Reduced Chemistry) is an automated method to reduce and optimize detailed chemical scheme (<http://orch.coria-cfd.fr>) [115, 59]. ORCh simulates the time evolution of thermochemical variables (such as the temperature, the mass fraction of species, etc.) without solving the flow, by applying a stochastic turbulent micro-mixing closure with chemistry and other relevant phenomena (evaporation, dilution, etc.) representing the mixture evolution inside the real system.

In ORCh, the inlet are modelled into a set of stochastic particles which carry the thermochemical informations of the inlet which they belong to. The thermochemical variables $\phi_k^p(t)$ of p^{th} particle evolves temporally by solving the stochastic equations.

$$\frac{\partial \phi_k^p(t)}{\partial t} = \text{MIX}^p(\tau_T) + \dot{\omega}_{\phi_k}^p, \quad (3.1)$$

in which $\dot{\omega}_{\phi_k}^p$ is the stochastic chemical source term and $\text{MIX}^p(\tau_T)$ corresponds to the Curl [116] or Euclidean Minimum Spanning Tree (EMST) [117] micro-mixing closure characterised by the mixing time τ_T . It is noteworthy that the number of particles from each inlet are set proportionally with the injection mass flow rate.

The procedure of ORCh generally consists of three major stages (cf. Figure 3.2). In the first stage, the trajectories simulated from the fully detailed scheme are calculated and serve as the references for conducting the reduction and optimisation procedure. Secondly, the species and the reactions are removed from the detailed scheme by the Direct Relation Graph with Error Propagation method (DRGEP) [118, 119] depending on its level of importance against the target species which have been selected. After this stage, a reduced scheme is available but the reaction rates from the Arrhenius equation (pre-exponential constant A, temperature exponent b and activation energy B) still remain the original values of the detailed scheme, thus, this main limitation of this technique leads to the incorrect fuel/air reactivity (estimate through ignition delay time). By this reasoning, the optimisation process is applied in the last stage using a genetic algorithm to correct the rate parameters to match the response of the reduced scheme over the reference trajectories.

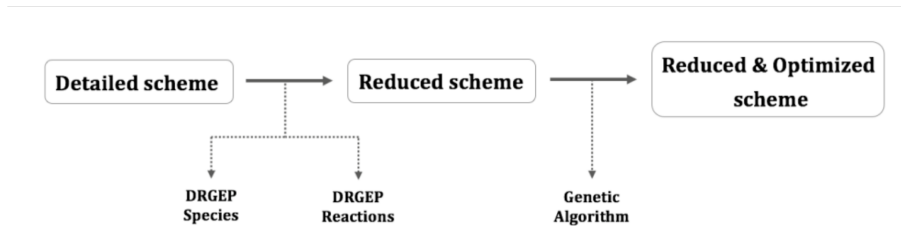


Figure 3.2: ORCh methodology

The optimization process is unable to adapt directly on the stochastic trajectories due to the large number of particles presented. Hence, the stochastic informations are compressed into N_i deterministic trajectories where N_i corresponds to the number of inlets modelled. The deterministic thermochemical variables $\phi_k^D(t)$ are computed by solving the *Linear Mean-Square Estimation* (LMSE) [120] or *Interaction by Exchange with the Mean* (IEM) [121] equations coupling with the relaxation by the average of N stochastic particles.

$$\frac{\partial \phi_k^D(t)}{\partial t} = \frac{1}{\tau_T} \left(\frac{\sum_{p=1}^N \phi_k^p(t)}{N} - \phi_k^D(t) \right) + \dot{\omega}_{\phi_k}^D. \quad (3.2)$$

in which $\dot{\omega}_{\phi_k}^D$ refers to the deterministic chemical source term.

ORCh has been validated first for the methane combustion [58, 59, 57]. Its applications spread from aircraft engines [57] to the large-scale furnaces with urea DeNOx [28] and the perfluorocarbon CxFy decomposition process. Reduced chemistry produced by ORCh has also been employed for the simulation of the micro- and meso-scale combustion systems [122, 123, 124].

3.2 Strategy for chemical schemes reduction including heat loss

This PhD work contributes to ORCh by adding the capability of considering the heat loss due to convection and radiation, in order to generate a reduced and optimised scheme for numerical simulation of furnaces operating at specific condition under flameless combustion regime. This concept has been attempted on a lab-scale furnace (called UMONS furnace - cf. section 3.3 below). This concept, inspired from [125], intends to calibrate the variation of enthalpy (or heat loss) in the ORCh calculation process by using the data collected from 3D CFD simulation as a resource. The procedure is decomposed into the following steps:

- The 3D Fluent [126] RANS simulation of UMONS furnace is performed by using the verified scheme KEE58 [47] (containing 18 species & 58 reactions) with validation against experiments [32]. The simulation data allows to map the variation of enthalpy across the z-position axis $h_{CFD}(z)$ (ie. stream-wise direction) by using the cross-section average (Area Weighted Average) on multiple plans.
- ORCh provides the variable trajectories in time (i.e. $T(t_{ORCh}), Y(t_{ORCh})$). Hence, a transformation from the physical space quantities of 3D Fluent simulation $h_{CFD}(z)$ into the time fields of 0D ORCh calculation $h_{CFD}(t_{ORCh})$ is required and obtained through the formula below.

$$t_{CFD}(z) = \int_0^z \frac{1}{u(z)} dz. \quad (3.3)$$

where $t_{CFD}(z)$ is the average time needed for the fluid particles entering the system to reach the stream wise position z and $u(z)$ is the averaged space velocity (Area Weighted Average) across the z-position axis collected from 3D simulation.

- Once the residence time distribution $t_{CFD}(z)$ is known, the time evolution of enthalpy $h_{CFD}(t_{CFD})$ is imposed to the stochastic particles evolution in ORCh. In other words, each particle loses a specific amount of heat calculated from h_{CFD} at the residence time t_{CFD} .
- The heat loss capture procedure from CFD and the particle heat loss calculation inside ORCh are shown in the figure 3.3 (respectively left and right side). In the calculation process, the coefficient $weight_p$ represents the different amount of heat loss depending on the characteristic of each particle (subscript p for particle). Many hypotheses were attempted to establish this coefficient under the constraint that the sum of particles enthalpy after loss should be equal to the enthalpy of CFD simulation. The decisive formula which is determined with the idea of "Cold particles loses less" is given below (T_p is the particle temperature).

$$weight_p = \frac{T_p}{\sum_{p=1}^N T_p}. \quad (3.4)$$

At this stage, ORCh can then handle the actual heat loss in the furnace to generate the reduced and optimised scheme for UMONS furnace case accordingly. The procedure of this strategy is summarized in the figure 3.3.

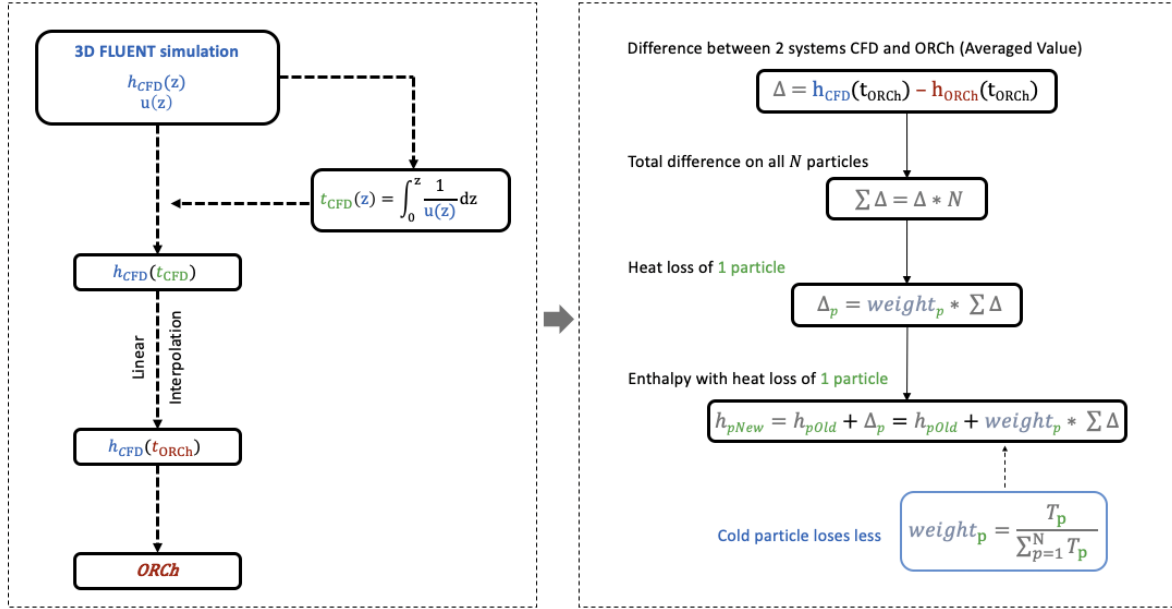


Figure 3.3: Novel strategy to introduce the heat loss from CFD into ORCh. Heat loss capture procedure on the left. Particle heat loss calculation procedure inside ORCh on the right.

From the equation 3.1, the enthalpy stochastic equations ($\phi_k^p(t) = h_s^p(t)$) are modified to include the heat loss Δ_p calculated for each particle p .

$$\frac{\partial h_s^p(t)}{\partial t} = \text{MIX}^p(\tau_T) + \dot{\omega}_{h_s}^p + \Delta_p, \quad (3.5)$$

3.3 UMONS case configuration

Lab-scale UMONS case is the test rig of the University of Mons, it will serve as a database for refined validations [127, 128, 129]. This 30kW pilot furnace operates under the flameless mode, hence with high dilution by burnt gases and strong heat transfer to the thermal charge and the radiation stands for about 80% of the total heat transfer. This lab-scale furnace was designed to mimic some of the main features of industrial furnaces (injection system, geometry, air preheating, variable thermal charge).

The combustion chamber is made of stainless steel and is equipped with a fibrous ceramic heat insulation layer. It has a square inner section of 0.35 m x 0.35 m with 1.0 m high. One air injection with 24.8 mm exit diameter is located in the center. Two gas injectors with 11° tilt angle are symmetrically located around the air injector. The exit diameter of the gas injector was designed to stabilize flameless combustion. The overview of this pilot furnace is showed at Figure 3.4 and 3.5. More information can be found in the PhD thesis of G. Mosca [128].

The combustion chamber is fed with the preheated air (up to 800°C by an electrical preheater) and the LHV fuel, named B50, which is composed of 50%vol of blast-furnace gases (BFG) and 50%vol of coke-oven gases (COG) while both are the auto-produced by-product fuel gases. The blast-furnace gases

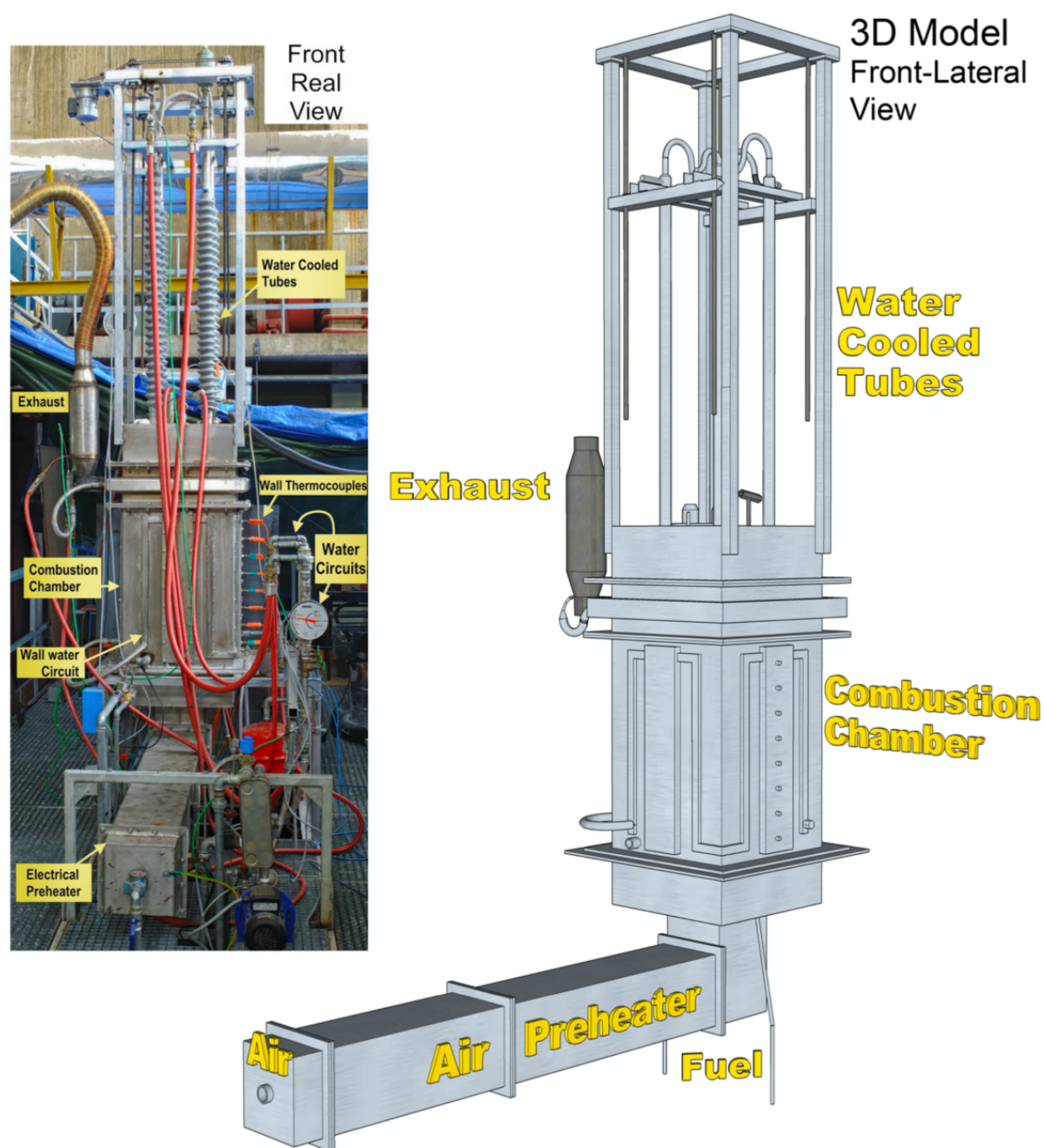


Figure 3.4: UMONS flameless combustion furnace. Front real picture (left) and 3D model (right) [128].

have a very low heating value, hence, it could not be used individually. The fuel gas compositions are realized using a mixing unit equipped with mass flow meters and controllers fed through pure gas bottles. The thermal charge and the furnace temperature are controlled through four water cooling tubes (heat sink) the immersion of which can be regulated from 0 to 90 *cm* and a reduced water circuit along the outer walls. Each vertical wall of the combustion chamber has a removable part. A wall (on the rear side) is equipped with a quartz window to allow for optical access and image recording. A LaVision intensified camera with UV filter centered at 329 nm is used to take images of chemiluminescent self-emission of

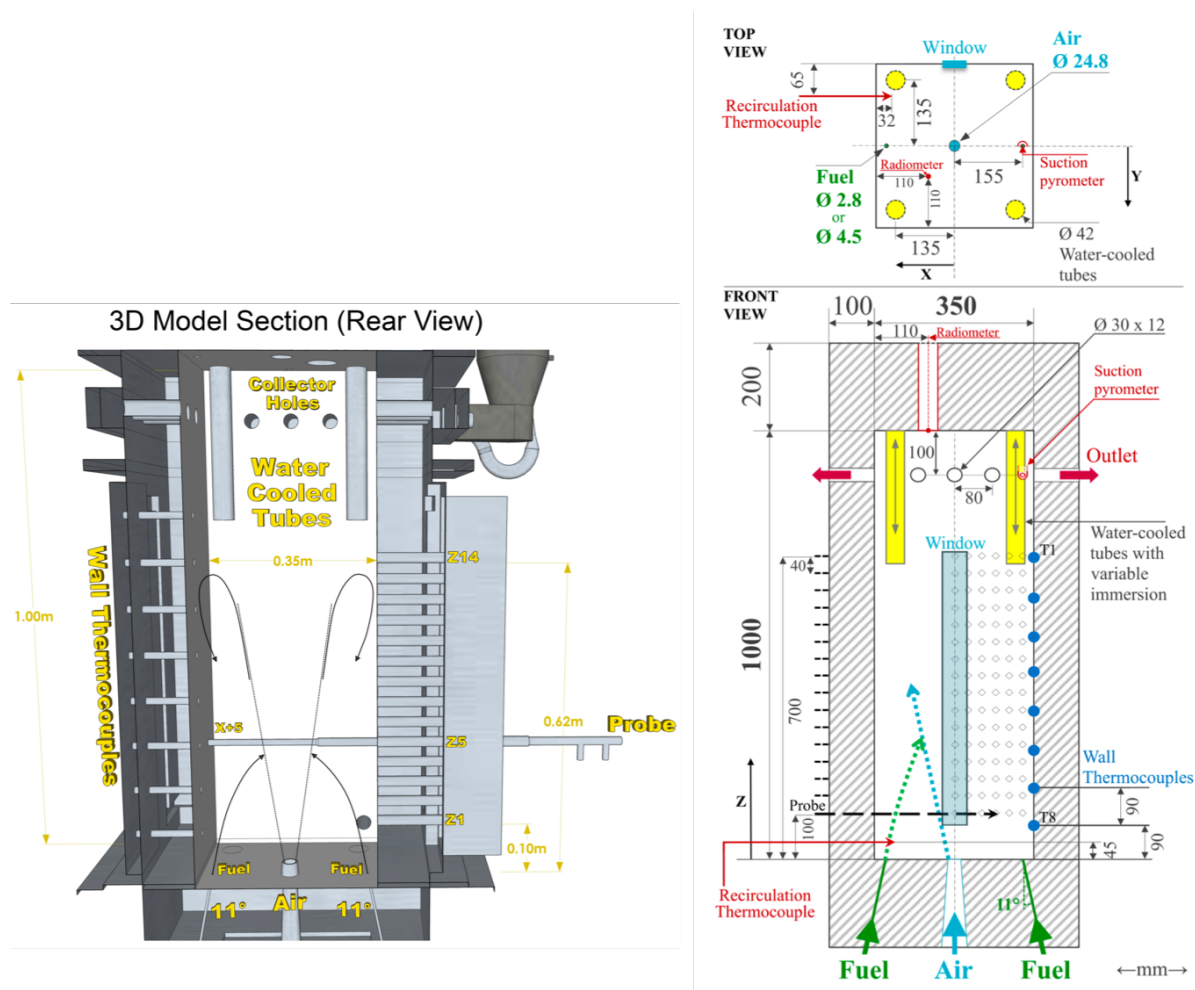


Figure 3.5: Schematic representation of UMONS furnace (left) and the dimensions in mm (right) [128].

OH* radicals at 308nm wave-length [130]. OH* imaging allowed for determining the position of main reaction zones. A side wall (on the right) is equipped with eight S-type thermocouples, 0.09m separated each other and mounted flush with the insulation layer, in order to get a wall temperature profile along the furnace height in the vertical symmetry plane containing the air and gas injectors. The measurements of temperature and species concentration at the furnace exit and inside the furnace were realized by the two home-made probes which are inserted inside the furnace through fourteen holes on the wall opposite to the thermocouples wall. The suction pyrometer probe is equipped with a S-type thermocouple and works with a Venturi's tube connected to an air compressed circuit. The gas sampling probe is equipped with a vacuum pump to extract burnt gases with a flowrate equal to 210Nl/h. Water is removed and the dry sample is sent in parallel to the chromatograph and gas analysers. The concentrations of O₂, CH₄, CO₂ and CO (on dry basis) were measured by the paramagnetic and infrared gas analysers. Measurement of H₂ and N₂ and another measurement of O₂, CH₄ and CO were realized by the gas chromatograph. More details regarding the experimental procedure and measurements can be found in our previous works [32, 128, 131, 132]. The composition and mass flow rate of the B50 and air inlets are taken from the experimental conditions (cf. Table 3.1).

For the purpose of modelling the recirculation gas into the 0D ORCh calculation, a virtual inlet is added (named recirculation inlet). This inlet represents the fumes recirculated from the top of the

furnace. The mass flow rate of this inlet is calculated from the dilution rate. It should be noted that the dilution rate is varied depending on the type of fuel to achieve the MILD combustion regime. According to our studies [128, 129], the dilution rate (cf. equation 1.7) for B50 fuel is around 5 ($K_v = 5$). The composition and temperature of the recirculation inlet should be determined under the constraints that the global equivalence ratio remains the same as the operating conditions of the UMONS 2-inlets case (as a result of the atomic mass conservation of each element such as C, H, O, N). From a practical point of view, the outlet condition can be chosen as the third virtual recirculation inlet. Therefore, the outlet temperature and composition, as shown in Table 3.1, are considered as the recirculation inlet condition taken from the 3D Fluent simulation result (averaged values from outlet).

Inlet	B50	Air	Recirculation
X_{CH_4}	0.1425	-	-
X_{H_2}	0.325	-	0.0000311
X_{N_2}	0.28	0.79	0.6962957
X_{O_2}	-	0.21	0.0171846
X_{CO_2}	0.12	-	0.1124177
X_{CO}	0.1325	-	0.0000858
X_{H_2O}	-	-	0.1738373
X_{OH}	-	-	0.0001407
T(K)	290.65	1075.66	1376.1825
Mass flow rate (kg/s)	0.002572941	0.010293228	0.064330844
Pressure (Pa)	101325	101325	101325

Table 3.1: UMONS inlet conditions.

3.4 Results and discussions

3.4.1 0D time evolution simulation of ORCh

3.4.1.1 Heat loss implementation

In the first place, the heat loss has been implemented into ORCh by applying the procedure presented in the section 3.1 and 3.2 on the two detailed chemical schemes GRI3.0 [36] (53 species and 325 elementary reactions), POLIMI version 1412 [37] (107 species and 2642 reactions) (cf. section 1.1.5). Figure 3.6 shows the averaged enthalpy calculated from Fluent and from ORCh (with or without heat loss implementation). The results confirm that ORCh is able to reconstruct the enthalpy in the heat loss case with only a small variation.

Scheme	Number of species	Number of reactions
GRI3.0	53	325
POLIMI1412	107	2642
KEE58	18	58

Table 3.2: Two detailed chemical schemes GRI3.0 and POLIMI1412, and one reduced scheme KEE58.

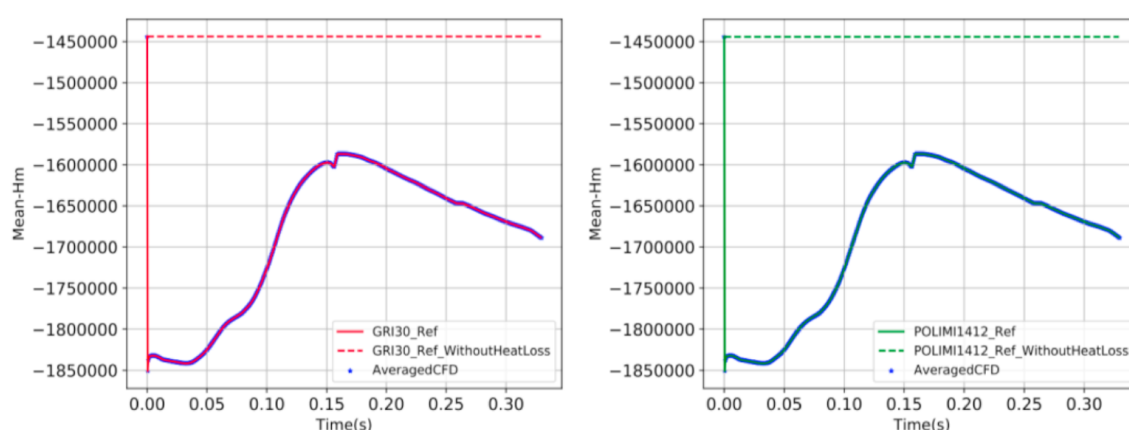


Figure 3.6: Averaged enthalpy collected in the case tested with GRI3.0 (red) and POLIMI1412 (green) from Fluent (blue star markers), ORCh with heat loss implementation (red and green solid line) and without heat loss implementation (red and green dashed line).

The deterministic trajectories from each inlet are also computed for three different schemes (cf. Table 3.2) in two cases with and without the heat loss for further analysis (cf. Figure 3.7 and Figure 3.8). The trajectories indicate that in the case without the heat loss (dashed lines), the three detailed chemical schemes return similar trajectories of the temperature and the major species (CH_4 , H_2 , O_2 , CO , CO_2 , H_2O , N_2 - Figure 3.7). However, the minor species (CH_3 , CH_2O , HO_2 , OH , O , H , HCO - Figure 3.8) in this case (i.e. without heat loss) achieve different peaks. The heat loss (solid lines) affects the evolution of both major and minor species and also the ignition delay time. The final state of temperature is different between the cases with and without heat loss. The final equilibrium state of all major and minor species is not profoundly modified by heat loss because of the weak impact on intermediate species dissociation of the heat loss levels considered. However, this is not exactly the case for OH . The equilibrium state of OH in the case with heat loss is slightly lower (in the order of 10^{-5}) as compared to the case without heat loss because of the lower temperature caused by the thermal loss. The final state in the case with heat loss is also compared with the outlet result obtained with the CFD simulation (cf. Table 3.3). A good agreement is obtained for the temperature, the mass fractions of the combustion products (CO_2 , H_2O , N_2) and the excess O_2 while the mass fractions of reactants (CH_4 , H_2 , CO) present discrepancies but their values are extremely low as they are supposed to be fully oxidated.

It should be reminded that G. Mosca [128] simulated this UMONS furnace using KEE58 mechanism (which is a reduced scheme derived from GRI) and reported the good overall trends of species mole fraction but the important differences in proximity of the air jet and the significant over-prediction of the temperature peak. It is also important to note that the full CFD simulation using the detailed scheme such as GRI3.0 and POLIMI1412 is remarkably rare, even has not been performed, especially in MILD combustion regime for the industrial furnaces. The interesting aim of this work is to carry out these simulations on the reduced schemes but highly optimised to mimic the behaviour of the detailed scheme. The simulation results will be observed and compared with the experiment data and the difference between the schemes will be analysed in the next section 3.4.2.

	Final state ORCh	CFD UMONS outlet
T(K)	1396.2	1376.1825
Y_{H_2}	5.29898e-08	2.21004e-06
Y_{CH_4}	1.33949e-14	1.19033e-14
Y_{CO}	1.11311e-06	8.53729e-05
Y_{CO_2}	0.175468	0.175860
Y_{N_2}	0.693336	0.693160
Y_{O_2}	0.0201569	0.019551
Y_{H_2O}	0.111023	0.111249

Table 3.3: Comparison between the final equilibrium state from ORCh and the outlet conditions of UMONS CFD case.

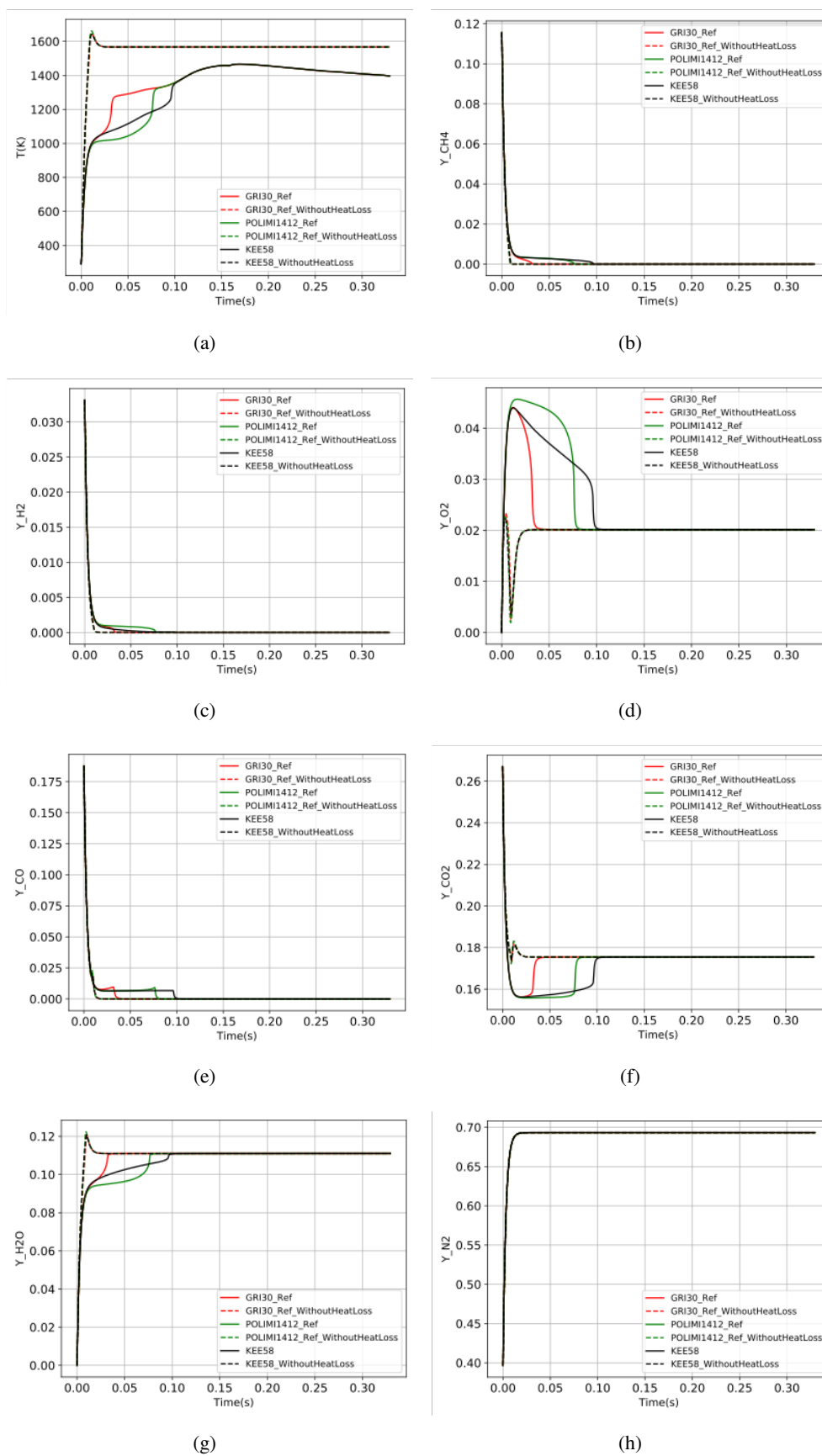


Figure 3.7: Deterministic trajectories of temperature and major species at B50 inlet for 2 cases: with (solid line) and without (dashed line) heat loss. Schemes used: GRI3.0 (red), POLIMI1412 (green), KEE58 (black).

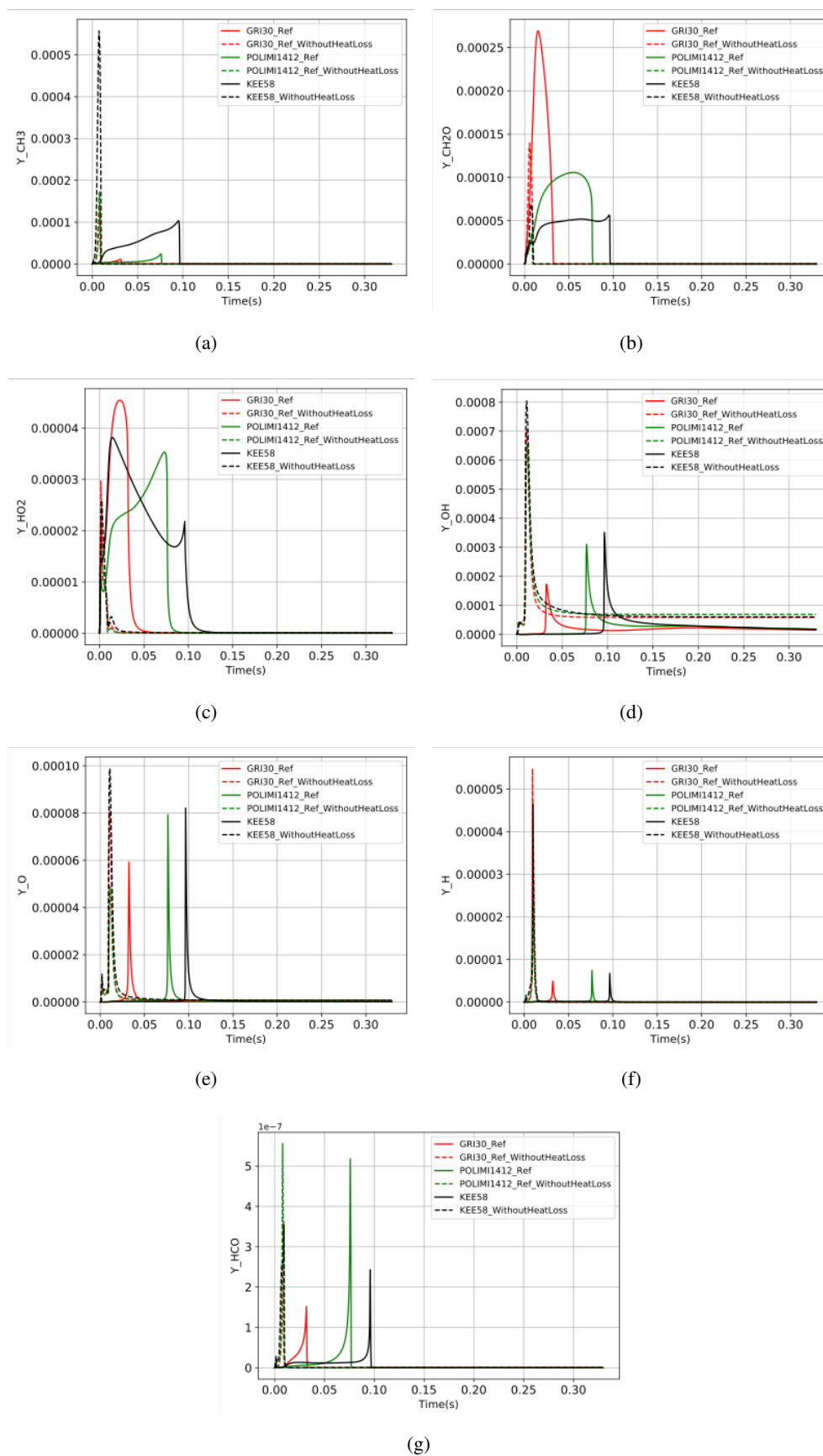


Figure 3.8: Deterministic trajectories of minor species at B50 inlet for 2 cases: with (solid line) and without (dashed line) heat loss. Schemes used: GRI3.0 (red), POLIMI1412 (green), KEE58 (black).

3.4.1.2 Reduction and optimisation

For the reduction and optimisation including heat loss effect, the species CH_4 , O_2 , CO_2 , CO , H_2O and H_2 were chosen as targets. As a result, two 14 species and 15 reactions schemes (cf. Table 3.4 and 3.5) are generated, named respectively **GRI30-14S15R** (Table 3.6) and **POLIMI1412-14S15R** (Table 3.7). The 14 species are identical within 2 schemes but the reactions are different. It is worth noting that their scheme reaction rates were also optimised to procure the well fitted trajectories.

Scheme	Number of species	Number of reactions
GRI30-14S15R	14	15
POLIMI1412-14S15R	14	15

Table 3.4: Two reduced chemical schemes generated.

Species													
H_2	H	O	O_2	OH	H_2O	HO_2	CH_3	CH_4	CO	CO_2	HCO	CH_2O	N_2

Table 3.5: Remained important species after ORCh reduction.

GRI30-14S15R		A	β	E_a
1	$\text{O} + \text{CH}_3 \rightleftharpoons \text{H} + \text{CH}_2\text{O}$	1.64e+13	0	0
2	$\text{H} + \text{O}_2 + \text{M} \rightleftharpoons \text{HO}_2 + \text{M}$	5.58e+17	-0.86	0
3	$\text{H} + \text{O}_2 + \text{H}_2\text{O} \rightleftharpoons \text{HO}_2 + \text{H}_2\text{O}$	8.28e+18	-0.68	0
4	$\text{H} + \text{O}_2 \rightleftharpoons \text{O} + \text{OH}$	9.92e+16	-0.63	16230
5	$\text{H} + \text{HO}_2 \rightleftharpoons 2\text{OH}$	9.19e+13	0	673
6	$\text{H} + \text{CH}_2\text{O} \rightleftharpoons \text{HCO} + \text{H}_2$	1.52e+07	1.97	2987
7	$\text{OH} + \text{H}_2 \rightleftharpoons \text{H} + \text{H}_2\text{O}$	1.5e+08	1.47	3765
8	$2\text{OH} \rightleftharpoons \text{O} + \text{H}_2\text{O}$	47300	2.43	0
9	$\text{OH} + \text{HO}_2 \rightleftharpoons \text{O}_2 + \text{H}_2\text{O}$	9.57e+13	0	0
10	$\text{OH} + \text{HO}_2 \rightleftharpoons \text{O}_2 + \text{H}_2\text{O}$	6.1e+14	0	15916
11	$\text{OH} + \text{CH}_4 \rightleftharpoons \text{CH}_3 + \text{H}_2\text{O}$	1.02e+08	1.55	2925
12	$\text{OH} + \text{CO} \rightleftharpoons \text{H} + \text{CO}_2$	5.49e+07	1.19	71
13	$\text{OH} + \text{CH}_2\text{O} \rightleftharpoons \text{HCO} + \text{H}_2\text{O}$	2.91e+09	1.34	0
14	$\text{HCO} + \text{M} \rightleftharpoons \text{H} + \text{CO} + \text{M}$	1.76e+17	-0.86	15591
15	$\text{HCO} + \text{O}_2 \rightleftharpoons \text{HO}_2 + \text{CO}$	7.61e+13	0	459

Table 3.6: Reduced & optimised GRI30-14S15R scheme (14 species & 15 reactions). Units are cal/mole , mole , cm^{-3} , s , K .

The results are regrouped in Figure 3.9 (B50 inlet) and Figure 3.10 (Air inlet). The results reveal that the reduced scheme (dotted line) is able to mimic the progress of the variables (temperature and mass fraction) of the detailed scheme (solid line) with a fewer number of species and reactions (39 species & 310 reactions for GRI30 case and 92 species & 2627 reactions for POLIMI1412 case have been removed). This confers a considerable advantage in computational cost in 3D CFD simulation, even compared to the reduced scheme KEE58 from literature (consisting of 18 species and 58 reactions).

	POLIMI1412-14S15R	A	β	E_a
1	$\text{H} + \text{O}_2 \rightleftharpoons \text{OH} + \text{O}$	7.88e+15	-0.16	18910
2	$\text{H} + \text{O}_2 (+ \text{M}) \rightleftharpoons \text{HO}_2 (+ \text{M})$	3.4e+13	0.39	0
3	$\text{OH} + \text{HO}_2 \rightleftharpoons \text{H}_2\text{O} + \text{O}_2$	1.07e+15	0	820
4	$\text{H} + \text{HO}_2 \rightleftharpoons \text{OH} + \text{OH}$	3.06e+14	0	2037
5	$\text{OH} + \text{OH} \rightleftharpoons \text{O} + \text{H}_2\text{O}$	35800	2.37	0
6	$\text{O}_2 + \text{HCO} \rightleftharpoons \text{HO}_2 + \text{CO}$	3.54e+13	0	0
7	$\text{CO} + \text{OH} \rightleftharpoons \text{CO}_2 + \text{H}$	6.55e+11	0.14	7839
8	$\text{CO} + \text{OH} \rightleftharpoons \text{CO}_2 + \text{H}$	1.08e+11	0.03	0
9	$\text{HCO} + \text{M} \rightleftharpoons \text{CO} + \text{H} + \text{M}$	4.02e+18	-1.01	17023
10	$\text{OH} + \text{CH}_3 \rightleftharpoons \text{CH}_2\text{O} + \text{H}_2$	3.14e+13	0	0
11	$\text{OH} + \text{CH}_3 \rightleftharpoons \text{O} + \text{CH}_4$	1.61e+12	0	8298
12	$\text{H} + \text{H}_2\text{O} \rightleftharpoons \text{H}_2 + \text{OH}$	5.61e+09	0.93	15504
13	$\text{OH} + \text{CH}_4 \rightarrow \text{H}_2\text{O} + \text{CH}_3$	1.72e+06	1.95	1581
14	$\text{CH}_3 + \text{H}_2\text{O} \rightarrow \text{CH}_4 + \text{OH}$	478000	2.13	15832
15	$\text{OH} + \text{CH}_2\text{O} \rightarrow \text{H}_2\text{O} + \text{HCO}$	1.09e+07	2.13	0

Table 3.7: Reduced & optimised POLIMI1412-14S15R scheme (14 species & 15 reactions). Units are *cal/mole, mole, cm⁻³, s, K*.

In the Figure 3.10, a slight difference of CH₄, H₂, CO mole fraction in both GRI30 and POLIMI1412 case are reported. The difference is caused by the lack of reactions describing further the chemical paths of these species, which were deleted by the reduction procedure.

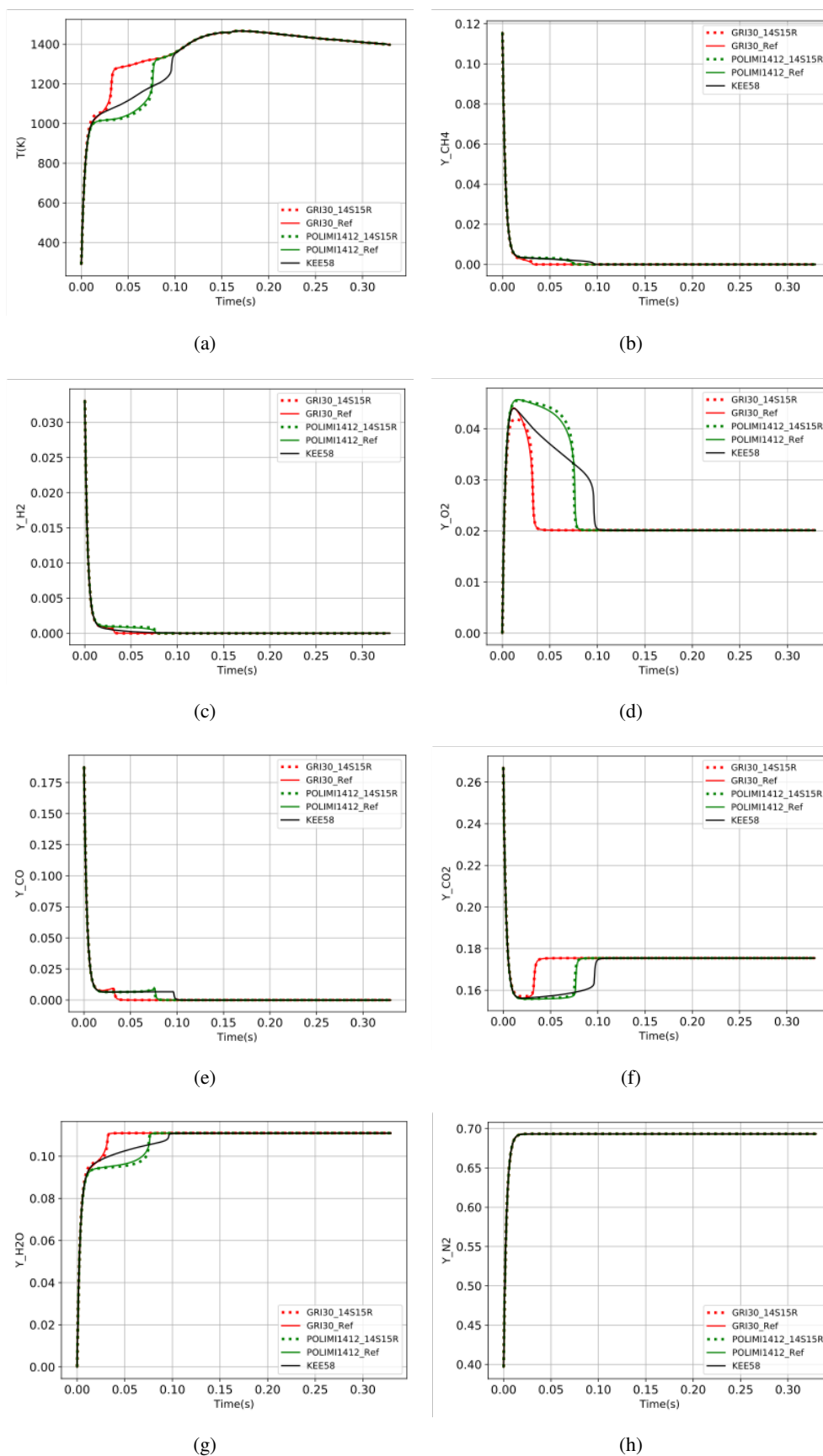


Figure 3.9: Deterministic trajectories of temperature and major species at B50 inlet after ORCh reduction and optimisation. Detailed scheme: solid line, Reduced scheme: dotted line. GRI3.0: red, POLIMI1412: green, KEE58: black.

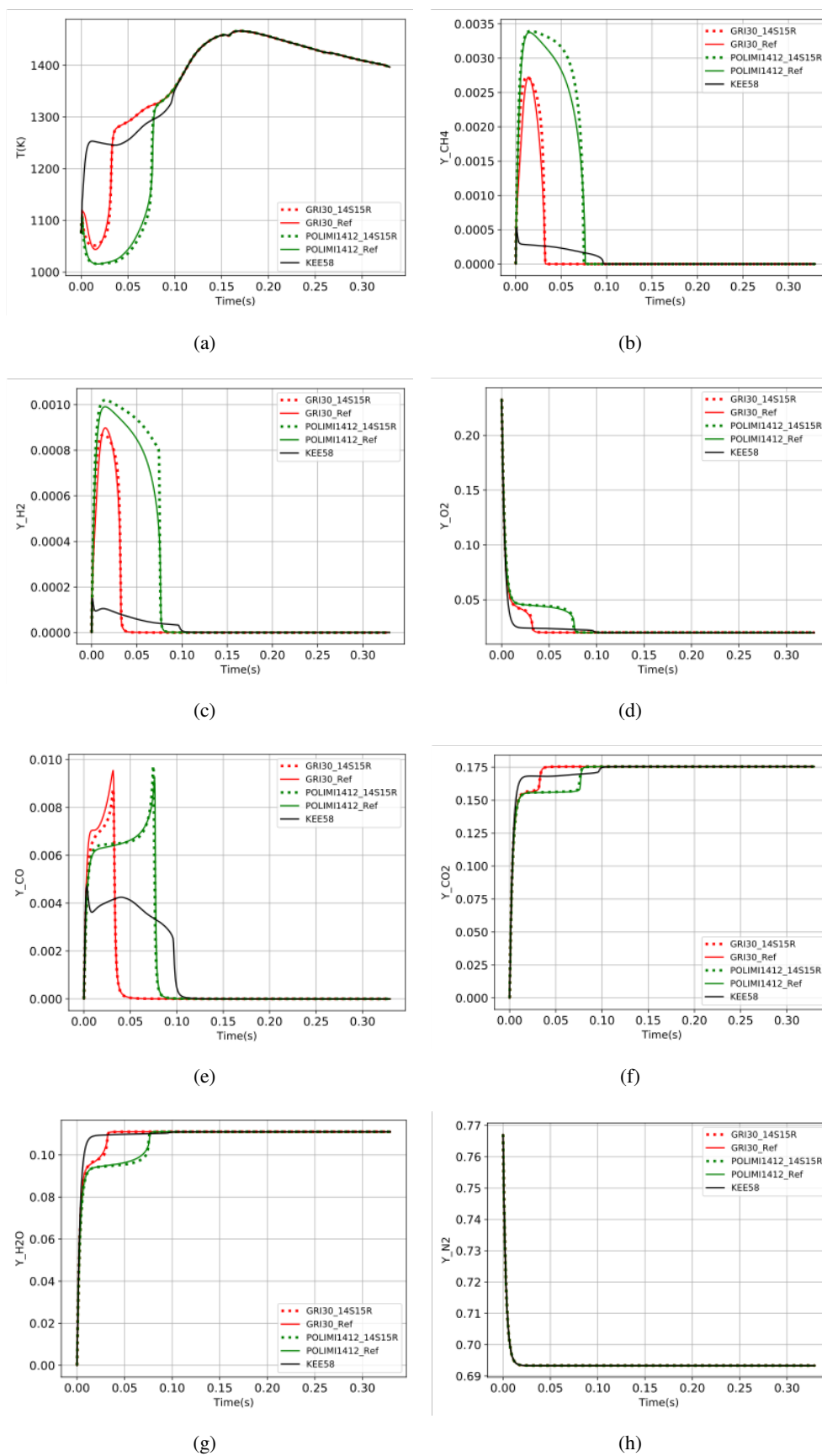


Figure 3.10: Deterministic trajectories of temperature and major species at Air inlet after ORCh reduction and optimisation. Detailed scheme: solid line, Reduced scheme: dotted line. GRI3.0: red, POLIMI1412: green, KEE58: black.

3.4.2 3D CFD RANS simulation

3.4.2.1 Numerical simulation setup

The two reduced and optimised schemes described in the previous section and the KEE58 scheme [47] were implemented into the Ansys Fluent© [126] flow solver and the simulations were carried out for the flameless combustion of the UMONS furnace (cf. section 3.3). The KEE58 scheme was validated for MILD combustion for various mixtures of H₂ and CH₄ [133, 134, 135]. In Galletti et al. [134], the KEE58 mechanism gave very similar results as compared to GRI-3.0 detailed mechanism [36] in term of mean temperature prediction and the error is less than 5% in comparison with experiment. Also in Aminian et al. [133], KEE58 showed more reliable predictions than other schemes such as DRM-19 and DRM-22 [136] in terms of temperature and species concentrations for MILD combustion of CH₄ and H₂ mixtures. In the recent studies of Silei et al. [137] and Ferrarotti et al. [138] for the MILD and flameless combustion systems which are similar to that in the present study, i.e., MILD or flameless conditions are obtained by burner designs to create internal flow recirculation, the KEE58 scheme provided satisfied predictions. It is also to notice that MILD combustion was studied in the framework of RANS modeling, using EDC [139, 133, 140, 141, 134, 135] or FGM (Flamelet Generated Manifold) [142] to account for turbulence chemistry interaction.

The CFD solution is obtained numerically by solving RANS equations in steady state. The choice of $k - \epsilon$ RNG turbulence model [143] for this study is recommended from the study on the same furnace of Lupant [32, 132] who carried out a deep analysis of the effect of different turbulence models (of the two families $k - \epsilon$ and $k - \omega$) considering the species distribution in a non-reacting mixture, to validate the turbulence model independently from the combustion model. The $k - \epsilon$ RNG model developed for strained flows is found appropriate to predict the turbulent flow field in the flameless combustion characterized by intense recirculation.

The turbulence-chemistry interaction was modeled using Eddy- Dissipation Concept (EDC) [34, 144] to consider finite rate chemistry effects. A transport equation for each of these chemical species is solved except for nitrogen. The in-situ adaptive tabulation (ISAT) [145] was used to accelerate the chemistry integration. EDC model was used in its standard form even though some improvement for temperature prediction can be obtained by modifying or calculating directly volume fraction and residence time constants of species in fine structures based on local flow characteristics [139, 133, 140, 141]. However, in the recent study of Silei et al. [137] for the MILD combustion system which is similar to that in the present study in the sense that MILD condition is obtained by burner design to promote internal flue gas recirculation, the standard EDC model (with KEE58 chemical scheme) provided satisfied prediction while the EDC models with modified or locally calculated model constants did not show effective improvement. The flameless condition in the current study is different from that of Jet-in-Hot-Coflow flames for which EDC constants modifications were proposed [139, 133, 140].

The gaseous radiative properties are modelled using the weighted-sum-of-gray-gases (WSGG) approach [146]. In the WSGG approach, the non-gray gas is replaced by an equivalent number of gray gases with different absorption coefficients and emissivity, for which the heat transfer rates are calculated independently. The total heat flux is then calculated by adding the heat fluxes of each gray gas. In the present work, the gaseous radiative properties (emissivity weighting factor and absorption coefficient) of combustion products (H₂O and CO₄) are calculated using the widely used correlation proposed by Smith et al. [111]. Three gray gases were considered in the study to keep CPU time and memory requirements acceptable [147, 148, 129]. The discrete ordinate method (DOM) [149] was used for angu-

lar discretization of the radiative transfer equation (RTE) with nine solid angles per octant (3x3). DOM was chosen, because it is sufficiently accurate, acceptable in terms of computational cost [150], and applicable across a wide range of optical thicknesses, which is not well known in flameless combustion [31].

The computational domain corresponds to the whole gas volume inside the furnace. The grid was made unstructured with nearly six million hexahedral cells considering the grid independence study carried out in the same furnace operating on natural gas for a quarter of domain thanks to symmetry [32, 132]. The results showed that when the grid size increased from 640 thousand hexahedral cells to 1.3 million hexahedral cells (equivalently 2.56 million hexahedral cells to 5.2 million hexahedral cells for the full domain in the present study), no more sensibility to grid size was observed for temperature and chemical species. $y^+ = 1$ on the walls of the air and gas injections while on the furnace walls y^+ is mainly around 15 and does not exceed 30. The resolution in the shear layer is $h = 7\mu m$. The boundary conditions were calibrated using the experimental measurements. Temperature, gas composition and mass flow rates are fixed at inlets. For the other walls, the total heat loss (p_{loss}) from experimental heat balance is considered uniformly distributed on the walls with total surface (s_{wall}), and used to deduce a global heat transfer coefficient (k) between the inner wall temperature (T_{inn}) (average measured value) and the external environment temperature (T_{ext}). The expression for k is:

$$k = \frac{p_{loss}}{s_{wall}(T_{inn} - T_{ext})}, \quad (3.6)$$

3.4.2.2 Energy balance and measurements at the furnace exit

Table 3.8 compares the energy terms between the experiment and the simulation. It is noticed that the air preheating power was subtracted from the flue gas loss in order to consider the fuel power as a single input (this would be the case if the air was preheated by the flue gases as in an industrial recuperative or regenerative burner). The numerical simulation is able to reproduce the different terms measured experimentally, confirming the closure of the energy balance. 57% of the power input is transferred to the thermal charge and 80% of which is transferred by radiation and 20% by convection. This result confirms a consistency between the simulations and the experiment.

	Experiment	KEE58	GRI30-14S15R	POLIMI1412-14S15R
Fuel power	30.0 ± 0.01	31.202	29.788	29.452
Thermal charge	17.16 ± 0.58	17.107	17.003	16.983
Flue gas loss	8.96 ± 0.11	8.703	8.649	8.653
Wall loss	3.86 ± 0.61	4.223	4.212	4.209

Table 3.8: Comparison of energy terms (in kW) between simulation and experiment.

Table 3.9 shows the comparison of the temperature, CO₂ and O₂ content between the numerical predictions and the experimental measurements, obtained at the furnace exit. The species concentration is expressed on dry basis using the following expression:

$$X_{dry} = \frac{100X_{wet}}{(1 - X_{H_2O})}, \quad (3.7)$$

In general, a good agreement is obtained between the numerical predictions and measurements, validating the mass balance. This result also confirms that the modeling using the new reduced chemical schemes is able to predict correctly the measurements at the furnace exit.

	Experiment	KEE58	GRI30-14S15R	POLIMI1412-14S15R
Temperature (K)	1386.45	1376.45	1372.76	1374.14
X_{O_2} (% vol. dry)	2.12	2.08	2.11	2.10
X_{CO_2} (% vol. dry)	13.98	13.61	13.59	13.41

Table 3.9: Temperature and species content at the furnace exit.

3.4.2.3 Comparison of numerical results with in-furnace measurements

The streamwise (Z direction) profiles of temperature and chemical species in the symmetrical plan ($Y=0$) at several X lateral positions are considered for the comparison between the numerical prediction and the experimental measurements.

Figure 3.11 shows the comparison for the temperature between the measurement and the simulation results. Both the experimental and numerical results show rather flat temperature profiles; this is a characteristic of flameless combustion in which the temperature field is quasi-homogeneous and distributed largely in the whole volume, local hot spots related to flames were not observed. The simulation over-predicts the experimental profiles by about 9% to 14%. It is observed, at the locations of $x = \pm 0.12m$ and $\pm 0.15m$, that the measured temperature decreases in the vicinity of the fuel jet and this trend is well recovered by the simulation. The over-prediction of the temperature in highly diluted zones, where local extinctions and high fluctuations occur at $x = \pm 0.06m$, may be attributed to the EDC turbulence chemistry interaction modeling. Christo and Dally [31] also found the same trend for the simulation of the most diluted case, the lowest 3% oxygen level in a hot co-flow, using EDC with the detailed chemistry GRI-3.0 [36]. Discussions to improve temperature prediction by modifying or calculating directly volume fraction and residence time constants of species in fine structures based on local flow characteristics can be found in [139, 133, 140, 141]. This is beyond the scope of this work which focuses on the implementation of the chemical schemes reduced including heat loss effect during the reduction step. Overall, the results obtained confirm that the integration of heat loss into the chemistry reduction can provide a reasonable prediction of temperature level and trend in the context of flameless combustion simulation.

Figures 3.12, 3.13 and 3.14 show the comparison between the measurement and the simulation results for three reactive species present in the fuel, namely H_2 , CH_4 , and CO . The peak in each profile corresponds to the fuel jet and these peaks are decreasing due to the mixing with the recirculated burnt gases and the air when moving farther from the fuel injector located at $x = \pm 0.155m$. The measured species profiles at the location of $x = \pm 0.15m$ indicate a significant asymmetry of the fuel jet while the numerical results show rather symmetrical profiles for all locations. The computed species profiles at $x = \pm 0.15m$ agree only with the measured species profile at $x = -0.15m$. As indicated by the experimental profiles at $x = +0.15m$, the content of three reactive species (H_2 , CH_4 , CO) is very low in the vicinity of the fuel jet on the side of positive abscissa (the right side in the left figure of Figure 3.5) where the sampling probe was introduced into the furnace. It could be possible that the interaction between the sampling probe and the fuel jet plays a role in such phenomenon; the upstream of the sampling point in the fuel jet is perturbed by the probe while it is not the case for the side of negative abscissa.

Figure 3.15 shows the comparison between the measurement and the simulation results for the oxidizer O_2 and the combustion product CO_2 . It is noted that the distribution of oxygen is not symmetrical between the two measured O_2 profiles at $x = +0.09m$ and $x = -0.09m$ while it is not the case for the predicted O_2 profiles. The experimental trend of the measured O_2 profiles at $x = \pm 0.12m$ is not fully recovered by the simulation. As far as the profiles of CO_2 are concerned, the distribution is quite homo-

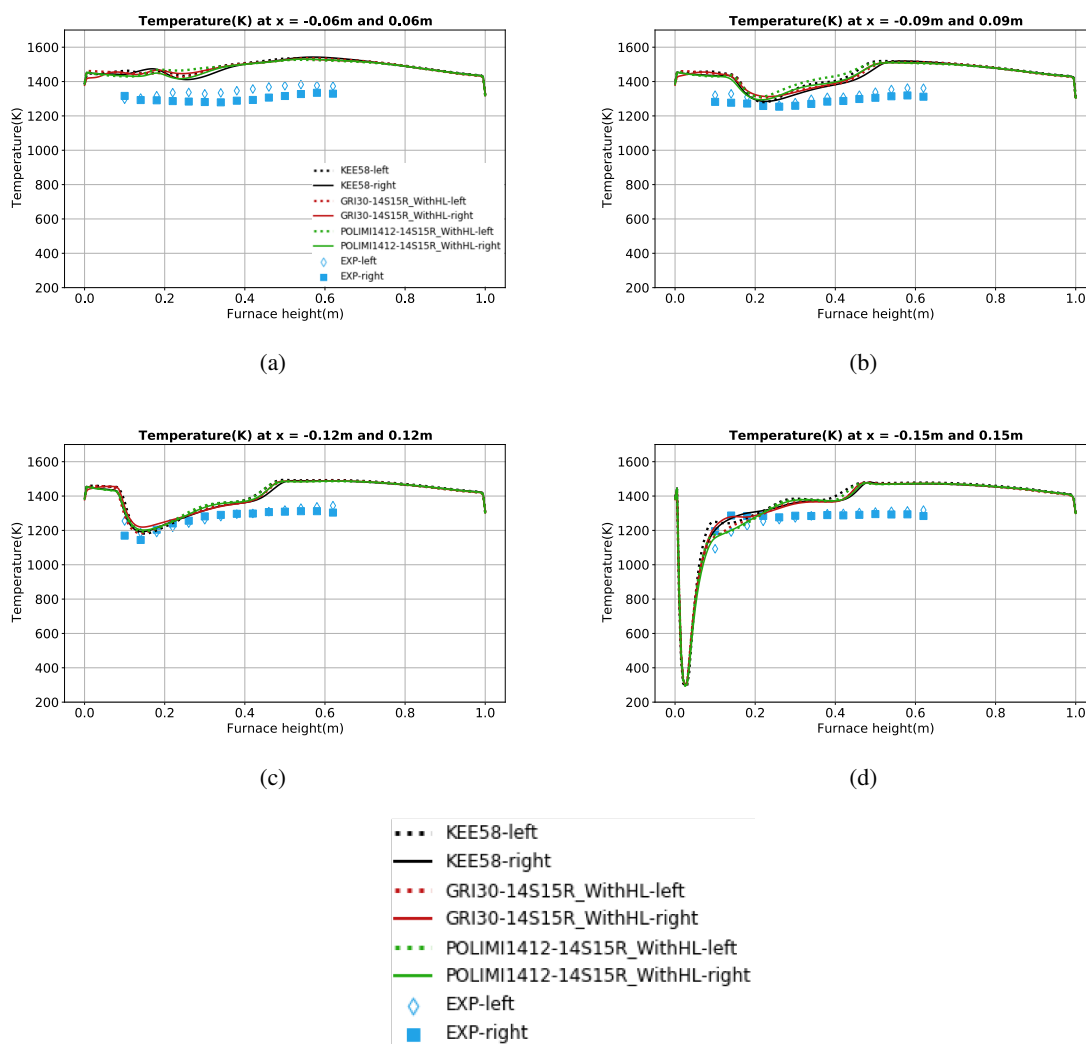


Figure 3.11: Comparison between the experimental and computed profiles of temperature obtained at different (negative and positive) x positions and along the furnace height z . (a) $x = \pm 0.06$, (b) $x = \pm 0.09$, (c) $x = \pm 0.12$, (d) $x = \pm 0.15$. Left and right mean negative and positive x , respectively. Maximum measurement uncertainty is $7.6K$.

geneous and the level is always higher than 13% (by volume) confirming that the combustion is highly diluted by the combustion products. The prediction of CO_2 can be seen acceptable as compared to the measurement.

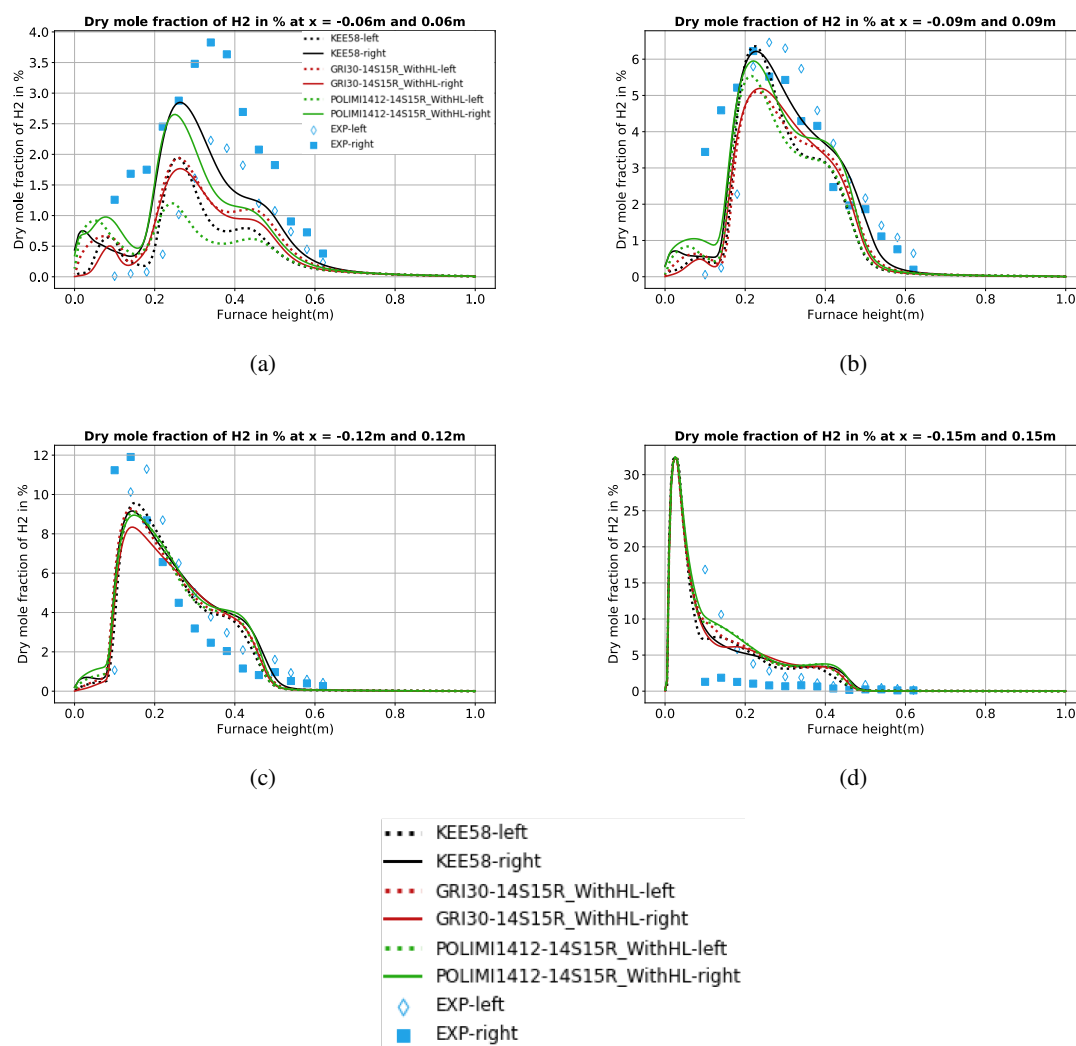


Figure 3.12: Comparison between the experimental and computed profiles of H_2 in volume percentage on dry basis, obtained at different (negative and positive) x positions and along the furnace height z . (a) $x = \pm 0.06$, (b) $x = \pm 0.09$, (c) $x = \pm 0.12$, (d) $x = \pm 0.15$. Left and right mean negative and positive x , respectively. Maximum measurement uncertainty is 0.72%.

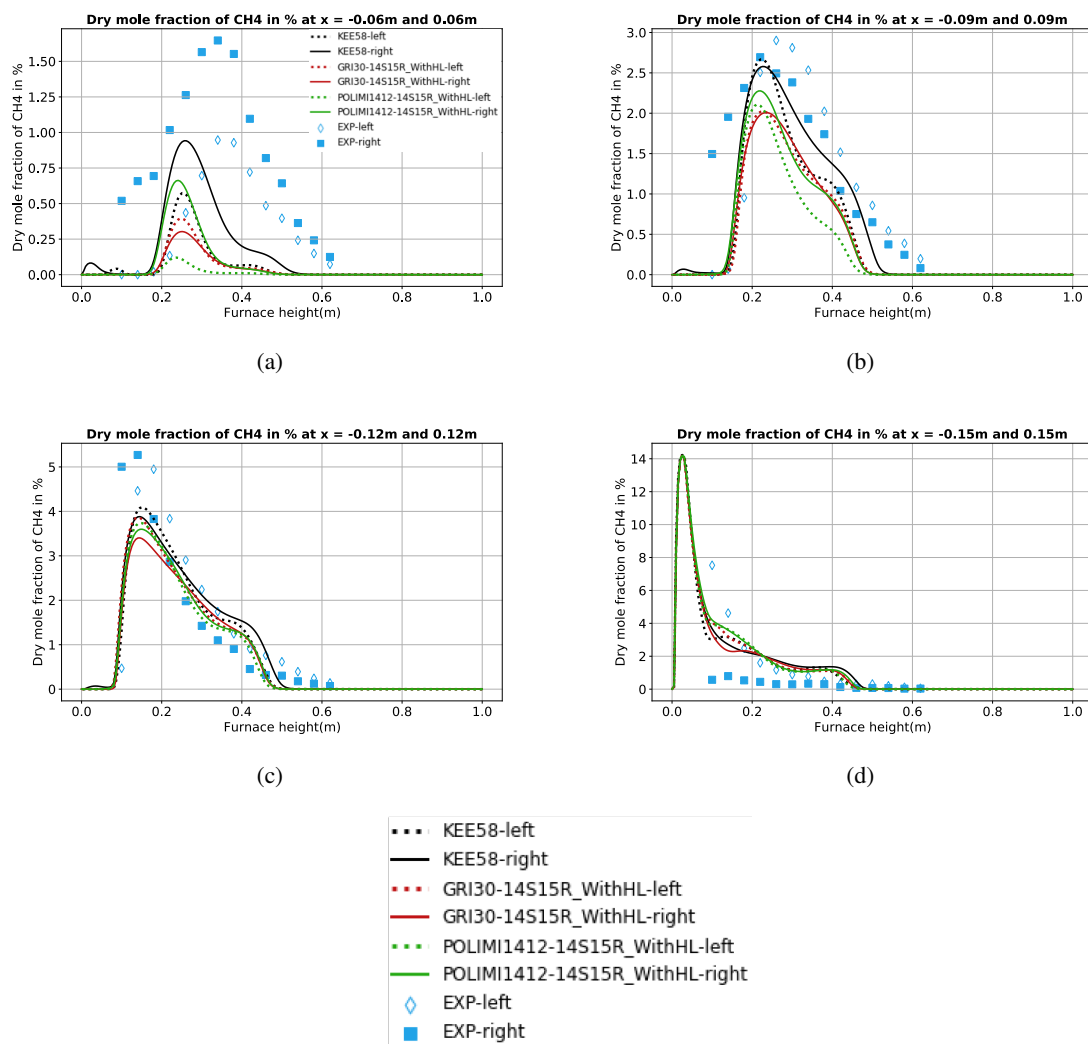


Figure 3.13: Comparison between the experimental and computed profiles of CH₄ in volume percentage on dry basis, obtained at different (negative and positive) x positions and along the furnace height z. (a) $x = \pm 0.06$, (b) $x = \pm 0.09$, (c) $x = \pm 0.12$, (d) $x = \pm 0.15$. Left and right mean negative and positive x, respectively. Maximum measurement uncertainty is 0.27%.

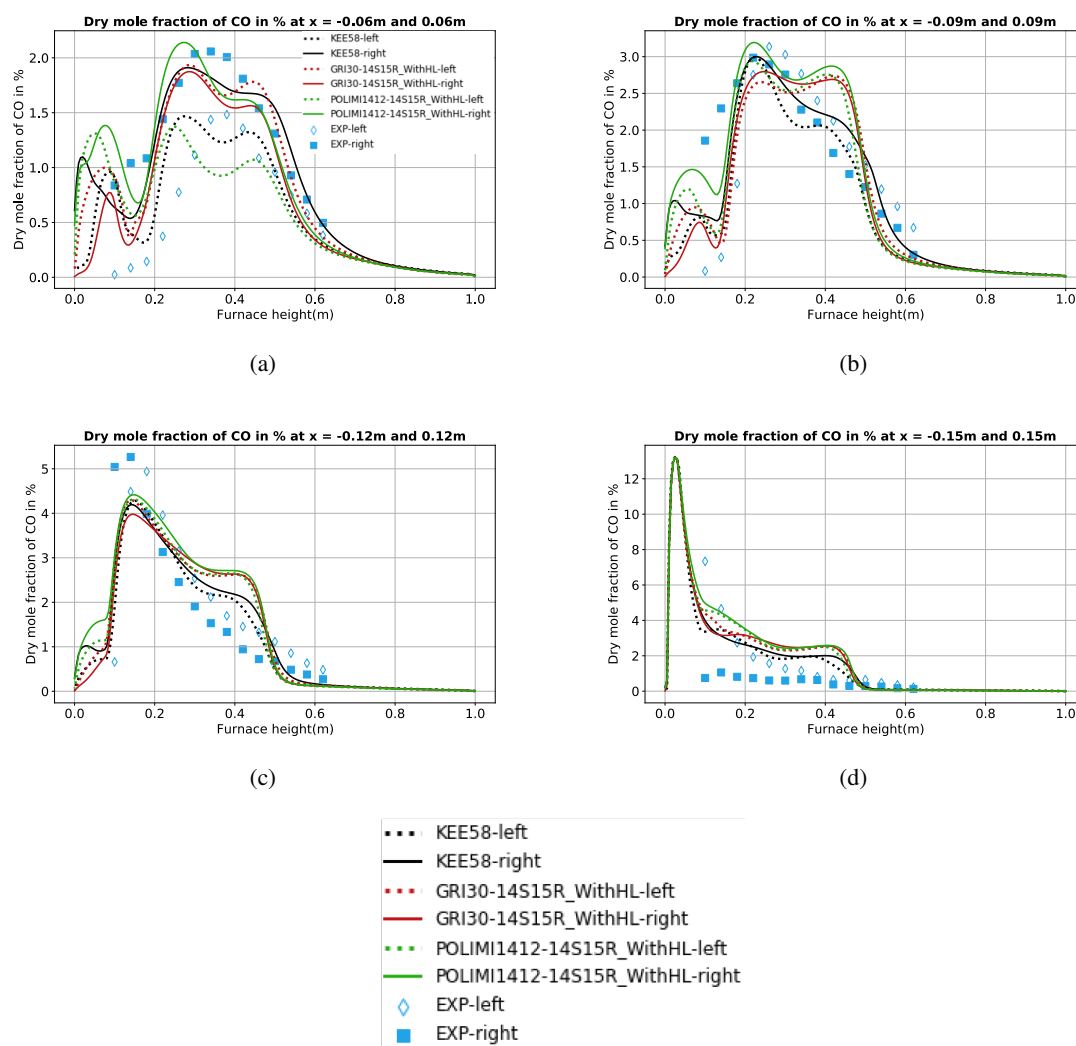


Figure 3.14: Comparison between the experimental and computed profiles of CO in volume percentage on dry basis, obtained at different (negative and positive) x positions and along the furnace height z . (a) $x = \pm 0.06$, (b) $x = \pm 0.09$, (c) $x = \pm 0.12$, (d) $x = \pm 0.15$. Left and right mean negative and positive x , respectively. Maximum measurement uncertainty is 0.28%.

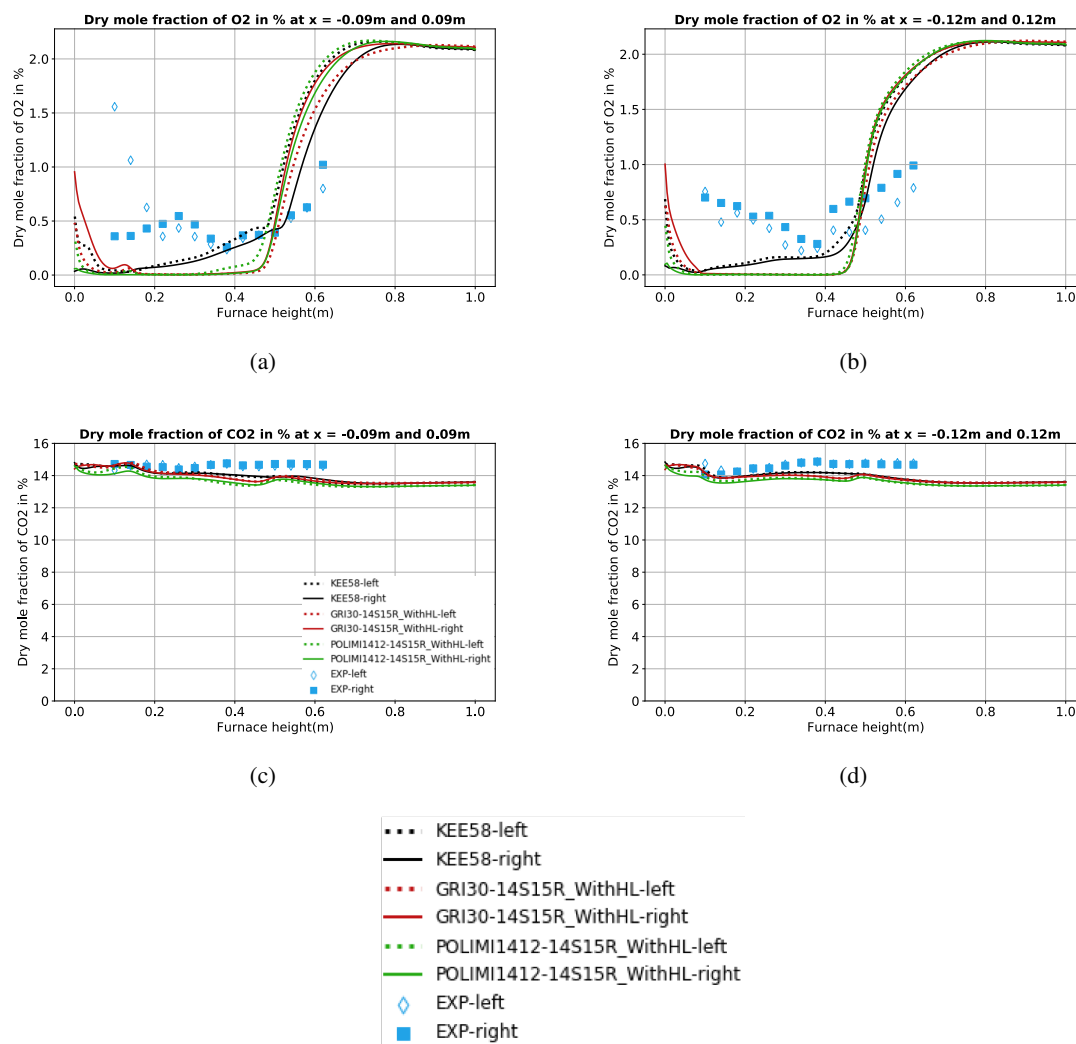


Figure 3.15: Comparison between the experimental and computed profiles of O_2 and CO_2 in volume percentage on dry basis, obtained at two (negative and positive) x positions and along the furnace height z . (a) $x = \pm 0.09$ and (b) $x = \pm 0.12$ for O_2 , (c) $x = \pm 0.09$ and (d) $x = \pm 0.12$ for CO_2 . Left and right mean negative and positive x , respectively. Maximum measurement uncertainty is 0.35% and 0.85% for O_2 and CO_2 , respectively.

3.5 Conclusion

In this chapter, a novel strategy to include heat loss effects into the chemistry reduction tool ORCh was developed and implemented. The results have proven that it is possible to reconstruct precisely the heat loss from a 3D CFD simulation into a 0D ORCh calculation. The trajectories of the detailed schemes in the case with or without heat loss demonstrates the effect of the heat loss on reaction path. The detailed schemes have the identical major species evolution in the case without heat loss, but each detailed scheme responds differently while imposing the heat loss. Two reduced schemes from GRI30 and POLIMI1412 are highly optimised in order to imitate the behaviour of the detailed schemes. The two reduced schemes were implemented into Fluent to perform RANS simulations of a lab-scale flameless combustion furnace UMONS. The comparison between the simulation and the experiment confirms the validity of the method; heat transfer, energy balance, temperature and chemical species fields were fairly predicted by the simulation. This promising approach provides an interesting framework for combustion modeling in which case-specific chemistry reduction can be considered for practical applications.

Chapter 4

Machine learning for integrating combustion chemistry in numerical simulations

Contents

4.1 Database generation	80
4.2 Data pre-treatment	82
4.2.1 Data clustering	83
4.2.2 Local principal component analysis (LPCA)	84
4.3 Neural network	87
4.4 Results of 0D time evolution simulation of ORCh	87
4.5 ANN reduced chemistry for flameless combustion	91
4.5.1 Training database	91
4.5.2 Clustering thermochemical data and ANN structure	92
4.5.3 ANNs verification and database blurring	94
4.5.4 Flow solver and modeling	97
4.6 Results and comparison against measurements	99
4.7 Conclusion	104

Despite of the continuous progress in supercomputing methodologies, all the degrees of freedom required to fully describe the detail of combustion chemistry cannot be introduced in the numerical simulations of large-scale combustion systems such as the furnace shown in Figure 3.1. Several methods have been proposed to reduce and optimize large chemical kinetic schemes such as the one developed in the chapter 3. The development of reduced chemical schemes allowed for CFD simulations of real applications with a reasonable CPU cost.

However after reducing the number of differential equations solved, because of the very stiff character of differential systems associated to combustion chemistry, the CPU time devoted to their integration remains still high as compared to fluid flow solving. The objective is to reduce even more CPU cost to allow simultaneous multiple simulations needed for the search of optimal design of a combustion

system or for the training of reduced order model with application in digital twins. This motivates the introduction of machine learning (ML) and artificial neural networks (ANN) to accelerate chemistry integration in numerical simulation. Indeed, ANNs were employed to deal with chemistry reduction and its time integration [77] and also to develop data driven turbulent combustion modeling [151], or to analyse experimental measurements [75] and to setup digital-twins for process control [76].

Amongst these works, ANN and convolutional neural networks (CNN) were trained on a representative dataset to replace chemistry integration [69, 152] and the method was applied to perform direct numerical simulation (DNS) of a syngas oxy-flame. Nevertheless, the training of the full dataset using a single or two ANNs required specific treatments, such as data augmentation through manufactured intermediate solution points for dealing with some fast reacting species [69]. These operations requiring fine tuning by the user were found necessary to secure good accuracy over the whole domain covering from chemically frozen-flow mixing up to the equilibrium state and pollutant emissions, with fast ignition and fuel oxidation in between.

To avoid relying on these additional more or less ad-hoc operations, thus allowing for having a computerised and fully automatic procedure, an effort has been made in this present thesis to propose a novel methods in which techniques such as data clustering with K-means [153] and dimension reduction using LPCA [154, 155], are combined with the deep learning ANN to secure, by construction, accuracy over the entire composition space domain (mixing, ignition, combustion and equilibrium state).

4.1 Database generation

The methodology for combustion chemistry integration will be tested under conditions representative of a non-premixed syngas oxy-flame with a chemical composition representative of those found in the steel industry in recycled exhaust gases [69, 152]. This non-premixed syngas oxy-flame operates under a pressure of 341.3kPa, with the two inlets: (i) syngas fuel injected at 1223K for a mass flow rate of 0.74kg/s and the composition in mass fraction H_2 : 0.0085, CO : 0.7852, CO_2 : 0.0514, N_2 : 0.1549; (ii) pure oxygen at 298K with a mass flow rate of 0.69kg/s.

The ORCh database of chemical evolutions is first generated by solving for the mass fractions and the enthalpy of a set stochastic particles featuring at initial condition the concentration in the fuel or in the oxidizer inlet. Then, the species mass fraction $Y_i^p(t)$ and sensible enthalpy $h_s^p(t)$ of each stochastic particle evolve according to the following equations:

$$\frac{dY_i^p(t)}{dt} = \text{MIX}_i^p(\tau_T) + \dot{\omega}_i^p, \quad (4.1)$$

$$\frac{dh_s^p(t)}{dt} = \text{MIX}_{h_s}^p(\tau_T) + \dot{\omega}_{h_s}^p, \quad (4.2)$$

where ‘MIX’ denotes the stochastic turbulent micro-mixing closure for the diffusive budget. τ_T denotes the micro-mixing time and $\dot{\omega}_i^p$ and $\dot{\omega}_{h_s}^p$ are the species and enthalpy chemical sources, respectively. In the present study, the Euclidean minimum spanning tree (EMST) micro-mixing model developed by Subramaniam and Pope [117, 156] is used to model the turbulent micro-mixing.

This approach to generate thermochemical conditions representative of those observed in a real system for studying its chemical response, without explicitly solving for the flow, has been shown effective for partial oxidation of natural gas [157, 158], aircraft engines combustion chambers [159, 160], large-scale furnaces with urea DeNOx automated control [161], micro- and meso-scale combustion systems [162, 163, 164] and also to build the database for machine learning application to sooting flames [165].

Here a total number of 1429 stochastic particles is employed with 740 particles (corresponding to the mass flow rate of 0.74kg/s) assigned to Fuel inlet and 689 particles (corresponding to the mass flow rate of 0.69kg/s) to O₂ inlet.

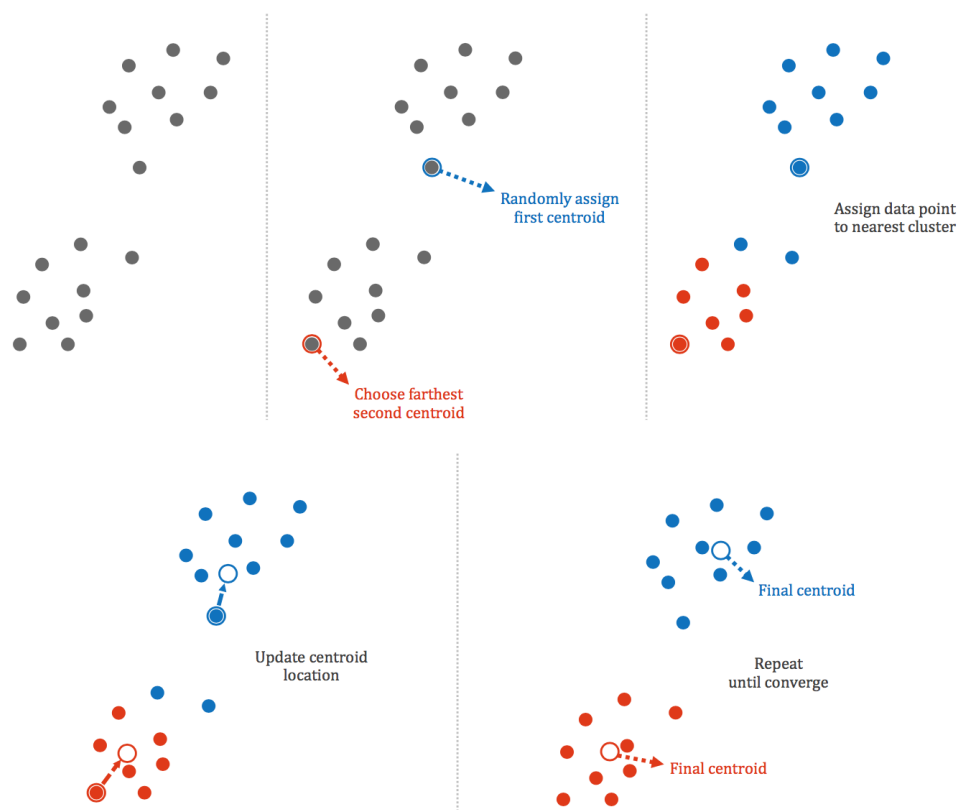


Figure 4.1: Clustering with K-means.

From the evolution of these particles, the first step consists of identifying, from a detailed chemical scheme, the important species to be retained and whose evolutions shall be learned by the ANNs. This is done using the direct relation graph with error propagation method (DRGEP) [166]. For the present operating conditions, this step was previously performed and reported in [69]. Starting from the detailed scheme GRI3.0 [167], 11 species were identified as essential to follow the dynamics of the syngas chemical evolutions: O, O₂, H, H₂, OH, HO₂, H₂O, H₂O₂, CO, CO₂ and N₂. A companion reduced chemistry involving 23 reactions was then optimised (see Table 2 of [152]).

To save CPU time during training and to demonstrate the integration of chemistry with ANN, this 11-species and 23 elementary reactions scheme is used to build the time evolution dataset of all stochastic particles, over 4999 time-steps of $0.3\mu s$ with a mixing time $\tau_T = 0.3ms$ (a representative value for a characteristic turbulent mixing-time as observed in shear layers for Reynolds numbers typical of burners). N₂ was removed from the database for the pre-treatment and ANN learning steps. The full database thus consists of the 11 feature columns (10 species and temperature) of the 1429 stochastic particles collected over 4999 time-steps, therefore the raw data is composed of $1429 \times 4999 = 7143571$ vectors of 10 components.

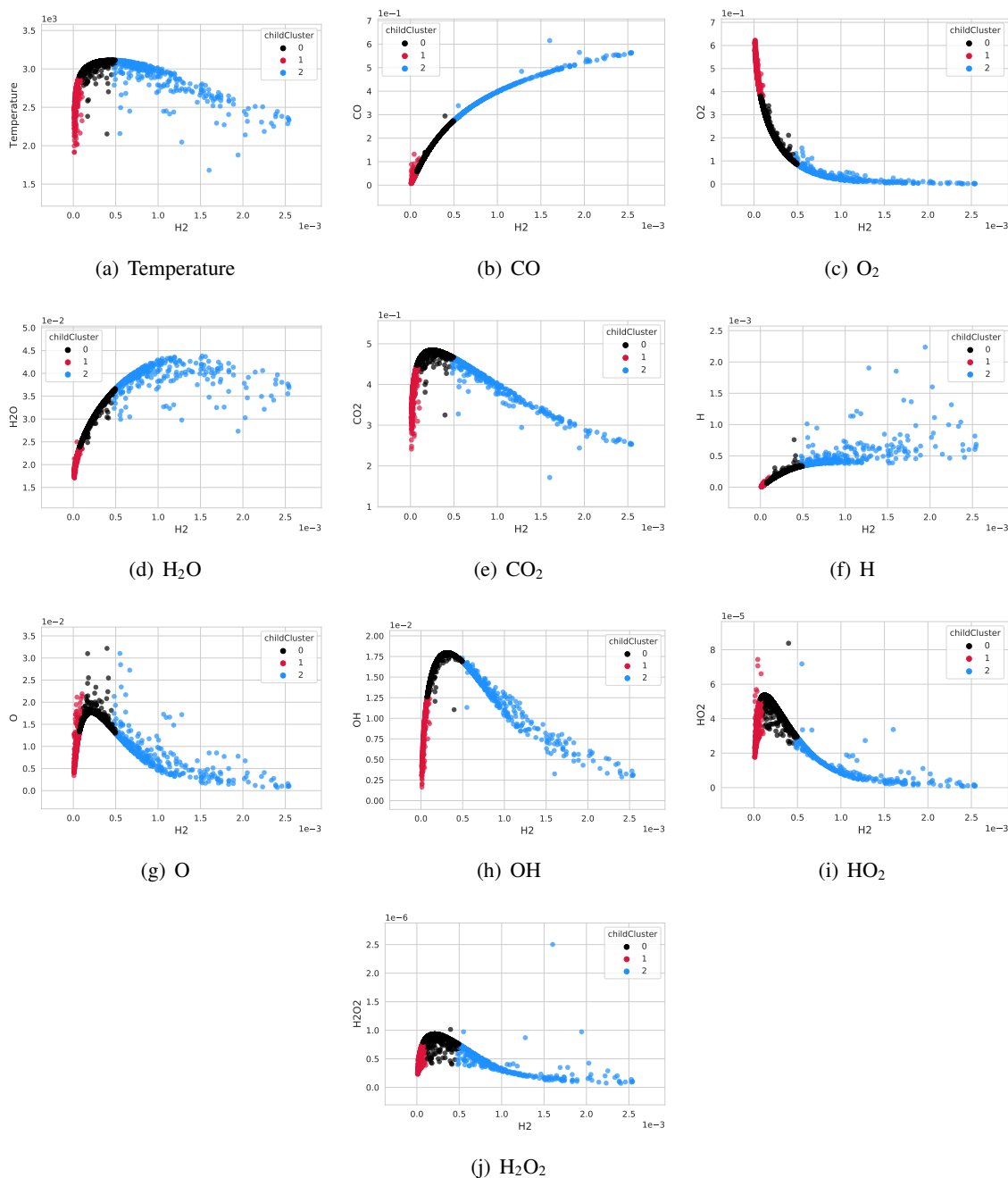


Figure 4.2: Data clustering for parentCluster1. Temperature [K] (a) and species mass fraction [-] (b)-(j) vs H₂ mass fraction. Red: childCluster1_0. Black: childCluster1_1. Blue: childCluster1_2.

4.2 Data pre-treatment

To secure an appropriate analysis of the multivariate nature of the problem, the thermochemical variables obtained from the solving of Eqs. 4.1 and 4.2 are going through pre-treatments, such as centering and rescaling and unsupervised machine learning, like clustering with K-means [153], and dimension reduction with LPCA [155], before the ANN training is to be applied. This strategy is expected to close the gap between the previous works [69], in which artificial data augmentation was required to secure

accuracy, and the introduction of complex chemistry in the numerical simulation of large scale furnaces.

Following the recent study by D'Alessio et al. [168] in the context of adaptive chemistry for reacting flow simulation, the original dataset is first pre-processed with centering and auto-scaling (standardizing) to insure reliable and robust results.

4.2.1 Data clustering

K-means [153] is a widely used and well-established unsupervised machine learning algorithm, which consists in grouping similar data into different clusters. K-means is particularly suited for the classification of the micro-mixing stochastic particles, which evolve through a large variety of stages from chemically-frozen flow mixing, rapid ignition, fuel oxidation and combustion up to the chemical equilibrium state. Moreover, the particles from Fuel and O₂ inlets feature different time histories, which benefit from being classified in separate clusters for chemistry ANN integration. After clustering into separate groups, every individual subset of data has similar and regular distribution to ensure effectiveness of the subsequent operations.

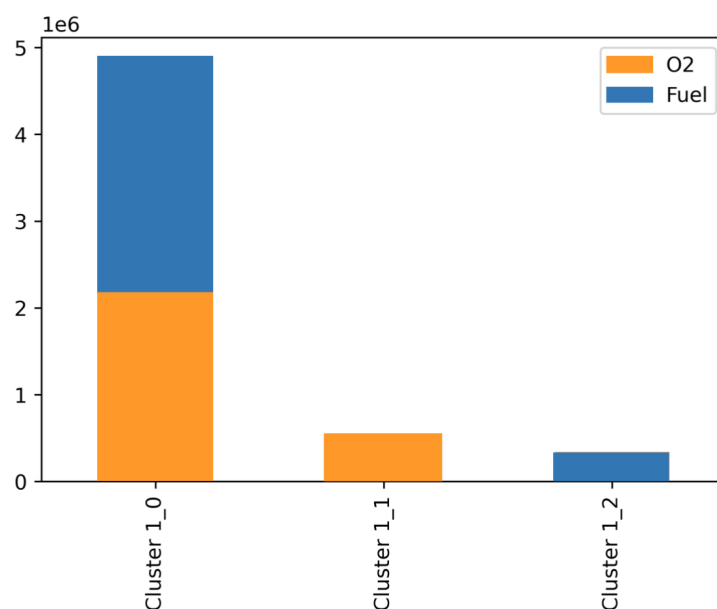


Figure 4.3: Repartition of data points in childCluster1_0, childCluster1_1 and childCluster1_2. Abscissa is cluster numbering, ordinate is number of data points. Orange: particles from O₂ inlet. Blue: particles from Fuel inlet.

The different steps in K-means used for the thermochemical quantities (species mass fractions and temperature) are illustrated in Figure 4.1 and summarized as follows:

- Definition of the number of clusters.
- Selecting randomly an initial cluster centroid: To ensure the quality of clustering and improve the convergence speed, the K-means++ initialization algorithm [169] is applied. The algorithm assigns randomly a first centroid, a second centroid is then chosen as farthest as possible to the first centroid, a third centroid is as farthest as possible to the first two centroids, and so on.
- Assigning data point to cluster with shortest Euclidean distance.

- Updating centroid locations by averaging all data points in each cluster.
- Repeat the process until the centroid locations are converged by evaluating the shifting tolerance, which is chosen at $1e-20$.

Defining an adequate number of clusters is crucial. The usual K-means++ initialization algorithm may lead to poor clustering in our case, where the majority of clusters concentrate in the ignition and combustion stages. To overcome this difficulty, an additional hierarchical clustering strategy was adopted; the first clustering leads to only 2 clusters (named `parentCluster0` and `parentCluster1`), which separates the low and high temperature zones. The first parent containing the data of mixing, ignition and combustion stages is then clustered into 14 child clusters (`childCluster0_0` to `childCluster0_13`). The subset of data in the second parent, representing the end of combustion followed by the equilibrium state, requires a special treatment to guarantee the accuracy of ANN training and prediction. For this reason, the second parent is classified into only 3 child clusters (`childCluster1_0`, `childCluster1_1` and `childCluster1_2`), and then these 3 child clusters will have, respectively, 20, 10, 10 grandchildren (`grandChild1_0_0` to `grandChild1_0_19`, `grandChild1_1_0` to `grandChild1_1_9`, `grandChild1_2_0` to `grandChild1_2_9`). Each child cluster of the first parent and each grandchild cluster of the second parent benefits from its own ANN training.

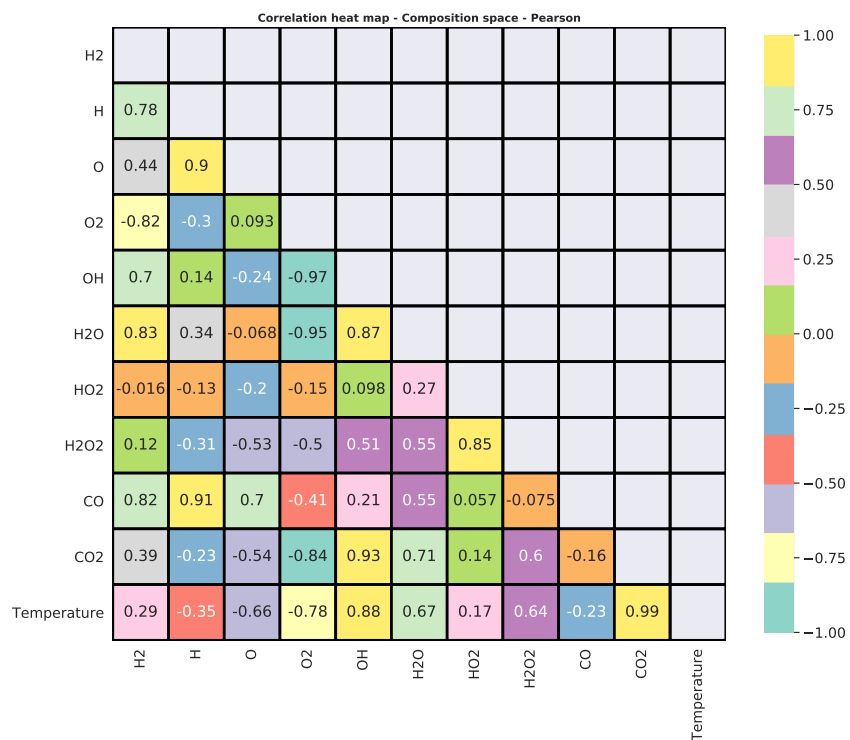
The effectiveness of K-means algorithm applied to the flame turbulence/chemistry interaction (Eqs. 4.1 and 4.2) is illustrated in figures 4.2 and 4.3. Figure 4.2 shows how K-means automatically classifies data in `parentCluster1` (representing the end of combustion and the equilibrium state) into 3 distinct subsets, i.e. `childCluster1_0`, `childCluster1_1` and `childCluster1_2`. The `childCluster1_1` contains the particles from O_2 inlet, while the `childCluster1_2` gathers the particles from Fuel inlet (Figure 4.3); both child-clusters represent the end of combustion. The particles from O_2 and Fuel inlets finally approach the equilibrium state and their data points are classified in a single common cluster `childCluster1_0`.

4.2.2 Local principal component analysis (LPCA)

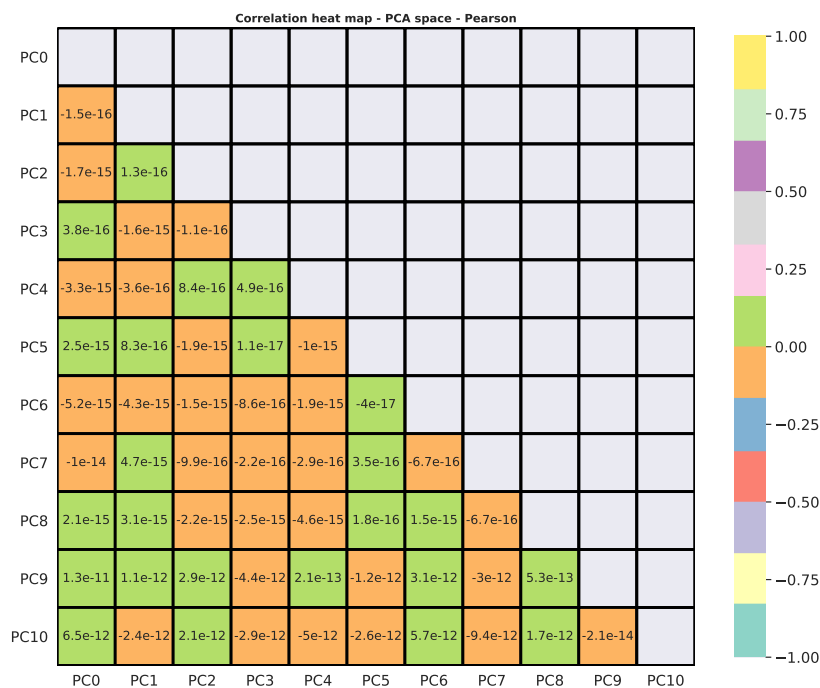
Principal component analysis (PCA), also known as a dimensional reduction technique, is used to reduce a large number of correlated variables (species mass fractions and temperature, in our case) to a smaller number of uncorrelated variables (principal components) [170]. Because of the strongly non-linear character of combustion chemistry, it is usually recommended to adopt a locally linear approach called ‘local PCA’ (LPCA) [155], to properly describe such dynamical system.

In our case, each cluster represents a piece-wise variation of species mass fractions and temperature during a specific combustion stage. The application of LPCA in each cluster transforms correlated variables of high variance into the most important uncorrelated principal components (PCs), which will be carefully addressed during the ANN training process. The choice of the number of PCs is essential to secure a good quality of ANN prediction, and a quite high number of PCs is usually required dealing with chemistry in reacting flows [168]. In practice, it was observed that reducing from 11 PCs to 6-8 PCs would still allow for keeping more than 98% of the relevant information. However, here the full set of control variable is transformed into PC (i.e., 10 chemical species and temperature). Therefore, this does not reduce the size of the problem to be learned, but the parametrisation of the data from the PCs considerably eases the ANN learning process. Indeed, species and temperature are usually well-correlated, the PCA analysis transposes these variables to non-correlated PCs and the performances of ANNs then become much greater with these non-correlated inputs.

Two heat maps are presented in Figure 4.4 to show the correlation of original variables in composition



(a) Composition space



(b) PCA space

Figure 4.4: Heat map showing correlation coefficients of data in grandChildCluster1_1_5. (a) Original variables in composition space. (b) PCs in PCA space.

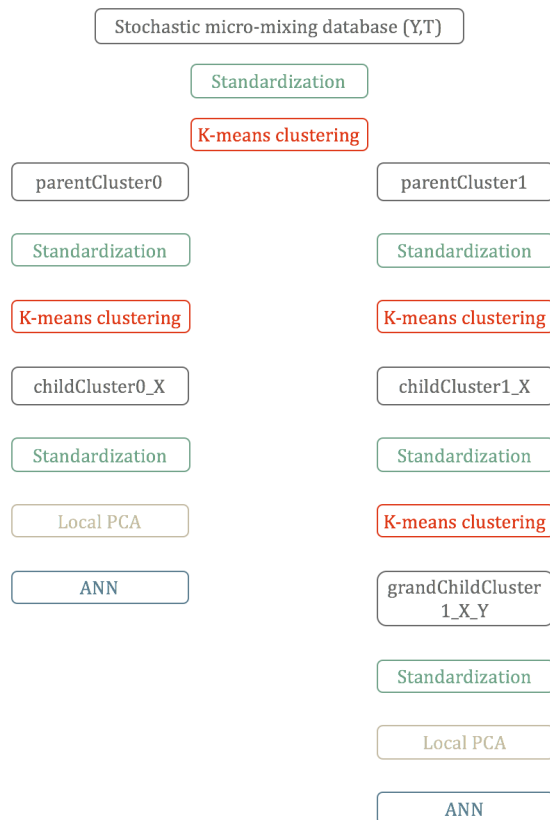


Figure 4.5: Chemistry reduction with trained ANN.

space and of PCs in PCA space. These heat maps display the Pearson correlation coefficients, negative (respectively positive) value means that two variables vary in opposite (respectively same) directions, zero shows the absence of correlation. It is confirmed that the original variables in composition space are strongly correlated (Figure 4.4.a) and that PCs in PCA space are clearly uncorrelated, with practically zero correlation coefficients (Figure 4.4.b).

Layer	Activation function	Output shape
Input	-	(None,11)
Dense	ReLU	(None,512)
Dense	ReLU	(None,256)
Dense	ReLU	(None,128)
Dense	ReLU	(None,64)
Dense (Output)	-	(None,11)

Table 4.1: Structure of ANNs [69, 152]

4.3 Neural network

The ANN regression structure (Table 4.3) used in this study is adopted from our previous works [69]. The ANN consists of 1 input layer, 4 dense hidden layers with the rectified linear activation function (ReLU) and 1 output layer. The total number of parameters (weights and biases) is 179851.

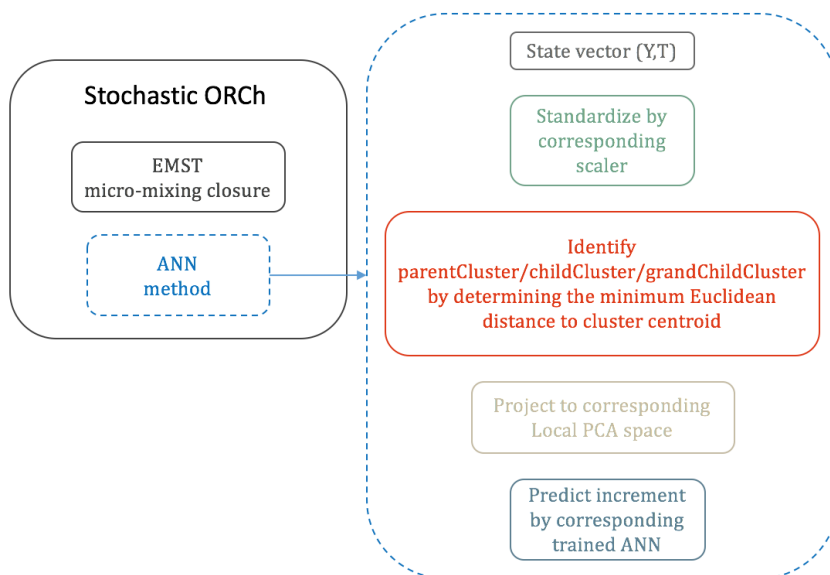


Figure 4.6: Flowchart of the a posteriori test. ('ORCh': Optimised and Reduced Chemistry.)

The ANN input is fed by the data in PCA space, composed of 11 PCs which are obtained by the projection of the 11 original variables from composition space into PCA space. The target is the increment of species composition and temperature (i.e., the ANN learns how to integrate the time evolution of chemistry). The database is split into training set (81%), validation set (9%) and test set (10%) for model performance evaluation.

The training process is performed using Tensorflow 2 with GPU support (NVIDIA GeForce GTX 1080 Ti) and the Adam optimizer in default setting. To prevent the overfitting, the early stopping callback is adopted and set as 200 epochs, which means that the training will be halted after 200 epochs without improvement. Additionally, the check point callback saves the best model with the lowest mean squared error (MSE) during the training process. The total training time for all ANNs is about 11 hours.

4.4 Results of 0D time evolution simulation of ORCh

The methodology adopted in the study is summarised in Figure 4.5. To perform a posteriori tests of the model, the evolutions of the stochastic particles are recomputed replacing the integration of chemistry by the ANN, as summarised in Figure 4.6.

The time evolutions of temperature and species mass fractions averaged over the stochastic particles issued from one of the inlets and computed with and without ANNs, are shown in figures 4.7-4.9.

The case without any pre-treatment of the data (dashed-line) and a single ANN rapidly deviates from the reference solution (symbols). Without pre-treatment, the ANN captures the very first part of ignition, but fails to reach the equilibrium condition, see for instance the temperature response in figure 4.7.

(Notice that one does not make use here of the introduction of manufactured intermediate solutions for H_2O_2 , as discussed in [69].)

The solution with data pre-treatment (solid lines in figures 4.7-4.9) is in good agreement with the reference solution obtained using a CPU consuming stiff-solver for chemistry (symbols). This is the case for temperature and all species considered, even radicals and intermediate ones such as O, H, OH, HO_2 and H_2O_2 . All the evolution stages (mixing, ignition, combustion and equilibrium) are well predicted.

Figure 4.7 shows that the ignition delay of 0.08 ms is correctly predicted by the ANN model. After the ignition, the temperature profiles feature a sharp increase to attain high values due to oxy-combustion (the highest value is 3081K for the particles from the fuel side). Then, the temperature proceed towards its equilibrium state at 3037K. The trajectories of reactants (H_2 , CO, O_2), and main combustion products (CO_2 , H_2O) are also perfectly captured by the ANNs-based model during their evolution in all specific stages, i.e. mixing, ignition, combustion and equilibrium (Figure 4.8).

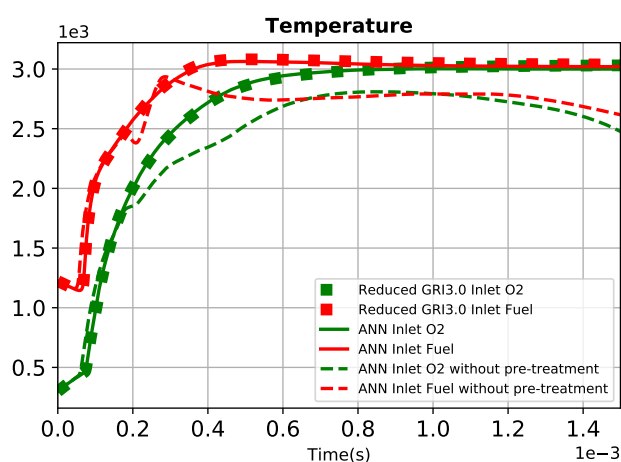


Figure 4.7: Time evolution of temperature [K] averaged over stochastic particles. Symbols: reference reduced scheme (Table 2 of [152]). Continuous line: Kmeans-PCA-ANN. Dashed-line: ANN without data pre-treatment. Green: O_2 inlet. Red: Fuel inlet.

Regarding minor and radicals species (Figure 4.9), the shape and peak of the trajectories are also correctly predicted except a very slight discrepancy for H_2O_2 species departing from the oxygen inlet.

The computation time is drastically reduced by using the ANN model as given in Table 4.2. The simulation with ANNs (single processor calculation) is 8 times faster than the simulation for the reduced scheme, and 80 times faster than the simulation with the detailed GRI3.0 scheme. The CPU time reduction is measured here solving for micro-mixing and chemistry (Eq. (4.2)). This relative CPU reduction thus differs from our previous works [69], also relying on ANN for chemistry, in which the speed-up was measured solving for the aerothermochemical equations in three-dimensional flows.

This quantification of the speed-up does not account for the preprocessing time needed to train the neural networks. However, the CPU effort required for training stays much smaller than the time spent performing the numerous operations required to generate a reduced chemical scheme (analysis of the most important chemical species and reaction paths and optimisation of the rate constants). What could slightly increase the CPU cost with ANN is the introduction of more degrees of freedom which may become mandatory to reproduce very specific combustion characteristics (cool flame effects, etc.).

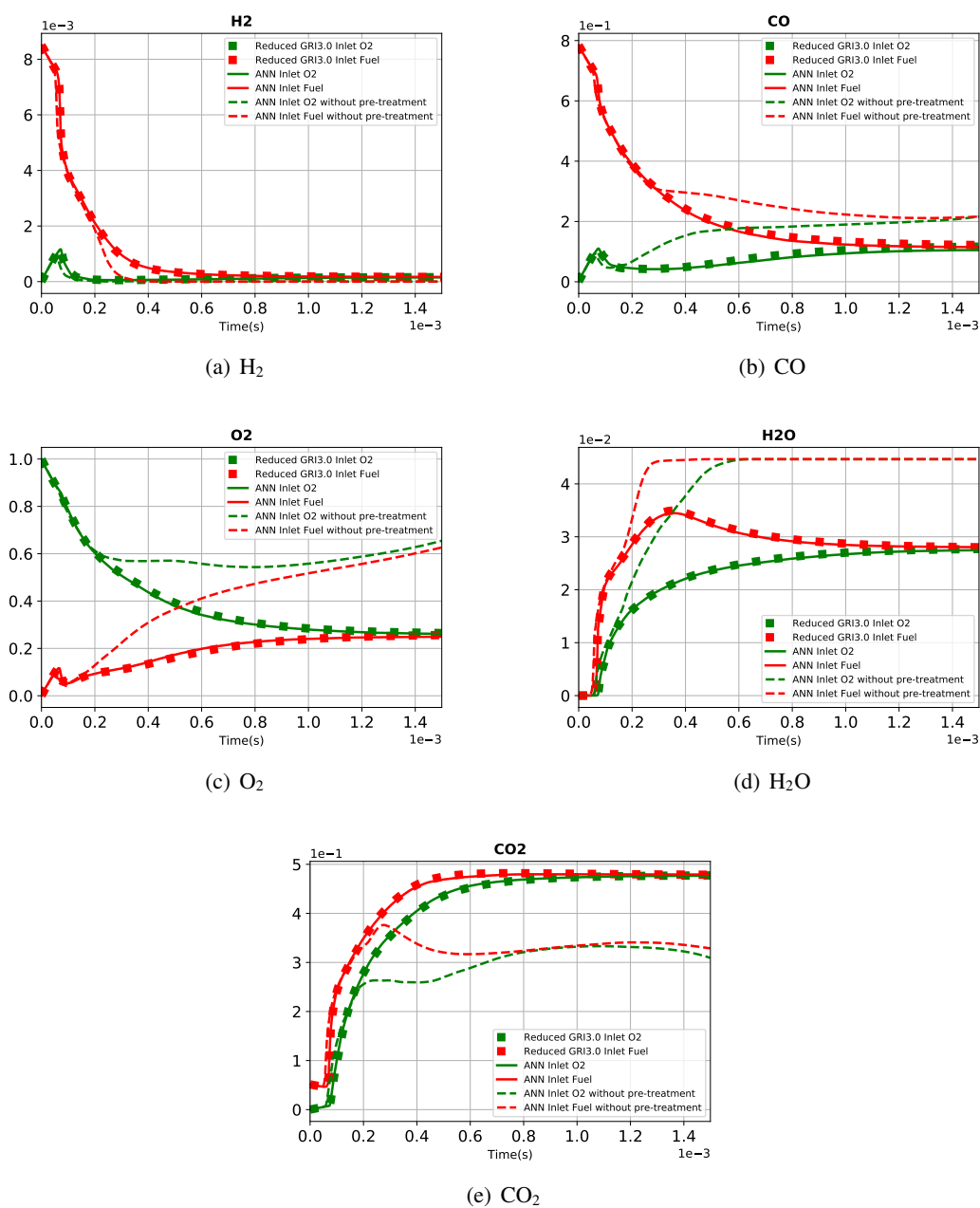


Figure 4.8: Time evolution of major species mass fractions averaged over stochastic particles. Symbols: Reference chemical scheme (Table 2 of [152]). Continuous line: Kmeans-PCA-ANN. Dashed-line: ANN without data pre-treatment. Green: O_2 inlet. Red: Fuel inlet.

Chemistry	Speed-up
GRI3.0 detailed scheme	1
Reduced scheme	10
ANNs (present work)	80

Table 4.2: Speed-up between chemistry descriptions.

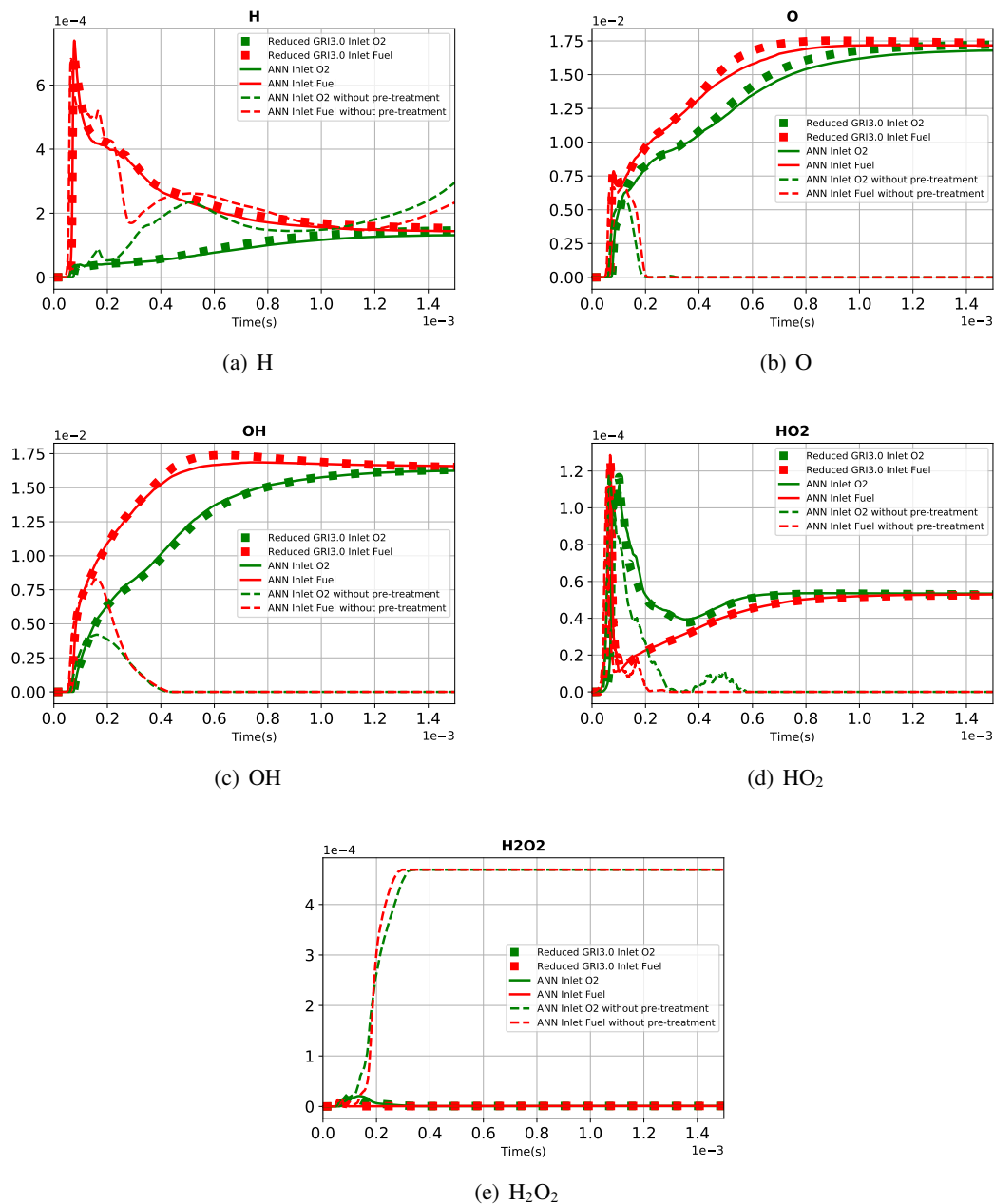


Figure 4.9: Time evolution of radicals and intermediate species mass fractions averaged over stochastic particles. Symbols: Reference chemical scheme (Table 2 of [152]). Continuous line: Kmeans-PCA-ANN. Dashed-line: ANN without data pre-treatment. Green: O₂ inlet. Red: Fuel inlet.

4.5 ANN reduced chemistry for flameless combustion

The following section stems from the article submitted to the journal Applications in Energy and Combustion Science in 2022.

4.5.1 Training database

The strategy for building the neural networks training database relies on previous works [171, 79]. Stochastic micromixing modeling is combined with complex chemistry to generate, prior to any flow simulation, the variety of thermochemical conditions expected in the combustion system. In this approach, the fraction of flow rate injected through a given inlet defines the number of stochastic particles taking the thermochemical properties of that inlet at initial time. Each particle carries information on the species mass fraction vector and enthalpy. From this non-premixed initial condition, the stochastic particles evolve in time according to¹.

$$\frac{\partial Y_k^p(t)}{\partial t} = \text{MIX}^p(\tau_T) + \dot{\omega}_{Y_k}^p, \quad (4.3)$$

$$\frac{\partial h_s^p(t)}{\partial t} = \text{MIX}^p(\tau_T) + \dot{\omega}_{h_s}^p + \alpha_{loss}(T_p - T_{wall}). \quad (4.4)$$

$Y_k^p(t)$ is the mass fraction of the p-th particle, $\text{MIX}^p(\tau_T)$ denotes the Euclidian Minimum Spanning Tree micromixing model [117] and $\dot{\omega}_{Y_k}^p$ is the chemical source. The characteristic value of the micromixing time, $\tau_T = 0.3\text{ms}$, was determined from previous simulations of the furnace [129]. Varying τ_T in Eqs. (4.3)-(4.4) around its nominal value was found to have a relatively weak impact for the purpose of database generation in view of chemistry reduction, at least as long as ignition occurs [58]. To account for the non-adiabatic character of the flow, a linear heat loss term is added and calibrated with the variable coefficient α_{loss} , the temperature of the particle T_p and the average wall temperature measured in the experiments $T_{wall} = 1259.4\text{K}$. The parameter α_{loss} is chosen so that the mean chemical equilibrium temperature of the ensemble of stochastic particles ranges between 1200 and 1500K, as reported experimentally in the recirculating burnt gases. The first training database is then composed of three set of stochastic particles evolving from their initial condition up to equilibrium, for α_{loss} taking the values $3 \cdot 10^5$, $5 \cdot 10^5$ and $7 \cdot 10^5 \text{ W}\cdot\text{kg}^{-1}\cdot\text{K}^{-1}$. Equations (4.3) and (4.4) are solved with routines from the Cantera package [173].

Three inlets are imposed to build every set of time evolving stochastic particles. These inlets carry respectively the B50 gas, air and a given amount of recirculating equilibrium burnt products (Table 3.1). This third inlet is necessary because with separated jet injection, the reactants are mixed with recirculating burnt gases before they meet and this specific behavior must be included in the training thermochemical dataset. The estimated mass flow rate of recirculating burnt gases, as provided experimentally, is given in Table 3.1. In practice, the system of equations (4.3)-(4.4) is then solved with, at initial time, 25 stochastic particles of B50, 102 particles of air and 643 particles of recirculating burnt gases. A composition space (CO-mixture fraction) distribution of the particles representative of these conditions is shown in Fig. 4.10.

The time evolution of the relevant species mean mass fractions and temperature computed over the stochastic particles are shown in symbol with the GRI-3.0 detailed chemistry mechanism [36] for

¹Other applications of this class of model problem for chemistry reduction and process control may be found in the literature [58, 172]

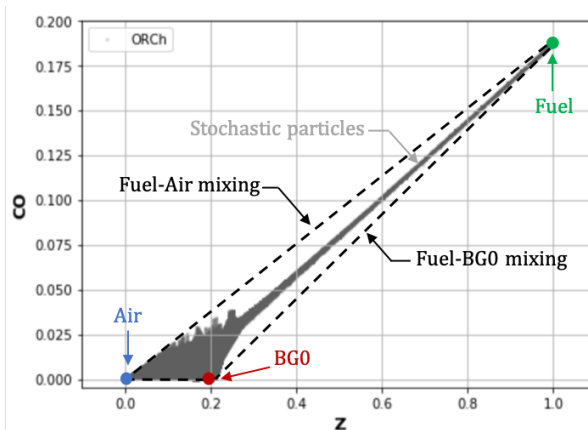


Figure 4.10: CO stochastic particles mass fraction versus mixture fraction (grey dots). BG0: Burnt gases inlet. Fuel: B50 gas inlet (Table 3.1).

$\alpha_{loss} = 3 \cdot 10^5$ and a time-step of $5 \cdot 10^{-7}$ s in Fig. 4.11 for major species and in Fig. 4.12 for minor species. The identification of the species relevant to capture the thermochemistry, and whose increment in time shall be learned by the neural networks, is achieved applying the direct relation graph with error propagation analysis (DRGEP) [119] to the trajectories seen in these figures. Starting from the detailed scheme GRI3.0, 14 species were identified as essential to follow the dynamics of the chemical system evolution: H_2 , H , O , O_2 , OH , H_2O , HO_2 , CH_3 , CH_4 , CO , CO_2 , HCO , CH_2O and N_2 . These species mass fractions and the temperature will serve as input to the neural networks, which are trained to return their increments, or source terms, for a given time step. Meaning that 14 scalars will be solved in LES.

4.5.2 Clustering thermochemical data and ANN structure

A single neural network cannot handle the large variety of chemical conditions seen by the gases during their evolution from injection up to chemical equilibrium. Following a previously develop approach [79], the dataset is first decomposed in clusters and a dedicated neural network will be affected to every cluster. Multiplying the numbers of ANN to secure precision does not increase significantly the CPU time of the flow simulation, as all the ANNs are implemented as subroutines in the computational fluid dynamics (CFD) solver and called according to the thermochemical composition space location of the mesh cell to be advanced in time. However, this considerably impacts on the CPU devoted to training, as discussed in the next subsection.

The decomposition of the dataset into subdomains implies the application of pre-treatments, such as centering, rescaling and clustering with K-means [153]. More precisely, we use the K-means++ algorithm [169], which stands as a well-established unsupervised machine learning algorithm to group similar data into different clusters. The algorithm assigns randomly a first centroid, a second centroid is then chosen as farthest as possible to the first centroid, a third centroid is as farthest as possible to the first two centroids, and so on. Then, every data point is assigned to the cluster with the shortest Euclidean distance in the multi-dimensional composition space. The centroid locations are updated by averaging all data points in each cluster and the process is repeated until the centroid locations are converged by evaluating the shifting tolerance which is chosen at 10^{-20} .

There is a general trend of combustion data to cluster simply in two groups according to fresh and burnt gases. Also to refine the analysis, a hierarchical clustering strategy is adopted [79]. The first clus-

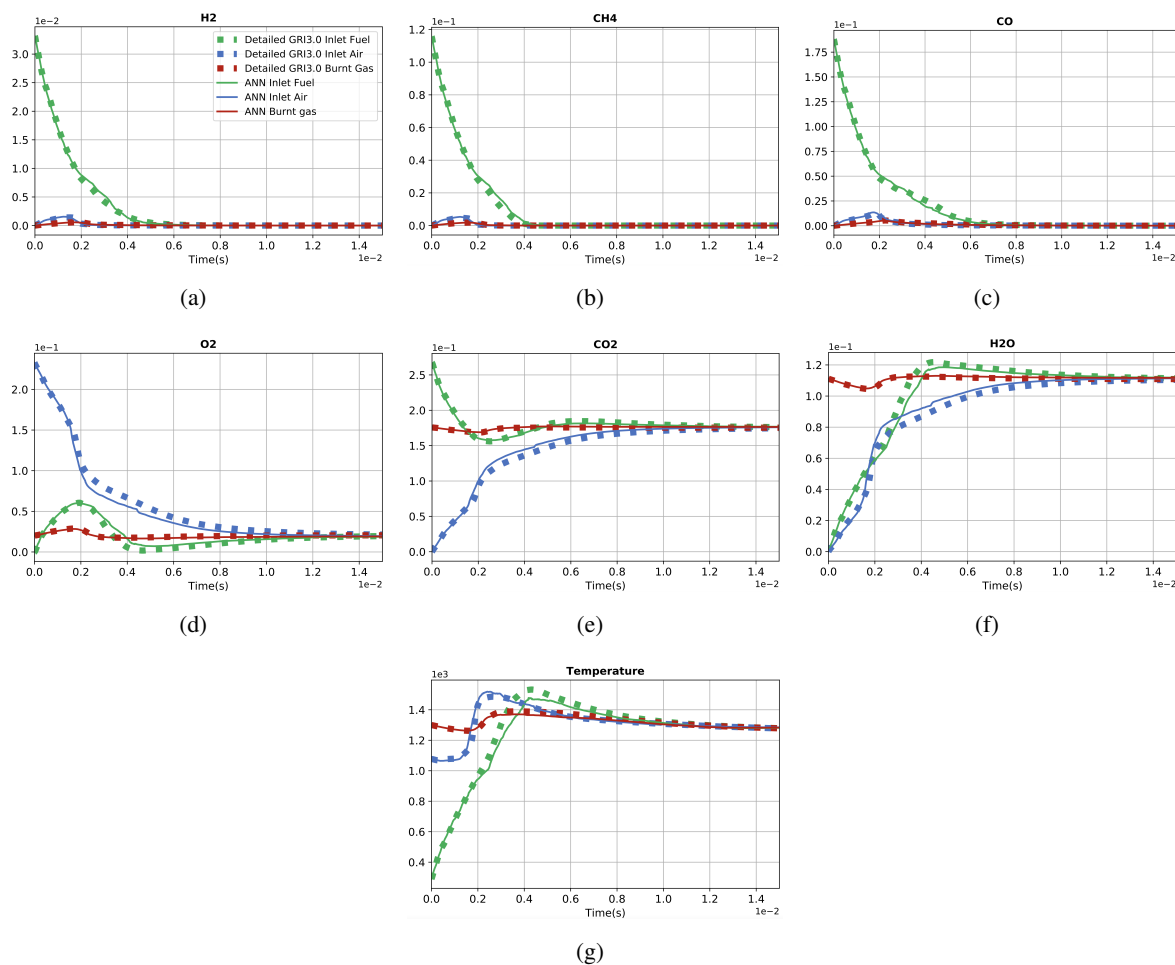


Figure 4.11: Time evolution of major species mass fraction and temperature averaged over stochastic particles with $\alpha_{loss} = 3 \cdot 10^5$ and time step of $5 \cdot 10^{-7} s$. Symbols: detailed chemistry. Line: ANN.

tering separates fresh and burnt gases (Parent 0 and Parent 1 in Fig. 4.13). The Parent 0 cumulates the data from mixing, ignition and combustion stages, it is further decomposed into into 20 child clusters. The data subset in the second parent, representing the final stage of combustion up to the ultimate equilibrium state, was found to require a special treatment in the case of flameless combustion in order to guarantee the success of ANN training. This second parent is decomposed into only 3 child clusters, which will have respectively, 40, 15 and 15 grandchildren. Each child cluster of the first parent and each grandchild cluster of the second parent benefits from its own ANN training.

The ANN regression structure (Table 4.3) is similar to previous works [171] (Table 4.3). Every ANN consists of 1 input layer, 4 dense hidden layers with the rectified linear activation function (ReLU) and 1 output layer. The total number of parameters (weights and biases) is 181438. The database is split into training set (81%), validation set (9%) and test set (10%) for model verification.

The training process is performed using Tensorflow 2 with GPU support (NVIDIA GeForce GTX 1080 Ti) and the Adam optimizer in default setting. To avoid overfitting, the early stopping callback is used and set as 200 epochs. The check point callback saves the best model with the lowest mean squared error (MSE) during the training process.

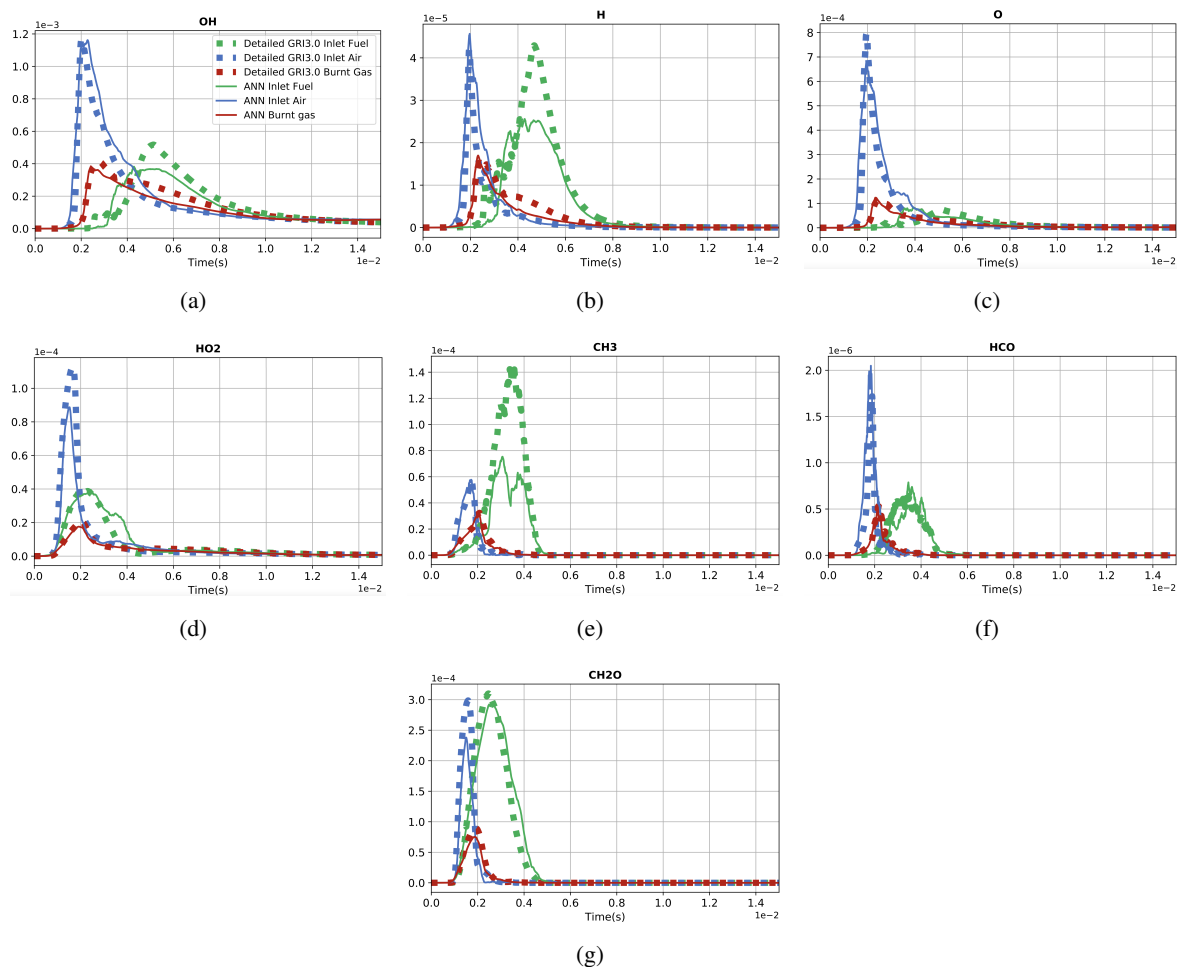


Figure 4.12: Time evolution of minor species mass fraction averaged over stochastic particles with $\alpha_{loss} = 3 \cdot 10^5$ and time step of $5 \cdot 10^{-7}$ s. Symbols: detailed chemistry. Line: ANN.

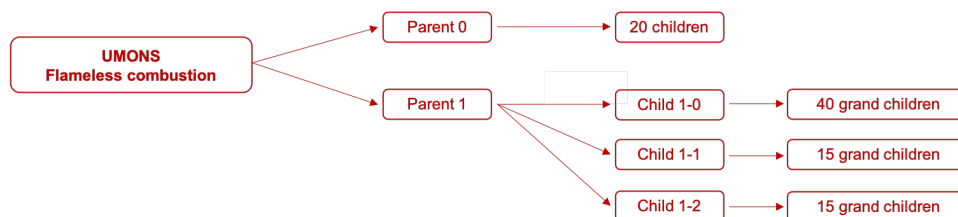


Figure 4.13: Schematic of the decomposition in clusters for ANN training.

4.5.3 ANNs verification and database blurring

The ANNs are trained to return the increments, or source terms, for the species mass fractions and temperature, knowing the vector of species mass fractions and temperature (ANN input). To verify the quality of the training, the evolution of the stochastic particles is simulated again from Eqs. (4.3) and (4.4), but replacing the computation of the chemical sources from the detailed mechanisms by the ANNs output.

The strategy reported in previous works [171] is applied to fully insure mass conservation after the

Layer	Output shape	Activation function
Input	(None,11)	-
Dense	(None,512)	ReLU
Dense	(None,256)	ReLU
Dense	(None,128)	ReLU
Dense	(None,64)	ReLU
Dense (Output)	(None,11)	-

Table 4.3: Structure of ANNs [171]

removal of the less influential species. The mass imbalance in the source of atom A is measured for reduced set of species

$$\Delta\dot{\omega}_A = \sum_{i=1}^{N_s^r} \frac{\beta_{A,i} W_A}{W_i} \dot{\omega}_i, \quad (4.5)$$

where W_A and W_i are molar weights and $\beta_{A,i}$ the number of atom 'A' in the i -th species. Sources of carbon containing species and of hydrogen containing species are corrected adding

$$\Delta\dot{\omega}_i = -\frac{Y_i}{Y_A} \Delta\dot{\omega}_A, \quad (4.6)$$

with the atom mass fraction $Y_A = \sum_{i=1}^{N_s^r} \beta_{A,i} (W_A/W_i) Y_i$. For oxygen, Eq. (4.6) is applied only to O_2 and with the already corrected sources of C and H containing species.

Comparing in Figs. (4.11) and (4.12) the time evolution of the major and minor species, results are quite convincing. Some departure exists for the minor species, but it is acceptable considering the strong reduction of the number of species transported, here from 53 to 14. Once the overall procedure setup has been verified for the micromixing canonical problem, it is extended to address the UMONS furnace test case.

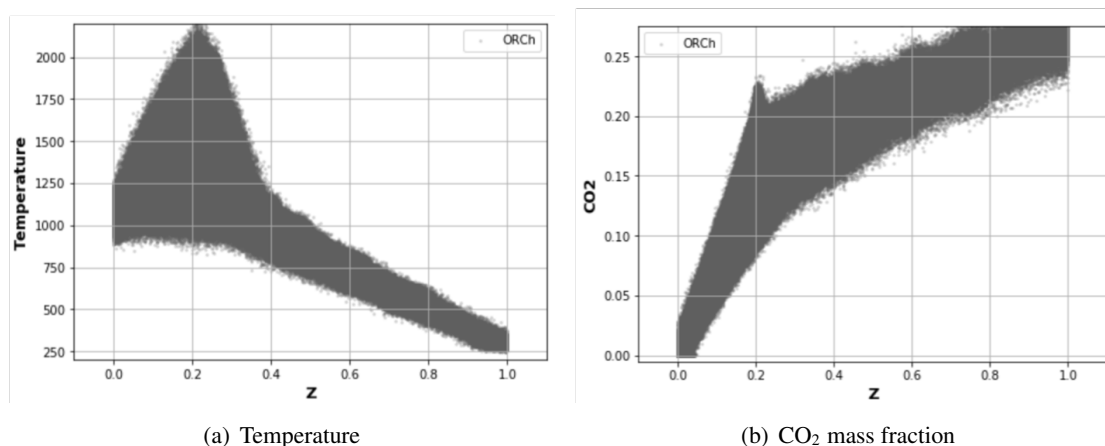


Figure 4.14: State diagram of stochastic particles in mixture fraction space for a noised case.

As a matter of fact, within the UMONS furnace, the diversity of the thermochemical conditions are more pronounced than those generated by the canonical problem reported above. One of the major issue

lies in the huge variability in the amount of burnt gases locally mixed with the reactants, mainly because the recirculation rate of burnt products is far from being uniform in space. The fuel may for instance be mixed only with burnt gases without air within coherent flow structures, which are then convected quite far downstream before meeting air.

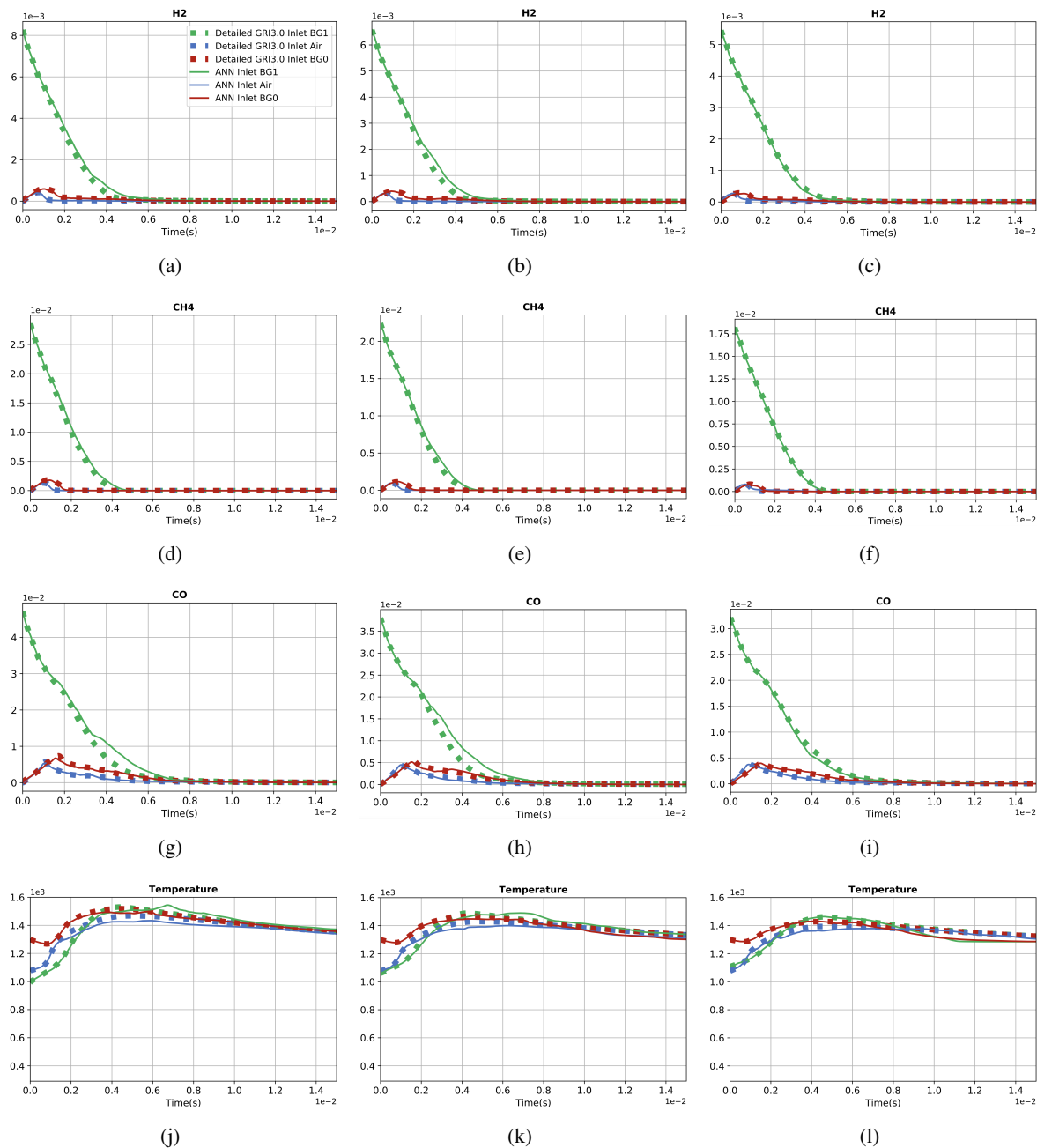


Figure 4.15: Time evolution of major species mass fraction and temperature averaged over stochastic particles with $\alpha_{loss} = 1.5 \cdot 10^5$ and time step of $5 \cdot 10^{-6} s$ for 3 ratios of burnt gases recirculation rate. Left: 3. Middle: 4. Right: 5.

A successful attempt was made to extend the above database by considering additional levels of burnt gases recirculation, i.e., varying the amount of stochastic particles within the third inlet of the

model problem (Eqs. (4.3)-(4.4)). However, these additional levels coupled together with the different heat-loss levels lead to a computing effort for training which rapidly became prohibitive.

Following previous works in which the control of database augmentation combined with improvement in training efficiency was achieved from a systematic blurring [68, 171, 165], 5% of Gaussian noise is added to all variables in all cases of the above dataset, still conserving mass thanks to Eqs. (4.5)-(4.6). The final database contains 25,238,581 rows. The training is performed in parallel using 8 GPUs (NVIDIA Tesla K80) and it is completed in about 7 hours runtime.

Figure 4.14 shows the temperature and CO₂ responses in mixture fraction space for the noised database. Following the same procedure as above, the ANNs obtained with this noised database are verified by solving Eqs. (4.3) and (4.4) with detailed and ANN-based chemistry. For this test, three dilutions ratios are considered (ratio between burnt gases mass flow rate and sum of fuel and air mass flow rates) and with a lower level of heat-loss $\alpha_{loss} = 1.5 \cdot 10^5$, in order to mimic different conditions. The trained ANNs capture quite well the thermochemical response.

4.5.4 Flow solver and modeling

The Navier-Stokes equations (momentum, energy and species mass fractions) are solved using the open source software Code_Saturne [174]. It relies on a co-located second order accurate cell-centred finite volume approach operating over unstructured grids. The full volume of the furnace is meshed, including the 12 exhaust cylinders, with a non-uniform mesh of 12 million cells, featuring tetrahedrons and hexahedrons (Fig. 4.16). On the bottom wall where gases are injected, the mesh is so that y^+ is just below unity, while $7 < y^+ < 15$ on the lateral walls. The mesh is strongly refined in the shear layers developing downstream of jet injection with a resolution down to 0.2mm. Figure 4.17 shows the vortical structures which develop from the three jets, to then be combined and merge further downstream, they are coloured by the temperature. At the bottom close to injections, the reactants are mixed with recirculating burnt products trapped between the jets, while the temperature is indeed almost uniform as expected in the flameless combustion regime.

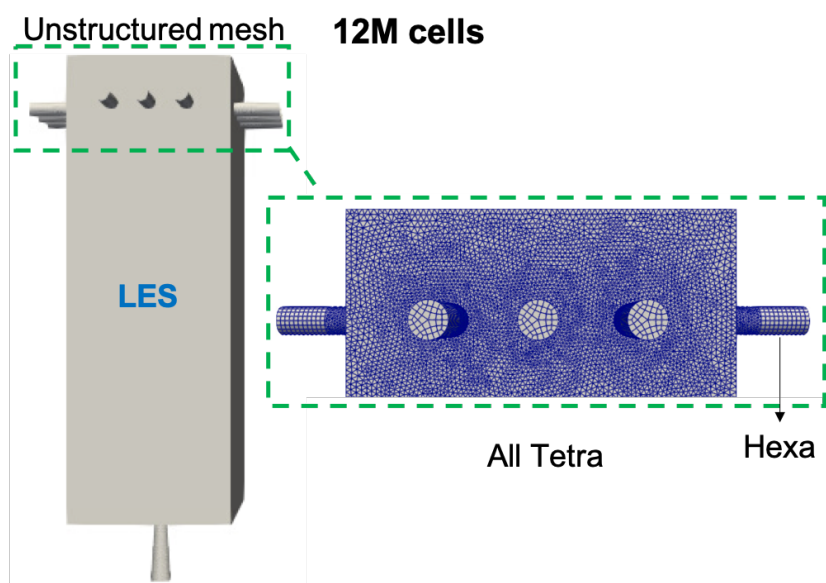


Figure 4.16: UMONS furnace configuration and mesh.

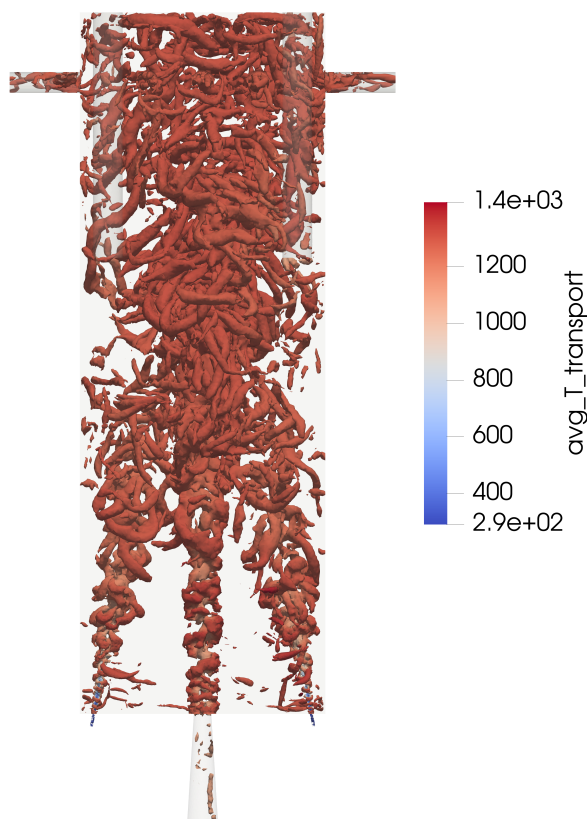


Figure 4.17: Instantaneous iso-surface of Q criterion [175] $Q = 6 \cdot 10^5 s^{-2}$, colored by time-averaged temperature.

4.5.4.1 Turbulence-chemistry interaction modelling

Combustion in separated jet injection systems, thus operating in the non-premixed mode, is overall controlled by a partial mixing of the reactants occurring at large and medium flow length scales, followed by micro-mixing and molecular diffusion at smaller scales, where reactant are put in contact and chemical reactions occur [176]. To mimic this overall two-stage mechanism, each computational cell is divided into a non-reacting part and a reacting part. The latter is pictured as a perfectly stirred reactor (PSR). Thereby, the turbulence-chemistry interaction is modeled from a description of the sub-grid scales relying on partially stirred reactors (PaSR) [177], as in previous works on burnt gases highly diluted combustion [178, 179, 180, 140, 138, 181, 182, 63, 183, 184, 185].

$\bar{\omega}_k$ denotes the LES filtered burning rate (or volume averaged over the mesh cell), which enters the balance equation for the k -th thermochemical quantity. $\hat{\omega}_k(\tilde{\underline{Y}}, \tilde{T})$ is the burning rate computed from quantities resolved by the mesh, where $\tilde{\underline{Y}}$ and \tilde{T} are the LES filtered vector of mass fractions and temperature respectively. $\hat{\omega}_k(\tilde{\underline{Y}}, \tilde{T})$ is weighted by the reacting fraction κ , so that the filtered burning rate reads

$$\bar{\omega}_k = \kappa \hat{\omega}_k(\tilde{\underline{Y}}, \tilde{T}). \quad (4.7)$$

The faster the chemistry (i.e. the smaller the chemical time t_c), the larger $\dot{\omega}_k(\tilde{\underline{Y}}, \tilde{T})$. However, in each computational cell, the reacting fraction κ must decrease if $t_{m,\Delta}$, the mechanical mixing time in the cell of characteristic size Δ , becomes larger than the chemical time, since mixing is then not fast enough to fully feed the reactions occurring at the smallest turbulent flow scales. Hence, $\kappa = \bar{\omega}_k / \dot{\omega}_k(\tilde{\underline{Y}}, \tilde{T})$ is assumed to be proportional to the ratio of the characteristic times [177]:

$$\kappa = \frac{t_c}{t_c + t_{m,\Delta}}, \quad (4.8)$$

with $t_c = 5 \cdot 10^{-6}$ s, the shortest representative ignition delay of the mixture for the present operating conditions, as observed in the detailed chemistry simulation reported thereafter. The mechanical mixing time $t_{m,\Delta}$ is approximated from the Smagorinsky SGS model [96, 186], used in the simulations to represent transport by unresolved velocity fluctuations:

$$t_{m,\Delta} = \frac{(C_s \Delta)^2}{\nu + \nu_{sgs}}. \quad (4.9)$$

C_s is the parameter of the dynamic procedure [105] applied to approximate the SGS viscosity in the simulation, $\nu_T = (C_s \Delta)^2 |S|$, where $|S| = (2S_{ij}S_{ij})^{1/2}$, with $S_{ij} = (\nabla \mathbf{u} + \nabla \mathbf{u}^T)/2$. \mathbf{u} is the velocity vector, ν is the molecular viscosity and $\Delta = V^{1/3}$, with V the volume of the cell.

Within this framework, the neural networks are trained to return $\delta Y_k = \dot{\omega}_k(\tilde{\underline{Y}}, \tilde{T}) \times \delta t$, where δt denotes the time-step. During time iterations in the flow solver, convection and diffusion are first solved, then the increment due to chemistry is directly read from the networks. Sub-iterations may be required in the cases where the time-step is larger in the flow solver than during the training phase of the network.

4.5.4.2 Radiative heat transfer modelling

The weighted-sum-of-gray-gases (WSGG) approach is applied to model radiative heat transfer [146]. The emissivity weighting factors and absorption coefficients of combustion products (H_2O and CO_2) are calculated using correlations [111]. Three gray gases are considered to minimise CPU time and memory requirements [147, 129]. The discrete ordinate method (DOM- S_4 , 24 directions) [150, 31] is used to discretise the radiative transfer equation (RTE) over the three-dimensional mesh.

4.6 Results and comparison against measurements

Figure 4.18(d) shows the comparison between measured and computed averaged temperature. The rather flat temperature profiles expected in a flameless combustion regime are observed. The temperature field is quasi-homogeneous in the simulation, without hot spots representative of thin flame reaction zones. Both locations on the left side ($x < 0$) and on the right side ($x > 0$) of the furnace are displayed. At the locations of $x = \pm 0.12\text{m}$ and $\pm 0.15\text{m}$, the measured temperature decreases in the vicinity of the fuel jet, a trend that is well recovered by the simulations.

The distributions of the three species, CO , H_2 and CH_4 , initially present in the fuel and produced /consumed by combustion, are compared against measurements in Figs 4.19-4.21. Results are also convincing. The peak values in the profiles correspond to the fuel jet. The measured species profiles at the location of $x = \pm 0.15\text{m}$ (Figs. 4.19(d), 4.20(d) and 4.21(d)) feature a significant asymmetry between the right and left sides, while the numerical results show rather similar profiles on both sides. Thereby, the computed species profiles agree with the measured species profile at $x = -0.15\text{m}$, but not at $x = +0.15\text{m}$.

According to these experimental profiles at $x = +0.15\text{m}$, the molar fractions of CO , H_2 and CH_4 stays very low in the vicinity of the fuel jet on the side of positive abscissa (the right side of the furnace), where the sampling probe was introduced. It is therefore likely that the discrepancy in the measurements between the two sides results from spurious perturbation by the probe.

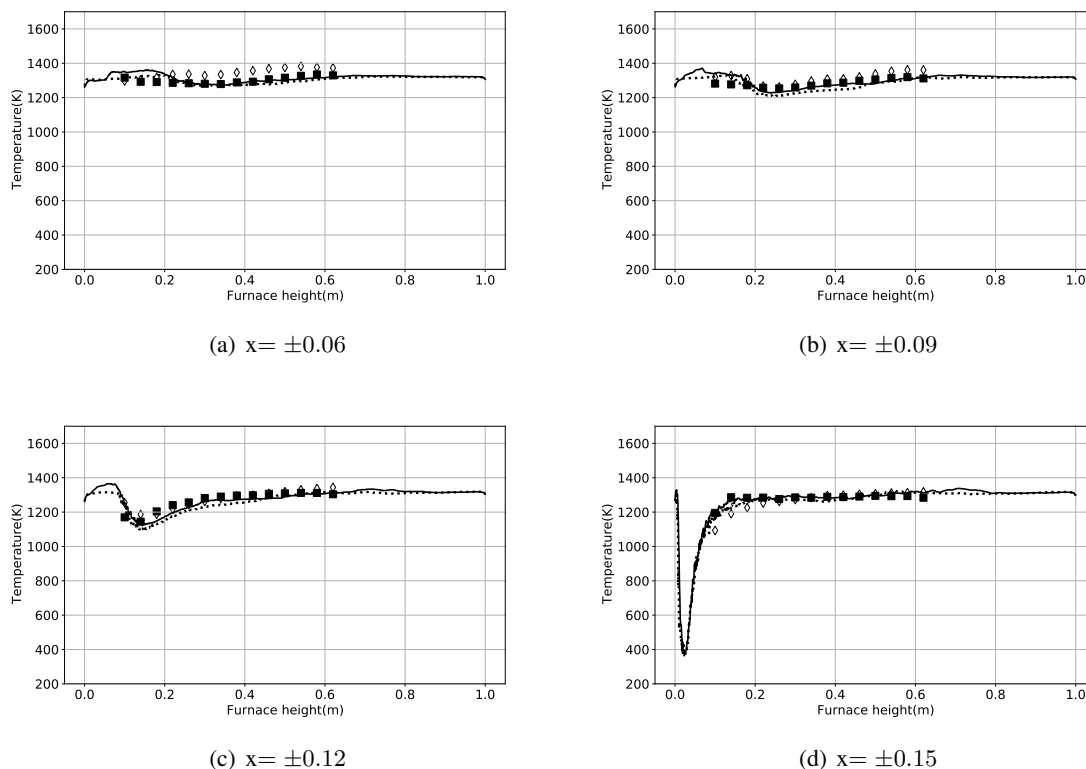


Figure 4.18: Experimental (symbol) and simulated (line) vertical profiles of mean temperature. Dashed line and empty symbols: $x < 0$ (left side of furnace). Line and symbols: $x > 0$ (right side). Maximum measurement uncertainty is 7.6K [131, 132].

Overall the CPU cost of the simulation with the ANN chemistry solver is only 1.6 times the CPU cost of the simulation of the variable density flow within the furnace without chemistry, thus opening many perspectives for the application of LES to such industrial combustion systems.

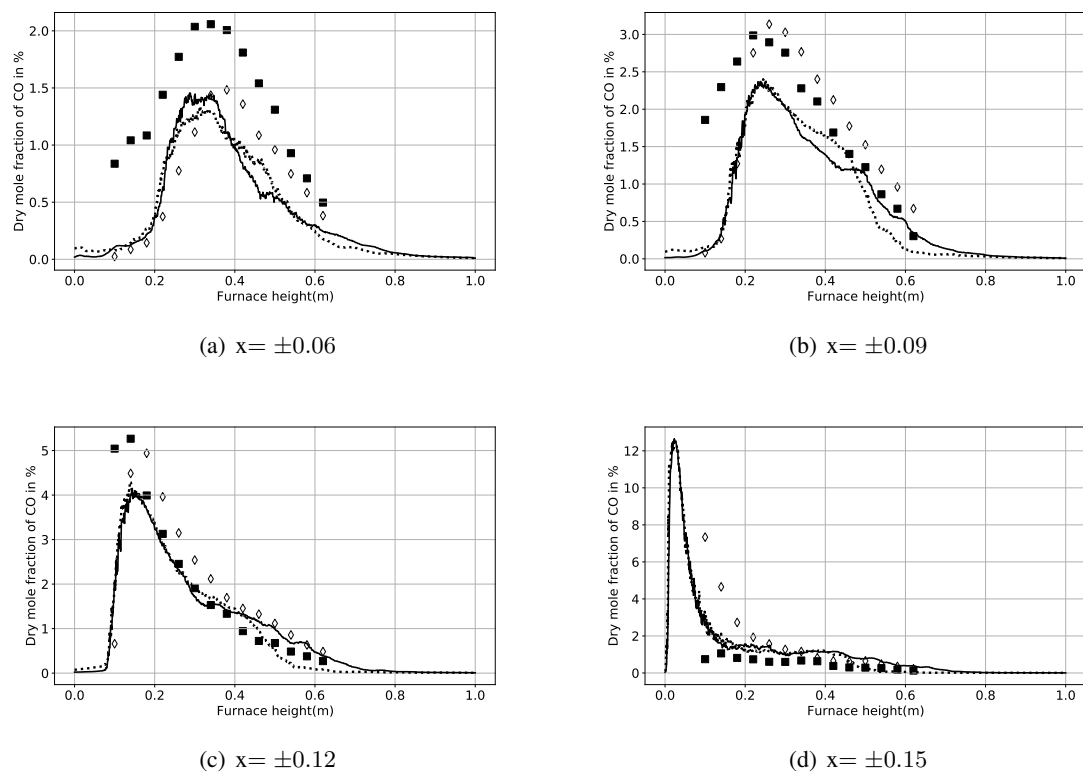


Figure 4.19: Experimental (symbol) and simulated vertical profiles of mean CO in volume percentage on dry basis. Dashed line and empty symbols: $x < 0$ (left side of furnace). Line and symbols: $x > 0$ (right side). Maximum measurement uncertainty is 0.28%.

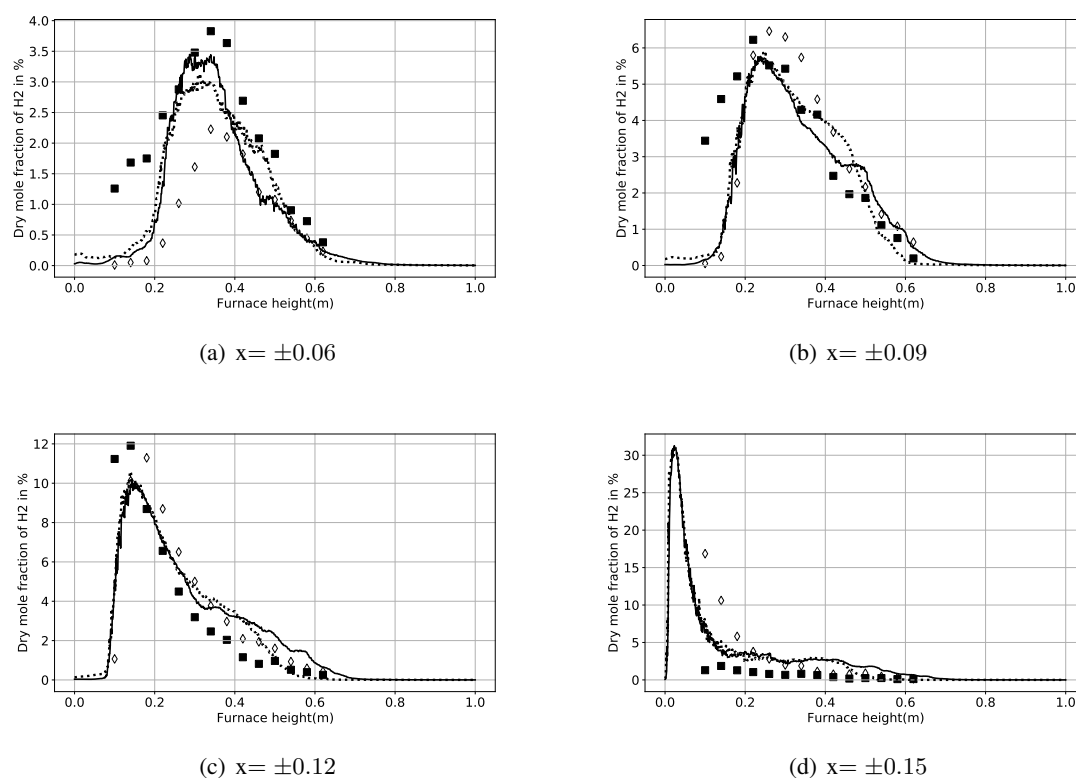


Figure 4.20: Experimental (symbol) and simulated vertical profiles of mean H_2 in volume percentage on dry basis. Dashed line and empty symbols: $x < 0$ (left side of furnace). Line and symbols: $x > 0$ (right side). Maximum measurement uncertainty is 0.72%.

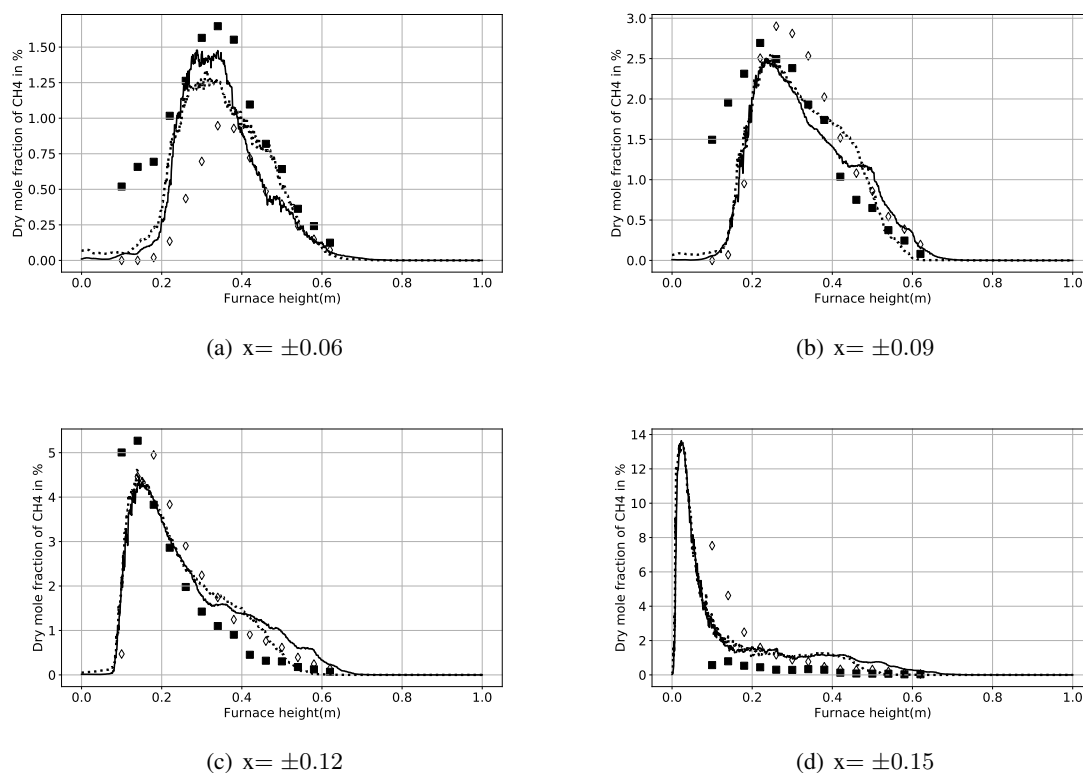


Figure 4.21: Experimental (symbol) and simulated vertical profiles of mean CH₄ in volume percentage on dry basis. Dashed line and empty symbols: $x < 0$ (left side of furnace). Line and symbols: $x > 0$ (right side). Maximum measurement uncertainty is 0.27%.

4.7 Conclusion

The introduction of machine learning in turbulent reacting flow simulations is a rapidly growing field [187]. Neural networks are becoming a standard ingredient of turbulent reactive flow simulations, to construct data oriented modeling of phenomena which are unresolved by meshes and also to speed up simulations by replacing specific time consuming tasks.

This application of neural networks has been addressed for introducing complex combustion chemistry in 0D calculations and then Large Eddy Simulation of flameless combustion. Storing the species mass fraction increments, the neural networks both reduce and pre-integrate stiff chemical systems. In a low-Mach number flow solver, with time-splitting for chemistry, the neural networks directly return the updated state of the thermochemical parameters, allowing for performing the complex chemistry simulations at a very moderate CPU cost.

This neural network approach for chemistry is applied to Large Eddy Simulation of the UMONS [131, 132] flameless combustion experiment. This furnace features a fully separated jet injection of a fuel representative of recycled gases burning with air, as found in the steel industry. To achieve the training prior to the flow simulation, a stochastic micro-mixing model problem with heat-loss and dilution by burnt gases is introduced and simulated with a detailed chemical scheme. Through their time evolution, these particles cover the range of thermochemical conditions expected in the flameless combustion chamber. A database is thus obtained which is then used to train a set of neural networks. It is shown that an acceptable level of accuracy can be achieved after clustering the data in the thermochemical composition space applying standard machine learning tools. A family of neural networks, each dedicated to a given cluster, are finally trained to be applied in the simulations.

The numerical results compare well with experiments, which is very encouraging considering the low computing cost of these simulations. However, to fully conclude on the validity and the robustness of this approach, additional test cases need to be considered, also including measurements of emissions such as NO_x or particulate to further develop and consolidate the modeling.

Chapter 5

General conclusions and perspectives

5.1 Conclusions

5.1.1 Chemical scheme reduction for applications under flameless combustion condition

A novel strategy to include heat loss effects into the chemistry reduction tool ORCh was developed and implemented. The results have proven that it is possible to reconstruct precisely the heat loss from a 3D CFD simulation into a 0D ORCh calculation. The trajectories of the detailed schemes in the case with or without heat loss demonstrates the effect of the heat loss on reaction path. The detailed schemes have the identical major species evolution in the case without heat loss, but each detailed scheme responds differently while imposing the heat loss. Two reduced schemes from GRI30 and POLIMI1412 are highly optimised in order to imitate the behaviour of the detailed schemes. The two reduced schemes were implemented into Fluent to perform RANS simulations of a lab-scale flameless combustion furnace UMONS. The comparison between the simulation and the experiment confirms the validity of the method; heat transfer, energy balance, temperature and chemical species fields were fairly predicted by the simulation.

This promising approach provides an interesting framework for combustion modeling in which case-specific chemistry reduction can be considered for practical applications. Indeed, this methodology has been successfully applied to generate reduced chemical schemes under specific conditions of furnaces at ArcelorMittal. The reduced schemes were implemented into the CFD simulations which help in the design of gas injectors for low-carbon-fuels to mitigate CO₂ emissions.

5.1.2 Machine learning for integrating combustion chemistry in numerical simulation

A novel methodology based on the training of neural networks was proposed to reduce combustion chemistry and applied to a non-premixed syngas oxy-flame canonical configuration. The unsupervised learning technique K-means was used to cluster the entire dataset, obtained from the solution of stochastic particles in a turbulent micro-mixing system, into multiple subsets. In the case of a two-inlet problem, with one of the streams bringing the energy necessary for ignition, the proposed decomposition in clusters is likely to be robust and generic. Indeed, after some turbulent mixing, the mixture will always ignite to then evolve towards equilibrium. Some level of finite rate chemistry may appear, but full quenching is very unlikely, especially in the case of oxy-combustion studied here. However, the addition of heat losses and of non-adiabatic recirculating burnt gases may require further examination to determine the best compromise in terms of clustering, still following a similar approach.

Local Principal Component Analysis (LPCA) was then applied on each subset to reduce the dimension of the problem and most important principal components were retained for the ANN training process. Neural networks were finally trained with the aim to replace expensive chemistry integration. The simulation results showed that the proposed method is able to predict the evolution of the thermochemical variables (temperature and species concentration) with excellent accuracy over the whole domain covering from mixing to ignition, combustion and finally chemical equilibrium. All of those with a drastically reduced simulation time.

This method of chemistry reduction based on ANN training was coupled with the LES technique and applied to the simulation of flameless combustion with condition representative of industrial condition. A multi-physics numerical framework was proposed. The turbulence-chemistry interaction is modelled by the PaSR model which may be considered as the state-of-the-art model for flameless combustion simulation. The radiation is described by the three gray gases weighted-sum-of-gray-gases (WSGG) approach incorporated in the angular discretization discrete ordinate method (DOM). The comparison of the LES results with the experimental in-furnace measurements showed the validity of the entire proposed methodology. The CPU cost relating to the chemistry part is simply comparable to the fluid flow solving as the chemical source terms are just read from the ANN model; no chemistry integration is needed. This approach is opening an interesting perspective; with CPU cost being even more reduced, simultaneous multiple simulations can be carried out for the search of optimal design of a combustion system or for the training of reduced order model with application in digital twins.

5.2 Perspectives

Chemical scheme reduction including heat loss

The novel chemistry reduction methodology including heat loss is further applied into the Hydrogen ArcelorMittal project and will be exploited in futur projects aiming to the 2050 carbon neutralization target of ArcelorMittal. In practice, the methodology could be improved by estimating heat loss (enthalpy) levels using energy balance to avoid prior CFD simulations.

Neural network potential

The neural network methodology proposed in this thesis use the fully-connected ANN structure. Different neural network structure, such as Convolutional neural network (CNN), Long short time memory (LSTM), Generative adversarial network (GAN) are also the promising candidates.

Decreasing ORCh time step could improve the prediction quality of neural networks by well describing the evolution of minor species. Including time step as an additional features of neural network is an encouraging method [188].

Another method to improve the prediction of minor species with large time step is to force the focus of the ANN on the minor species by customising the loss function during training process [189]. Along this line, the physic-informed neural network (PINN) [190, 191, 192] could also be exploited and included in the loss functions to strengthen the neural networks prediction quality.

Last but not least, the ANN chemical integration methodology allows the simulation process acceleration which is the key of the development of the reduced-order model toward the digital twin [193]. Along with the prompt revolution in the AI domain and the emerging of novel and more-accessible so-

lutions for data management and model deployment (such as Microsoft Azure, Amazon Web Services, etc.), the potential of digital twin in industry will undoubtedly become boundless in the next few years to come.

Bibliography

- [1] Valérie Masson-Delmotte, Panmao Zhai, Hans-Otto Pörtner, Debra Roberts, Jim Skea, Priyadarshi R. Shukla, Anna Pirani, W. Moufouma-Okia, C. Péan, R. Pidcock, et al. Global warming of 1.5°C. *An IPCC Special Report on the impacts of global warming of 1.5°C*, 1(5), 2018.
- [2] Centre for Research on the Epidemiology of Disasters. 2020: The Non-COVID year in disasters. 2021.
- [3] Jack O'Connor, Caitlyn Eberle, Davide Cotti, Michael Hagenlocher, Jonathan Hassel, Sally Janzen, Liliana Narvaez, Amy Newsom, Andrea Ortiz-Vargas, Simon Schuetze, et al. Interconnected Disaster Risks. 2021.
- [4] Vietnam Insider. Typhoon Molave caused estimated damage of VND 10 trillion in Vietnam. 2020.
- [5] Scott Duncan. September Heatwave, Europe (2020). 2020.
- [6] Alexander I Filkov, Tuan Ngo, Stuart Matthews, Simeon Telfer, and Trent D. Penman. Impact of Australia's catastrophic 2019/20 bushfire season on communities and environment. Retrospective analysis and current trends. *Journal of Safety Science and Resilience*, 1(1):44–56, 2020.
- [7] Bureau of Meteorology Australian government. Annual climate statement 2019. 2020.
- [8] Bureau of Meteorology Australian government. Special climate statement 73–Extreme heat and fire weather in December 2019 and January 2020. 2020.
- [9] Hannah Ritchie. Sector by sector: where do global greenhouse gas emissions come from?, 2020.
- [10] Paris Agreement. Paris agreement. In *Report of the Conference of the Parties to the United Nations Framework Convention on Climate Change (21st Session, 2015: Paris)*. Retrived December, volume 4, page 2017. HeinOnline, 2015.
- [11] J.A. Wüning and J.G. Wüning. Flameless oxidation to reduce thermal NO-formation. *Progress in energy and combustion science*, 23(1):81–94, 1997.
- [12] C.P. Fenimore. Formation of nitric oxide in premixed hydrocarbon flames. In *Symposium (International) on Combustion*, volume 13, pages 373–380. Elsevier, 1971.
- [13] P.C. Malte and D.T. Pratt. The role of energy-releasing kinetics in NOx formation: fuel-lean, jet-stirred CO-air combustion. *Combustion science and technology*, 9(5-6):221–231, 1974.
- [14] Task Force on Techno-Economic Issues. Reduction of NOx emissions.

- [15] Toshiaki Hasegawa and Ryoichi Tanaka. High Temperature Air Combustion: Revolution in Combustion Technology: Part I: New Findings on High Temperature Air Combustion. *JSME International Journal Series B Fluids and Thermal Engineering*, 41(4):1079–1084, 1998.
- [16] Antonio Cavaliere and Mara De Joannon. Mild combustion. *Progress in Energy and Combustion science*, 30(4):329–366, 2004.
- [17] Eric Masson. *Etude expérimentale des champs dynamiques et scalaires de la combustion sans flamme*. PhD thesis, INSA de Rouen, 2005.
- [18] S. Murer, B. Pesenti, and P. Lybaert. Air temperature influence on flameless combustion of natural gas in a 30 kW combustor. In *7th European Conference on Industrial Furnaces and Boilers. Presented at the INFUB7, Porto*, 2006.
- [19] Ambrogio Milani, Alessandro Saponaro, et al. Diluted combustion technologies. *IFRF Combustion Journal*, 1:1–32, 2001.
- [20] André A.V. Perpignan, Arvind Gangoli Rao, and Dirk J.E.M. Roekaerts. Flameless combustion and its potential towards gas turbines. *Progress in Energy and Combustion Science*, 69:28–62, 2018.
- [21] G. Mosca. *Experimental and numerical study on MILD combustion of low LHV fuels*. PhD thesis, Belgium, University of Mons, 2017.
- [22] Ambrogio Milani and J.G. Wüning. Flameless oxidation technology. In *Advanced Combustion and Aerothermal Technologies*, pages 343–352. Springer, 2007.
- [23] D. Roekaerts and L. Vervisch. Best Practice Guidelines for Computational Fluid Dynamics of Turbulent Combustion. *BPG, ERCOFTAC: Brussels, Belgium*, 2016.
- [24] Olivier Gicquel, Nasser Darabiha, and Dominique Thévenin. Liminar premixed hydrogen/air counterflow flame simulations using flame prolongation of ILDM with differential diffusion. *Proceedings of the Combustion Institute*, 28(2):1901–1908, 2000.
- [25] P. Domingo, L. Vervisch, and D. Veynante. Large-eddy simulation of a lifted methane jet flame in a vitiated coflow. *Combustion and Flame*, 152(3):415 – 432, 2008.
- [26] P.-D. Nguyen, L. Vervisch, V. Subramanian, and P. Domingo. Multidimensional flamelet-generated manifolds for partially premixed combustion. *Combust. Flame*, 157(1):43–61, 2010.
- [27] P. Domingo and L. Vervisch. Large eddy simulation of premixed turbulent combustion using approximate deconvolution and explicit flame filtering. *Proc. Combust. Inst.*, 35:1349–1357, 2015.
- [28] Carlo Locci, Luc Vervisch, Benjamin Farcy, Pascale Domingo, and Nicolas Perret. Selective non-catalytic reduction (SNCR) of nitrogen oxide emissions: a perspective from numerical modeling. *Flow, Turbulence and Combustion*, 100(2):301–340, 2018.
- [29] D. Tabacco, C. Innarella, and C. Bruno. Theoretical and numerical investigation on flameless combustion. *Combustion Science and Technology*, 174(7):1–35, 2002.

- [30] Stefano Orsino, ROMAN WEBER*, and Ugo Bollettini. Numerical simulation of combustion of natural gas with high-temperature air. *Combustion Science and Technology*, 170(1):1–34, 2001.
- [31] F.C. Christo and Bassam B. Dally. Modeling turbulent reacting jets issuing into a hot and diluted coflow. *Combustion and flame*, 142(1-2):117–129, 2005.
- [32] Delphine Lupant. Caractérisation expérimentale détaillée et modélisation numérique de la combustion diluée du gaz naturel sur une installation de laboratoire de 30kW. *Doctorat en sciences appliquées, Polytech de Mons*, 2011.
- [33] Bjørn F. Magnussen and Bjørn H. Hjertager. On mathematical modeling of turbulent combustion with special emphasis on soot formation and combustion. In *Symposium (international) on Combustion*, volume 16, pages 719–729. Elsevier, 1977.
- [34] B. Magnussen. On the structure of turbulence and a generalized eddy dissipation concept for chemical reaction in turbulent flow. In *19th aerospace sciences meeting*, page 42, 1981.
- [35] D. LUPANT*, B. Pesenti, P. Evrard, and P. Lybaert. Numerical and experimental characterization of a self-regenerative flameless oxidation burner operation in a pilot-scale furnace. *Combustion Science and Technology*, 179(1-2):437–453, 2007.
- [36] G. P. Smith, D. M. Golden, M. Frenklach, N. W. Moriarty, B. Eiteneer, M. Goldenberg, C. T. Bowman, R. K. Hanson, S. Song, W. C. Gardiner, V. V. Lissianski, and Z. Qin. Technical report, 1999. <http://www.me.berkeley.edu/gri-mech/>.
- [37] Eliseo Ranzi, Carlo Cavallotti, Alberto Cuoci, Alessio Frassoldati, Matteo Pelucchi, and Tiziano Faravelli. New reaction classes in the kinetic modeling of low temperature oxidation of n-alkanes. *Combustion and flame*, 162(5):1679–1691, 2015.
- [38] Chong-Wen Zhou, Yang Li, Eoin O’connor, Kieran P. Somers, Sébastien Thion, Charles Keesee, Olivier Mathieu, Eric L. Petersen, Trent A. DeVerter, Matthew A. Oehlschlaeger, et al. A comprehensive experimental and modeling study of isobutene oxidation. *Combustion and Flame*, 167:353–379, 2016.
- [39] Peter Glarborg and Line L.B. Bentzen. Chemical effects of a high CO₂ concentration in oxy-fuel combustion of methane. *Energy & Fuels*, 22(1):291–296, 2008.
- [40] Christian Lund Rasmussen, Anja Egede Rasmussen, and Peter Glarborg. Sensitizing effects of NO_x on CH₄ oxidation at high pressure. *Combustion and Flame*, 154(3):529–545, 2008.
- [41] Jorge Gimenez Lopez, Christian Lund Rasmussen, Maria U Alzueta, Yide Gao, Paul Marshall, and Peter Glarborg. Experimental and kinetic modeling study of c₂h₄ oxidation at high pressure. *Proceedings of the Combustion Institute*, 32(1):367–375, 2009.
- [42] Charles K. Westbrook and Frederick L. Dryer. Simplified reaction mechanisms for the oxidation of hydrocarbon fuels in flames. *Combustion science and technology*, 27(1-2):31–43, 1981.
- [43] Debasis Chakraborty, P.J. Paul, and H.S. Mukunda. Evaluation of combustion models for high speed H₂/air confined mixing layer using DNS data. *Combustion and Flame*, 121(1-2):195–209, 2000.

- [44] B. Franzelli, E. Riber, M. Sanjosé, and Thierry Poinso. A two-step chemical scheme for kerosene–air premixed flames. *Combustion and Flame*, 157(7):1364–1373, 2010.
- [45] W.P. Jones and R.P. Lindstedt. Global reaction schemes for hydrocarbon combustion. *Combustion and flame*, 73(3):233–249, 1988.
- [46] N. Peters. Numerical and asymptotic analysis of systematically reduced reaction schemes for hydrocarbon flames. In *Numerical simulation of combustion phenomena*, pages 90–109. Springer, 1985.
- [47] R.W. Bilger, S.H. Stårner, and R.J. Kee. On reduced mechanisms for methane air combustion in nonpremixed flames. *Combustion and Flame*, 80(2):135–149, 1990.
- [48] Mitchell D. Smooke. *Reduced kinetic mechanisms and asymptotic approximations for methane-air flames: a topical volume*. Springer, 1991.
- [49] T. Lu and C. K. Law. A directed relation graph method for mechanism reduction. *Proceedings of the Combustion Institute*, 30(1):1333–1341, 2005.
- [50] Tianfeng Lu and Chung K. Law. Linear time reduction of large kinetic mechanisms with directed relation graph: n-Heptane and iso-octane. *Combustion and flame*, 144(1-2):24–36, 2006.
- [51] X. L. Zheng, T. F. Lu, and C. K. Law. Experimental counterflow ignition temperatures and reaction mechanisms of 1, 3-butadiene. *Proceedings of the Combustion Institute*, 31(1):367–375, 2007.
- [52] Megan Frances Karalus. *An investigation of lean blowout of gaseous fuel alternatives to natural gas*. PhD thesis, 2014.
- [53] T. Lu and C. K. Law. Strategies for mechanism reduction for large hydrocarbons: n-heptane. *Combustion and flame*, 154(1-2):153–163, 2008.
- [54] J. Y. Chen. Development of reduced mechanisms for numerical modelling of turbulent combustion. In *Workshop on Numerical Aspects of Reduction in Chemical Kinetics*. CERMICS-ENPC Cite Descartes Champus sur Marne, France, 1997.
- [55] Alessandro Stagni, Alessio Frassoldati, Alberto Cuoci, Tiziano Faravelli, and E. Ranzi. Skeletal mechanism reduction through species-targeted sensitivity analysis. *Combustion and Flame*, 163:382–393, 2016.
- [56] Kyle E. Niemeyer, Chih-Jen Sung, and Mandhapati P. Raju. Skeletal mechanism generation for surrogate fuels using directed relation graph with error propagation and sensitivity analysis. *Combustion and flame*, 157(9):1760–1770, 2010.
- [57] N. Jaouen. *An automated approach to derive and optimise reduced chemical mechanisms for turbulent combustion*. Phd thesis, INSA Rouen, 2017.
- [58] N. Jaouen, L. Vervisch, and P. Domingo. Auto-thermal reforming (ATR) of natural gas: An automated derivation of optimised reduced chemical schemes. *Proc. Combust. Inst.*, 36(3):3321–3330, 2017.

- [59] N. Jaouen, L. Vervisch, P. Domingo, and G. Ribert. Automatic reduction and optimisation of chemistry for turbulent combustion modeling: Impact of the canonical problem. *Combust. Flame*, 175:60–79, 2017.
- [60] Magnus Fürst, Pino Sabia, Marco Lubrano Lavadera, Gianmarco Aversano, Mara De Joannon, Alessio Frassoldati, and Alessandro Parente. Optimization of chemical kinetics for methane and biomass pyrolysis products in moderate or intense low-Oxygen dilution combustion. *Energy & fuels*, 32(10):10194–10201, 2018.
- [61] Nguyen Anh Khoa Doan. *Physical insights of non-premixed MILD combustion using DNS*. PhD thesis, University of Cambridge, 2019.
- [62] Erjiang Hu, Xiaotian Li, Xin Meng, Yizhen Chen, Yu Cheng, Yongliang Xie, and Zuohua Huang. Laminar flame speeds and ignition delay times of methane–air mixtures at elevated temperatures and pressures. *Fuel*, 158:1–10, 2015.
- [63] Marco Ferrarotti, M. FuÀrst, Enrico Cresci, Ward De Paepe, and Alessandro Parente. Key modeling aspects in the simulation of a quasi-industrial 20 kw moderate or intense low-oxygen dilution combustion chamber. *Energy & fuels*, 32(10):10228–10241, 2018.
- [64] Warren S. McCulloch and Walter Pitts. A logical calculus of the ideas immanent in nervous activity. *The bulletin of mathematical biophysics*, 5(4):115–133, 1943.
- [65] F. Rosenblatt. *The Perceptron, a Perceiving and Recognizing Automaton Project Para*. Report: Cornell Aeronautical Laboratory. Cornell Aeronautical Laboratory, 1957.
- [66] Andrey Kurenkov. A brief history of neural nets and deep learning. *Skynet Today*, 2020.
- [67] Jia Deng, Wei Dong, Richard Socher, Li-Jia Li, Kai Li, and Li Fei-Fei. Imagenet: A large-scale hierarchical image database. In *2009 IEEE conference on computer vision and pattern recognition*, pages 248–255. Ieee, 2009.
- [68] Andrea Seltz, Pascale Domingo, Luc Vervisch, and Zacharias M Nikolaou. Direct mapping from LES resolved scales to filtered-flame generated manifolds using convolutional neural networks. *Combustion and Flame*, 210:71–82, 2019.
- [69] K. Wan, C. Barnaud, L. Vervisch, and P. Domingo. Chemistry reduction using machine learning trained from non-premixed micro-mixing modeling: Application to DNS of a syngas turbulent oxy-flame with side-wall effects. *Combustion and Flame*, 220:119–129, 2020.
- [70] Kaidi Wan, Camille Barnaud, Luc Vervisch, and Pascale Domingo. Machine learning for detailed chemistry reduction in dns of a syngas turbulent oxy-flame with side-wall effects. *Proceedings of the Combustion Institute*, 38(2):2825–2833, 2021.
- [71] Andréa Seltz. *Application of deep learning to turbulent combustion modeling of real jet fuel for the numerical prediction of particulate emissions*. PhD thesis, Normandie, 2020.
- [72] ZM Nikolaou, C. Chrysostomou, Luc Vervisch, and S. Cant. Progress variable variance and filtered rate modelling using convolutional neural networks and flamelet methods. *Flow, Turbulence and Combustion*, 103(2):485–501, 2019.

- [73] Lucas L.C. Franke, Athanasios K. Chatzopoulos, and Stelios Rigopoulos. Tabulation of combustion chemistry via Artificial Neural Networks (ANNs): Methodology and application to LES-PDF simulation of Sydney flame L. *Combustion and Flame*, 185:245–260, 2017.
- [74] Tianhan Zhang, Yuxiao Yi, Yifan Xu, Zhi X Chen, Yaoyu Zhang, Zhi-Qin John Xu, et al. A multi-scale sampling method for accurate and robust deep neural network to predict combustion chemical kinetics. *arXiv preprint arXiv:2201.03549*, 2022.
- [75] Kaidi Wan, Sandra Hartl, Luc Vervisch, Pascale Domingo, Robert S. Barlow, and Christian Hasse. Combustion regime identification from machine learning trained by raman/rayleigh line measurements. *Combustion and Flame*, 219:268–274, 2020.
- [76] Gianmarco Aversano, Aurelie Bellemans, Zhiyi Li, Axel Coussement, Olivier Gicquel, and Alessandro Parente. Application of reduced-order models based on PCA & Kriging for the development of digital twins of reacting flow applications. *Computers & chemical engineering*, 121:422–441, 2019.
- [77] Cheng Chi, Gábor Janiga, and Dominique Thévenin. On-the-fly artificial neural network for chemical kinetics in direct numerical simulations of premixed combustion. *Combustion and Flame*, 226:467–477, 2021.
- [78] J.A. Blasco, N. Fueyo, C. Dopazo, and J. Ballester. Modelling the temporal evolution of a reduced combustion chemical system with an artificial neural network. *Combustion and Flame*, 113(1-2):38–52, 1998.
- [79] Huu-Tri Nguyen, Pascale Domingo, Luc Vervisch, and Phuc-Danh Nguyen. Machine learning for integrating combustion chemistry in numerical simulations. *Energy and AI*, 5:100082, 2021.
- [80] Tianjie Ding, Thomas Readshaw, Stelios Rigopoulos, and W.P. Jones. Machine learning tabulation of thermochemistry in turbulent combustion: An approach based on hybrid flamelet/random data and multiple multilayer perceptrons. *Combustion and Flame*, 231:111493, 2021.
- [81] Alisha J. Sharma, Ryan F. Johnson, David A. Kessler, and Adam Moses. Deep learning for scalable chemical kinetics. In *AIAA scitech 2020 forum*, page 0181, 2020.
- [82] Joseph O Hirschfelder, Charles F Curtiss, Robert Byron Bird, and Maria Goeppert Mayer. *Molecular theory of gases and liquids*, volume 165. Wiley New York, 1964.
- [83] V. Giovangigli. Multicomponent flow modeling. *Science China Mathematics*, 55(2):285–308, 2012.
- [84] C. F. Curtiss and J. O. Hirschfelder. Transport properties of multicomponent gas mixtures. *The Journal of Chemical Physics*, 17(6):550–555, 1949.
- [85] M. Ugur Göktolga, Jeroen A. van Oijen, and L. Philip H. de Goey. 3D DNS of MILD combustion: a detailed analysis of heat loss effects, preferential diffusion, and flame formation mechanisms. *Fuel*, 159:784–795, 2015.
- [86] D. Veynante and L. Vervisch. Turbulent combustion modeling. *Progress in Energy and Combustion Science*, 28(3):193 – 266, 2002.

- [87] T. Poinso and D. Veynante. *Theoretical and Numerical Combustion*. R. T. Edwards Incorporated, 2005.
- [88] R.W. Bilger. The structure of turbulent nonpremixed flames. *Symposium (International) on Combustion*, 22(1):475 – 488, 1989.
- [89] N. Peters. Partially premixed diffusion flamelets in non-premixed turbulent combustion. In *Symposium (International) on Combustion*, volume 20, pages 353–360. Elsevier, 1985.
- [90] H Yamashita, M Shimada, and T Takeno. A numerical study on flame stability at the transition point of jet diffusion flames. In *Symposium (International) on Combustion*, volume 26, pages 27–34. Elsevier, 1996.
- [91] Osborne Reynolds. XXIX. An experimental investigation of the circumstances which determine whether the motion of water shall be direct or sinuous, and of the law of resistance in parallel channels. *Philosophical Transactions of the Royal society of London*, (174):935–982, 1883.
- [92] Stephen B Pope. *Turbulent flows*. Cambridge university press, 2011.
- [93] Andrei Nikolaevich Kolmogorov. The local structure of turbulence in incompressible viscous fluid for very large reynolds numbers. *Proceedings of the Royal Society of London. Series A: Mathematical and Physical Sciences*, 434(1890):9–13, 1991.
- [94] P. Moin and K. Mahesh. Direct numerical simulation: a tool in turbulence research. *Annual review of fluid mechanics*, 30(1):539–578, 1998.
- [95] T. Jaravel. *Prediction of pollutants in gas turbines using large eddy simulation*. Phd thesis, INP Toulouse, 2016.
- [96] Joseph Smagorinsky. General circulation experiments with the primitive equations: I. the basic experiment*. *Monthly weather review*, 91(3):99–164, 1963.
- [97] T. Poinso and D. Veynante. *Theoretical and Numerical Combustion*. Edwards, 2005.
- [98] Philippe Spalart and Steven Allmaras. A one-equation turbulence model for aerodynamic flows. In *30th aerospace sciences meeting and exhibit*, page 439, 1992.
- [99] B.E. Launder and D.B Spalding. *Lectures in Mathematical Models of Turbulence*, volume -. Academic Press, London, 1972.
- [100] David C Wilcox et al. *Turbulence modeling for CFD*, volume 2. DCW industries La Canada, CA, 1998.
- [101] Victor Yakhot and Steven A Orszag. Renormalization group analysis of turbulence. i. basic theory. *Journal of scientific computing*, 1(1):3–51, 1986.
- [102] VSASTBCG Yakhot, S.A. Orszag, Siva Thangam, T.B. Gatski, and C.G. Speziale. Development of turbulence models for shear flows by a double expansion technique. *Physics of Fluids A: Fluid Dynamics*, 4(7):1510–1520, 1992.
- [103] CFD-online. RNG k-epsilon model.

- [104] J. Boussinesq. *Théorie de l'écoulement tourbillonnant*, pages 23–46. Mem. Pres. Acad. Sci., 1877.
- [105] M. Germano, U. Piomelli, P. Moin, and W. H. Cabot. A dynamic subgrid-scale eddy viscosity model. *Physics of Fluids A: Fluid Dynamics (1989-1993)*, 3(7):1760–1765, 1991.
- [106] D. K. Lilly. A proposed modification of the germano subgrid-scale closure method. *Physics of Fluids A: Fluid Dynamics (1989-1993)*, 4(3):633–635, 1992.
- [107] A.A. Wray and J.C.R. Hunt. Algorithms for classification of turbulent structures. *Topological fluid mechanics*, pages 95–104, 1990.
- [108] F. Nicoud and F. Ducros. Subgrid-scale stress modelling based on the square of the velocity gradient tensor. *Flow, turbulence and Combustion*, 62(3):183–200, 1999.
- [109] Michael F. Modest and Daniel C. Haworth. *Radiative heat transfer in turbulent combustion systems: theory and applications*. Springer, 2016.
- [110] J. Taine. A line-by-line calculation of low-resolution radiative properties of CO₂-CO-transparent nonisothermal gases mixtures up to 3000 K. *Journal of Quantitative Spectroscopy and Radiative Transfer*, 30(4):371–379, 1983.
- [111] T.F. Smith, Z.F. Shen, and J.N. Friedman. Evaluation of coefficients for the weighted sum of gray gases model. 1982.
- [112] P.-D. Nguyen, G. Ghazal, A. Gambale, D. Lupant, and G. Mosca. Combustion CFD of diluted combustion in pilot and industrial furnaces. In *10th European Combustion Meeting*, 2015.
- [113] Phuc Danh Nguyen, Ghassan Ghazal, Víctor Cuervo Piñera, Valerio Battaglia, Anders Rensgard, Tomas Ekman, and Moncef Gazdallah. Modelling of flameless oxy-fuel combustion with emphasis on radiative heat transfer for low calorific value blast furnace gas. *Energy Procedia*, 120:492–499, 2017.
- [114] Víctor Cuervo-Piñera, Diego Cifrián-Riesgo, Phuc-Danh Nguyen, Valerio Battaglia, Massimiliano Fantuzzi, Alessandro Della Rocca, Marco Ageno, Anders Rensgard, Chuan Wang, John Niska, et al. Blast furnace gas based combustion systems in steel reheating furnaces. *Energy Procedia*, 120:357–364, 2017.
- [115] N. Jaouen, P. Domingo, and L. Vervisch. Using genetic algorithm for automated optimization of reduced chemical schemes. In *7th European Combustion Meeting*, 2015.
- [116] R. I. Curl. Dispersed phase mixing. Theory and effects in simple reactors. *AIChE*, 9(2):175–181, 1963.
- [117] S. Subramaniam and S. B. Pope. A mixing model for turbulent reactive flows based on euclidean minimum spanning trees. *Combustion and Flame*, 115(4):487–514, 1998.
- [118] P. Pepiot and H. Pitsch. Systematic reduction of large chemical mechanisms. In *4th joint meeting of the US Sections of the Combustion Institute, Philadelphia, PA*, 2005.
- [119] P. Pepiot and H. Pitsch. An efficient error propagation based reduction method for large chemical kinetic mechanisms. *Combust. Flame*, 154(1-2):67 – 81, 2008.

- [120] C. Dopazo and E. O'Brien. Functional formulation of nonisothermal turbulent reactive flows. *Phys. Fluids*, 17:1968–1975, 1974.
- [121] R. Borghi. Turbulent combustion modelling. *Prog. Energy Combust. Sci.*, 14:245–292, 1988.
- [122] Kevin Bioche, Guillaume Ribert, and Luc Vervisch. Simulating upstream flame propagation in a narrow channel after wall preheating: Flame analysis and chemistry reduction strategy. *Combustion and Flame*, 200:219–231, 2019.
- [123] K Bioche, L Vervisch, and Guillaume Ribert. Premixed flame–wall interaction in a narrow channel: impact of wall thermal conductivity and heat losses. *Journal of Fluid Mechanics*, 856:5–35, 2018.
- [124] Kevin Bioche, Amanda Pieyre, Guillaume Ribert, Franck Richecoeur, and Luc Vervisch. The role of gravity in the asymmetry of flames in narrow combustion chambers. *Combustion and Flame*, 203:238–246, 2019.
- [125] B. Farcy, L. Vervisch, P. Domingo, and N. Perret. Reduced-order modeling for the control of selective noncatalytic reduction of nitrogen monoxide. *AIChE Journal*, 62(3):928–938, 2016.
- [126] ANSYS FLUENT. Theory and user guide. v19.4.
- [127] Gabriele Mosca, Delphine Lupant, and Paul Lybaert. Effect of increasing load on the MILD combustion of COG and its blend in a 30 kW furnace using low air preheating temperature. *Energy Procedia*, 120:262–269, 2017.
- [128] Gabriele Mosca. Experimental and numerical study on MILD combustion of low LHV fuels. *PhD thesis, Polytech de Mons*, 2017.
- [129] Phuc-Danh Nguyen, Huu-Tri Nguyen, Pascale Domingo, Luc Vervisch, Gabriel Mosca, Moncef Gazdallah, Paul Lybaert, and Véronique Feldheim. Flameless combustion of low calorific value gases, experiments and simulations with advanced radiative heat transfer modeling. *Physics of Fluids, special topic: Development and validation of models for turbulent reacting flows*, 34:–, 2022.
- [130] Ludwig Christian Haber. *An investigation into the origin, measurement and application of chemiluminescent light emissions from premixed flames*. PhD thesis, Virginia Tech, 2000.
- [131] D. Lupant, B. Pesenti, and P. Lybaert. Influence of probe sampling on reacting species measurement in diluted combustion. *Experimental thermal and fluid science*, 34(5):516–522, 2010.
- [132] Delphine Lupant and Paul Lybaert. Assessment of the EDC combustion model in MILD conditions with in furnace experimental data. *Applied Thermal Engineering*, 75:93–102, 2015.
- [133] Javad Aminian, Chiara Galletti, Shahrokh Shahhosseini, and Leonardo Tognotti. Numerical investigation of a MILD combustion burner: analysis of mixing field, chemical kinetics and turbulence-chemistry interaction. *Flow, turbulence and combustion*, 88(4):597–623, 2012.
- [134] Chiara Galletti, A. Parente, Marco Derudi, Renato Rota, and Leonardo Tognotti. Numerical and experimental analysis of NO emissions from a lab-scale burner fed with hydrogen-enriched fuels and operating in MILD combustion. *international journal of hydrogen energy*, 34(19):8339–8351, 2009.

- [135] Alessandro Parente, Chiara Galletti, and Leonardo Tognotti. A simplified approach for predicting NO formation in MILD combustion of CH₄-H₂ mixtures. *Proceedings of the Combustion Institute*, 33(2):3343–3350, 2011.
- [136] A. Kazakov and M. Frenklach. Technical report. <http://combustion.berkeley.edu/drm/>.
- [137] T. Silei, G. Sorrentino, R. Ragucci, and C. Galletti. Reaction-rate based modeling of MILD Combustion in a cyclonic burner. In *10th European Combustion Meeting*, pages 1288–1293. ITA, 2021.
- [138] Marco Ferrarotti, Ward De Paepe, and Alessandro Parente. Reactive structures and NO_x emissions of methane/hydrogen mixtures in flameless combustion. *International Journal of Hydrogen Energy*, 46(68):34018–34045, 2021.
- [139] Ashoke De, Ernst Oldenhof, Pratap Sathiah, and Dirk Roekaerts. Numerical simulation of Delft-jet-in-hot-coflow (djhc) flames using the eddy dissipation concept model for turbulence–chemistry interaction. *Flow, Turbulence and Combustion*, 87(4):537–567, 2011.
- [140] Alessandro Parente, Mohammad Rafi Malik, Francesco Contino, Alberto Cuoci, and Bassam B. Dally. Extension of the Eddy Dissipation Concept for turbulence/chemistry interactions to MILD combustion. *Fuel*, 163:98–111, 2016.
- [141] Naiara Romero-Anton, Xu Huang, Hesheng Bao, Koldo Martin-Eskudero, Erik Salazar-Herran, and Dirk Roekaerts. New extended eddy dissipation concept model for flameless combustion in furnaces. *Combustion and Flame*, 220:49–62, 2020.
- [142] Xu Huang, Mark J. Tummers, Eric H. van Veen, and Dirk JEM Roekaerts. Modelling of MILD combustion in a lab-scale furnace with an extended FGM model including turbulence–radiation interaction. *Combustion and Flame*, 237:111634, 2022.
- [143] V. Yakhot. Renormalization Group Modeling and Turbulence Simulations. *International Conference on Near-Wall Turbulent Flows, Arizona, Tempe*, 1993.
- [144] Inge R. Gran and Bjørn F. Magnussen. A numerical study of a bluff-body stabilized diffusion flame. part 2. influence of combustion modeling and finite-rate chemistry. *Combustion Science and Technology*, 119(1-6):191–217, 1996.
- [145] Stephen B. Pope. Computationally efficient implementation of combustion chemistry using in situ adaptive tabulation. 1997.
- [146] H.C. Hottel and A.F. Sarofim. Radiative Transfer, McGraw-Hill, New York, 1967.
- [147] Robert Johansson, Klas Andersson, Bo Leckner, and Henrik Thunman. Models for gaseous radiative heat transfer applied to oxy-fuel conditions in boilers. *International Journal of Heat and Mass Transfer*, 53(1-3):220–230, 2010.
- [148] Aline Ziemniczak, Rogério Brittes, Fabiano Cassol, and Francis Henrique Ramos França. Evaluation of the number of gray gases in the WSGG model. In *22nd International Congress of Mechanical Engineering*, 2013.

- [149] W.A. Fiveland. Discrete-ordinates solutions of the radiative transport equation for rectangular enclosures. 1984.
- [150] Pedro J. Coelho. Numerical simulation of the interaction between turbulence and radiation in reactive flows. *Progress in energy and combustion science*, 33(4):311–383, 2007.
- [151] Z. Nikolaou, C. Chrysostomou, L. Vervisch, and R. S. Cant. Progress variable variance and filtered rate modelling using convolutional neural networks and flamelet methods. *Flow Turbulence Combust.*, 103(2):485–501, 2019.
- [152] K. Wan, C. Barnaud, L. Vervisch, and P. Domingo. Machine learning for detailed chemistry reduction in DNS of a syngas turbulent oxy-flame with side-wall effects. *Proceedings of the Combustion Institute, In Press*, 2020.
- [153] J. MacQueen. Some methods for classification and analysis of multivariate observations. In *Proceedings of the fifth Berkeley symposium on mathematical statistics and probability*, volume 1, pages 281–297. Oakland, CA, USA, 1967.
- [154] S. Alqahtani and T. Echehki. A data-based hybrid model for complex fuel chemistry acceleration at high temperatures. *Combustion and Flame*, 223:142–152, 2021.
- [155] N. Kambhatla and T. K. Leen. Dimension reduction by local principal component analysis. *Neural computation*, 9(7):1493–1516, 1997.
- [156] Z. Ren, S. Subramaniam, and SB. Pope. Implementation of the emst mixing model. <https://tcg.mae.cornell.edu/emst>.
- [157] N. Jaouen, L. Vervisch, P. Domingo, and G. Ribert. Automatic reduction and optimisation of chemistry for turbulent combustion modelling: Impact of the canonical problem. *Combustion and Flame*, 175:60–79, 2017.
- [158] N. Jaouen, L. Vervisch, and P. Domingo. Auto-thermal reforming (ATR) of natural gas: an automated derivation of optimised reduced chemical schemes. *Proceedings of the Combustion Institute*, 36(3):3321–3330, 2017.
- [159] A. Bouaniche, N. Jaouen, P. Domingo, and L. Vervisch. Vitiated high Karlovitz n-decane/air turbulent flames: Scaling laws and micro-mixing modeling analysis. *Flow Turbulence and Combustion*, 102(1):235–252, 2019.
- [160] N. Jaouen. *An automated approach to derive and optimise reduced chemical mechanisms for turbulent combustion*. PhD thesis, Normandie, 2017.
- [161] C. Locci, L. Vervisch, B. Farcy, and N. Perret. Selective non-catalytic reduction (SNCR) of nitrogen oxide emissions: A perspective from numerical modeling. *Flow Turbulence and Combust.*, 100(2):301–340, 2018.
- [162] K. Bioche, G. Ribert, and L. Vervisch. Simulating upstream flame propagation in a narrow channel after wall preheating: Flame analysis and chemistry reduction strategy. *Combust. Flame*, 200:219–231, 2019.

- [163] K. Bioche, L. Vervisch, and G. Ribert. Premixed flame-wall interaction in a narrow channel: Impact of wall thermal conductivity and heat losses. *J. Fluid Mech.*, 856:5–35, 2018.
- [164] K. Bioche, A. Pieyre, G. Ribert, F. Richecoeur, and L. Vervisch. The role of gravity in the asymmetry of flames in narrow combustion chambers. *Combust. Flame.*, 203:238–246, 2019.
- [165] A. Seltz, P. Domingo, and L. Vervisch. Solving the population balance equation for non-inertial particles dynamics using probability density function and neural networks: Application to a sooting flame. *Physics of Fluids*, 33(1):013311, 2021.
- [166] P. Pepiot-Desjardins and H. Pitsch. An efficient error-propagation-based reduction method for large chemical kinetic mechanisms. *Combustion and Flame*, 154(1-2):67–81, 2008.
- [167] Gregory P. Smith, David M. Golden, Michael Frenklach, Nigel W. Moriarty, Boris Eiteneer, Mikhail Goldenberg, C. Thomas Bowman, Ronald K. Hanson, Soonho Song, William C. Gardiner, Jr. Vitali, V. Lissianski, and Zhiwei Qin. GRI mech. <http://combustion.berkeley.edu/gri-mech/version30/text30.html>.
- [168] G. D’Alessio, A. Parente, A. Stagni, and A. Cuoci. Adaptive chemistry via pre-partitioning of composition space and mechanism reduction. *Combustion and Flame*, 211:68–82, 2020.
- [169] David Arthur and Sergei Vassilvitskii. K-means++: The advantages of careful seeding. Technical report, Stanford, 2006.
- [170] J. Jolliffe. Principal component analysis. *International Encyclopedia of Statistical Science*, Springer, pages 1094–1096, 2011.
- [171] K. Wan, C. Barnaud, L. Vervisch, and P. Domingo. Chemistry reduction using machine learning trained from non-premixed micro-mixing modeling: Application to DNS of a syngas turbulent oxy-flame with side-wall effects. *Combust. Flame*, 220:119–129, 2020.
- [172] B. Farcy, L. Vervisch, P. Domingo, and N. Perret. Reduced-order modeling for the control of selective non-catalytic reduction (SNCR). *AIChE Journal*, 62(3):928–938, 2016.
- [173] D. Goodwin. Cantera: An object-oriented software toolkit for chemical kinetics, thermodynamics, and transport processes, 2009.
- [174] EDF. Code_Saturne V7.
- [175] J. C. R. Hunt, A. A. Wray, and P. Moin. Eddies, stream, and convergence zones in turbulent flows. In *Annual Research Briefs*, pages 193–208. Center for Turbulence Research, Stanford, 1988.
- [176] K. N. C. Bray. The challenge of turbulent combustion. *Symp. (Int.) on Combust.*, 26:1–26, 1996.
- [177] Jery Chomiak and Anders Karlsson. Flame liftoff in diesel sprays. In *Symposium (International) on Combustion*, volume 26, pages 2557–2564. Elsevier, 1996.
- [178] Yashar Afarin and Sadegh Tabejamaat. Effect of hydrogen on H₂/CH₄ flame structure of mild combustion using the LES method. *International Journal of Hydrogen Energy*, 38(8):3447–3458, 2013.

- [179] C. Duwig and L. Fuchs. Large eddy simulation of a H₂/N₂ lifted flame in a vitiated co-flow. *Combust. Sci. Technol.*, 180(3):453–480, 2008.
- [180] C. Duwig, K.-J. Nogenmyr, C.-K. Chan, and M. J. Dunn. Large eddy simulation of a piloted lean premixed jet flame using finite-rate chemistry. *Combust. Theory Modeling*, 15(4):537–568, 2011.
- [181] Marie Cordier. Large eddy simulation of MILD combustion, application to free-jets and a lab-scale furnace. *Doctor in Engineering sciences and Technology, Université de Mons*, 2021.
- [182] Marco Ferrarotti, Andrea Bertolino, Ruggero Amaduzzi, and Alessandro Parente. On the influence of kinetic uncertainties on the accuracy of numerical modeling of an industrial flameless furnace fired with nh₃/h₂ blends: a numerical and experimental study. *Frontiers in Energy Research*, 8:597655, 2020.
- [183] Marco Ferrarotti, Zhiyi Li, and Alessandro Parente. On the role of mixing models in the simulation of MILD combustion using finite-rate chemistry combustion models. *Proceedings of the combustion institute*, 37(4):4531–4538, 2019.
- [184] Ruggero Amaduzzi, Giuseppe Ceriello, Marco Ferrarotti, Giancarlo Sorrentino, and Alessandro Parente. Evaluation of modeling approaches for mild combustion systems with internal recirculation. *Frontiers in Mechanical Engineering*, 6:20, 2020.
- [185] Ruggero Amaduzzi, Marco Ferrarotti, and Alessandro Parente. Strategies for hydrogen-enriched methane flameless combustion in a quasi-industrial furnace. *Frontiers in Energy Research*, 8:353, 2021.
- [186] P. Sagaut. *Large Eddy Simulation for Incompressible Flows: An Introduction*. Springer-Verlag, Berlin Heidelberg, 2nd edition, 2001.
- [187] M. Ihme, W. T. Chung, and A. A. Mishra. Combustion machine learning: Principles, progress and prospects. *Prog. Energy Combust. Sci.*, 91(101010), 2022.
- [188] Ryno Laubscher. *Utilization of artificial neural networks to resolve chemical kinetics in turbulent fine structures of an advanced CFD combustion model*. PhD thesis, Stellenbosch: Stellenbosch University, 2017.
- [189] Wen Yu Peng and Nicolas H Pinkowski. Efficient and accurate time-integration of combustion chemical kinetics using artificial neural networks. 2017.
- [190] Maziar Raissi, Paris Perdikaris, and George E Karniadakis. Physics-informed neural networks: A deep learning framework for solving forward and inverse problems involving nonlinear partial differential equations. *Journal of Computational physics*, 378:686–707, 2019.
- [191] Jared Willard, Xiaowei Jia, Shaoming Xu, Michael Steinbach, and Vipin Kumar. Integrating scientific knowledge with machine learning for engineering and environmental systems. *arXiv preprint arXiv:2003.04919*, 2020.
- [192] Ryno Laubscher and Pieter Rousseau. Application of mixed-variable physics-informed neural networks to solve normalised momentum and energy transport equations for 2d internal convective flow. *arXiv preprint arXiv:2105.10889*, 2021.

-
- [193] Gianmarco Aversano, Marco Ferrarotti, and Alessandro Parente. Digital twin of a combustion furnace operating in flameless conditions: reduced-order model development from CFD simulations. *Proceedings of the Combustion Institute*, 38(4):5373–5381, 2021.

Appendix: Flameless combustion of low calorific value gases, experiments and simulations with advanced radiative heat transfer modeling

Flameless combustion of low calorific value gases, experiments, and simulations with advanced radiative heat transfer modeling

Cite as: Phys. Fluids **34**, 045123 (2022); <https://doi.org/10.1063/5.0087077>

Submitted: 01 February 2022 • Accepted: 06 April 2022 • Published Online: 25 April 2022

 Phuc-Danh Nguyen,  Huu-Tri Nguyen,  Pascale Domingo, et al.



View Online



Export Citation



CrossMark

APL Machine Learning

Open, quality research for the networking communities

COMING SOON

LEARN MORE



Flameless combustion of low calorific value gases, experiments, and simulations with advanced radiative heat transfer modeling

Cite as: Phys. Fluids **34**, 045123 (2022); doi: 10.1063/5.0087077

Submitted: 1 February 2022 · Accepted: 6 April 2022 ·

Published Online: 25 April 2022



View Online



Export Citation



CrossMark

Phuc-Danh Nguyen,^{1,a)}  Huu-Tri Nguyen,^{1,2}  Pascale Domingo,²  Luc Vervisch,²  Gabriel Mosca,³  Moncef Gazdallah,⁴  Paul Lybaert,⁴  and Véronique Feldheim⁴ 

AFFILIATIONS

¹ArcelorMittal Global Research and Development, Maizières Process, Voie Romaine, BP 30320, 57283 Maizières-lès-Metz Cedex, France

²CORIA-CNRS, Normandie Université, INSA Rouen Normandie, 76801 Saint-Etienne-du-Rouvray, France

³BuildWind, Rue Bara 175, 1070 Brussels, Belgium

⁴Université de Mons, Service de Thermique et Combustion, Rue de l'Épargne 56, 7000 Mons, Belgium

Note: This paper is part of the special topic, Development and Validation of Models for Turbulent Reacting Flows.

^{a)} Author to whom correspondence should be addressed: phucdanh.nguyen@arcelormittal.com

ABSTRACT

Thermal radiation is the dominant mode of heat transfer in many combustion systems, and in typical flameless furnaces, it can represent up to 80% of the total heat transfer. Accurate modeling of radiative heat transfer is, thus, crucial in the design of these large-scale combustion systems. Thermal radiation impacts the thermochemistry, thereby the energy efficiency and the temperature sensitive species prediction, such as NO_x and soot. The requirement to accurately describe the spectral dependence of gaseous radiative properties of combustion products interacts with the modeling of finite rate chemistry effects and conjugates heat transfer and turbulence. Additionally, because of the multiple injection of fuels and/or oxidizers of various compositions, case-specific radiative properties' expressions are required. Along these lines, a comprehensive modeling to couple radiation and combustion in reacting flows is attempted and applied to the simulation of flameless combustion. Radiation is modeled using the spectral line-based weighted-sum-of-gray-gases approach to calculate gaseous radiative properties of combustion products using the correlation of the line-by-line spectra of H_2O and CO_2 . The emissivity weights and absorption coefficients were optimized for a range of optical thicknesses and temperatures encountered in the considered furnace. Efforts were also made on the development of a reliable and detailed experimental dataset for validation. Measurements are performed in a low calorific value syngas furnace operating under flameless combustion. This test rig features a thermal charge which can extract about 60% of combustion heat release via 80% of radiative heat transfer, making it of special interest for modeling validation. The comparison between the simulation and the experiment demonstrated a fair prediction of heat transfer, energy balance, temperature, and chemical species fields.

Published under an exclusive license by AIP Publishing. <https://doi.org/10.1063/5.0087077>

I. INTRODUCTION

With increasing energy cost, natural resources limitation of fossil fuels, and more stringent regulation on CO_2 and pollutant emissions, it is mandatory to look for alternative low-carbon fuels and to develop more energy efficient and cleaner combustion systems. Industrial auto-produced low calorific value (LCV) fuel gases constitute a promising alternative energy source combined with advanced combustion technologies. Diluted, flameless, or “MILD” combustion^{1–3} is one of the best candidates that fulfill the requirements in terms of improved combustion efficiency, low emissions of soot and NO_x , and fuel

flexibility. Such a flameless or MILD combustion mode is obtained by the dilution of reactants with combustion products before the reactants are mixed so that the reaction rates are slow, and the reaction occurs in a larger volume compared to a classical flame combustion. The success in the design of such advanced combustion applications relies heavily on accurate and efficient coupled combustion and radiation modeling, which also requires a reliable and detailed experimental database for validation. Today, multiple injection of fuels and/or oxidizers can feature in a single furnace to allow for flexible energy source utilization and for CO_2 mitigation, and this requires the development

of case-specific radiative properties modeling. Along this line, radiation modeling based on the spectral line-based weighted-sum-of-gray-gases (SLWSSG) approach^{4–8} was proposed to build a comprehensive multi-physics CFD model, which is applied to simulate a flameless combustion furnace. All of these are in the framework of RANS simulation.

The gaseous radiative properties of combustion products are calculated using the correlation of the line-by-line spectra of H₂O and CO₂.^{9–15} The emissivity weights and absorption coefficients were evaluated and optimized for a range of optical thicknesses and temperatures encountered in the furnace under consideration. An experimental database of flameless combustion of a LCV syngas on a lab-scale furnace was built specifically for the validation of the proposed comprehensive modeling methodology.

Experimental study of flameless combustion for high calorific value (HCV) gases, such as methane or hydrogen, can be found in the literature; jet-in-hot-coflow burners,¹⁶ Delft lab-scale furnace,¹⁷ or MILD combustion of methane/hydrogen mixtures¹⁸ can be cited as a few. There was often the absence of a strong heat sink to reproduce important radiative heat transfer as observed in large-scale combustion systems. It is also noticed that there was lack of discussion on experimental databases regarding LCV gases in the literature. Along these lines, a lab-scale furnace designed to stabilize flameless combustion of a LCV syngas is proposed in the present study, and the experimental database serves to validate the developed modeling. Main relevant features of flameless combustion as observed in the industrial context are mimicked: strong entrainment of burnt gases by the aerodynamics of high velocity reactant jets to promote highly diluted combustion, air preheated to very high temperature up to 1000 °C to reproduce air preheating with regenerative burner technology, and the presence of the strong heat sink (cooling tubes) to simulate important radiative heat transfer from combustion to thermal charge. Combustion of natural gas with air was first studied^{19–21} in the same test rig, and then the gas injector was redesigned to stabilize flameless combustion of a LCV syngas, a co-product gas produced in the steel industry.^{22,23} Flameless combustion was then characterized with detailed in-furnace measurements of temperatures and chemical species.

In the test rig of the present study, the thermal charge extracts about 60% of combustion heat release, 80% of which by radiative heat transfer, and 20% by convection. Radiative heat transfer is clearly the dominant mode of heat transfer as observed in large-scale combustion systems. This makes the test rig a special interest with detailed in-furnace measurements for validation of radiation and/or combustion models.

Many difficulties arise when dealing with radiation modeling: Highly spectral dependence of gaseous radiative properties, large CPU cost going with the solving of the radiative transfer equation (RTE), and consideration of finite rate chemistry for highly diluted combustion can be cited among others.^{24,25} In a recent review paper, Liu *et al.*²⁵ outlined the challenges associated with radiative transfer predictions in combustion applications and the different approaches that may be used with tradeoffs. The SLWSSG model has the advantages and the capability to extend to modeling large-scale industrial furnaces, featuring multi-injection of low-carbon fuels and/or oxidizers in different zones for decarbonization. Because of various compositions and conditions, case-specific radiative properties' expressions are required. The SLWSSG model appears to be the best choice, and most adapted for that purpose while keeping a compromise between

accuracy and CPU cost. If we focus on the radiation aspect, it is noted that efforts were spent mainly on the modeling of gaseous radiative properties for HCV gases such as natural gas, and there is a lack of discussion on radiation modeling of LCV gases.

Radiation modeling based on the spectral line-based weighted-sum-of-gray-gases (SLWSSG) approach^{4,5,8} is proposed to calculate radiative properties of combustion products of different fuel gases with application to the combustion of a LCV syngas. The parameters in the SLWSSG model are obtained from the correlation of the line-by-line spectra of H₂O and CO₂.^{9–15} In fact, together with the absorption distribution function (ADF)²⁶ and statistical narrow band full spectrum correlated K (SNB-FSCK)²⁷ models, the SLWSSG model belongs to the non-gray global model family, which has a special interest for complex combustion system simulations for two reasons: First, it is more accurate than the simple gray gas model, and second, it is more computationally efficient than the statistical narrow band correlated K (SNB-CK) model.²⁸ The SLWSSG approach is also straightforward to incorporate into the widely used discrete ordinate method (DOM)²⁹ to discretize the radiative transfer equation (RTE), thus ensuring a good compromise between solution accuracy over a wide range of optical thicknesses and computational cost.³⁰ Three gray gases were considered in the study to mitigate the CPU time.^{31,32} The emissivity weights and absorption coefficients of the syngas combustion products were evaluated and optimized over a range of optical thicknesses and temperatures encountered in the considered test rig. The radiative properties were integrated into the Ansys Fluent® flow solver³³ using user defined functions for a full coupling of combustion and radiation.

Section II describes briefly the experimental setup and numerical modeling approach. The results will be presented in Sec. III. Finally, some concluding remarks will be formulated in the conclusion.

II. EXPERIMENTATION AND NUMERICAL MODELING

A. Experimental setup and measurement

Figure 1 shows a picture of the flameless combustion furnace^{19–23} with its schematic and dimensions of the burner section. The combustion chamber is made of stainless steel and equipped with a fibrous ceramic heat insulation layer. It has a square inner section of 0.35 × 0.35 m² with 1.0 m high. One air injection with 24.8 mm exit diameter is located in the center. Two gas injectors with 11° tilt angle are symmetrically located around the air injector. The diameter of the fuel gas injector was designed to stabilize flameless combustion. The air was preheated up to 800 °C by an electrical preheater. The fuel gas compositions are realized using a mixing unit equipped with mass flow meters and controllers fed through pure gas bottles. The thermal charge and the furnace temperature are controlled through four water cooling tubes (heat sink), and the immersion of which can be regulated from 0 to 90 cm and a reduced water circuit along the outer walls. Each vertical wall of the combustion chamber has a removable part. A wall [on the rear side of Fig. 1(a)] is equipped with a quartz window to allow for optical access and image recording. A LaVision intensified camera with an UV filter centered at 329 nm is used to take images of chemiluminescent self-emission of OH* radicals at 308 nm wavelength.³⁴ OH* imaging allowed for determining the position of main reaction zones. A sidewall [on the right of Fig. 1(a)] is equipped with eight S-type thermocouples, 0.09 m separated each other and mounted flush with the insulation layer in order to get a wall temperature profile

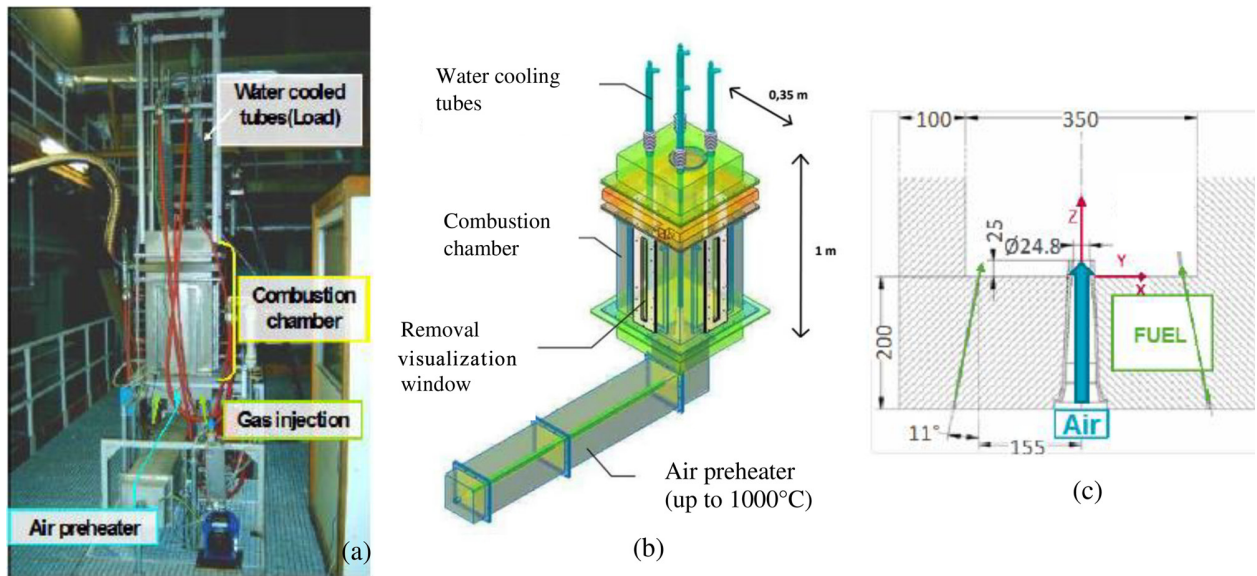


FIG. 1. (a) Picture of the flameless combustion furnace, (b) its schematic representation, and (c) the dimensions in mm of the burner section.

along the furnace height in the vertical symmetry plane containing the air and gas injectors. The measurements of the temperature and species concentration at the furnace exit and inside the furnace were realized by the two home-made probes, which are inserted inside the furnace through 14 holes on the wall opposite to the thermocouples wall. The suction pyrometer probe is equipped with a S-type thermocouple and works with a Venturi's tube connected to an air compressed circuit. The gas sampling probe is equipped with a vacuum pump to extract burnt gases with a flow rate equal to 210 NI/h. Water is removed, and the dry sample is sent in parallel to the chromatograph and gas analyzers. The concentrations of O_2 , CH_4 , CO_2 , and CO (on dry basis) were measured by the paramagnetic and infrared gas analyzers. Measurement of H_2 and N_2 and another measurement of O_2 , CH_4 , and CO were realized by the gas chromatograph. More details regarding the experimental procedure and measurements can be found in our previous works.^{19–23} The studied syngas composition is (by volume): 32.5% H_2 , 14.25% CH_4 , 13.25% CO , 12% CO_2 , and 28% N_2 . A flameless combustion regime was established at 30 kW of fuel power.

B. Numerical modeling and simulation

In the concept of the weighted-sum-of-gray-gases (WSGG) model, the non-gray gas is replaced by an equivalent number of gray gases with different absorption coefficients and emissivity,³⁵ for which the heat transfer rates are calculated independently. The total heat flux is then calculated by adding the heat fluxes of each gray gas. The WSGG concept was extended to consider spectral lines information called the spectral line-based weighted-sum-of-gray-gases (SLWSGG) model.^{4,5,8} The SLWSGG model is applied in its very fine integration form. However, it should be noted that Webb *et al.*³⁶ and Badger *et al.*²⁴ proposed the most recent implementation of the model named the rank correlated SLW model, which can produce accurate results

with as few as three gray gases requiring no optimization. The detailed theoretical background of such models can be found in the book of Modest.²⁷ Only a brief description of the concept is given. The radiative transfer equation (RTE) to be solved is

$$\frac{dI_i}{ds} = k_i p_a (a_i I_b - I_i), \tag{1}$$

where I_i (W/m) is the radiation intensity along the direction s of the i th gray gas, I_b (W/m) is the blackbody radiation intensity, k_i ($m^{-1} atm^{-1}$) is the pressure-based absorption coefficient of the i th gray gas, p_a (atm) is the sum of the partial pressures of the absorbing species, and a_i is the emissivity weighting factor of the i th gray gas with temperature dependence. The RTE is solved for each gray gas $i = 1, 2, \dots, N$ (N is the total number of gray gas) with the boundary condition given by

$$s = 0 : I_i = \varepsilon_w a_i I_b(T_w) + \frac{1 - \varepsilon_w}{2\pi} \int_{\bar{s} \cdot \bar{n} < 0} I_i d\omega \tag{2}$$

(ε_w and T_w are the wall emissivity and wall temperature, respectively) using the discrete ordinate method (DOM).²⁹ The emissivity weighting factors and absorption coefficients are evaluated and optimized over a range of optical thicknesses and temperatures encountered in the considered domain. Total emissivity is calculated from the contribution of all gray gas emissivities as such

$$\varepsilon(T, L, p_a) = \sum_{i=0}^N a_i (1 - e^{-k_i p_a L}), \tag{3}$$

where T (K) is the gas temperature and L (m) is the optical thickness. Each gray gas is characterized by an emissivity weighting factor and an absorption coefficient, which can be described by temperature dependent polynomials of $J - 1$ degree written in the form of

$$a_i = \sum_{j=1}^J \alpha_{i,j} T^{j-1}, \quad (4)$$

$$k_i = \sum_{j=1}^J \beta_{i,j} T^{j-1}, \quad (5)$$

where $\alpha_{i,j}$ and $\beta_{i,j}$ denote the polynomial coefficients for the emissivity weighting factor and the absorption coefficient, respectively. For transparent regions of the spectrum (clear gas $i = 0$), the absorption coefficient is set to zero ($k_0 = 0$) in order to account for windows in the spectrum between spectral regions of high absorptions, and the clear gas emissivity weighting factor is $a_0 = 1 - \sum_{i=1}^N a_i$.

The polynomial coefficients $\alpha_{i,j}$ and $\beta_{i,j}$ of Eqs. (4) and (5) are determined and optimized following the steps:

- (i) For a given molar fraction of H₂O and CO₂, a range of optical thicknesses encountered in the considered domain and a fixed temperature T, the SLWSSG model with 30 gray gases is used to calculate the “true” emissivity curves $\varepsilon(T, p, L)$. In the SLWSSG model, the absorption distribution function is computed using the correlations proposed by Modest and Mehta¹⁴ and Modest and Singh¹⁵ for the cumulative full-spectrum k -distribution functions of H₂O and CO₂. The true emissivity weighting factor a_i is calculated by the difference of the absorption line blackbody distribution function F evaluated at the two bounds ($i, i - 1$) of the gray gas interval

$$a_i = F(C_{abs,i}, T_g, T_b, X_s, P) - F(C_{abs,i-1}, T_g, T_b, X_s, P), \quad (6)$$

$$F(C_{abs,i}, T_g, T_b, X_s, P) = \frac{\pi}{\sigma T_g^4} \sum_{m=0}^{\infty} \int_{\eta_m}^{\eta_{m+1}=\eta_m+\Delta\eta} g_m(C_{abs,i}, \eta, T_g, X_s, P) I_{b,\eta}(T_b, \eta) d\eta, \quad (7)$$

where $C_{abs,i}$, T_g , T_b , X_s , P , and η are the absorption cross-sectional area (m²/mole), the gas temperature (K), the black body temperature (K), the species mole fraction, the absolute pressure (bar), and the wave number (m⁻¹), respectively. The absorption coefficient k_i is related with the absorption cross-sectional area by $k_i = C_{abs,i} N_{mole}$ with N_{mole} being the mole density. The cumulative full-spectrum k -distribution functions g_m for H₂O and CO₂ using spectral correlations proposed by Modest and Mehta¹⁴ and Modest and Singh¹⁵ are given by

$$g_m = \frac{1}{2} \tanh [P_m(T_g, T_b, X_s, P; k)] + \frac{1}{2}, \quad (8)$$

where

$$P_m = \sum_{l=0}^3 \sum_{m=0}^3 \sum_{n=0}^3 a_{lmn} \left[\frac{T_g}{1000} \right]^n \left[\frac{T_b}{1000} \right]^m [\log_{10} k]^l. \quad (9)$$

The correlation forms are similar for H₂O and CO₂, but the coefficients for the full-spectrum k -distribution a_{lmn} of H₂O and CO₂ are different and given in the studies of Modest and Mehta¹⁴ and Modest and Singh.¹⁵

- (ii) A least square method is used to calculate the absorption a_i and weight k_i coefficients for a fixed gray gas number N ($N = 3$ in our case), which best fit the “true” emissivity curve.

- (iii) Steps (i) and (ii) are repeated for a set of M temperature points ranging from 300 to 1700 K as encountered in the considered domain.
- (iv) The profiles of absorption and weight coefficients vs temperature obtained are used to calculate the polynomial coefficients.

Equations (4) and (5) were integrated into the Ansys Fluent flow solver³³ using user defined functions. The absorption coefficient and the emissivity weighting factor are updated before each solving of the RTE. The parameters of the model are obtained from the correlation of the line-by-line spectra of H₂O and CO₂.⁹⁻¹⁵ The extension of the model to situations featuring multiple injection of fuels and/or oxidizers is straightforward. The number of gray gases $N = 3$ or 4 was found to be adequate for good quality of emissivity fittings, and further increase in the gray gases number did not lead to consistent improvement in accuracy.^{31,32} Three gray gases were then considered in the study to keep CPU time and memory requirements acceptable. The DOM method²⁹ was used for angular discretization of RTE with nine solid angles per octant (3×3). DOM was chosen, because it is sufficiently accurate and applicable across a wide range of optical thicknesses, which is not well known in flameless combustion.³⁷

The CFD solution is obtained numerically by solving RANS equations in steady state. The choice of the $k - \varepsilon$ RNG turbulence model³⁸ for this study is recommended from the study on the same furnace of Lupant,^{20,21} who carried out a deep analysis of the effect of different turbulence models (of the two families $k - \varepsilon$ and $k - \omega$) considering the species distribution in a non-reacting mixture, to validate the turbulence model independently from the combustion model. The $k - \varepsilon$ RNG model developed for strained flows is found appropriate to predict the turbulent flowfield in the flameless combustion characterized by intense recirculation. The turbulence-chemistry interaction was modeled using the eddy-dissipation concept (EDC)^{39,40} to consider finite chemistry effects. The chemical kinetics scheme KEE58⁴¹ including 18 species and 58 elementary reversible reactions was used. A transport equation for each of these chemical species is solved except for nitrogen. The EDC model was used in its standard form even though some improvement for temperature prediction can be obtained by modifying or calculating directly volume fraction and residence time constants of species in fine structures based on local flow characteristics.⁴²⁻⁴⁵ However, in the recent study of Silei *et al.*⁴⁶ for the MILD combustion system, which is similar to that in the present study in the sense that the MILD condition is obtained by burner design to promote internal flue gas recirculation, the standard EDC model (with the KEE58 chemical scheme) provided satisfied prediction while the EDC models with modified or locally calculated model constants did not show effective improvement. The flameless condition in the current study is different from that of jet-in-hot-coflow flames for which EDC constant modifications were proposed.⁴²⁻⁴⁴

The *in situ* adaptive tabulation (ISAT)⁴⁷ was used to accelerate the chemistry integration. The KEE58 scheme was validated for MILD combustion for various mixtures of H₂ and CH₄.^{43,48,49} In Ref. 48, the KEE58 mechanism gave very similar results as compared to the GRI-3.0 detailed mechanism⁵⁰ in terms of mean temperature prediction, and the error is less than 5% in comparison with experiment. Prediction of NO formation in MILD combustion of CH₄-H₂ mixtures reasonably matched experimental values when post-processed from thermo-chemical field obtained with KEE58.⁴⁹ Also in Ref. 43,

KEE58 showed more reliable predictions than other schemes such as DRM-19 and DRM-22⁵¹ in terms of temperature and species concentrations for MILD combustion of CH₄-H₂ mixtures. In the recent studies of Silei *et al.*⁴⁶ and Ferrarotti *et al.*⁵² for the MILD and flameless combustion systems, which are similar to that in the present study, i.e., MILD or flameless conditions are obtained by burner designs to create internal flow recirculation, the KEE58 scheme provided satisfied predictions. It is also to notice that MILD combustion was studied in the framework of RANS modeling using EDC^{42-45,48,49} or FGM (flamelet generated manifold)⁵³ to account for turbulence chemistry interaction.

The computational domain corresponds to the whole gas volume inside the furnace. The grid was made unstructured with nearly 6×10^6 hexahedral cells considering the grid independence study carried out in the same furnace operating on natural gas for a quarter of the domain thanks to symmetry.^{20,21} The results showed that when the grid size increased from 640 thousand hexahedral cells to 1.3×10^6 hexahedral cells (equivalently 2.56×10^6 hexahedral cells to 5.2×10^6 hexahedral cells for the full domain in the present study), no more sensibility to grid size was observed for temperature and chemical species. $y^+ = 1$ on the walls of the air and gas injections while on the furnace walls y^+ is mainly around 15 and does not exceed 30. The resolution in the shear layer is $h = 7 \mu\text{m}$. The boundary conditions were calibrated using the experimental measurements. Temperature, gas composition, and mass flow rates are fixed at inlets. For the other walls, the

total heat loss (p_{loss}) from experimental heat balance is considered uniformly distributed on the walls with total surface (s_{wall}) and used to deduce a global heat transfer coefficient (k) between the inner wall temperature (T_{inn}) (average measured value) and the external environment temperature (T_{ext}). The expression for k is

$$k = \frac{P_{loss}}{s_{wall} (T_{inn} - T_{ext})}. \quad (10)$$

III. RESULTS OF NUMERICAL MODELING AND COMPARISON AGAINST THE MEASUREMENTS

A. Radiative properties SLWGG modeling

The total emissivity was calculated and compared to the Hottel and Sarofim's database³⁵ as well as with the results obtained with Soufiani and Djavdan⁵⁴ and Smith *et al.*⁵⁵ methods for the available nearest configurations in terms of water vapor and carbon dioxide partial pressures. The SLWGG used the correlation of the line-by-line spectra of H₂O and CO₂,⁹⁻¹⁵ and the emissivity was evaluated and optimized over a range of optical thicknesses and temperatures encountered in the furnace. Figure 2 shows the emissivity of burnt gases issued from the stoichiometric combustion between the air and the studied syngas as well as the two other gases named COG (28.5%CH₄, 62%H₂, 6%CO, 1.5%CO₂, and 2%N₂ by volume), a HCV gas, and BFG (3%H₂, 20.5%CO, 22.5%CO₂, and 54%N₂ by volume), a

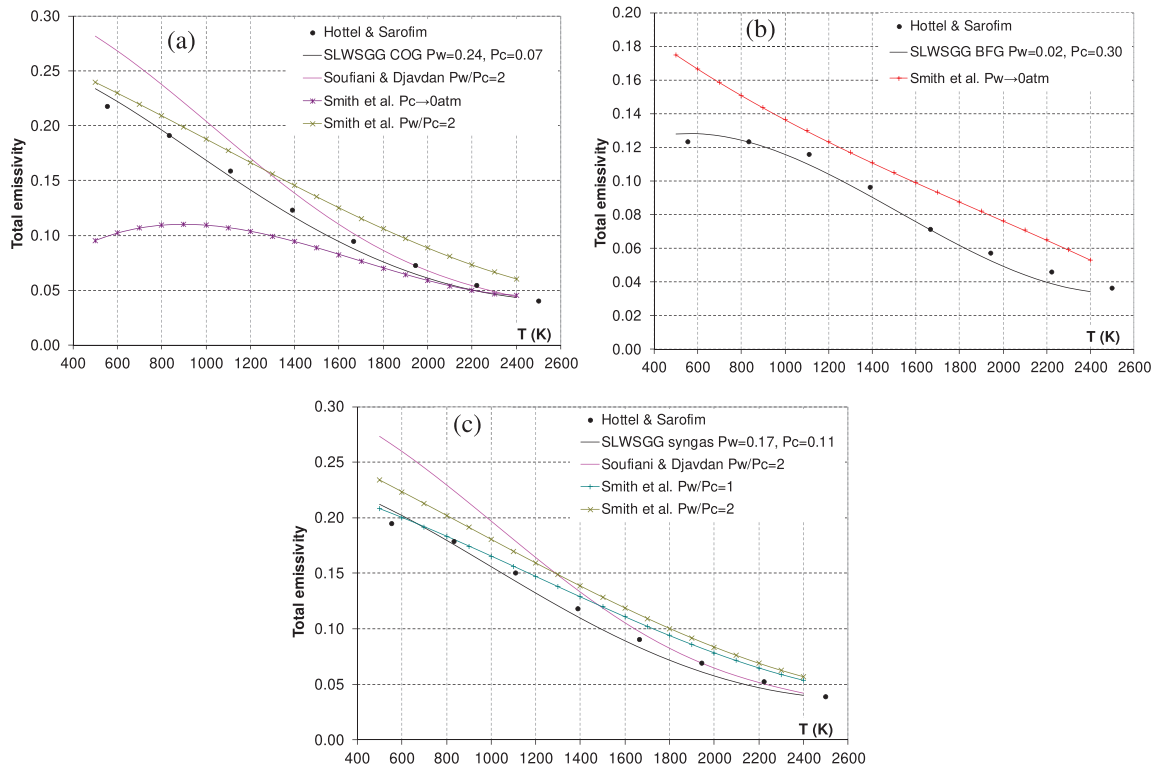


FIG. 2. Comparison of total emissivity calculated from different models for HCV COG (a), LCV BFG (b), and syngas (c). P_w and P_c are partial pressures of water vapor and carbon dioxide, respectively.

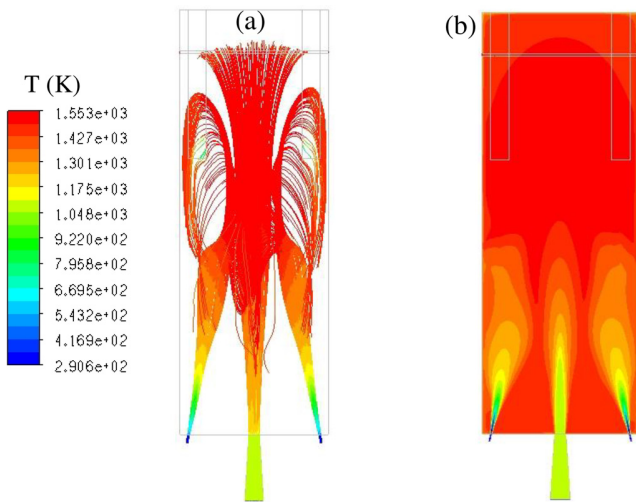


FIG. 3. (a) Pathlines of reactants jets colored by temperature. (b) Temperature contour obtained by CFD in the symmetrical plane.

LCV gas. The studied syngas is indeed composed of 50% of COG and 50% of BFG by volume.

The results shown in Fig. 2 were obtained using the averaged optical length of the studied geometry for all models and Hottel and Sarofim’s database. The SLWSSG model results were obtained using three gray gases, and the same number of gray gases was used in the CFD simulations. Regarding the HCV case, as shown in Fig. 2(a), the SLWSSG model is closer to Hottel and Sarofim’s database than the method of Soufiani and Djavdan⁵⁴ and Smith *et al.*,⁵⁵ the configuration $P_c \rightarrow 0$ atm of Smith *et al.*⁵⁵ showed an important departure from the Hottel and Sarofim’s database. For the LCV case [Fig. 2(b)], the SLWSSG model agrees with Hottel and Sarofim’s database while the total emissivity obtained with the $P_w \rightarrow 0$ atm configuration of

Smith *et al.*⁵⁵ shows a departure from the Hottel and Sarofim’s database. Finally concerning the syngas case [Fig. 2(c)], the SLWSSG also showed better performance. This confirms that the development of case-specific radiative properties’ modeling is required to secure accurate prediction of radiative heat transfer particularly in combustion systems featuring multiple injection of HCV and LCV fuels for optimized energy sources utilization.

B. Characterization of flameless combustion

Flameless or MILD combustion is characterized by dilution of reactants with low enthalpy combustion products before the mixing between the reactants themselves so that the reaction rates are slow, and the reaction zone spreads over a much larger volume compared to a classical flame combustion. The dilution is obtained by a high flow recirculation induced by the aerodynamics of the high velocity reactants jets as shown by the pathlines of the reactants jets in Fig. 3(a). Figure 3(b) shows the temperature distribution obtained by simulation in the symmetrical plane. It is observed that the temperature distribution is quite homogeneous in the combustion zone with no local hot spots, confirming the flameless mode. The two lateral syngas jets emerge into the combustion chamber with a high velocity of nearly 100 m/s entraining the burnt gases and creating two important recirculation zones. In this condition, the air and fuel gas are highly diluted by the burnt gases.

Figure 4(a) presents the theoretical trajectory of the fuel jet, which is calculated based on the strong jet/weak jet (SJWJ) interaction theory developed by Grandmaison *et al.*⁵⁶ (only the left part of the furnace is presented for the sake of brevity). The line representing the air jet opening was also plotted in the same figure. The ordinate z of the SJWJ theory fuel trajectory is given by

$$z = \xi d_{12}, \tag{11}$$

$$\xi = - \int_1^\eta f^{-1} \cos \theta d\eta, \tag{12}$$

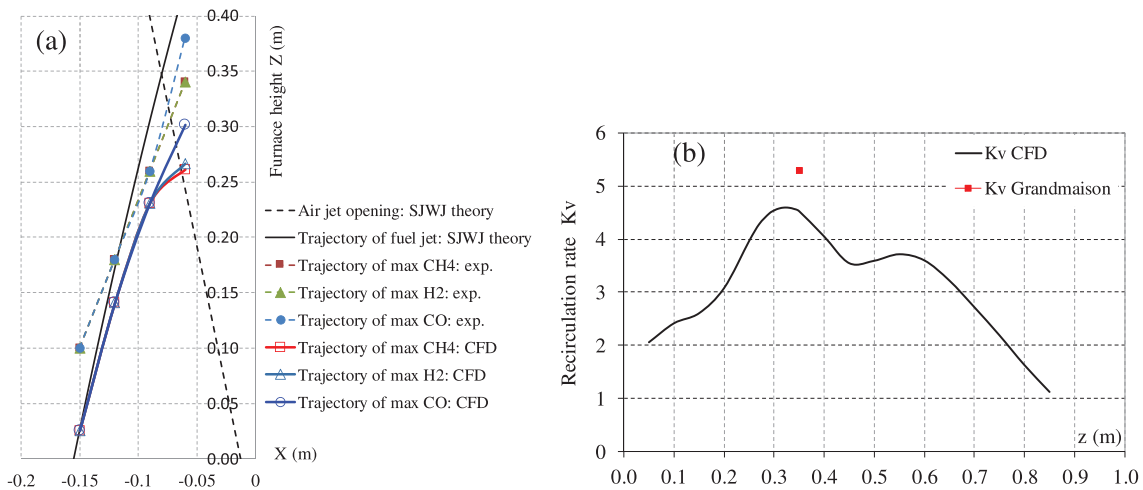


FIG. 4. (a) Trajectories of reactants jets: strong jet/weak jet (SJWJ) theory, experiment and CFD results. (b) Evolution of the recirculation rate along the furnace height z obtained from numerical simulation (black line), $K_v = 5.3$ calculated from the SJWJ theory (red symbol).

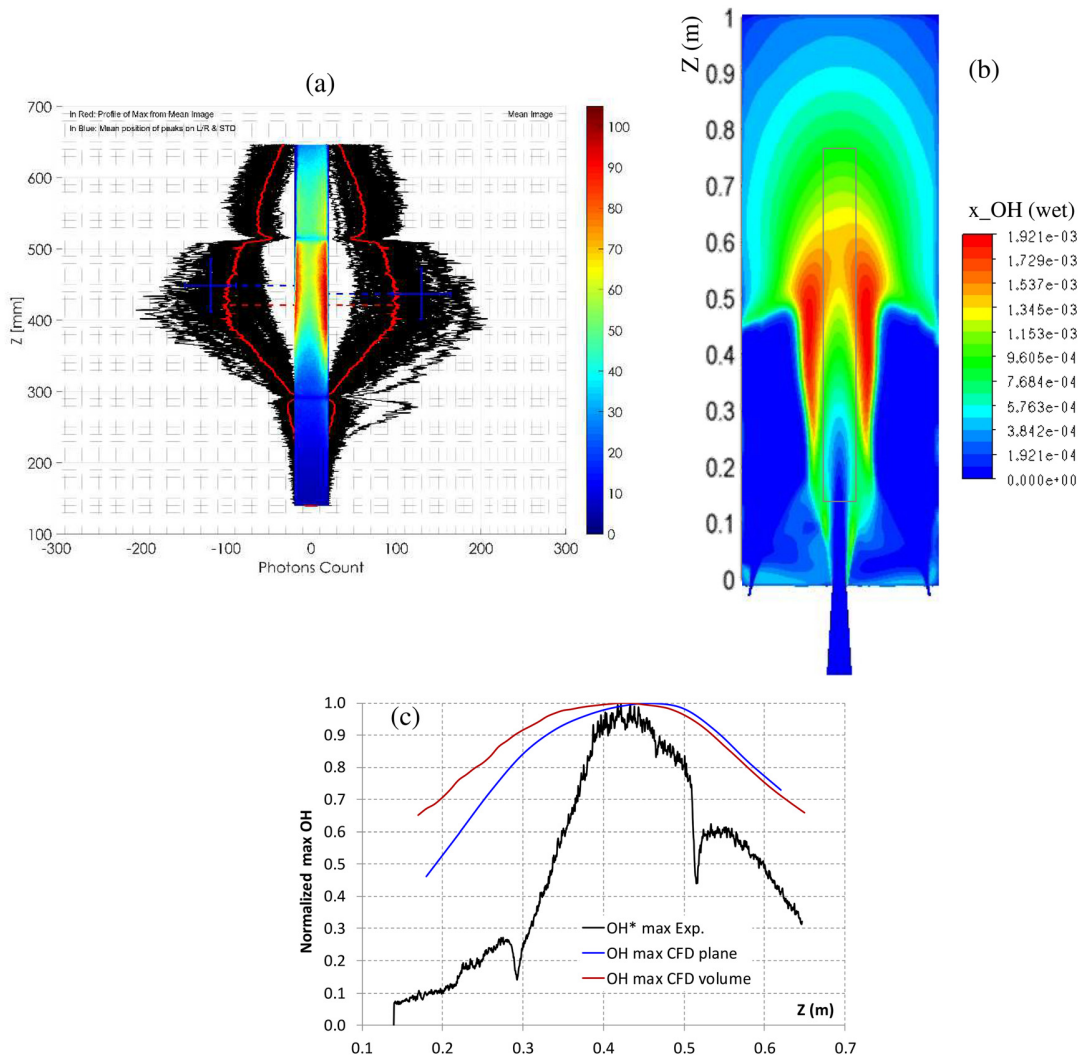


FIG. 5. (a) Experimental OH* radical chemiluminescence imaging. (b) OH mole fraction from CFD in the symmetrical plane. (c) Normalized maximum OH profiles; Exp.: considering the maximum of the averaged image of OH* photons count at each Z (black line). CFD: The maximum of (wet basis) OH mole fraction of each horizontal line (blue line) and each horizontal plane (red line) at each Z.

TABLE I. Energy balance and measurements at the furnace exit.

	Input (kW) Fuel power	Output (kW)			Measurements at the furnace exit		
		Charge	Flue gas loss	Wall loss	Temperature (K)	CO ₂ (vol. %-dry basis)	O ₂ (vol. %-dry basis)
Experiment	30	17.16	8.96	3.88	1386	13.98	2.12
Simulation	30	16.97	8.98	4.05	1393	13.57	2.17

$$f = \sqrt{\left[1 - \frac{C_e^2 \ln(\eta)}{16 \sqrt{\psi}}\right]^4 - \cos^2 \theta}, \quad (13)$$

where ζ and η are the relative coordinates such as $\zeta = z/d_{12}$ and $\eta = x/d_{12}$, respectively, d_{12} is the distance between the jets, C_e is the constant equal to 0.32, θ is the angle created by the injection axis of two jets, ψ is the ratio of impulse between two jets (impulse is the

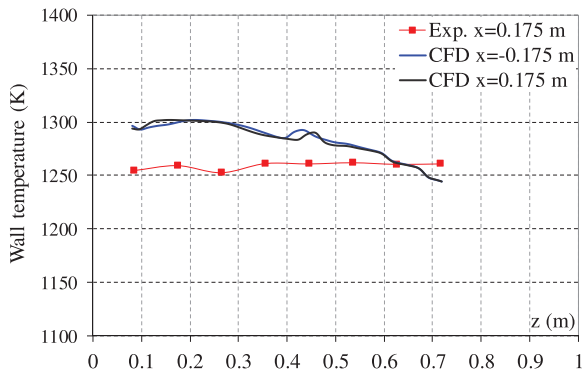


FIG. 6. Profiles of wall temperature along the furnace height obtained from experiment and simulation (CFD).

product of mass flow rate and bulk velocity), and x and z are the abscissa and ordinate as indicated in Fig. 1(c), respectively.

The evolution of maximum concentration of the three reactive species CH_4 , H_2 , and CO along the height in the symmetrical plane is displayed to visualize the fuel jet trajectories obtained experimentally and numerically. It is seen that, in experiment or in the simulation, the

trajectories of max CH_4 , H_2 , and CO nearly collapse into each other, and the experimental and CFD fuel trajectories fairly follow the theoretical fuel trajectory until $z = 0.25$ m, after which they are bended toward the furnace axis. The intersection between the air jet opening and the fuel trajectories is called the confluence point, which is evaluated at $z = 0.35$ m for the SJWJ theory, which is considered as an upper limit, at $z = 0.3$ m for the experiment and between 0.25 and 0.3 m in the simulation.

The recirculated burnt gases flow rate is calculated from the simulation by determining, at each location z , the area portion for which the vertical velocity is negative. The recirculation rate, K_v , is then defined as the ratio between the recirculated burnt gases flow rate and the total inlet flow rate. The result of K_v is presented in Fig. 4(b). It is observed that K_v reaches the maximum value of 4.6 at $z = 0.32$ m slightly after the confluence point estimated at between $z = 0.25$ and 0.3 m. The value of K_v above four together with the furnace temperature above 1100 K (as be shown in the next section) fully satisfies the flameless combustion condition as expressed by Wünnig and Wünnig.¹ The recirculation rate can also be estimated using the Grandmaison’s SJWJ theory⁵⁶

$$K_v^{SJWJ} = \frac{t_{air,\xi} q_{air} + t_{fuel,\xi} q_{fuel}}{q_{air} + q_{fuel}}, \quad (14)$$

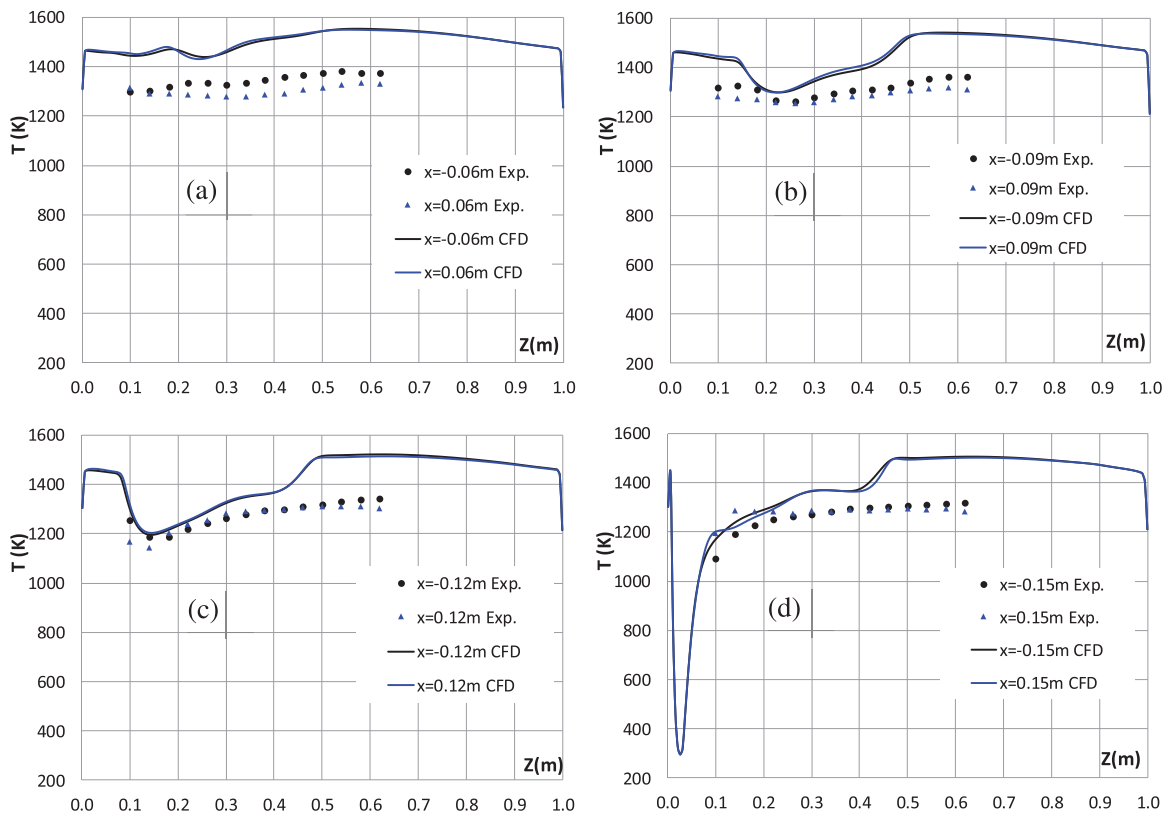


FIG. 7. Comparison between the experimental and computed profiles of temperature obtained at different (negative and positive) x positions and along the furnace height z . (a) $x = \pm 0.06$ m, (b) $x = \pm 0.09$ m, (c) $x = \pm 0.12$ m, and (d) $x = \pm 0.15$ m. Maximum measurement uncertainty is 7.6 K.

where q is the mass flow rate, $t_{air,\xi}$ and $t_{fuel,\xi}$ are the rates of entrainment of burnt gases by the air and fuel jets, respectively, which are calculated as follows:

$$t_{air,\xi} = C_e \frac{d_{12}}{d_{air,s}} \xi - 1, \quad (15)$$

$$t_{fuel,\xi} = \frac{C_e}{\cos \theta} \frac{d_{12}}{d_{fuel,s}} \int_0^\xi \left(1 - \frac{C_e^2 \ln(\eta)}{16 \sqrt{\psi}} \right)^3 d\xi - 1, \quad (16)$$

where $d_{air,s}$ and $d_{fuel,s}$ are the effective diameters of the air and fuel jets in the exit section, respectively, which are given by $d\sqrt{\rho_0/\rho_\infty}$ (ρ_0, ρ_∞ are the densities of the jet in the exit section and of the surrounding fluid, respectively). The result of $K_v^{S/WJ} = 5.3$ at $z = 0.35$ m is also reported in Fig. 4(b). The interest of the SJWJ theory is to obtain a quick estimation of the recirculation rate at the confluence point by considering only flowrates of reactants and burner geometry. This can be used to give first burner sizing for new design or modification of existing design.

The reaction zone is experimentally visualized by OH* chemiluminescence imaging. OH* represents a good indicator of the reaction zone, and its emission is at 308 nm in UV,³⁴ a spectral region where the contribution of wall emission is negligible. Fifty instantaneous OH* images were recorded by the intensified camera (OH* images integrated over the depth of the furnace) and processed to get an average. Figure 5 shows the experimental result of OH* imaging, the contour of OH mole fraction obtained from the simulation, and the

normalized maximum OH profiles obtained from both experiment and simulation. The contour of OH* [expressed in photons count, Fig. 5(a)] is the averaged image, the solid red profile was extracted from the maximum photons count on each horizontal line of the averaged image, and the maximum location is marked by the dashed red line. The black profiles were extracted from the maximum photons count on each horizontal line of the instantaneous image, and the blue crosses represent maximum photons count and its location with the corresponding standard deviations. The main reaction zones fluctuate with their peak locations varying from 0.40 to 0.49 m.

The frame in Fig. 5(b) corresponds to the optical window dimension, i.e., the frame of the contour of OH* photons count in Fig. 5(a). It is observed that the shape of the reaction zone is well captured by the simulation with one reaction zone stabilized on each side of the furnace axis. Figure 5(c) shows the experimental OH* peak at the location of $z = 0.42$ m. The simulation predicted the location of the maximum OH mole fraction at $z = 0.46$ m considering the OH distribution in the vertical symmetrical plane (CFD plane) and at $z = 0.43$ m when the distribution of OH in the whole volume is considered (CFD volume). It can be said that, by considering whole volume as it is the case with experimental OH* chemiluminescence, the simulation shows a good prediction of the location of the OH peak; the form and the location of the reaction zone are well recovered.

Table I compares the energy terms and the measurements at the furnace exit between the experiment and the simulation. It is noticed that the air preheating power was subtracted from the flue gas loss in

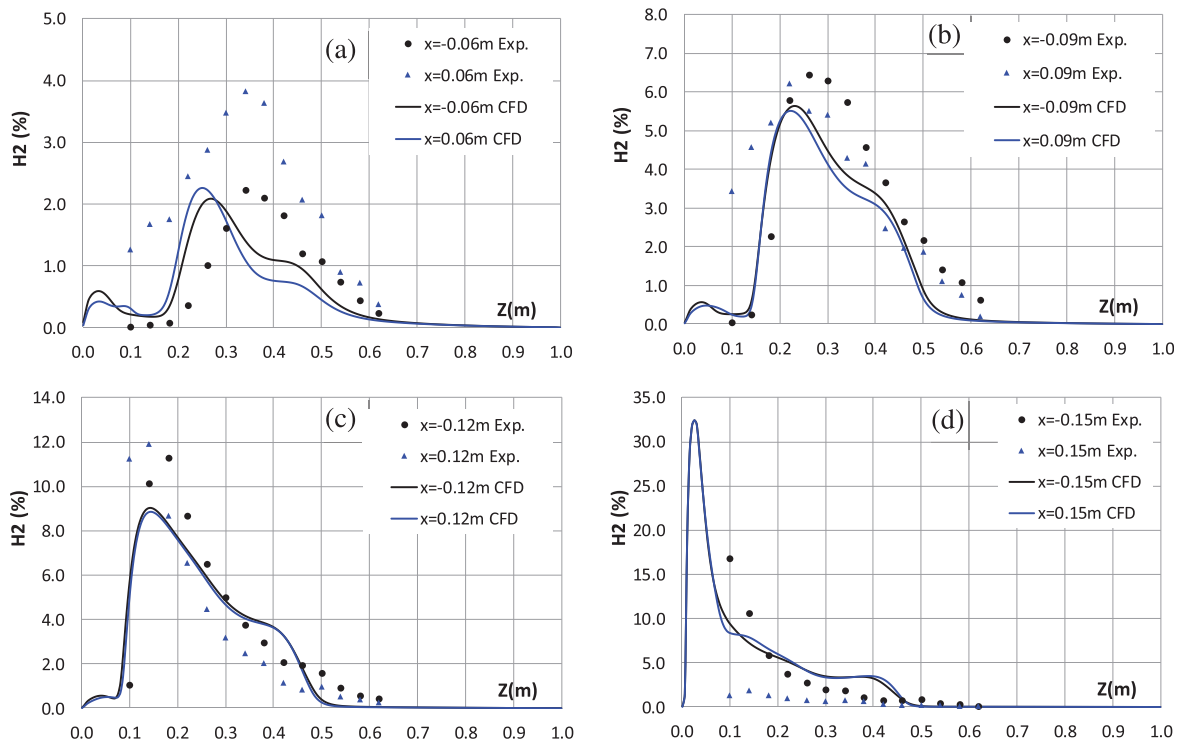


FIG. 8. Comparison between the experimental and computed profiles of H₂ in volume percentage on dry basis, obtained at different (negative and positive) x positions and along the furnace height z. (a) x = ±0.06 m, (b) x = ±0.09 m, (c) x = ±0.12 m, and (d) x = ±0.15 m. Maximum measurement uncertainty is 0.72%.

order to consider the fuel power as a single input. (This would be the case if the air were preheated by the flue gases as in an industrial regenerative burner.) The numerical simulation is able to reproduce the different terms measured experimentally, confirming the closure of the energy balance. 57% of the power input is transferred to the thermal charge and 80% of which is transferred by radiation and 20% by convection. This result confirms that the modeling of radiative properties based on the SLWSSG approach is able to predict correctly the heat transfer dominated by the radiation. Table I also shows the comparison for temperature and CO_2 and O_2 contents at the furnace exit between the experiment and the simulation with good agreement, validating the mass balance.

C. Comparison of numerical results with in-furnace measurements

Figure 6 compares the evolution of the vertical furnace wall temperature obtained from the experimental measurement and the simulation at the level of the symmetrical plane. The simulation provides an acceptable prediction; in average, the numerical result overpredicts only by 25 K the experimental value. It is also noted that the furnace wall temperature is always higher than 1250 K, a temperature value above which flameless combustion occurs. The variation of the wall temperature does not exceed 60 K in the experiment and in the

simulation, confirming relatively good homogenization of temperature observed in the combustion chamber.

Figure 7 shows the comparison for the temperature between the measurement and the simulation results. Both the experimental and numerical results show rather flat temperature profiles; this is a characteristic of flameless combustion in which the temperature field is quasi-homogeneous and distributed largely in the whole volume, and local hot spots related to flames were not observed. The simulation overpredicts the experimental profiles by about 9%–14%. It is observed, at the locations of $x = \pm 0.12$ and ± 0.15 m, that the measured temperature decreases in the vicinity of the fuel jet, and this trend is well recovered by the simulation. The over-prediction of the temperature in highly diluted zones, where local extinctions and high fluctuations occur at $x = \pm 0.06$ m, may be attributed to the EDC turbulence chemistry interaction modeling. Christo and Dally³⁷ also found the same trend for the simulation of the most diluted case, the lowest 3% oxygen level in a hot co-flow, using EDC with the detailed chemistry GRI-3.0.⁵⁰ Discussions to improve temperature prediction by modifying or calculating directly volume fraction and residence time constants of species in fine structures based on local flow characteristics can be found in Refs. 42–45. This is beyond the scope of this work, which focuses on the implementation of the radiative properties model. Overall, the results obtained confirm that the integration of the radiative properties' SLWSSG model into the simulation provides a

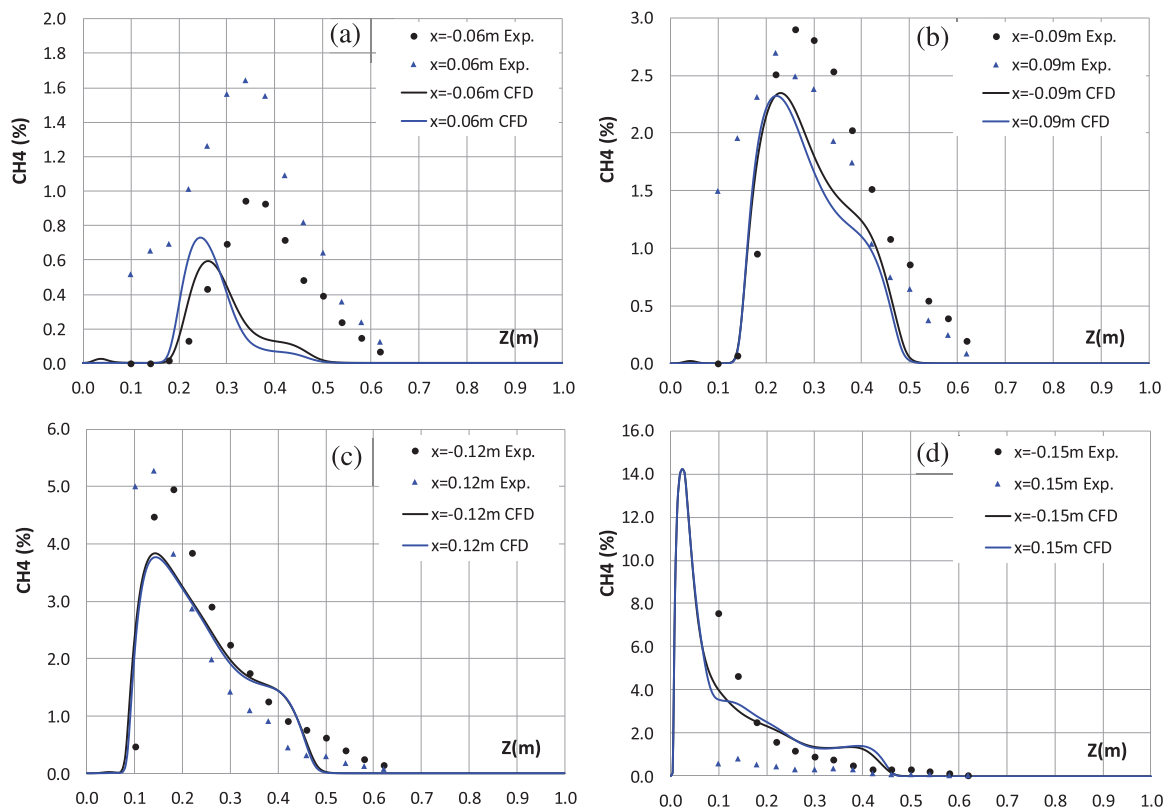


FIG. 9. Comparison between the experimental and computed profiles of CH_4 in volume percentage on dry basis, obtained at different (negative and positive) x positions and along the furnace height z . (a) $x = \pm 0.06$ m, (b) $x = \pm 0.09$ m, (c) $x = \pm 0.12$ m, and (d) $x = \pm 0.15$ m. Maximum measurement uncertainty is 0.27%.

reasonable prediction of the temperature level and trend in the context of flameless combustion simulation.

Figures 8–10 show the comparison between the measurement and the simulation results for three reactive species present in the fuel, namely, H_2 , CH_4 , and CO . The peak in each profile corresponds to the fuel jet, and these peaks are decreasing due to the mixing with the recirculated burnt gases and the air when moving farther from the fuel injector located at $x = \pm 0.155$ m. The measured species profiles at the location of $x = \pm 0.15$ m indicate a significant asymmetry of the fuel jet while the numerical results show rather symmetrical profiles for all locations. The computed species profiles at $x = \pm 0.15$ m agree only with the measured species profile at $x = -0.15$ m. As indicated by the experimental profiles at $x = +0.15$ m, the content of three reactive species (H_2 , CH_4 , and CO) is very low in the vicinity of the fuel jet on the side of positive abscissa [the right side in Fig. 1(c)] where the sampling probe was introduced into the furnace. It could be possible that the interaction between the sampling probe and the fuel jet plays a role in such a phenomenon; the upstream of the sampling point in the fuel jet is perturbed by the probe while it is not the case for the side of negative abscissa.

The measurements show a farther penetration of the fuel jets in the flow field as compared to the results obtained from the simulation;

higher peaks in the experimental species profiles are observed for all locations except $x = \pm 0.15$ m. The shapes of the profiles of the two reactive species H_2 and CH_4 are quite similar while the CO profiles appear to be wider particularly at $x = \pm 0.06$ m, because CO is not only the fuel species but also the intermediate minor species formed from oxidation of CH_4 . The latest point is quite clear from the simulation profiles, as shown in Fig. 10; at $x = \pm 0.06$ m, the CO profiles are rather flat between $z = 0.2$ and 0.5 m where oxidation occurs, and there is contribution of CO intermediately produced. Overall, most of the expected levels, shapes, and trends observed in experiment are captured by the numerical results.

Figure 11 shows the comparison between the measurement and the simulation results for the oxidizer O_2 and the combustion product CO_2 . It is noted that the distribution of oxygen is not symmetrical between the two measured O_2 profiles at $x = +0.09$ m and $x = -0.09$ m while it is not the case for the predicted O_2 profiles. The experimental trend of the measured O_2 profiles at $x = \pm 0.12$ m is not fully recovered by the simulation. As far as the profiles of CO_2 are concerned, the distribution is quite homogeneous, and the level is always higher than 13% (by volume), confirming that the combustion is highly diluted by the combustion products. The prediction of CO_2 can be seen acceptable as compared to the measurement.

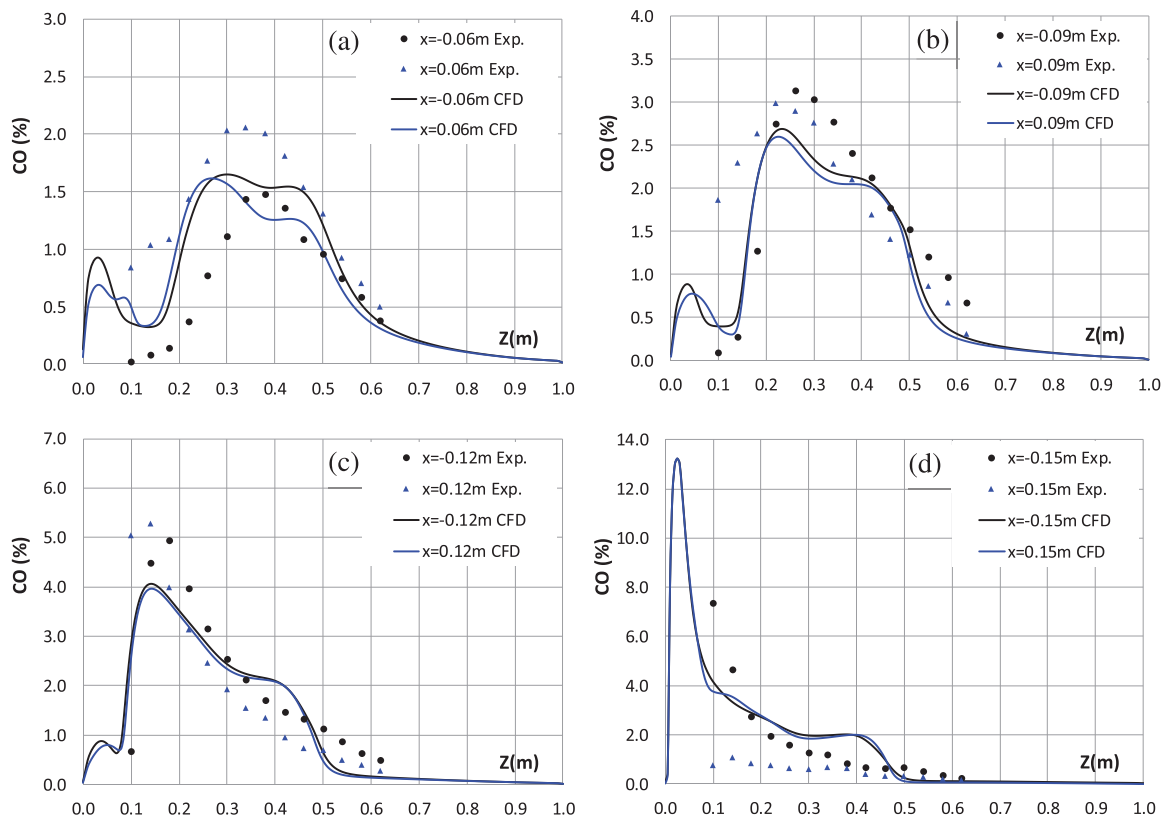


FIG. 10. Comparison between the experimental and computed profiles of CO in volume percentage on dry basis, obtained at different (negative and positive) x positions and along the furnace height z . (a) $x = \pm 0.06$ m, (b) $x = \pm 0.09$ m, (c) $x = \pm 0.12$ m, and (d) $x = \pm 0.15$ m. Maximum measurement uncertainty is 0.28%.

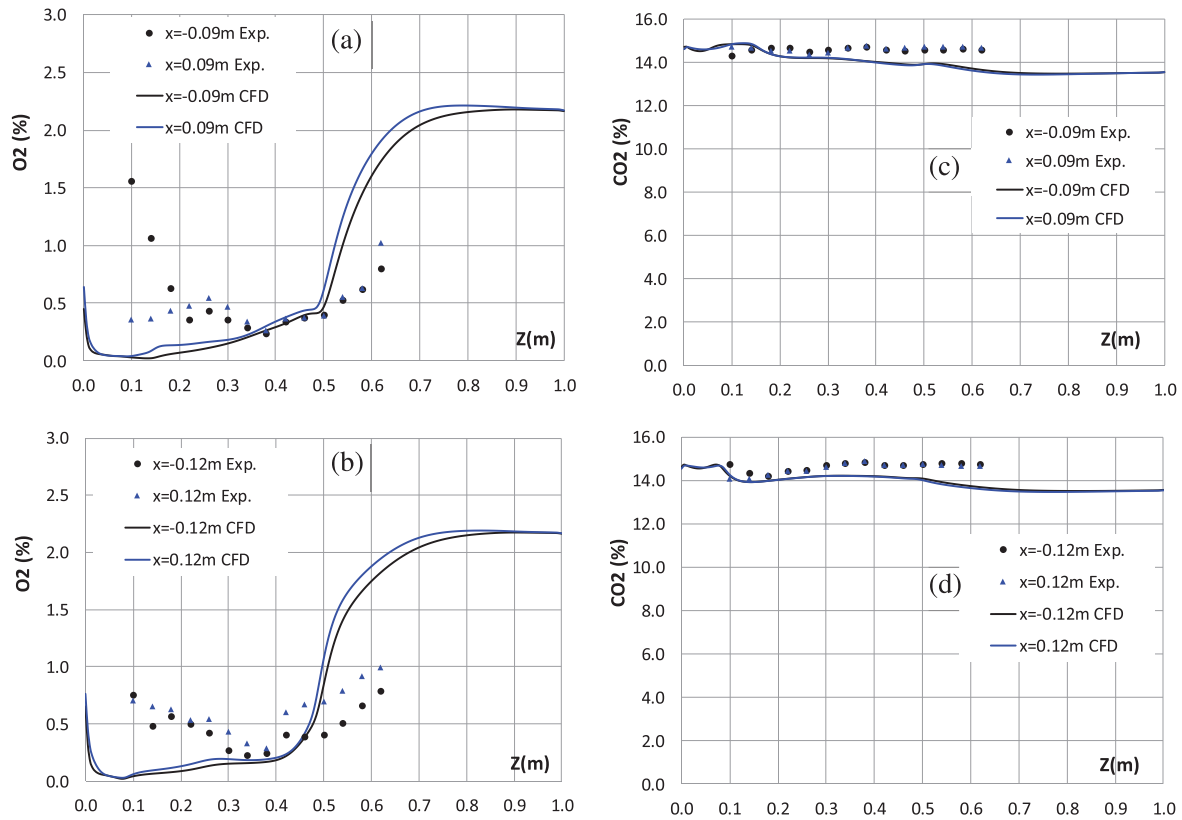


FIG. 11. Comparison between the experimental and computed profiles of O_2 and CO_2 in volume percentage on dry basis, obtained at two (negative and positive) x positions and along the furnace height z . (a) $x = \pm 0.09$ m and (b) $x = \pm 0.12$ m for O_2 and (c) $x = \pm 0.09$ m and (d) $x = \pm 0.12$ m for CO_2 . Maximum measurement uncertainty is 0.35% and 0.85% for O_2 and CO_2 , respectively.

IV. CONCLUSIONS AND PERSPECTIVES

A comprehensive modeling approach was proposed to model flameless combustion of low calorific value gases in which gaseous radiative properties were modeled with the spectral line-based weighted-sum-of-gray-gases (SLWSSG) approach. The emissivity weights and absorption coefficients were evaluated using the correlation of the line-by-line spectra of H_2O and CO_2 and optimized for a range of optical thicknesses and temperatures encountered in the considered furnace. The development of an experimental dataset of the combustion of a low calorific value syngas in a pilot furnace was used for the validation of the modeling approach. The furnace operates under flameless combustion, and the radiation is the dominant mode of heat transfer. The comparison between the simulation and the experiment confirms the need for such comprehensive modeling in the combustion system; heat transfer, energy balance, temperature, and chemical species fields were fairly predicted by the simulation.

This promising approach provides an interesting framework for comprehensive combustion modeling, which can include soot and NO_x formation featuring strong interactions with radiative heat transfers. The discussed methodology can be easily extended to multiple fuel injection systems and to the combustion of green

hydrogen or ammonia, which has gained much interest in research and industry decarbonization. The gas radiative properties can be calculated using spectroscopic databases presented under a lookup table, which may yield more accuracy than correlations.^{57,58} Another perspective is also opening regarding the development of the reduced order model or digital twins using machine learning techniques. Each physical phenomenon should then be described in the framework of comprehensive multi-physics modeling to secure the production of large reliable databases for training of these machine learning based models.

ACKNOWLEDGMENTS

This paper was prepared to honor Professor Michael Pfitzner for his inspiring and seminal works on the modeling of complex combustion systems. H.-T.N. is funded by Agence Nationale de la Recherche et de la Technologie (ANRT) and ArcelorMittal under CIFRE No. 2019/0056. The experiment of G.M. was funded by the Walloon Government and ArcelorMittal. The help in different experimental and numerical aspects of Dr. Delphine Lupant, Mrs. Patricia Evrard, Mr. Marcel Rustin, and Mr. Christophe Coetsier at the University of Mons is gratefully acknowledged.

AUTHOR DECLARATIONS

Conflict of Interest

The authors have no conflicts to disclose.

DATA AVAILABILITY

The data that support the findings of this study are available from the corresponding author upon reasonable request.

REFERENCES

- ¹J. A. Wünnig and J. G. Wünnig, "Flameless oxidation to reduce thermal NO-formation," *Prog. Energy Combust. Sci.* **23**, 81–94 (1997).
- ²T. Hasegawa and R. Tanaka, "High temperature air combustion-revolution in combustion technology; Part I: New findings on high temperature air combustion," *JSME Int. J. Ser. B* **41**, 1079–1084 (1998).
- ³A. Cavaliere and M. de Joannon, "Mild combustion," *Prog. Energy Combust. Sci.* **30**, 329–366 (2004).
- ⁴M. K. Denison and B. W. Webb, "A spectral line-based weighted-sum-of-gray-gases model for arbitrary RTE solvers," *J. Heat Transfer* **115**, 1004–1012 (1993).
- ⁵V. P. Solovjov, D. Lemonnier, and B. W. Webb, "The SLW-1 model for efficient prediction of radiative transfer in high temperature gases," *J. Quant. Spectrosc. Radiat. Transfer* **112**(7), 1205–1212 (2011).
- ⁶P. Evrard, V. Feldheim, and P. Lybaert, "An alternative method to optimise the SLW grey gases," *J. Phys.* **395**, 012007 (2012).
- ⁷P.-D. Nguyen, A. Danda, M. Embouazza, M. Gazdallah, P. Evrard, and V. Feldheim, "Application of the spectral line-based weighted-sum-of-gray-gases model (SLWGG) to the calculation of radiative heat transfer in steel reheating furnaces firing on low heating value gases," *J. Phys.* **369**, 012008 (2012).
- ⁸B. W. Webb, V. P. Solovjov, and F. André, "The spectral line weighted-sum-of-gray-gases (SLW) model for prediction of radiative transfer in molecular gases," in *Advances in Heat Transfer*, edited by E. M. Sparrow, J. P. Abraham, J. M. Gorman, and W. J. Minkowycz (Academic Press, New York, 2019), Vol. 51, pp. 207–298.
- ⁹M. K. Denison and B. W. Webb, "An absorption-line blackbody distribution function for efficient calculation of gas radiative transfer," *J. Quant. Spectrosc. Radiat. Transfer* **50**, 499–510 (1993).
- ¹⁰M. K. Denison and B. W. Webb, "Development and application of an absorption-line blackbody distribution function for CO₂," *Int. J. Heat Mass Transfer* **38**, 1813–1821 (1995).
- ¹¹L. S. Rothman, C. Camy-Peyret, J.-M. Flaud, R. R. Gamache, A. Goldman, D. Górvitch, R. L. Hawkins, J. Schroeder, J. E. A. Selby, and R. B. Watson, <http://www.hitran.com> for "HITEMP, The High-Temperature Molecular Spectroscopic Database" (2000).
- ¹²S. A. Tashkun, V. I. Perevalov, A. D. Bykov, N. N. Lavrentieva, and J.-L. Teffo, <ftp://ftp.iao.ru/pub/CDS-1000> for "Carbon Dioxide Spectroscopic Databank (CDS-1000)" (2002).
- ¹³S. A. Tashkun, V. I. Perevalov, J.-L. Teffo, A. D. Bykov, and N. N. Lavrentieva, "CDS-1000, the high temperature carbon dioxide spectroscopic databank," *J. Quant. Spectrosc. Radiat. Transfer* **82**(1–4), 165–196 (2003).
- ¹⁴M. F. Modest and R. S. Mehta, "Full spectrum k-distribution correlations for CO₂ from the CDS-1000 spectroscopic databank," *Int. J. Heat Mass Transfer* **47**, 2487–2491 (2004).
- ¹⁵M. F. Modest and V. Singh, "Engineering correlations for full spectrum k-distributions of H₂O from the HITEMP spectroscopic databank," *J. Quant. Spectrosc. Radiat. Transfer* **93**, 263–271 (2005).
- ¹⁶B. A. Dally, A. N. Karpetis, and R. S. Barlow, "Structure of turbulent non-premixed jet flames in a diluted hot flow," *Proc. Combust. Inst.* **29**, 1147–1154 (2002).
- ¹⁷E. Oldenhof, M. J. Tummers, E. H. van Veen, and D. Roekaerts, "Role of entrainment in the stabilisation of jet-in-hot-coflow flames," *Combust. Flame* **158**, 1553–1563 (2011).
- ¹⁸M. Ayoub, C. Rottier, S. Carpentier, C. Villiermaux, A. M. Boukhalfa, and D. Honoré, "An experimental study of mild flameless combustion of methane/hydrogen mixtures," *Int. J. Hydrogen Energy* **37**, 6912–6921 (2012).
- ¹⁹D. Lupant, B. Pesenti, and P. Lybaert, "Influence of probe sampling on reacting species measurement in diluted combustion," *Exp. Therm. Fluid Sci.* **34**, 516–522 (2010).
- ²⁰D. Lupant, "Caractérisation expérimentale détaillée et modélisation numérique de la combustion diluée du gaz naturel sur une installation de laboratoire de 30kW," Ph.D. thesis (University of Mons, 2011).
- ²¹D. Lupant and P. Lybaert, "Assessment of the EDC combustion model in MILD conditions with in-furnace experimental data," *Appl. Therm. Eng.* **75**, 93–102 (2015).
- ²²G. Mosca, D. Lupant, and P. Lybaert, "Effect of increasing load on the MILD combustion of COG and its blend in a 30 kW furnace using low air preheating temperature," *Energy Proc.* **120**, 262–269 (2017).
- ²³G. Mosca, "Numerical and experimental study on MILD combustion of low LHV fuels," Ph.D. thesis (University of Mons, 2017).
- ²⁴J. Badger, B. W. Webb, and V. P. Solovjov, "An exploration of advanced SLW modeling approaches in comprehensive combustion predictions," *Combust. Sci. Technol.* **194**, 225–241 (2022).
- ²⁵F. Liu, J.-L. Consalvi, P. J. Coelho, F. André, M. Gu, V. Solovjov, and B. W. Webb, "The impact of radiative heat transfer in combustion processes and its modeling—with a focus on turbulent flames," *Fuel* **281**, 118555 (2020).
- ²⁶L. Pierrot, P. Rivière, A. Soufiani, and J. Taine, "A fictitious-gas-based absorption distribution function global model for radiative transfer in hot gases," *J. Quant. Spectrosc. Radiat. Transfer* **62**, 609–624 (1999).
- ²⁷M. F. Modest, *Radiative Heat Transfer*, 2nd ed. (McGraw-Hill, New York, 2003).
- ²⁸A. A. Lacis and V. Oinas, "A description of the correlated-k distribution method for modelling nongray gaseous absorption, thermal emission, and multiple scattering in vertically inhomogeneous atmospheres," *J. Geophys. Res.* **96**, 9027–9063, <https://doi.org/10.1029/90JD01945> (1991).
- ²⁹W. A. Fiveland, "Discrete-ordinates solution of the radiative transport equation for rectangular enclosures," *J. Heat Transfer* **106**, 699–706 (1984).
- ³⁰P. J. Coelho, "Numerical simulation of the interaction between turbulence and radiation in reactive flows," *Prog. Energy Combust. Sci.* **33**, 311–383 (2007).
- ³¹R. Johansson, K. Andersson, B. Leckner, and H. Thunman, "Models for gaseous radiative heat transfer applied to oxy-fuel conditions in boilers," *Int. J. Heat Mass Transfer* **53**(1–3), 220–230 (2010).
- ³²A. Ziemniczak, R. Brittes, F. Cassol, and F. França, "Evaluation of the number of gray gases in the WSGG model," in Proceedings 22nd International Congress of Mechanical Engineering (COBEM 2013), Ribeirão Preto, SP, Brazil, 2013.
- ³³ANSYS FLUENT theory and user guide. v19.4.
- ³⁴L. C. Haber, "An investigation into the origin, measurement and application of chemiluminescent light emissions from premixed flames," Ph.D. thesis (VirginiaTech, 2000).
- ³⁵H. C. Hottel and A. F. Sarofim, *Radiative Transfer* (McGraw-Hill, New York, 1967).
- ³⁶B. W. Webb, V. P. Solovjov, and F. André, "An exploration of the influence of spectral model parameters on the accuracy of the rank correlated SLW model," *J. Quant. Spectrosc. Radiat. Transfer* **218**, 161–170 (2018).
- ³⁷F. C. Christo and B. B. Dally, "Modeling turbulent reacting jets issuing into a hot and diluted coflow," *Combust. Flame* **142**, 117–129 (2005).
- ³⁸S. A. Orszag, V. Yakhot, W. S. Flannery, F. Boysan, D. Choudhury, J. Maruzewski, and B. Patel, "Renormalization group modeling and turbulence simulations," in International Conference on Near-Wall Turbulent Flows, Tempe, Arizona, 1993.
- ³⁹B. F. Magnussen, "On the structure of turbulence and generalized eddy dissipation concept for chemical reaction in turbulent flow," in 19th AIAA Aerospace Science Meeting (1981).
- ⁴⁰I. R. Gran and B. F. Magnussen, "A numerical study of a bluff-body stabilized diffusion flame. Part 2. Influence of combustion modeling and finite-rate chemistry," *Combust. Sci. Technol.* **119**, 191–217 (1996).
- ⁴¹R. W. Bilger, S. H. Starner, and R. J. Kee, "On reduced mechanisms for methane-air combustion in nonpremixed flames," *Combust. Flame* **80**, 135–149 (1990).
- ⁴²A. De, E. Oldenhof, P. Sathiah, and D. Roekaerts, "Numerical simulation of delft-jet-in-hot-coflow (DJHC) flames using the eddy dissipation concept

- model for turbulence-chemistry interaction,” *Flow. Turbul. Combust.* **87**, 537–567 (2011).
- ⁴³J. Aminian, C. Galletti, S. Shahhosseini, and L. Tognotti, “Numerical investigation of a MILD combustion burner: Analysis of mixing field, chemical kinetics and turbulence-chemistry interaction,” *Flow. Turbul. Combust.* **88**, 597–623 (2012).
- ⁴⁴A. Parente, M. R. Malik, F. Contino, A. Cuoci, and B. B. Dally, “Extension of the eddy dissipation concept for turbulence/chemistry interactions to mild combustion,” *Fuel* **163**, 98–111 (2016).
- ⁴⁵N. Romero, H. Bao, X. Huang, K. Martin, and D. Roekaerts, “Simulation of flameless combustion in delft lab-scale furnace using EDC model,” in Proceedings of the 9th European Combustion Meeting, 2019.
- ⁴⁶T. Silei, G. Sorrentino, R. Ragucci, and C. Galletti, “Reaction-rate based modeling of MILD combustion in a cyclonic burner,” in Proceedings of the 10th European Combustion Meeting, 2021.
- ⁴⁷S. B. Pope, “Computationally efficient implementation of combustion chemistry using in situ adaptive tabulation,” *Combust. Theory Model.* **1**, 41–63 (1997).
- ⁴⁸C. Galletti, A. Parente, M. Derudi, R. Rota, and L. Tognotti, “Numerical and experimental analysis of NO emissions from a lab-scale burner fed with hydrogen-enriched fuels and operating in MILD combustion,” *Int. J. Hydrogen Energy* **34**, 8339–8351 (2009).
- ⁴⁹A. Parente, C. Galletti, and L. Tognotti, “A simplified approach for predicting NO formation in MILD combustion of CH₄-H₂ mixtures,” *Proc. Combust. Inst.* **33**, 3343–3350 (2011).
- ⁵⁰G. P. Smith, D. M. Golden, M. Frenklach, N. W. Moriarty, B. Eiteneer, M. Goldenberg, C. T. Bowman, R. K. Hanson, S. Song, W. C. Gardiner, Jr., V. V. Lissianski, and Z. Qin, see http://www.me.berkeley.edu/gri_mech/ for “GRI-Mech 3.0” (1999).
- ⁵¹A. Kazakov and M. Frenklach, see <http://combustion.berkeley.edu/drm/> (last accessed December 09, 2020).
- ⁵²M. Ferrarotti, W. De Paepe, and A. Parente, “Reactive structures and NO_x emissions of methane/hydrogen mixtures in flameless combustion,” *Int. J. Hydrogen Energy* **46**, 34018–34045 (2021).
- ⁵³X. Huang, M. J. Tummers, E. H. van Veen, and D. Roekaerts, “Modelling of MILD combustion in a lab-scale furnace with an extended FGM model including turbulence–radiation interaction,” *Combust. Flame* **237**, 111634 (2022).
- ⁵⁴A. Soufiani and E. Djavdan, “A comparison between weighted sum of gray gases and statistical narrow band radiation models for combustion applications,” *Combust. Flame* **97**, 240–250 (1994).
- ⁵⁵T. F. Smith, Z. F. Shen, and J. N. Friedman, “Evaluation of coefficients for the weighted sum of gray gases model,” *J. Heat Transfer* **104**, 602–608 (1982).
- ⁵⁶E. W. Grandmaison, I. Yimer, H. A. Becker, and A. Sobiesiak, “The strong jet/weak jet problem and aerodynamic modeling of the CGRI burner,” *Combust. Flame* **114**, 381–396 (1998).
- ⁵⁷J. Pearson, B. W. Webb, V. P. Solovjov, and J. Ma, “Updated correlation of the absorption-line blackbody distribution function for H₂O based on the HITEMP2010 database,” *J. Quant. Spectrosc. Radiat. Transfer* **128**, 10–17 (2013).
- ⁵⁸J. Pearson, B. W. Webb, V. P. Solovjov, and J. Ma, “Efficient representation of the absorption line blackbody distribution function for H₂O, CO₂, and CO at variable temperature, mole fraction, and total pressure,” *J. Quant. Spectrosc. Radiat. Transfer* **138**, 82–96 (2014).

